ACCEPTOR MOIETIES WITH EXTENDED CONJUGATION FOR SEMICONDUCTING POLYMERS

by

Xuyi Luo

A Dissertation

Submitted to the Faculty of Purdue University

In Partial Fulfillment of the Requirements for the degree of

Doctor of Philosophy

Department of Chemistry

West Lafayette, Indiana

May 2022

THE PURDUE UNIVERSITY GRADUATE SCHOOL

STATEMENT OF COMMITTEE APPROVAL

Dr. Jianguo Mei, Chair

Department of Chemistry

Dr. Christopher Uyeda

Department of Chemistry

Dr. Bryan Boudouris

Department of Chemistry

Dr. Letian Dou

Davidson School of Chemical Engineering

Approved by:

Dr. Christine Hrycyna

To my Family.

ACKNOWLEDGMENTS

First, I want to thank my advisor, Dr. Jianguo Mei for his constant mentorship; invaluable advice, and being the example in terms of hard work and leadership. I thank all my labmates for their support to help me complete my research. I would also like to thank my research collaborators especially Prof. Christopher Uyeda's group, Prof. Bryan Boudouris's group, and Prof. Letian Dou's group. They directly participated in the research and provided insightful discussion and feedback that helped me solve research problems. Finally, I want to appreciate the research financial support from the National Science Foundation (NSF CAREER Award No. 1653909) and Purdue University.

TABLE OF CONTENTS

LIST OF TABLES

LIST OF FIGURES

ABSTRACT

The field of semiconducting conjugated polymers has grown tremendously over the past few decades with innovations expanding the use of conjugated polymers into several devices such as transistors, light emitting diodes, and biocompatible electronics. For transistor devices, charge carrier mobility has rivaled the performance of amorphous silicon. The intrinsic properties of organic materials make them extremely attractive for further development and application. Organic materials are synonymous with terms such as lightweight, robust, flexible, and stretchable. A major advantage of conjugated polymers is their ability to be rendered solution processable with the alluring potential for large-area green manufacturing of electronic devices. However, these properties often fall short of their potential. Often strain engineering is often employed for favorable mechanical properties of polymer thin films.

Incorporation of acceptor-acceptor (A-A) type moieties into donor-acceptor (D-A) type conjugated polymers becomes a new strategy to tune their electronic properties. In this work, we first demonstrate an efficient convergent route to prepare isoindigo-based A-A type building blocks - bis-isoindigos - via the palladium-catalyzed oxidative coupling. Bis-isoindigo-based polymers show high planarity and delocalized frontier molecular orbitals with lowered LUMO and intact HOMO energy levels, in comparison with their corresponding mono-isoindigo counterparts. Moreover, fluorine substitution on donors only lowers HOMO levels of Bis-IID polymers. This study asserts that the D-A-A strategy is effective in selectively tuning FMO energy levels of conjugated polymers, complementary to the D-D-A approach for the HOMO energy level tuning. Finally, we investigated the effect ofisomer structure has on the properties of conjugation polymers utilizing diazines to decouple the effects of spatial arrangement from heteroatom placement. These studies highlight the significant impact of side-chain sequence regioisomerism on aggregation behaviors, morphologies, and subsequently charge transport properties of donor-acceptor type conjugated polymers.

CHAPTER.1 GENERAL INTRODUCTION TO ORGANIC SEMICONDUCTORS

The first high performing conjugated polymer was halogen doped poly acetylene studied by Shirakawa, MacDiaramid, and Heeger.Further developments into the nascent field of conducting polymers continued and resulted with the trio claiming the Nobel Prize in Chemistry in 2000. Since then, conjugated polymers have attracted a wide range of attention as functional organic materials for solar cells, light emitting diodes and field-effect transistors. Polymer materials are intrinsically lightweight, flexible, and capable of greener large-area solution manufacturing. Developments have led to high charge-carrier mobilities comparable with inorganic amorphous silicon. Additionally, conjugated polymers do not have to stand alone, high performing inorganic−organic perovskite solar cells contain organic semiconductors as hole or electron transporting layers as hybrid devices.

1.1 Charge Transport in Organic Semiconductors

There are two charge carrier species in electronics: holes and electrons. A hole is formed after oxidation of the polymer removes electrons leaving a positive charge or “hole”. Hole transporting materials are known as p-type materials and are the most common mode of transport found in organic polymers and therefore more studied. There are two charge carrier species in electronics: holes and electrons. A hole is formed after oxidation of the polymer removes electrons leaving a positive charge or “hole”. Hole transporting materials are known as p-type materials and are the most common mode of transport found in organic polymers and therefore more studied. Polymeric semiconductors however have much more complicated solid-state structure and are high disordered in comparison. Organic semiconductors are held together by secondary forces (van der Waals force), and the weak intermolecular interactions render these polymers to have poor charge transport characteristics.

1.2 Conjugated Polymers for Organic Electronics

The arrival of high-performance donor−acceptor (D−A) polymers however challenged the idea that high crystallinity was a requirement for high mobility. D−A polymers had lower crystallinity

and outperformed previously reported highly crystalline polythiophenes. A fast intramolecular charge transport along the polymer backbone in a quasi-one-dimensional process with infrequent charge hopping between πstacks was proposed. In this case it only requires low energy hopping between chains requiring highly planarized backbones to minimize torsion for efficient charge hopping. The intrachain transport predominates and charge hopping can occur between chains within short aggregated domains.

1.2.1 Organic Field Effect Transistors

A FET is a three terminal electronic device consisting of a semiconducting layer deposited between two ohmic contacts (source and drain), separated by a thin dielectric layer from a third contact, the gate. The gate can be positioned either on the top (top gate) or at the bottom (bottom gate). A FET provides amplifying and/or switching of electronic signals passing through the semiconducting layer as a response to a certain voltage applied to the gate contact (V_G) The amount of current that is able to flow between the source and drain—through the active layer—subsequently marks the device's performance in terms of its ability to transport charge carriers. In a such simplistic device architecture, OFETs have then been used as one of the robust ways to extract and benchmark the semiconducting properties of organic materials. These electronic devices have thus been widely studied to the extent of improving the primitive charge carrier mobilities from $\sim 10^{-5}$ to higher than tens of cm^2/Vs. Ordinarily, the transistor performance is tested by analyzing the channel layer's transductance as a response to an applied bias at the gate (V_G). By applying another voltage (V_{DS}) between source and drain contacts, the performance of the channel layer can be monitored from the current flow through the organic material. Extrapolating transfer and output curves, a few key parameters are usually reported to characterize OFET performance. First, charge carrier mobility (μ), ON/OFF current ratio, as well as the threshold voltage (V_{TH}) are to be evaluated. Charge carrier mobility tells how fast the charge carriers can move from one contact to the other, while the ON/OFF ratio shows the difference between currents before the device could be turned "ON" and when the device is switched on. The threshold voltage is an indication of the minimum voltage V_{DS} that must be applied before the device can be "turned on". V_{TH} is oftentimes reported with its subthreshold slope (SS) which is the voltage difference required to increase the current between source and drain by a factor of ten. The devices architectures, charge transport mechanisms, the

intrinsic structure-to-property dependence have been widely reported and are beyond the scope of this discussion.

1.2.2 Organic Electrochemical Transistors

An organic electrochemical transistor (OECT) is a coupled ionic-electronic device where the active layer material undergoes doping and de-doping based upon the electrolytic components upon application of a gate bias. Owing to the high-sensitivity sensing and sub-voltage operation properties of OECTs, various application advances have been achieved with respect to OECTs including biological sensors, memory and neuromorphic devices, and electrophysiological monitoring. Despite the high degree of initial success that many oft-studied macromolecular systems have had in the realm of OECTs, there are significant opportunities to develop next-generation electrochemically-active polymers to improve device performance, switching speed, and cycling stability.

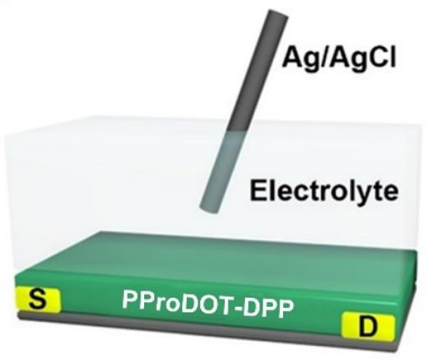

Figure 2.1 A typical device structure of the bottom-contact OECT device.

Semiconducting polymers with solubilizing hydrophilic side chains exhibit high volumetric capacitance, efficient charge transport, and rapid ion injection, as well as compatibility with aqueous electrolytes. Therefore, they have generated extensive scientific interest as a class of channel components for OECTs Among the various types of semiconducting polymers, 3,4-alkylenedioxythiophene-based polymers have achieved remarkable success in many electrochemical applications, such as electrochromic devices and supercapacitors. Moreover, they are useful for OECT channel materials due to their high redox stability and charge capacity. In

fact, a model material for many studies, poly(3,4-ethylene dioxythiophene) doped with poly(styrene sulfonate) (PEDOT:PSS) has recently reached high figure-of-merit (i.e., the product of charge mobility and volumetric capacitance, μC*) values of 1,500 F cm^{-1} V-1 s^{-1} in OECT devices.

1.3 Design Strategies of Conjugated Polymers

Understanding structure−property relationships is fundamental to achieve high performance. The typical structure of a semiconducting polymers is divided into two regimes: the flexible solubilizing side chains, and the semi-rigid conjugated backbone. These two regimes both impact the self-assembly of polymer chains into crystalline domains. The solid-state microstructure is extremely important the performance of devices, and the microstructure is heavily dependent on processing conditions. Polymer thin film structure is also host to many issues such as chemical structure defects, polymorphism, domain orientation, grain boundaries, impurities, and phase separation for blended systems. Below we will discuss the benefits and limitations of both approaches.

1.3.1 Backbone Engineering

Myriad of conjugated polymers have been made by introducing the combination of electron-rich aromatic donors (D) and electron-deficient aromatic acceptors (A). It is widely practiced that two or more donors (D-D) are chosen to tune the optoelectronic properties such as the HOMO levels and absorption profiles of D-A polymers. In contrast, the incorporation of a conjugated building block containing two electron-accepting subunits (A-A) is comparatively less adopted. A limited number of reports on A-A building blocks have only appeared in recent years, as summarized in Scheme 1. Berrouard et al. first obtained a thieno[3,4-c]pyrrole-4,6-dione (TPD) dimer by Ullmann reaction in 2011. Bis-TPD copolymers were subsequently reported with efficient ambipolar charge transport properties. Polander et al. synthesized a naphthalene diimides (NDI) dimer via Stille coupling, which showed a higher electron mobility than its monomeric parent. Yang et al. reported a bis-diketopyrrolopyrrole (bis-DPP) moiety as an electron acceptor. It is noted that Stille coupling with large excess of DPP dibromide was adopted in the synthetic approach. Several bis-DPP copolymers have shown excellent ambipolar mobilities. James et al.

reported a di-thieno-benzo-isoindigo (BdiTBI) based building block, connecting two thieno-benzo-isoindigo moieties at two phenyl groups by Suzuki coupling. More recently, a bis-Pyridalthiadiazole based building block was reported by Zhu et al.. A regioregular dual-acceptor strategy rendered the polymer with an outstanding charge transport behavior.

1.3.2 Side Chain Engineering

In molecular design of D-A polymers, side chain engineering has proved to be effective in tuning electronic and morphological properties of resulting polymer thin films. Rational combination of different side chains is one of such strategies. There are generally two approaches to introduce a combination of side chains. The first approach deals with the copolymerization of two monomers bearing the targeted side chains. For an example, Zhang et. al. developed a DPP (diketopyrrolopyrrole) monomer bearing urea-containing alkyl chains. Changing the ratio of the urea-chain DPP monomers to the branched-alkyl-chain DPP monomers in polymerization provided a series of DPP random copolymers with enhanced charge mobilities. The second approach involves a single monomer bearing two different side chains, which would produce alternating copolymers. We previously reported such an isoindigo building block with one alkyl chain and one siloxane hybrid chain. The corresponding polymer thin films adopted bimodal packing orientation and exhibited improved charge transport performance.

1.4 Objectives of This Dissertation

In this dissertation, we aim to further the understanding of structure-property relationships in semiconducting polymers with extended acceptor moieties. Our first target is to incorporate acceptor-acceptor (A-A) type moieties into donor-acceptor (D-A) type conjugated polymers. Therefore, a new molecular platform with an extended accepting unit will be established, potentially allowing for both further fundamental understandings, new electronic applications and bioimaging purposes. A comprehensive study into the effects of side-chain-enabled regioisomer acceptors in semiconducting polymers will be further investigated. This study will highlight the significant impact of side-chain sequence regioisomerism on charge transport properties of conjugated polymers with extended acceptors bearing multiple side chains and the new finding could be applied in future design of building blocks for functional D-A type semiconducting

polymers. Finally, next-generation design of polymers with extended acceptors for OECTs will be carried out. This effort will provide a roadmap for the design of electrochemically-active macromolecules for accumulation-mode OECTs where extended acceptor cores are incorporated into an all-donor polymer, and expand the application possibility for extended acceptors.

CHAPTER 2. BIS-ISOINDIGOS: NEW ELECTRON-DEFICIENT BUILDING BLOCKS FOR CONSTRUCTING CONJUGATED POLYMERS WITH EXTENDED ELECTRON DELOCALIZATION

2.1 Introduction

Conjugated polymers have attracted a wide range of attention as functional organic materials for solar cells, light emitting diodes and field-effect transistors, among others. A myriad of conjugated polymers have been made by introducing the combination of electron-rich aromatic donors (D) and electron-deficient aromatic acceptors (A). It is widely practiced that two or more donors (D-D) are chosen to tune the optoelectronic properties such as the HOMO levels and absorption profiles of D-A polymers.[1–3] In contrast, the incorporation of a conjugated building block containing two electron-accepting subunits (A-A) is comparatively less adopted. A limited number of reports on A-A building blocks have only appeared in recent years, as summarized in Scheme 1. Berrouard *et al.* first obtained a thieno[3,4-c]pyrrole-4,6-dione (TPD) dimer by Ullmann reaction in 2011 (Figure 2.1).[4] Bis-TPD copolymers were subsequently reported with efficient ambipolar charge transport properties.[5,6] Polander *et al.* synthesized a naphthalene diimides (NDI) dimer via Stille coupling, which showed a higher electron mobility than its monomeric parent.[7] Yang *et al.* reported a bis-diketopyrrolopyrrole (bis-DPP) moiety as an electron acceptor.[8] It is noted that Stille coupling with large excess of DPP dibromide was adopted in the synthetic approach. Several bis-DPP copolymers have shown excellent ambipolar mobilities.[9] James *et al.* reported a di-thieno-benzo-isoindigo (BdiTBI) based building block, connecting two thieno-benzo-isoindigo moieties at two phenyl groups by Suzuki coupling.[10] More recently, a bis-Pyridalthiadiazole based building block was reported by Zhu *et al.*. A regioregular dual-acceptor strategy rendered the polymer with an outstanding charge transport behavior.[11]

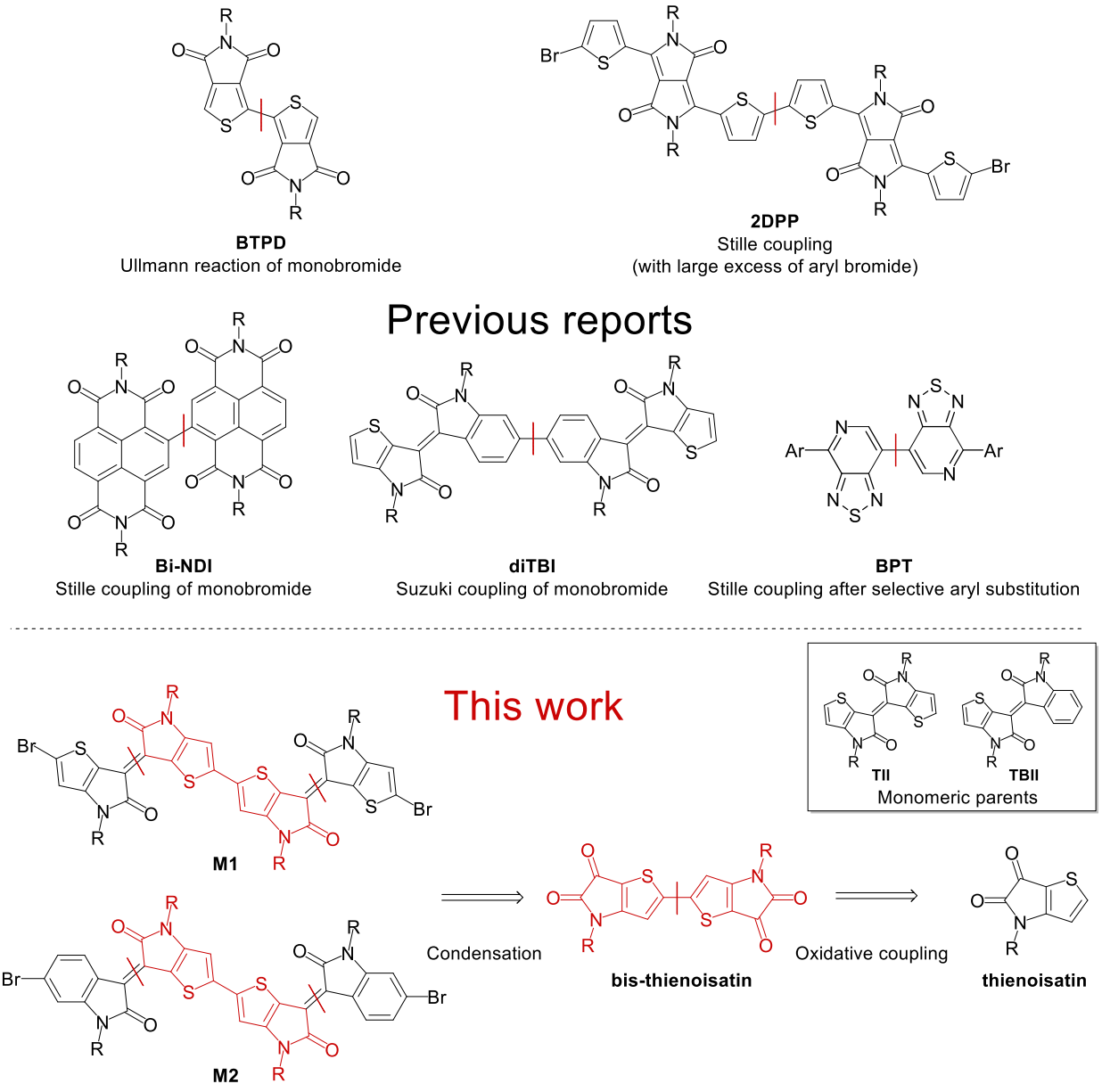

Figure 2.1 Examples of acceptor-acceptor building blocks

2.2 Polymer Design

We envision the D-A-A design as an alternative strategy to adjust the optoelectronic properties with an advantage of effective HOMO/LUMO level tuning and render desired optoelectronic properties when A-A building blocks become readily available. Unfortunately, we noticed that the synthesis of A-A building blocks listed above is undoubtedly challenging. For the coupling involving homocoupling of acceptor dihalides, it usually leads to low yields due to the presence

of undesired oligomerization. It also makes the purification difficult. For the homocoupling involving acceptor monohalides, the mono-functionalization of an electron deficient building block itself is very inefficient and challenging. To make the A-A strategy more appealing in synthesis of D-A conjugated polymers, it is imperative to design new synthetic routes to readily access functionalized A-A building blocks.

Here, we report two new isoindigo based A-A moieties (Bis-IIDs) M1 and M2 through an efficient synthetic route. Isoindigo (IID), first introduced by Reynolds *et al.*, was among the most studied building blocks.[12] Owing to its electron withdrawing lactam groups, rigid backbone, and straightforward synthesis, IID widely serves as an electron acceptor in D-A conjugated polymers.[13] Extensive design efforts including side chain engineering,[14,15] heteroatom fusion,[16–18] and conjugation length extension,[19–22] have been made to tune their optoelectronic properties and morphologies. In this report, M1 and M2 have two IID subunits linked through α positions of the corresponding thiophenes. We envision that such linkage would enable small thiophene-thiophene dihedral angles, ensuring the retention of planarity throughout the moiety.[23] This feature would further render planarized D-A-A type polymers with extended effective conjugation lengths and enhanced interchain interactions, which can be beneficial to charge transport. Moreover, we choose two different donors to study energy levels of their corresponding polymers (P1, P1F, P2 and P2F, Figure 2.2). In particular, we expect to obtain fine-tuned FMO levels. P1 and P2 should exhibit considerably lowered LUMO levels but only slightly altered HOMO levels compared to their monomeric based analogues, while P1F and P2F have further tuning on FMO levels due to fluorine substitution.[24]

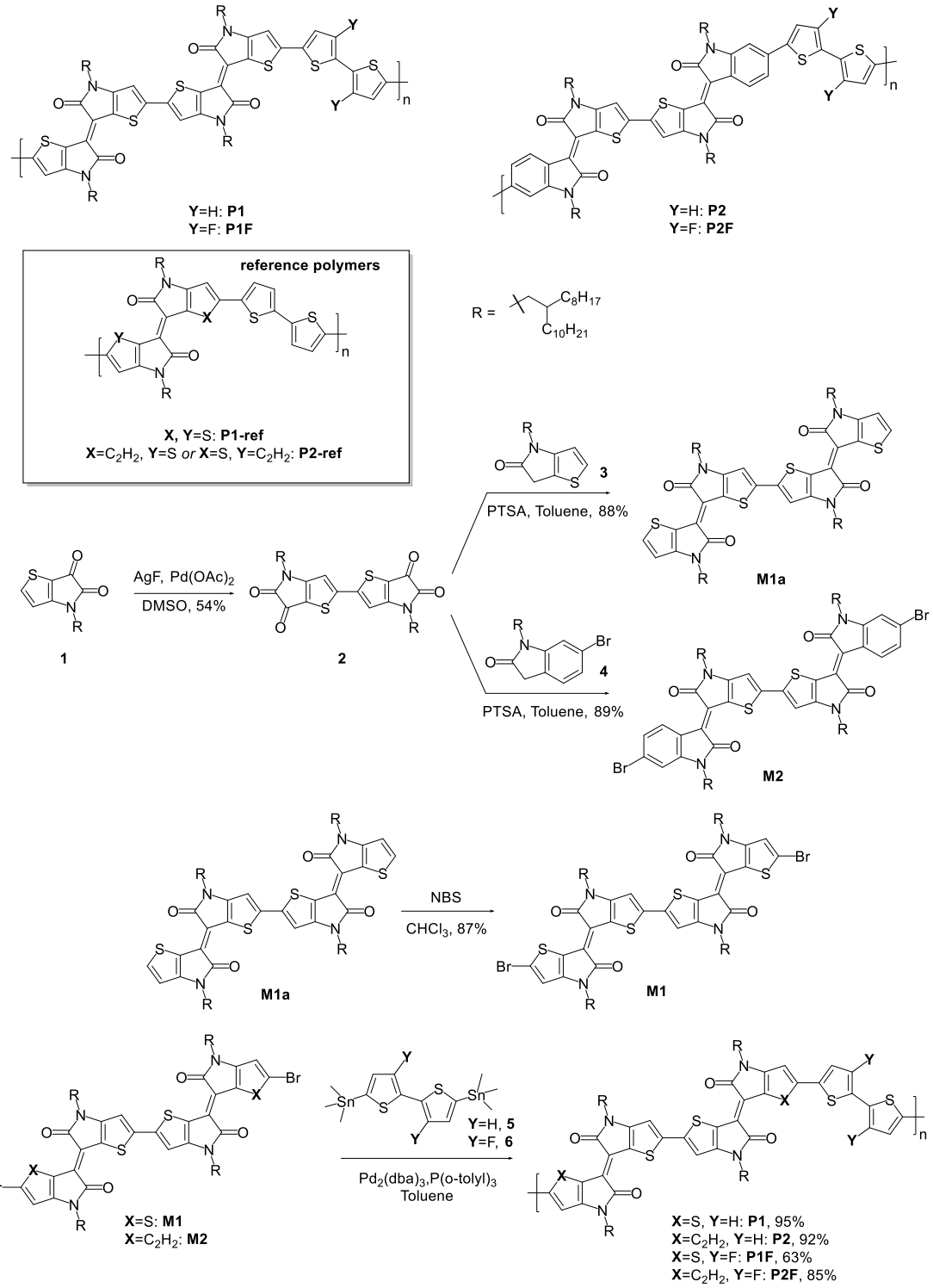

Figure 2.2 Synthetic scheme to Bis-IID polymers

2.3 Results and Discussion

2.3.1 Material and Synthesis

The synthesis for all Bis-IIDs was proposed and carried out in this work, as illustrated in Figure 2.2. We initially intended to prepare bis-thienoisatin 2 through cross-coupling of thienoisatin halide and its boronic ester.[9] Unfortunately, all attempts to turn thienoisatin 1 into its halide failed. Inspired by an oxidative coupling of thiophene derivatives, we decided to test oxidative coupling of 1 directly. To our delight, 2 was successfully synthesized from 1 in a single step, in spite of a low yield of 23%. After the optimization of reaction conditions, we were able to improve the yield up to 54% with palladium acetate as the catalyst and silver fluoride as the oxidant (Table 2.1).[12]

Table 2.1 optimization of oxidative coupling from 1 to 2. All conductions shown in the table were conducted with 200 mg compound 1 and 20 mL solvent, unless there is a special note.

Catalyst	Catalyst loading	AgF (eq.)	solvent	T (°C)	Time (h)	%Yield
$Pd_2(dba)_3$	3%	2.0	DMSO	65	12	25%[a]
$Pd_2(dba)_3$	3%	2.0	DMSO	90	20	49%
$Pd_2(dba)_3$	3%	4.0	DMSO	110	48	21%
$Pd(OAc)_2$	5%	0.75[b]	DMSO	90	24	40%[c]
$Pd(OAc)_2$	10%	2.1	DMSO	90	24	54%
$Pd_2(dba)_3$	3%	2.0	DMF[d]	90	20	36%[e]

[a]Most starting material remained unreacted. [b]Ag_2O was used in this condition instead of AgF, and 0.75 equivalent of benzoic acid was also added. [c]The reaction was conducted with 40 mg of compound 1. [d]20 mL DMF with several drops of DMSO was applied. [e]In this condition, the 2-octyldodecyl side chain of compound 1 was replaced with an n-octyl alkyl chain. Thieno-isatins (backbone of compound 1) with Linear alkyl chains dissolve better than those with branched alkyl chains in DMF.

After the aldol condensation with compound 3 and 4, M1a and M2 were obtained with high yields of 88% and 89%, respectively. Bromination of M1a gave M1 in a good yield of 87%. Finally, the polymers P1, P2, P1F and P2F were synthesized via Stille coupling of M1/M2 with compound 5/6. For a comparison, monomeric TII- and TBII-based analogues, P1-ref and P2-ref, were also synthesized following the reported procedures.[13] All polymers were purified by the Soxhlet extraction and fully characterized (see the supporting information). The molecular weights of P2 and P2F was evaluated by high-temperature gel permeation chromatography at 150 °C using 1,2,4-

trichlorobenzene as eluent. It's worth noting that the molecular weights for P1 and P1F cannot be accessed from the GPC measurements. Similar observations with TII substructures were previously reported, where thienoisoindigo polymers are believed to interact strongly with the column material.[14,15]

2.3.2 Density Functional Theory Simulations

To estimate the geometries and intrinsic electronic properties of Bis-IID polymers, density functional theory (DFT) calculations were performed on the trimers of Bis-IID polymers with methyl side chains as model molecules, shown in Figure 2.3. Computation was performed with Gaussian 09 using a hybrid B3LYP correlation functional and 6-31G(d) basis set. P1 and P1F display almost perfectly planar backbones with negligible dihedral angles between all thiophene-thiophene planes. By contrast, backbones of P2 and P2F are more twisted due to a 21° dihedral angle between thienyl and phenyl groups. Despite this, both A-A moieties (bis-IID subunits) still retain high planarity (2.9° and 0.9° dihedral angle between thiophene-thiophene planes respectively).

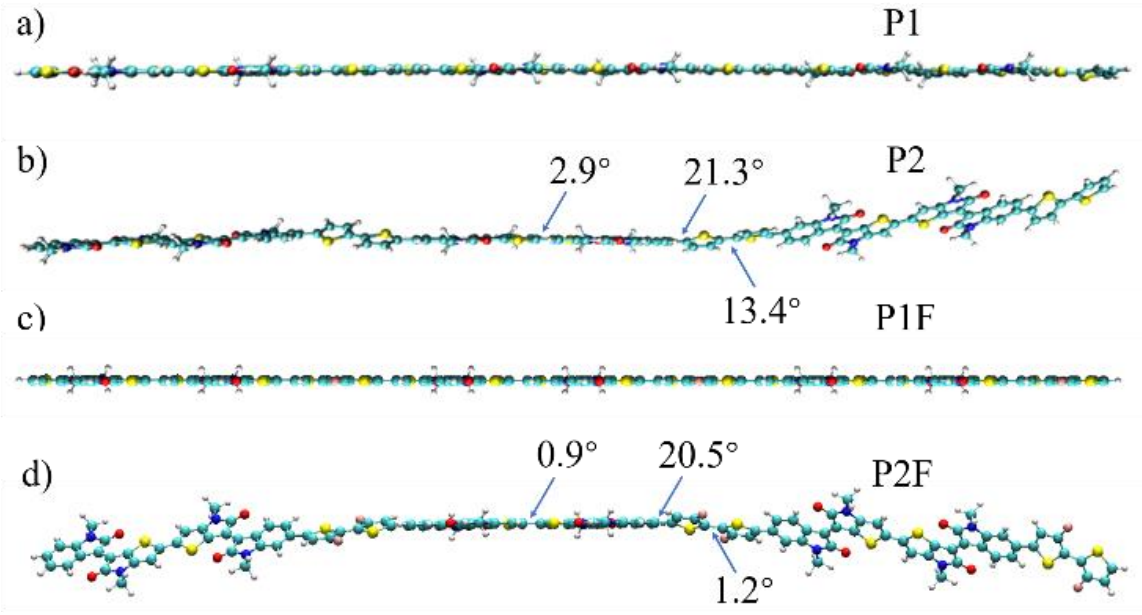

Figure 2.3 DFT optimized geometries of a) P1, b) P2, c) P1F and d) P2F trimer fragments (B3LYP/6-311g(d) level). Dihedral angles around single bonds are shown on P2 and P2F backbones.

The FMO electron distribution diagrams (Figure 2.4) reveal well dispersed frontier orbital electrons of all Bis-IID polymers, indicative of an effective delocalization along all polymer backbones. Fluorine substitutions on bithiophene have two major influences on the Bis-IID polymers. First, bithiophene subunits of P2F (1.2°) are much planer than those of P2 (13.4°), indicating F-S noncovalent interactions. Also, fluorine p_z orbitals contribute to HOMOs of P1F or P2F. Interestingly, fluorine p_z orbitals barely participate in LUMOs, showing that fluorine substitutions could have larger impact on HOMOs of Bis-IID polymers. Such prediction is verified in electrochemical estimations.

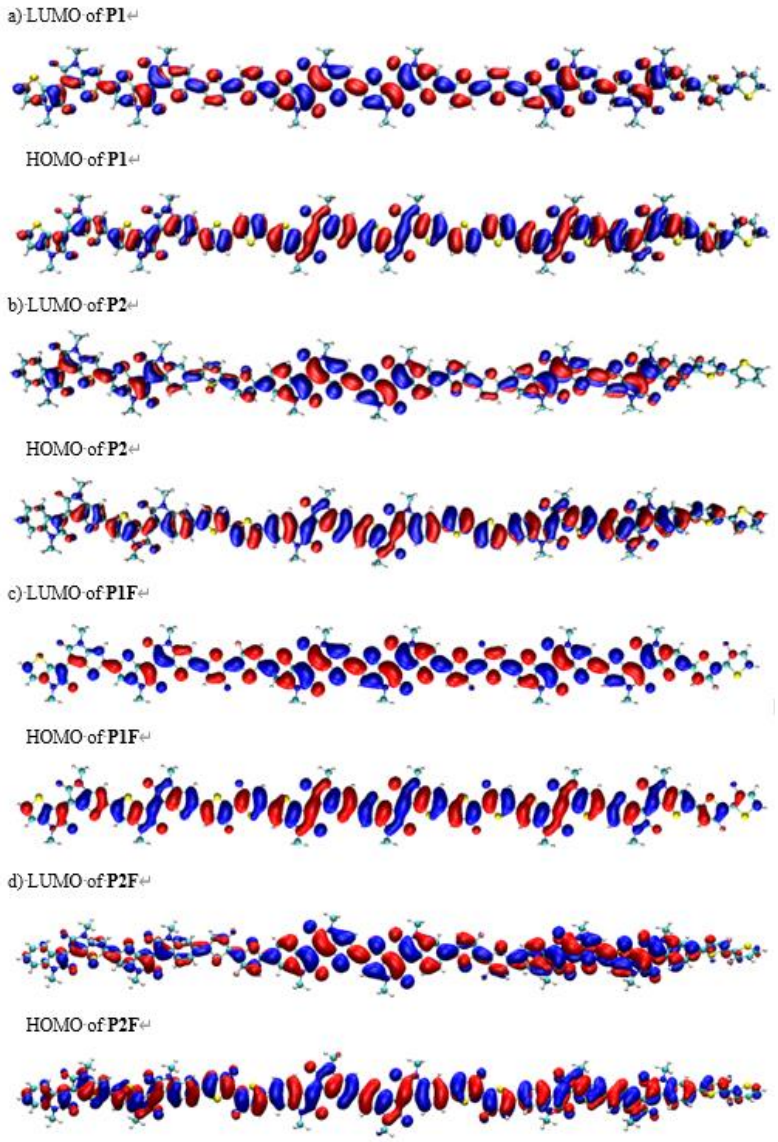

Figure 2.4 FMO electron distribution diagrams of Bis-IID trimers with density functional theory.

2.3.3 UV-Vis Spectroscopy

The photophysical properties of the polymers were studied with solution and solid-state UV-Vis-NIR spectroscopy. As shown in Figure 2.5, all polymers exhibit high energy π-π* transition bands and low energy charge transfer bands. All Bis-IID polymer films have most of charge transfer bands at NIR region. They show much higher absorption onsets than P1-ref and P2-ref. This observation agrees with our initial design of extended conjugation lengths. In addition, P1/P1F have much smaller band gaps than P2/P2F, which is attributed to their backbones with high planarity.

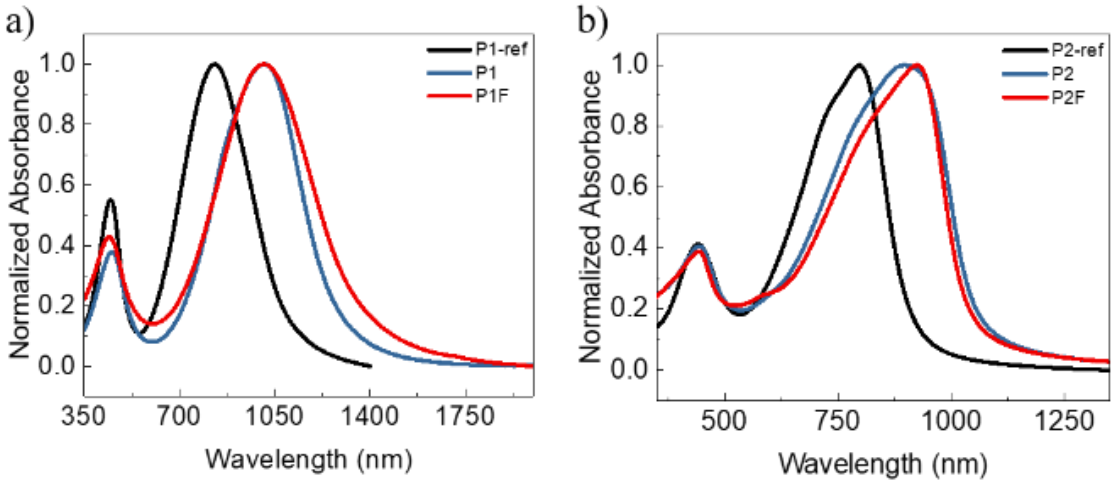

Figure 2.5 Normalized absorption spectra of a) P1-ref (black), P1 (blue) and P1F (red) films; b) Normalized absorption spectra of a) P2-ref (black), P2 (blue) and P2F (red) films.

The absorption profiles also reveal the different aggregation behaviors. While TII derivatives P1-ref and the TII monomer M1 show hypsochromic shifts in solid states, this phenomenon was not observed in TII derivative P1 and P1F. In fact, the solution and solid-state absorption profiles of Bis-IID polymers nearly overlap. This phenomenon strongly indicates a strong pre-aggregation in their solutions. To further understand the aggregation behavior of Bis-IIDs in solutions, temperature-dependent absorption spectra were taken at increasing temperature intervals of 10 °C in o-dichlorobenzene (Figure 2.6). Upon heating, P2 and P2F's intramolecular charge transfer peaks increase while the aggregation peaks noticeably decrease. By contrast, P1 and P1F only show a trend of peak intensity change, indicative of strong aggregation in o-dichlorobenzene even

at 100 °C. The stronger aggregation behavior of P1 and P1F reflects their strong interchain interaction induced by high planarity[29,30] and quinoidal character.[23,28]

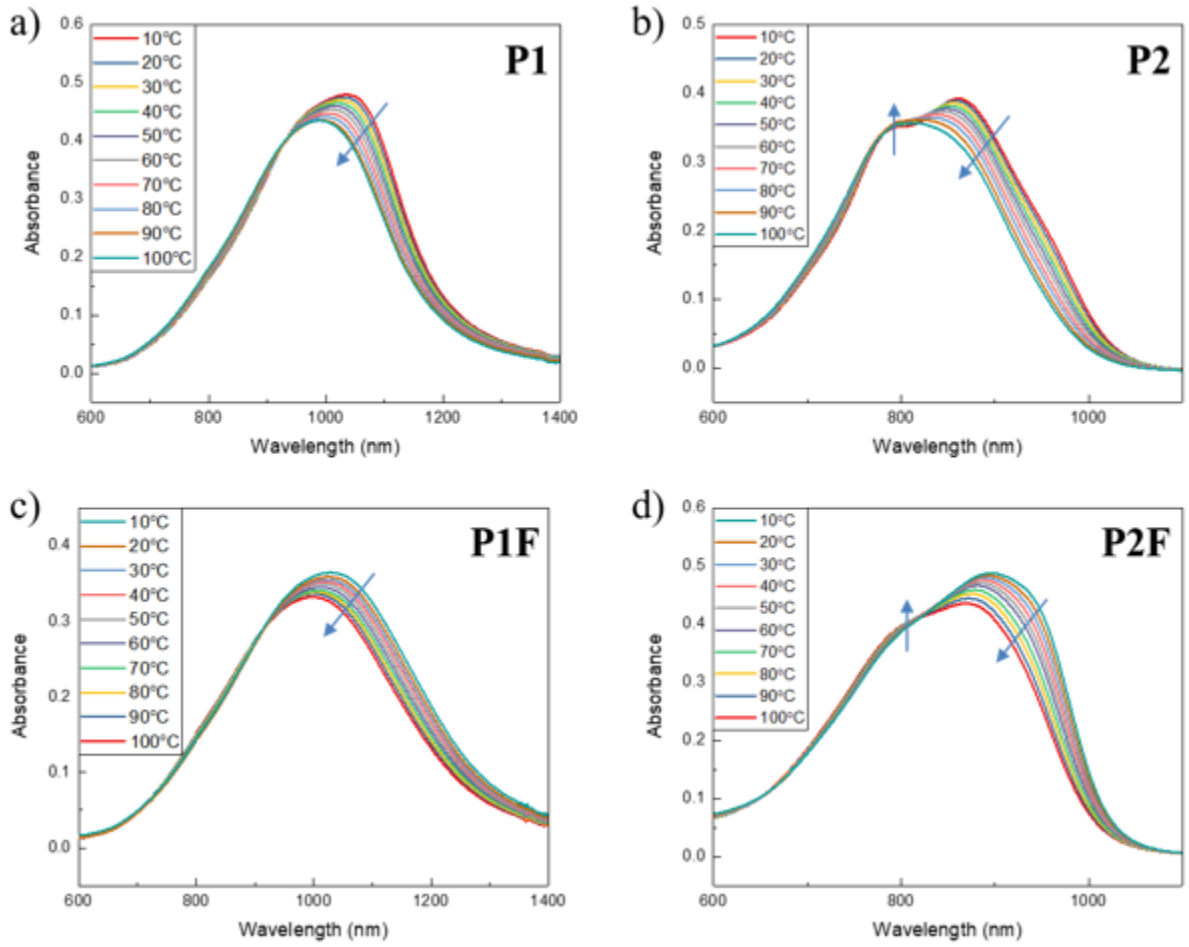

Figure 2.6 Temperature-dependent absorption spectra of a) P1, b) P2, c) P1F and d) P2F in *o*-dichlorobenzene.

2.3.4 Cyclic Voltammetry and Differential Pulse Voltammetry

To study the redox properties of polymer thin films, cyclic voltammetry (CV) and differential pulse voltammetry (DPV) were employed (Figure 2.7). Cyclic voltammograms of all Bis-IID polymers show quasi-reversible redox behavior, suggesting their potential as ambipolar semiconducting polymers. CV redox onsets are widely used to estimate HOMO/LUMO levels of semiconducting materials. However, like many IID based polymers, the optical band gaps of Bis-IID polymers are much narrower than those estimated from CV. This observation is partially

attributed to the sensitivity limitation of the CV measurement, resulting from its high capacitive charging currents background. With a reduced contribution from capacitive charging currents, differential pulse voltammetry (DPV) provides a much higher sensitivity than normal voltammetry measurements. It allows to record a sharper and clearer redox onset.[31] Thus, HOMO/LUMO energy levels of Bis-IID polymers were estimated from redox onset potentials of DPV.

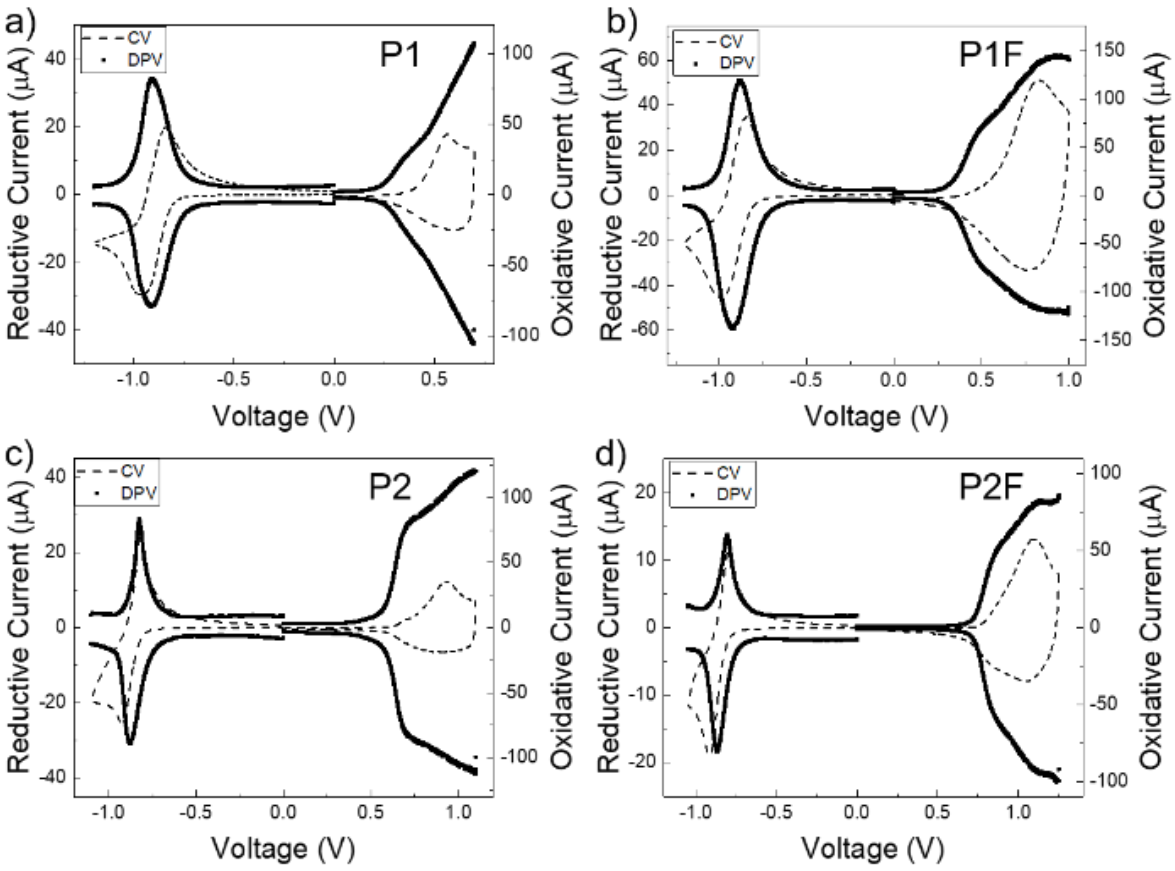

Figure 2.7 Cyclic Voltammograms (dashed lines) and differential pulse voltammograms (solid dots) of a) P1, b) P1F, c) P2 and d) P2F films in acetonitrile with 0.2 M n-Bu_4NPF_6 as supporting electrolyte. (scan rate: 40 mV s^{-1})

As references, P1-ref and P2-ref films were also characterized (Figure 2.8). The corresponding data were summarized in Table 2.2. Compared with D-A type P1-ref, D-A-A type P1 shows a drop of 0.12 eV in LUMO level, while the HOMO level is almost unchanged. In further comparison between P1 and P1F, P1F has a lowered HOMO level without changing the LUMO level. The

trends are similar for the P2-ref, P2 and P2F group. A 0.09 eV drop in LUMO and only a marginally deepened HOMO were observed from P2-ref to P2. Introduction of fluorine in P2F rendered a selective deepened HOMO level by 0.15 eV. The energy levels estimated by CV measurements also agree with DPV trends. The comparison between D-A polymers and D-A-A polymers clearly shows the potential of D-A-A strategy in selective tuning of the LUMO/HOMO energy lying, which makes it an attractive method to render ambipolar semiconducting materials and functional optoelectronic materials.

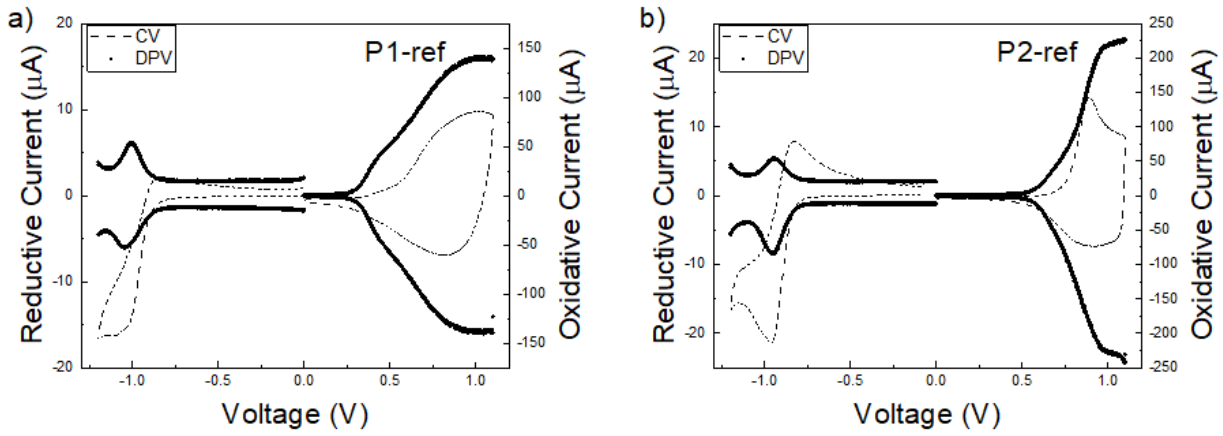

Figure 2.8 Cyclic Voltammograms (dashed lines) and differential pulse voltammograms (solid dots) of a) P1-ref film and b) P2-ref film in acetonitrile with 0.2 M *n*-Bu_4NPF_6 as supporting electrolyte (scan rate: 40 mV s^{-1}).

2.3.5 OFET Performance

Charge carrier transport properties of Bis-IID polymers were characterized by field-effect transistor measurements. Details of the device fabrication are described in the Experimental Section. Devices with bottom-gate bottom-contact (BGBC) architecture and Au as contacts under ambient conditions only shows p- type performance. Devices based on P2 and P2F films showed a typical p- type performance with highest μ_h of 0.024 cm^2 V^{-1} s^{-1} and 0.030 cm^2 V^{-1} s^{-1}, respectively (Figure 2.9).

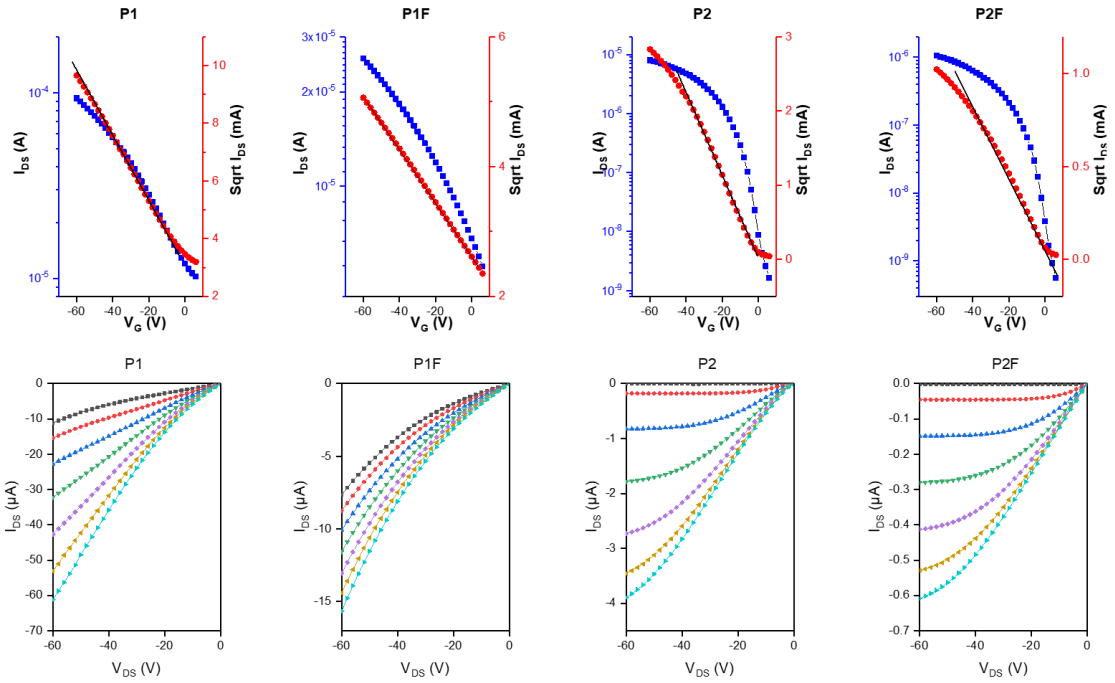

Figure 2.9 Typical transfer and output characteristics of FETs based on P1, P2, P1F and P2F with BGBC architecture and Au electrodes in ambient air.

Distinguished from P2 and P2F, both P1 and P1F devices exhibited an abnormally high "threshold" voltage and a small on-off ratio of 101. The high Vth and high off current imply a doping process by oxygen, given that materials with HOMO energy level above 5.0 eV are likely to make OFET devices unstable in air (Figure 2.10).[32,33]

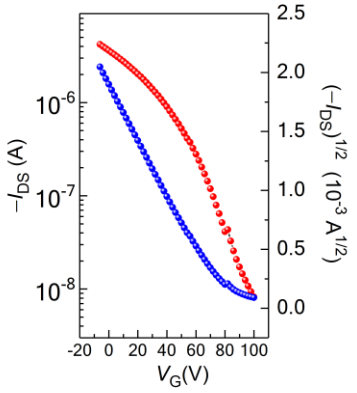

Figure 2.10 Transfer characteristics of the FET based on P1 with BGBC architecture and Au electrodes in ambient air. A very high positive gate voltage was applied to turn off the device.

Therefore, P2 and P2F were devices were tested under vacuum. These devices show normal p-type output and transfer characteristics, with highest μ_h of 0.017 $cm^2\ V^{-1}\ s^{-1}$ and 0.013 $cm^2\ V^{-1}\ s^{-1}$ respectively, and a moderate on-off ratio of 102 (Figure 2.11). Such result is also a corroboration of the doping behavior in its all-acceptor analogue, TII homo polymer, which has an even higher HOMO lying of 4.83 eV.[23]

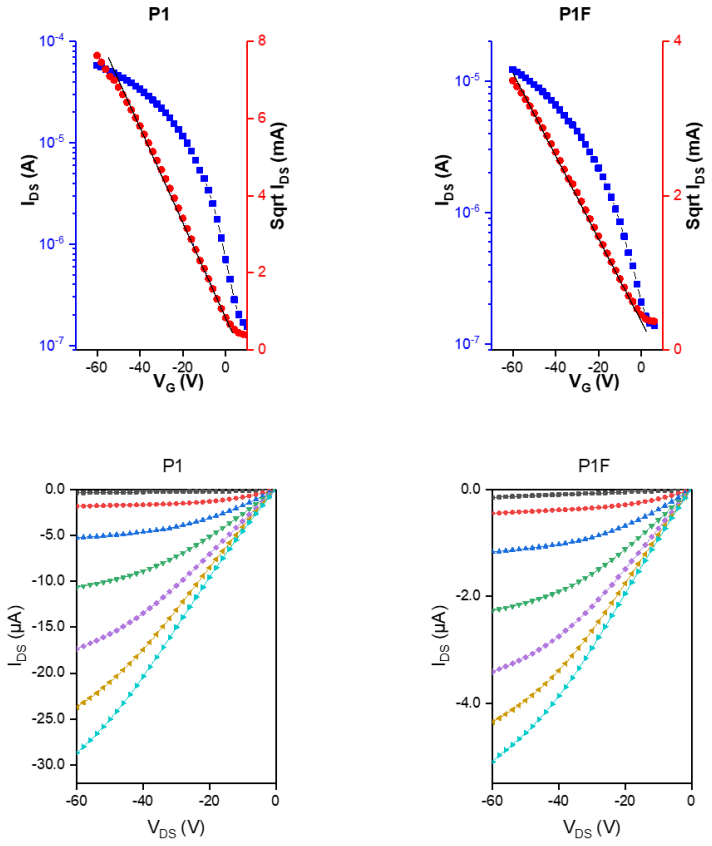

Figure 2.11 Transfer characteristics of the FET based on P2 and P2F with BGBC architecture and Au electrodes under vacuum.

All Bis-IID devices with bottom-gate top-contact (BGTC) architecture and Al as contacts exhibit ambipolar characters with μ_e around 10^{-4} to 10^{-3} $cm^2\ V^{-1}\ s^{-1}$ and μ_h around 10^{-3} to 10^{-2} $cm^2\ V^{-1}\ s^{-1}$ (Figure 2.12 and 2.13), showing n- type potential properties of A-A type Bis-IID building blocks. These results are summarized in Table 2.3.

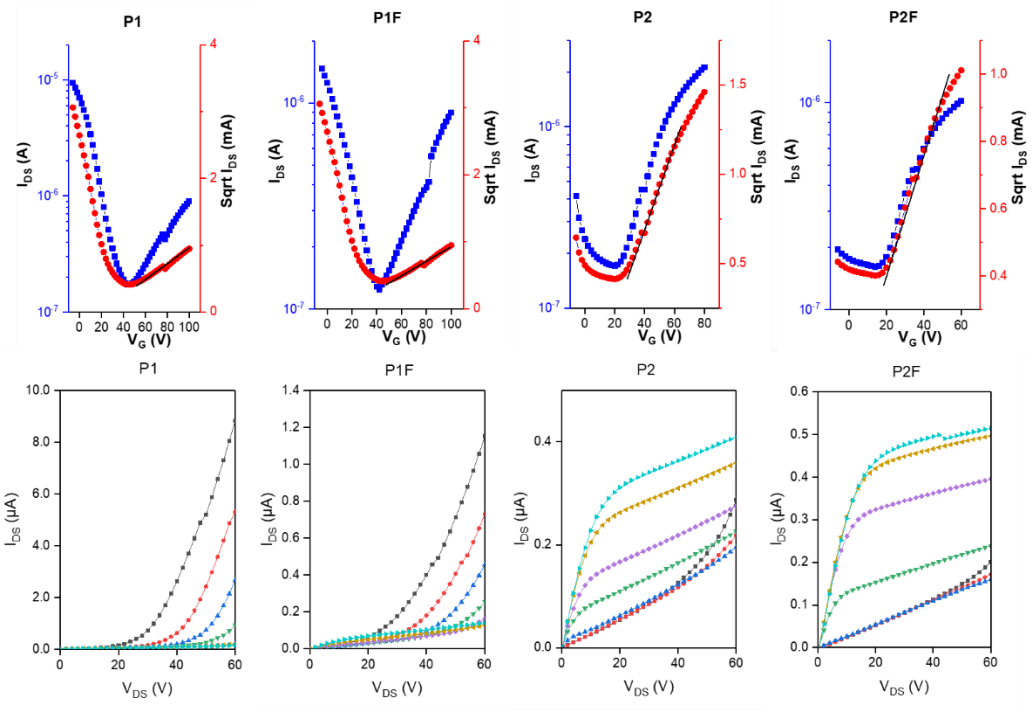

Figure 2.12 Typical n- type transfer and output characteristics of FETs based on P1, P2, P1F and P2F with BGTC architecture and Al contacts under vacuum.

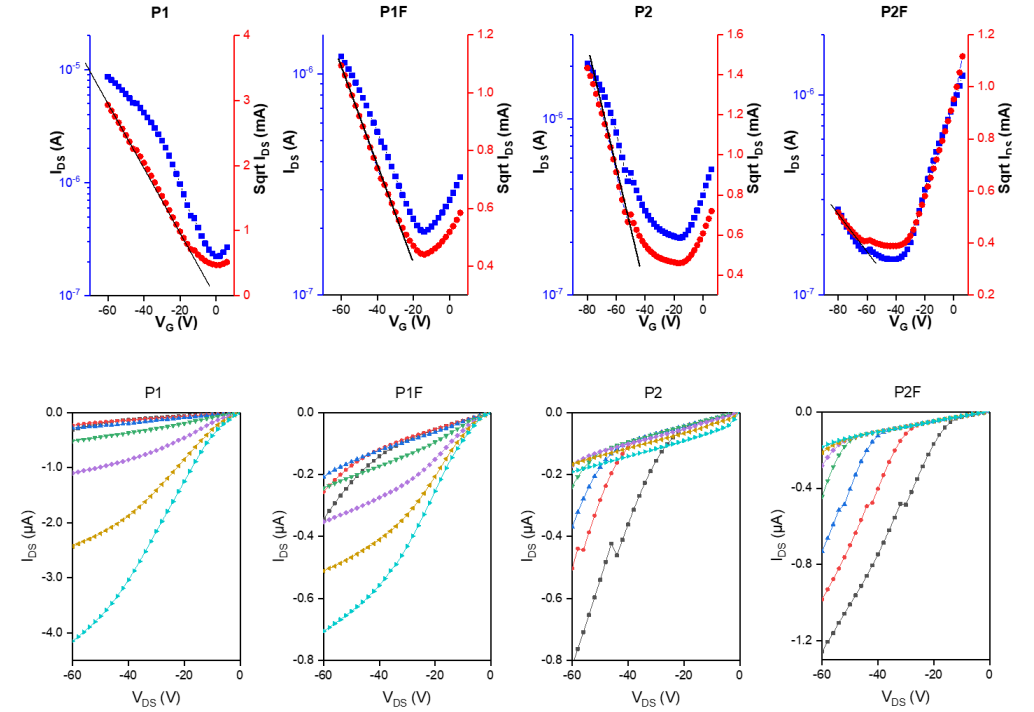

Figure 2.13 Typical p- type transfer and output characteristics of FETs based on P1, P2, P1F and P2F with BGTC architecture and Al contacts under vacuum.

Table 2.2 [a] The HOMO and LUMO energy levels are estimated from HOMO = − (5.10 + Eox – $E_{Fc/Fc+}$) and LUMO = − (5.10 + E_{red} – $E_{Fc/Fc+}$), where E_{ox} and E_{red} are onset potentials. [b] Data adopted from ref 24. All mobilities shown in table 2.2 are highest values. [c] Results obtained from BGTC architecture, Al contacts. [d] Results obtained from BGBC architecture, Au contacts.

Polymer	Differential Pulse Voltammetry[a]			Cyclic Voltammetry[a]			OFET performance	
	LUMO/eV	HOMO/eV	E_{gap}/eV	LUMO/eV	HOMO/eV	E_{gap}/eV	μ_e/cm^2 V^{-1} s^{-1}	μ_h/cm^2 V^{-1} s^{-1}
P1-ref	-3.83	-4.99	1.16	-3.80	-5.16	1.36	N/A	0.43[b]
P1	-3.95	-4.96	1.01	-3.89	-5.13	1.24	0.00046[c]	0.017[d]
P1F	-3.98	-5.05	1.07	-3.90	-5.28	1.38	0.00022[c]	0.013[d]
P2-ref	-3.88	-5.29	1.41	-3.85	-5.46	1.61	N/A	0.088[b]
P2	-3.97	-5.30	1.33	-3.90	-5.45	1.55	0.0022[c]	0.024[d]
P2F	-3.98	-5.45	1.47	-3.91	-5.54	1.63	0.0017[c]	0.030[d]

Table 2.3 Summary of Bis-IID OFET devices with BGTC architecture and Al contacts under vacuum.

Polymers	$\mu_{e,\ average}$ ($cm^2V^{-1}s^{-1}$)	$\mu_{e,\ max}$ ($cm^2V^{-1}s^{-1}$)	$I_{on/off}$	$\mu_{h,\ average}$ ($cm^2V^{-1}s^{-1}$)	$\mu_{h,\ max}$ ($cm^2V^{-1}s^{-1}$)	$I_{on/off}$
P1	$3.82x10^{-4}$	$4.63x10^{-4}$	~50	0.018	0.023	~50
P1F	$1.73x10^{-4}$	$2.15x10^{-4}$	~10	0.0011	0.0013	~10
P2	$1.67x10^{-3}$	$2.16x10^{-3}$	~15	0.003	0.005	10
P2F	$1.27x10^{-3}$	$1.71x10^{-3}$	~6	$2.25x10^{-4}$	$2.8x10^{-4}$	~5

2.4 Conclusions

In summary, we developed a new synthetic approach to obtain two isoinidgo-based acceptor-acceptor type building blocks M1 and M2. With thiophene-thiophene connection along the building block, the corresponding D-A-A polymers P1, P2, P1F and P2F show high planarity and extended conjugation length, which thus lead to strong interchain interaction. Compared with their D-A analogues, D-A-A polymers have noticeably lowered LUMO, but relatively unchanged HOMO. Further introduction of fluorine atoms into Bis-IID polymers only lowers their HOMO levels. This discovery asserts that our D-A-A design can tune FMO energy levels selectively. All Bis-IID polymers exhibit ambipolar charge transport properties. We expect the D-A-A approach will play a significant role in developing ambipolar materials. We also anticipate that our key

intermediate bis-thienoisatin 2 could serve as a moiety to build up novel functional conjugated polymers for organic electronics.

2.5 Experimental Section

All reagents purchased from suppliers were used without further purification. 1H- and 13C-NMR spectra were recorded using Varian Inova 300 in deuterated chloroform at 293 K. GPC was performed by high-temperature gel permeation chromatography at 150 °C using 1,2,4-trichlorobenzene (TCB) as eluent. Differential scanning calorimetry (DSC) measurements were acquired using a TA Q1000 calorimeter at a heating rate of 10 °C min^{-1} with nitrogen as purge gas. UV-vis-NIR spectra were measured with an Agilent Technologies Cary 6000i UV-Vis-NIR spectrophotometer (350-1800 nm). All the electrochemistry related experiments (CV, DPV) were performed using BioLogic SP-150. platinum electrode was used as a working electrode and a platinum wire as a counter electrode, and all potentials were recorded versus Ag/AgCl (saturated) as a reference electrode (scan rate: 40 mV s^{-1}). FET device characterization was carried out using Keithley 4200.

2.5.1 Device Fabrication and Characterization

Top-contact/Bottom-gate OTFT devices: The SiO_2/Si substrates were cleaned by piranha solution (H_2SO_4 98%: H_2O_2 30% = 2:1) at 85 °C for 20 mins. They were then washed with DI water, Ethanol and acetone for 6 mins each. After drying inside oven, the substrates were put in a clean petri dish with a small drop of OTS. The dish was annealed in a vacuum oven at 120 °C for at least 3h resulting in the formation of an OTS self-assembled monolayer on the surface. The OTS modified substrates were rinsed with hexane, ethanol and chloroform to remove physically-adsorbed OTS molecules before used. All polymers were dissolved in Chloroform and spin coated on the substrate at 2000 RPM inside a glove box. All the films were annealed inside the glovebox at 120 °C. To deposit Al electrode, A 40 nm layer of Al was thermally evaporated on top of the semiconductor film through a shadow mask. The channel length was 80 µm and the channel width was 4800 µm. All the devices were characterized by using Keithley 2400 in vacuum of 10-4 mbar. Bottom-contact/Bottom-gate OTFT devices: The substrates have SiO_2 as dielectric layer and gold electrode were pre-patterned by photolithography. They were cleaned by piranha solution and OTS

modified as the procedure above. All polymers were dissolved in Chloroform and spin coated on the substrate at 2000 RPM in air. All the films were annealed inside the glovebox at 120 °C. The channel width was 1000 μm and the channel length was ranging from 10 μm to 100 μm.

2.5.2 Synthetic Procedures

Compound 2: 4-(2-octyldodecyl)-4H-thieno[3,2-b]pyrrole-5,6-dione (1.17 g, 2.70 mmol) (1), Silver Fluoride (0.719 g, 5.67 mmol) and Palladium(II) acetate (60.6 mg, 0.270 mmol) were added to 30 mL of DMSO. The mixture was stirred under N_2 at 90 °C for 24 h before being allowed to cool to room temperature. The reaction was poured into water, extracted with dichloromethane and dried over Na_2SO_4. After removal of the solvent under reduced pressure, the residue was purified by silica chromatography (hexanes:CH_2Cl_2=1:3) to give the product (2) as a dark purple solid (627 mg, 54%). About 15% of the starting material was also recovered. 1H NMR (300 MHz, $CDCl_3$, ppm) δ: 6.93 (s, 2H), 3.57 (d, J = 7.3 Hz, 4H), 1.80 (m, 2H), 1.32-1.25 (m, 64H), 0.87 (t, J = 6.6 Hz, 12H). 13C NMR (75 MHz, $CDCl_3$, ppm) δ: 172.17, 164.69, 160.57, 151.59, 111.49, 110.88, 46.69, 37.08, 31.96, 31.37, 30.04, 29.72, 29.64, 29.43, 29.39, 26.37, 22.78, 14.24. HRMS (APCI) calcd. for $C_{52}H_{85}N_2O_4S_2$ ($[M+H]^+$): 865.5945; found 865.5939.

Compound 4: 6-bromo-1-(2-octyldodecyl)indoline-2,3-dione (4a) (2.0 g, 3.9 mmol) and hydrazine monohydrate (10 mL) were added to 10 mL of DMSO. The mixture was stirred under N_2 at 130 °C for 24 h before being allowed to cool to room temperature. The reaction was poured into water, extracted with dichloromethane and dried over Na_2SO_4. After removal of the solvent under reduced pressure, the residue was purified by silica chromatography (hexanes:CH_2Cl_2=3:2) to give the product (4) as a light-yellow oil (1.28 g, 66%). 1H NMR (300 MHz, CDCl3, ppm) δ: 7.16 – 7.06 (m, 2H), 6.91 (d, J = 1.6 Hz, 1H), 3.54 (d, J = 7.5 Hz, 2H), 3.45 (s, 2H), 1.92 – 1.73 (m, 1H), 1.29 – 1.24 (m, 32H), 0.87 (t, J = 6.6 Hz, 6H). 13C NMR (75 MHz, CDCl3, ppm) δ: 174.83, 146.30, 125.46, 124.69, 123.28, 121.19, 111.88, 44.66, 35.94, 35.40, 32.00, 31.55, 30.09, 29.74, 29.69, 29.64, 29.45, 29.40, 26.46, 22.80, 14.27. HRMS (ESI) calcd. for $C_{18}H_{46}BrNONa$ ($[M+Na]^+$): 514.2661; found 514.2657.

Compound M1a: p-Toluenesulfonic acid monohydrate (9.0 mg 0.052 mmol) was added to a solution of bis-tisatin 2 (150 mg, 0.173 mmol) and 4-(2-octyldodecyl)-4,6-dihydro-5H-thieno[3,2-b]pyrrol-5-one (3) (291 mg, 0.693 mmol) in Toluene (15 mL). The mixture was stirred under N_2

at 110 °C for 12 h before being allowed to cool to room temperature. After removal of the solvent under reduced pressure, the residue was purified by silica chromatography (hexanes:CH_2Cl_2=3:2) to give the product (M1a) as a dark green solid (256 mg, 88%). 1H NMR (300 MHz, CDCl3, ppm) δ: 7.37 (d, J = 5.1 Hz, 2H), 6.94 (s, 2H), 6.65 (d, J = 5.2 Hz, 2H), 3.67 (t, J = 6.8 Hz, 8H), 1.96-1.85 (m, 4H), 1.31-1.22 (m, 128H), 0.84 (t, J = 3.2 Hz, 24H). 13C NMR (75 MHz, CDCl3, ppm) δ: 170.93, 170.50, 151.88, 151.05, 145.31, 134.08, 119.74, 119.57, 115.49, 114.81, 111.12, 107.36, 46.60, 46.32, 37.25, 37.03, 31.99, 31.61, 31.31, 30.26, 30.10, 29.74, 29.45, 26.65, 26.38, 22.79, 14.23. HRMS (MALDI) calcd. for $C_{104}H_{170}N_4O_4S_4$ ($[M+H]^+$): 1668.5439; found 1668.5463.

Compound M1: To a solution of M1a (232 mg, 0.139 mmol) in Chloroform (10 mL) at 0 °C, a solution of N-Bromosuccinimide (54.4 mg 0.305 mmol) in Chloroform (10 mL) was added dropwise in 5 min. The mixture was stirred at 0 °C for another 30 min. The reaction was quenched by addition of saturated aqueous solution of $Na_2S_2O_3$. The organic phase was extracted with dichloromethane and dried over Na_2SO_4. After removal of the solvent under reduced pressure, the residue was purified by silica chromatography (hexanes:CH_2Cl_2=1:1) to give the product (M1) as a dark green solid (221 mg, 87%). 1H NMR (300 MHz, CDCl3, ppm) δ: 6.88 (s, 2H), 6.67 (s, 2H), 3.68 (m, 8H), 1.98 (s, 2H), 1.81 (s, 2H), 1.40 – 1.21 (m, 128H), 0.87 – 0.81 (m, 24H). 13C NMR (75 MHz, CDCl3, ppm) δ: 170.48, 169.74, 152.16, 149.50, 145.64, 122.66, 119.02, 118.24, 116.03, 115.13, 114.69, 107.20, 46.96, 46.45, 37.29, 37.15, 32.01, 31.63, 31.35, 30.34, 30.14, 29.84, 29.76, 29.69, 29.48, 26.71, 26.51, 22.80, 14.24. HRMS (MALDI) calcd. for $C_{104}H_{168}Br_2N_4O_4S_4$ ($[M+H]^+$): 1827.2345; found 1827.2419.

Compound M2: p-Toluenesulfonic acid monohydrate (16.5 mg, 0.087 mmol) was added to a solution of bis-tisatin 2 (150 mg, 0.173 mmol) and 6-bromo-1-(2-octyldodecyl)indolin-2-one (4) (172 mg, 0.350mmol) in Toluene (15 mL). The mixture was stirred under N_2 at 110 °C for 12 h before being allowed to cool to room temperature. After removal of the solvent under reduced pressure, the residue was purified by silica chromatography (hexanes:CH_2Cl_2=1:1) to give the product (M2) as a dark green solid (279 mg, 89%). 1H NMR (300 MHz, CDCl3, ppm) δ: 8.84 (d, J = 8.5 Hz, 2H), 7.03 (d, J = 8.6 Hz, 2H), 6.93 (s, 2H), 6.86 (s, 2H), 3.65 (d, J = 7.5 Hz, 8H), 1.96 – 1.90 (m, 4H), 1.34 – 1.22 (m, 128H), 0.87 – 0.83 (m, 24H). 13C NMR (75 MHz, CDCl3, ppm) δ: 169.80, 168.84, 153.51, 147.05, 144.60, 129.47, 128.40, 124.96, 124.76, 120.45, 119.86, 116.37, 111.37, 107.34, 46.77, 44.88, 37.00, 36.19, 32.01, 31.70, 31.37, 30.29, 30.14, 29.77, 29.67, 29.47,

26.70, 26.44, 22.80, 14.24. HRMS (MALDI) calcd. for $C_{108}H_{172}Br_2N_4O_4$ ($[M+H]^+$): 1815.4630; found 1815.4193.

General procedure for polymerization: To a Schlenk tube charged with a stir bar, M1 or M2 (1.0 equiv.), ditin Compound 5 or 6 (1.0 equiv.), $Pd_2(dba)_3$ (2.5 mol%), P(o-tol)3 (4 mol%) and 15 mL of toluene were added. The resulting solution was bubbled with argon for 20 min, and the mixture was stirred for 16 h at 110 °C. After the polymerization was complete, the mixture was taken up and precipitated into methanol. The solids were collected by a soxhlet thimble, which was purified by Soxhlet extraction successively with acetone, hexane, and chloroform. To remove residual catalyst, N,N-diethyl-2-phenyldiazenecarbothioamide was added to the chloroform fraction, and the mixture was stirred for 30 min at 60 °C before being precipitated into methanol. The collected polymer was dried at 60 °C under vacuum.

P1: 60.0 mg (0.033 mmol) of M1 and 16.2 mg of (0.033 mmol) 5 were used. Precipitation provided 57.0 mg (95% yield) of a dark solid. As mentioned in the main text, the exact molecular weight of P1 can't be determined.

P2: 103.8 mg (0.057 mmol) of M2 and 28.1 mg (0.057 mmol) of 5 were used. Precipitation provided 95.8 mg (92% yield) of a dark solid. Mn = 121 KDa, PDI = 1.70.

P1F: 81.0 mg (0.044 mmol) of M1 and 23.4 mg of (0.044 mmol) 6 were used. Precipitation provided 50.8 mg (63% yield) of a dark solid. As mentioned in the main text, the exact molecular weight of P1F can't be determined.

P2F: 80.1 mg (0.044 mmol) of M2 and 23.3 mg (0.044 mmol) of 6 were used. Precipitation provided 68.6 mg (85% yield) of a dark solid. Mn = 28 KDa, PDI = 3.0.

2.5.3 1H NMR and 13C NMR Spectra of New Compounds

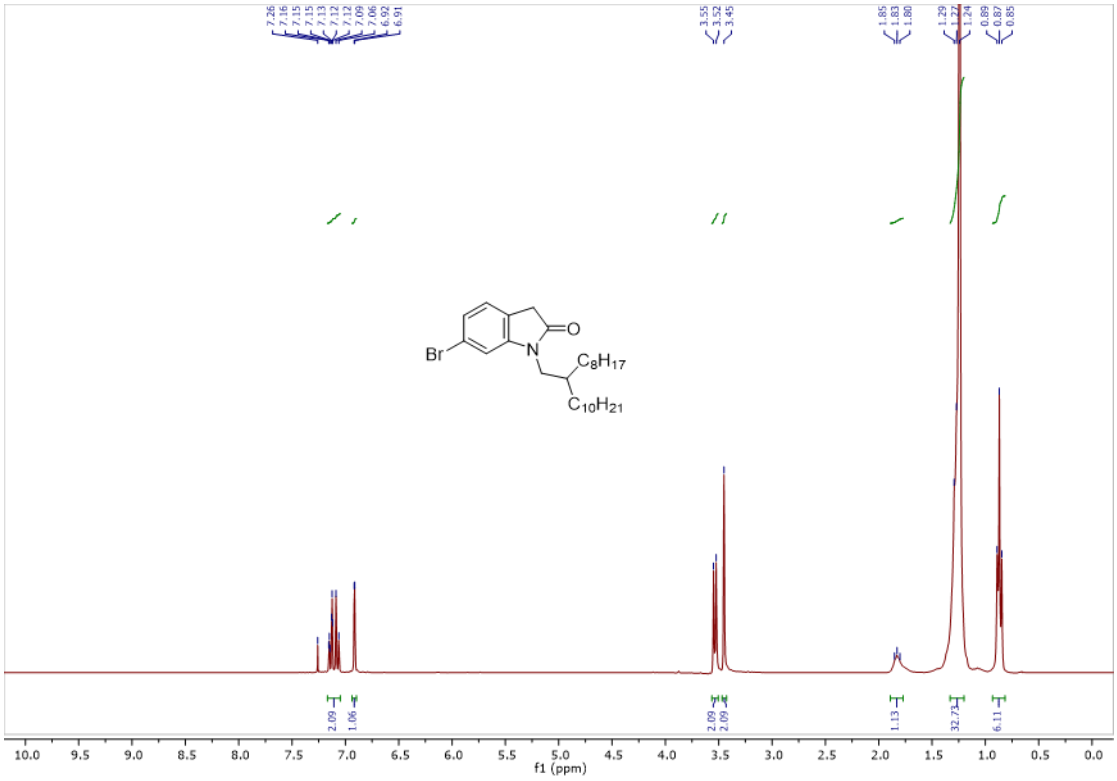

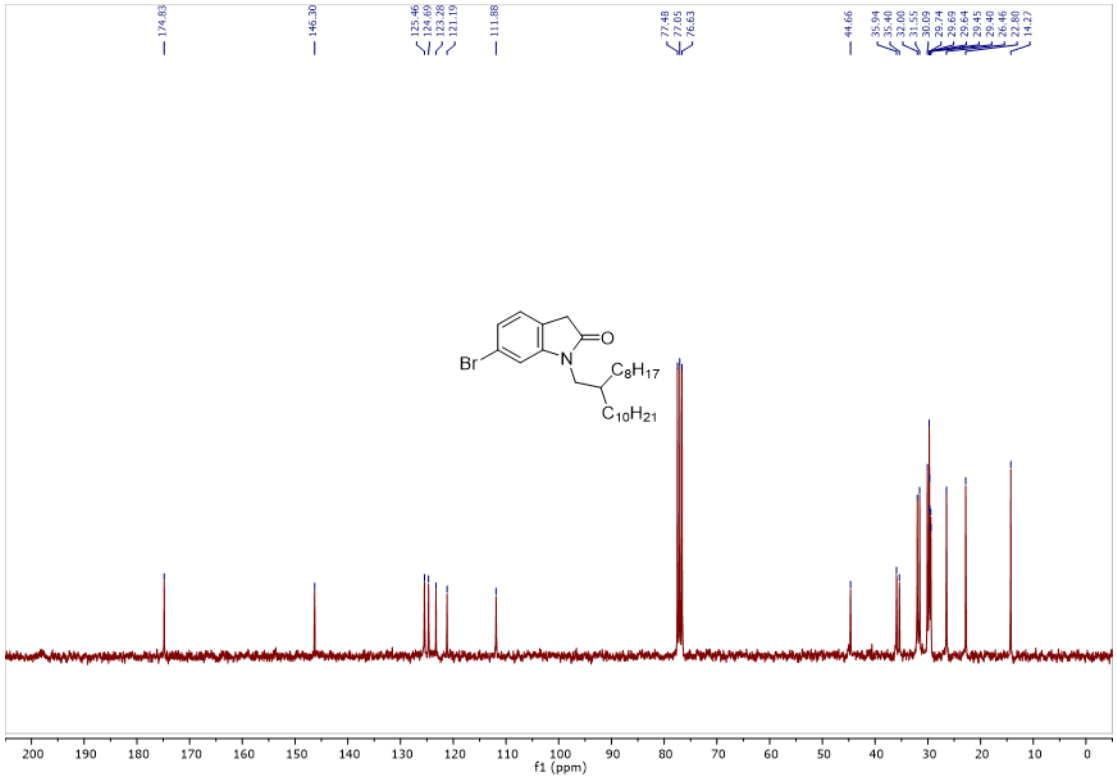

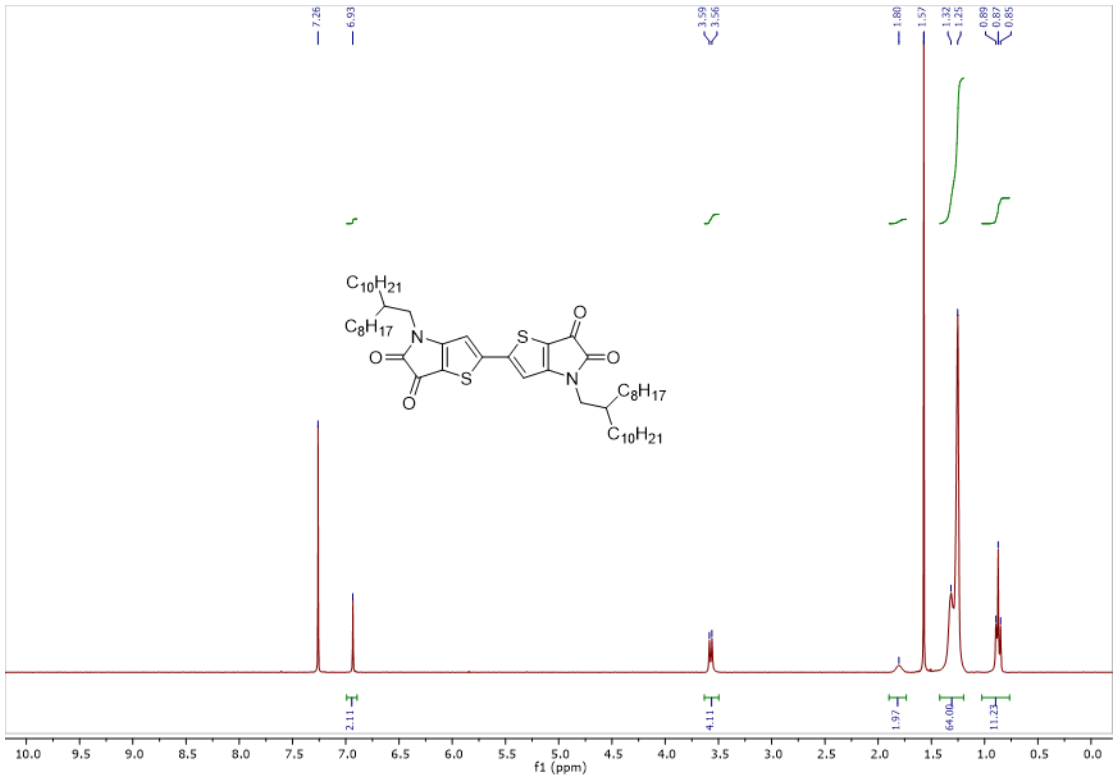
7.26
6.93
3.59
3.56
1.80
1.57
1.32
1.25
0.89
0.87
0.85
$C_{10}H_{21}$
C_8H_{17}
C_8H_{17}
$C_{10}H_{21}$
2.11
4.11
1.97
64.00
11.23
f1 (ppm)

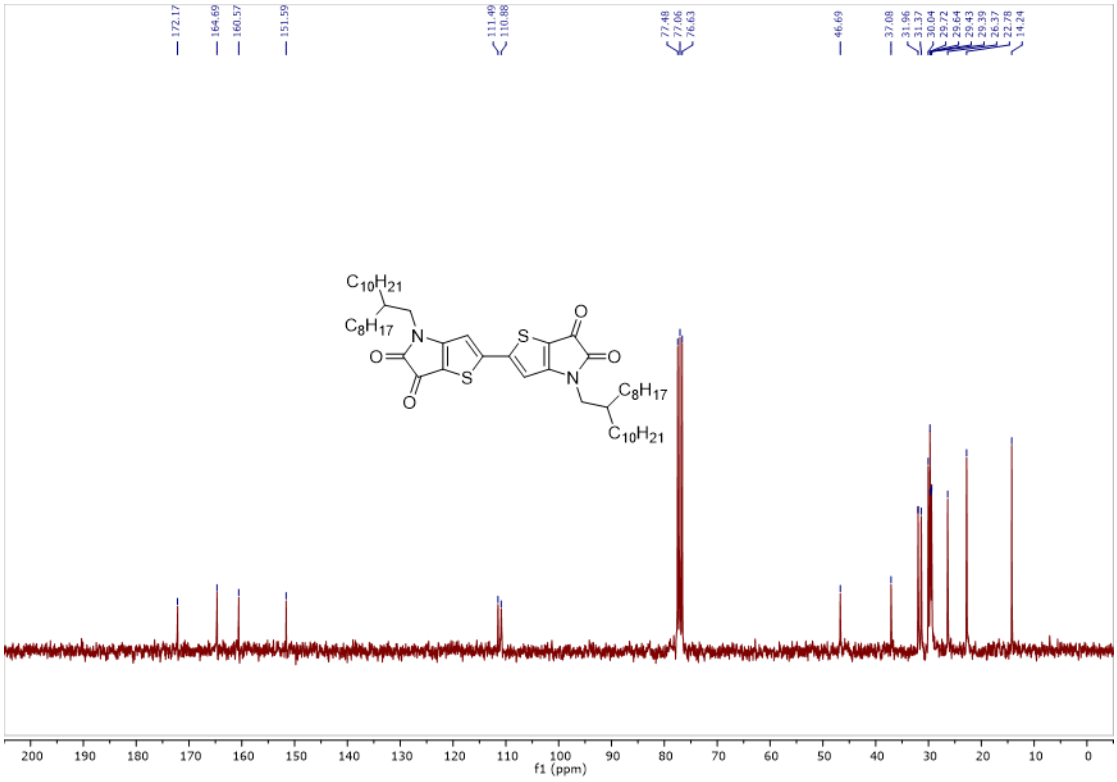
172.17
164.69
160.57
151.59
111.49
110.88
77.48
77.06
76.63
46.69
37.08
31.96
31.32
30.04
29.72
29.64
29.43
29.39
26.37
22.78
14.24
$C_{10}H_{21}$
C_8H_{17}
C_8H_{17}
$C_{10}H_{21}$
f1 (ppm)

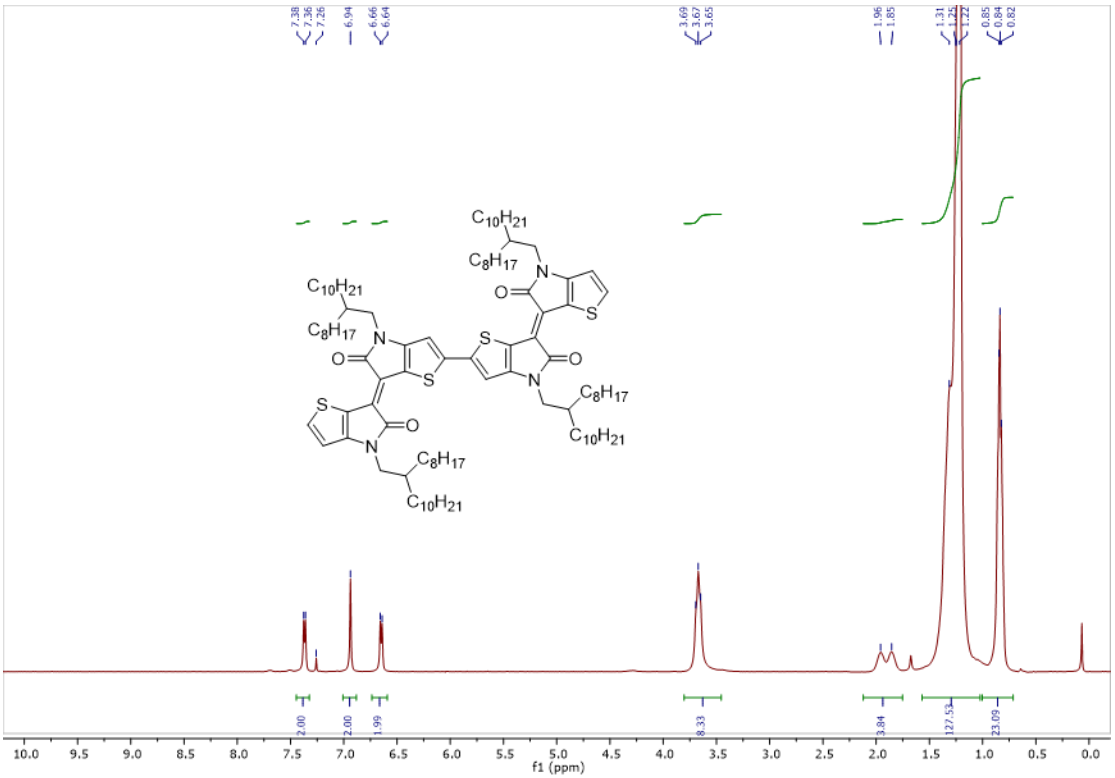
7.38
7.36
7.26
6.94
6.66
6.64
3.69
3.67
3.65
1.96
1.85
1.31
1.25
1.22
0.85
0.84
0.82
2.00
2.00
1.99
8.33
3.84
127.53
23.09
f1 (ppm)

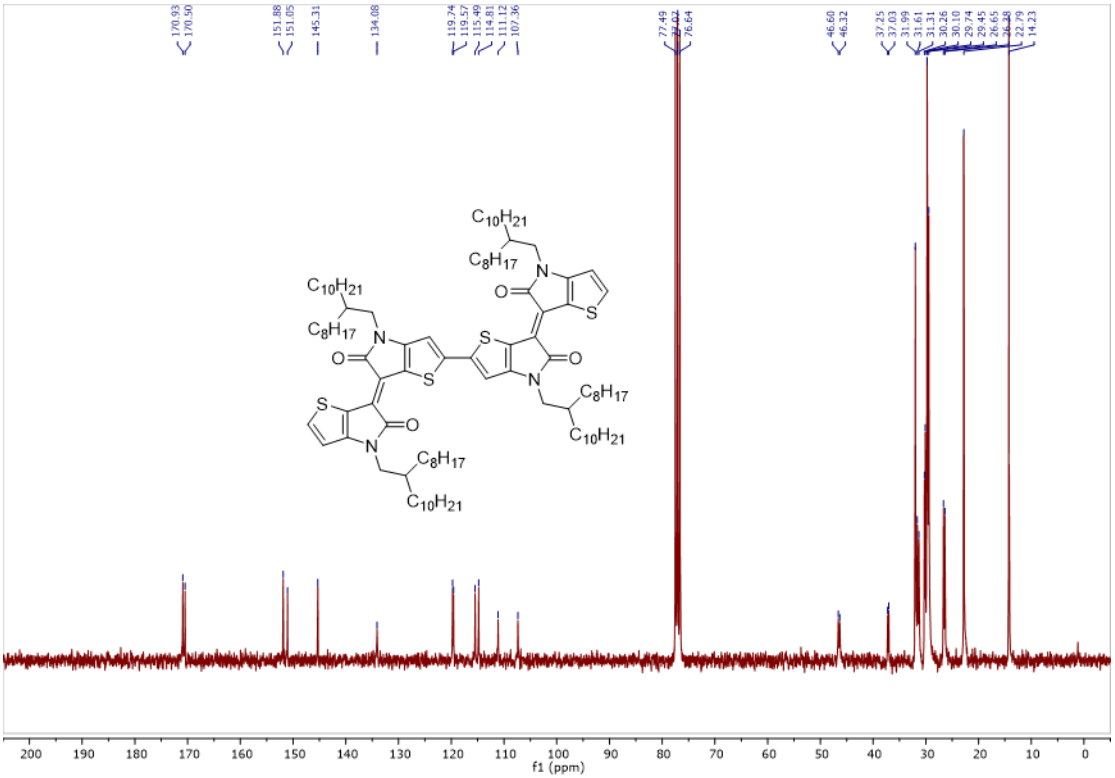
170.93
170.50
151.88
151.05
145.31
134.08
119.74
119.57
115.49
114.81
111.12
107.36
77.49
77.02
76.64
46.60
46.32
37.25
37.03
31.99
31.61
31.31
30.26
30.10
29.74
29.45
26.65
26.28
22.79
14.23
f1 (ppm)

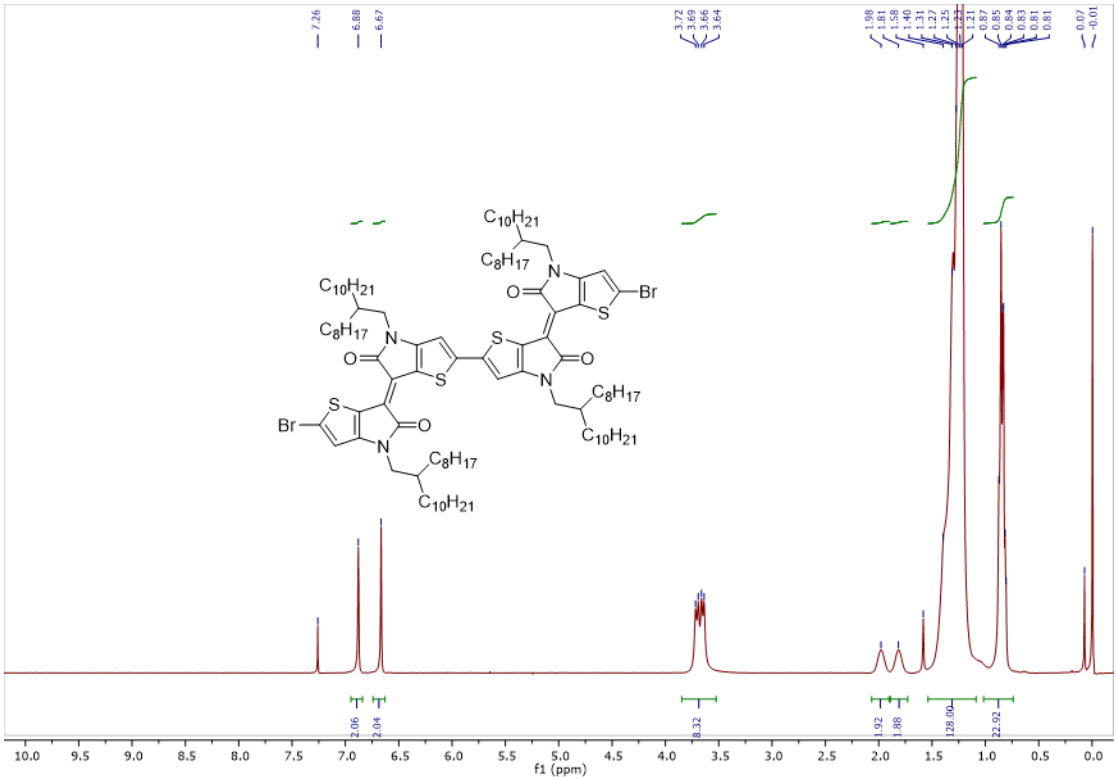
7.26
6.88
6.67
3.72
3.69
3.66
3.64
1.98
1.81
1.58
1.40
1.31
1.27
1.25
1.23
1.21
0.87
0.85
0.84
0.83
0.81
0.81
0.07
-0.01
2.06
2.04
8.32
1.92
1.88
128.00
22.92
f1 (ppm)

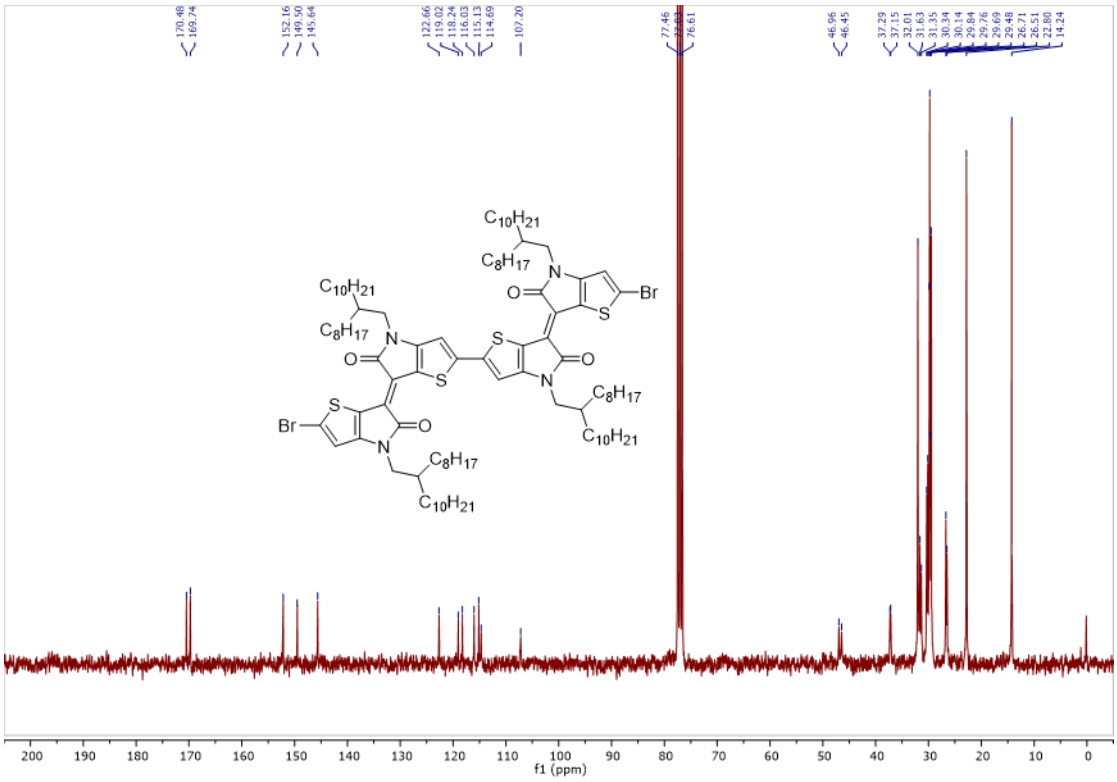
170.48
169.74
152.16
149.50
145.64
122.66
119.02
118.24
116.03
115.13
114.69
107.20
77.46
77.03
76.61
46.96
46.45
37.29
37.15
32.01
31.63
31.35
30.34
30.14
29.84
29.76
29.69
29.48
26.71
26.51
22.80
14.24
f1 (ppm)

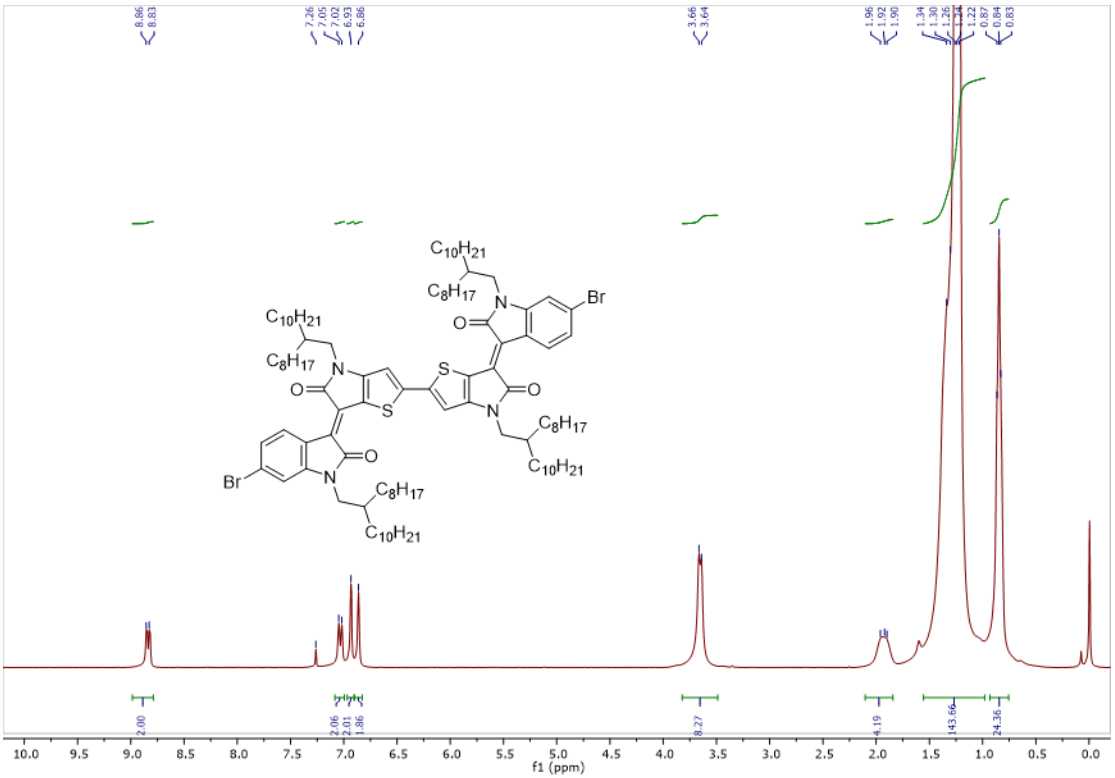
8.86
8.83
7.26
7.05
7.02
6.93
6.86
3.66
3.64
1.96
1.92
1.90
1.34
1.30
1.28
1.24
1.22
0.87
0.84
0.83
Br
2.00
2.06
2.01
1.86
8.27
4.19
143.66
24.36
f1 (ppm)

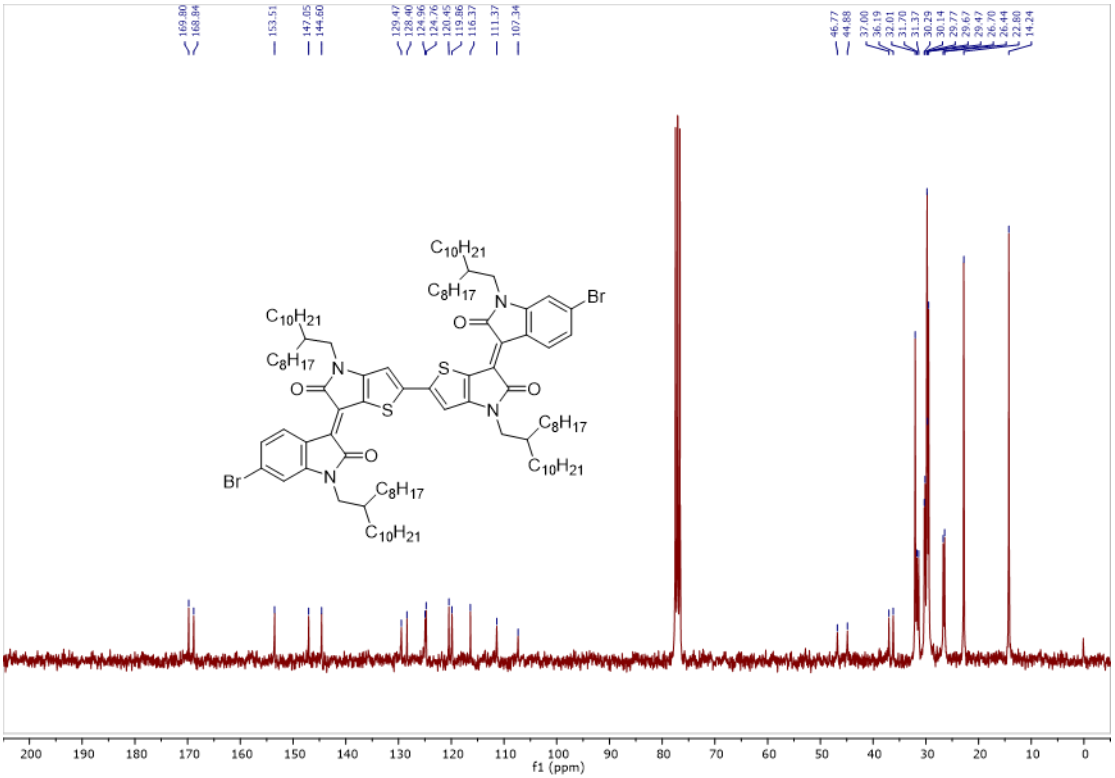
169.80
168.84
153.51
147.85
144.60
129.47
128.40
124.96
124.76
120.45
119.86
116.37
111.37
107.34
46.77
44.88
37.00
36.19
32.01
31.70
31.37
30.29
30.14
29.77
29.67
29.47
26.70
26.44
22.80
14.24
Br
f1 (ppm)

CHAPTER 3. SIDE-CHAIN SEQUENCE ENABLED REGIOISOMERIC ACCEPTORS FOR CONJUGATED POLYMERS

3.1 Introduction

Donor-acceptor (D-A) type conjugated polymers have attracted a great deal of attention as organic semiconductors in printed and flexible electronics because of the versatile chemistry available to tune their optical and electronic properties.[34–37] This potential has spurred the development of numerous π-conjugated polymer systems.[38–42] In molecular design of D-A polymers, side chain engineering has proved to be effective in tuning electronic and morphological properties of resulting polymer thin films.[43–49] Rational combination of different side chains is one of such strategies.[50–54] There are generally two approaches to introduce a combination of side chains. The first approach deals with the copolymerization of two monomers bearing the targeted side chains (Scheme 1a). For an example, Zhang *et. al.* developed a DPP (diketopyrrolopyrrole) monomer bearing urea-containing alkyl chains.[48] Changing the ratio of the urea-chain DPP monomers to the branched-alkyl-chain DPP monomers in polymerization provided a series of DPP random copolymers with enhanced charge mobilities. The second approach involves a single monomer bearing two different side chains, which would produce alternating copolymers (Figure 3.1a). We previously reported such an isoindigo building block with one alkyl chain and one siloxane hybrid chain.[55] The corresponding polymer thin films adopted bimodal packing orientation and exhibited improved charge transport performance.

3.2 Molecular Design

The presence of different types of side chains brings up the issue of side-chain sequence along the polymer backbones. It has been repeatedly shown in the case of polyalkylthiophenes that the side-chain sequence affects both physical and electronic properties.[56] (Figure 3.1b) However, little has been known about side-chain regioisomerism in D-A polymers.[57,58] Herein, we demonstrate for the first time side-chain sequence enabled regioisomeric acceptors for D-A copolymers based on the *bis*-thieno-benzo-isoindigo (*bis*-TBI) acceptor-acceptor type building block. (Figure 3.1c) Owing to its convergent synthetic approach, two pairs of side chains can be efficiently mounted onto *bis*-TBI compound.[59] In the current study, bulky branched alkyl chains (B) and linear alkyl

chains (L) are placed in two different sequences along the backbones, providing side-chain regioisomeric monomers *bis*-TBI-1 with a branched-linear-linear-branched (BLLB) side chain sequence and *bis*-TBI-2 with a linear-branched-branched-linear (LBBL) side chain sequence. It is worth noting that the two monomers share an identical conjugated core but with different side chain sequences away from the charge transport pathway, hence they are a different category of isomers than P3AT-like regioisomers. The corresponding D-A copolymers PTBI-1, PTBI-2, and a regiorandom copolymer PTBI-3 with mixed *bis*-TBI moieties are subsequently prepared to investigate the impact of side-chain-sequence regioisomerism on aggregation behaviors and charge transport properties of the polymers.

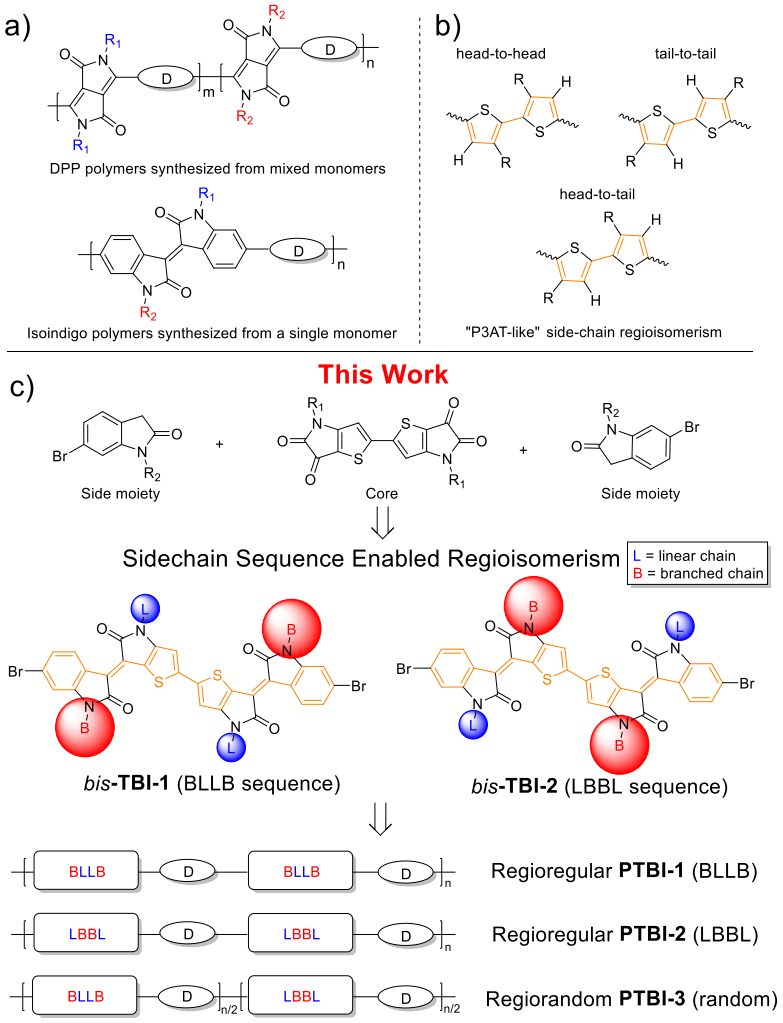

Figure 3.1 Previous work, and illustration of the design rationale for bis-TBI regioisomeric acceptors

3.3 Synthesis and Characterization

3.3.1 Synthesis of Polymers

The synthesis of PTBI polymers follows a similar convergent synthetic route we previously developed for *bis*-TBI moieties,[59] as illustrated in Figure 3.2. The core bis-thieno-isatin 3 bearing one type of side chain and the side moiety oxindole 5 bearing the other type were synthesized in good yields. After an aldol condensation reaction of compounds 3 and 5, regioisomers *bis*-TBI-1 (with BLLB sequence) and *bis*-TBI-2 (with LBBL sequence) were obtained in 76% and 86% yield respectively. Subsequently, Stille polymerization of *bis*-TBI monomers with bithiophene ditin compound 6 provided two regioregular PTBI polymers PTBI-1, PTBI-2 in 85% and 83% yields. The regiorandom PTBI-3 were also synthesized from the 1:1 *bis*-TBIs mixture and compound 6, giving a 79% yield. Due to solubility issue, all polymerizations were carried out for 1 h. The synthesis detail is described in the Supporting Information. All polymers were purified by the Soxhlet extraction and fully characterized. Molecular weights of PTBI polymers were evaluated by high-temperature gel permeation chromatography (Figure 3.3). All of PTBI polymers were estimated to have number-average molecular weights around 9 KDa and polydispersity indices (PDI) around 1.5. Similar molecular weight and polydispersity exclude the potential molecular weight effect when comparing PTBI polymers.[60]

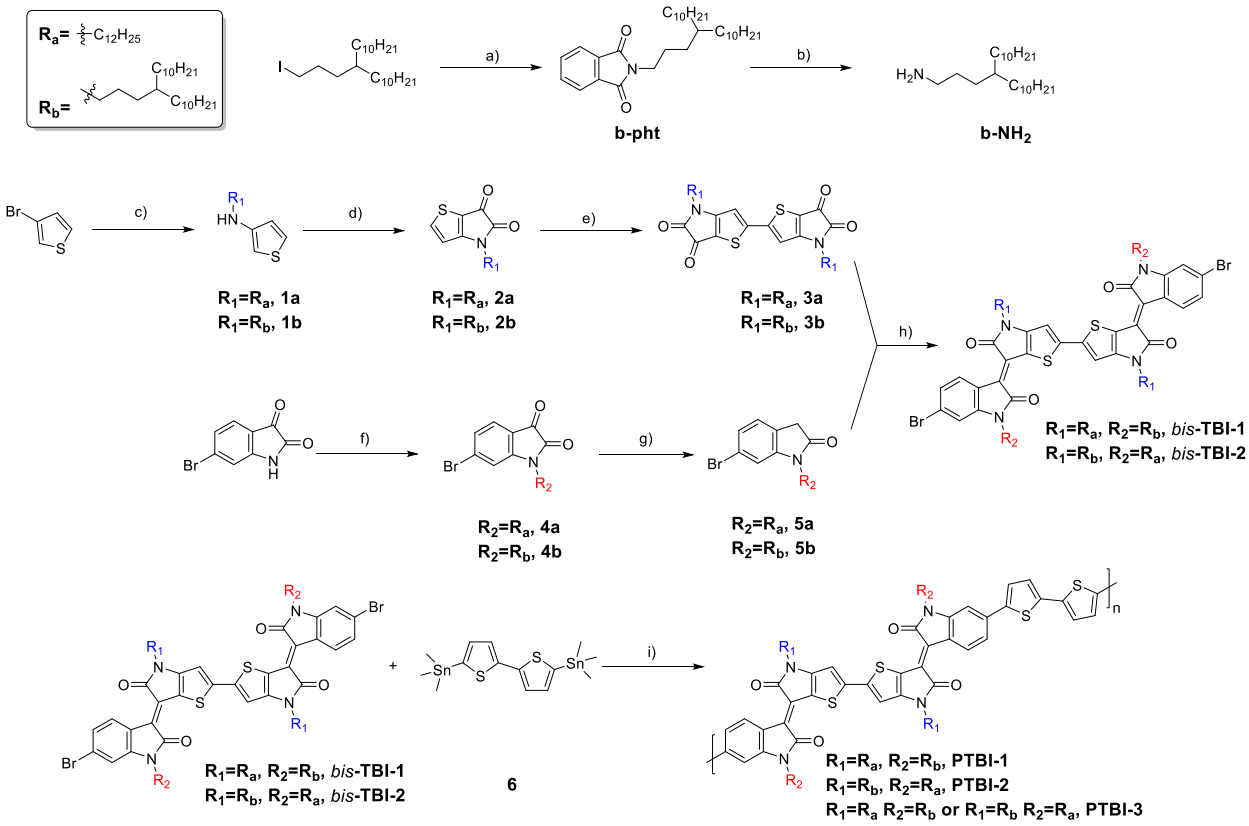

Figure 3.2 The synthetic route to bis-TBI monomers and PTBI polymers

a) potassium phthalimide, DMF, 80 °C, overnight, 90%; b) Hydrazine hydrate, MeOH, reflux, 12 h, 95%; c) alkylamine, CuI, K_3PO_4, DMEA, 80 °C, 48 h; d) Oxalyl chloride, NEt_3, DCM, 0 °C to RT, overnight, 26% (**2a**) / 17% (**2b**) over two steps; e) AgF, $Pd(OAc)_2$, DMSO/dioxane, 90 °C, 24 h, 47% (**3a**) / 60% (**3b**); f) K_2CO_3, alkyl halide, DMF, 100 °C, overnight, 69% (**4a**) / 83% (**4b**); g) Hydrazine hydrate, DMSO, 130 °C, 24 h, 61% (**5a**) / 71% (**5b**); h) PTSA, Toluene, 110 °C, 12 h, 76% (*bis*-**TBI-1**) / 86% (*bis*-**TBI-2**); i) $Pd_2(dba)_3$, P(*o*-tol)$_3$, Toluene, 110 °C, 1 h, 79%-85%.

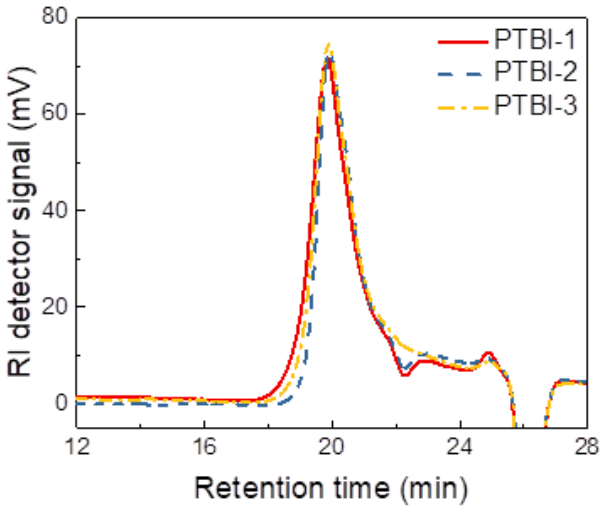

Figure 3.3 Gel permeation chromatograms of three PTBI polymers by gel permeation chromatography at 150 °C using 1,2,4-trichlorobenzene (TCB) as eluent.

3.3.2 Electrochemical and Optical Properties

The redox properties of PTBI polymers were evaluated by cyclic voltammetry (CV) and differential pulse voltammetry (DPV). Cyclic voltammograms of all polymer thin films show similar redox profiles and quasi-reversible redox behavior (Figure 3.4). HOMO/LUMO energy levels of PTBI polymers were estimated from the respective redox onset potentials of both CV and DPV. As summarized in Table 1, all three polymers show similar HOMO/LUMO levels within a range of 0.03 eV. The side-chain sequence has little impact on electrochemical properties of PTBI polymers. It is worth noting that for polymers having alkyl chain substitution positions directly on aromatic rings (*i.e.* P3AT-like side-chain regioisomers), their regioisomers typically present a noticeable HOMO/LUMO energy level difference.[57,58,61]

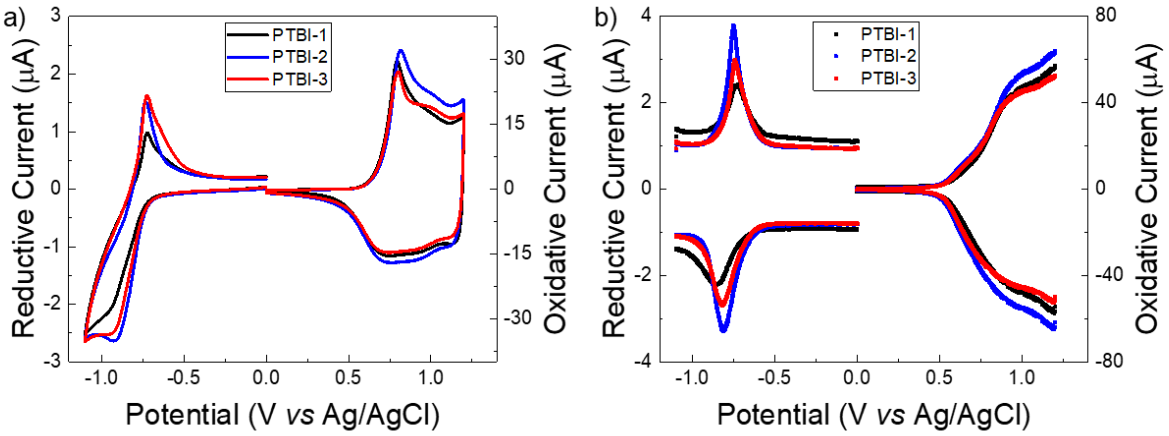

Figure 3.4 a) Cyclic Voltammograms of PTBI-1 (black), PTBI-2 (blue) and PTBI-3 (red); b) Differential pulse voltammograms of PTBI-1 (black), PTBI-2 (blue) and PTBI-3 (red). All polymer thin films were tested in propylene carbonate with 0.2 M *n*-Bu_4NPF_6 as supporting electrolyte (scan rate: 20 mV s^{-1}).

Photophysical properties of bis-TBI monomers and their polymers were characterized by solution and solid-state UV-Vis-NIR spectroscopy. As shown in figure 3.5a, two bis-TBI monomers bis-TBI-1 and bis-TBI-2 exhibit identical absorption profiles in diluted chloroform solutions, suggesting that their absorption properties are not influenced by the sequence of side chains in solutions.

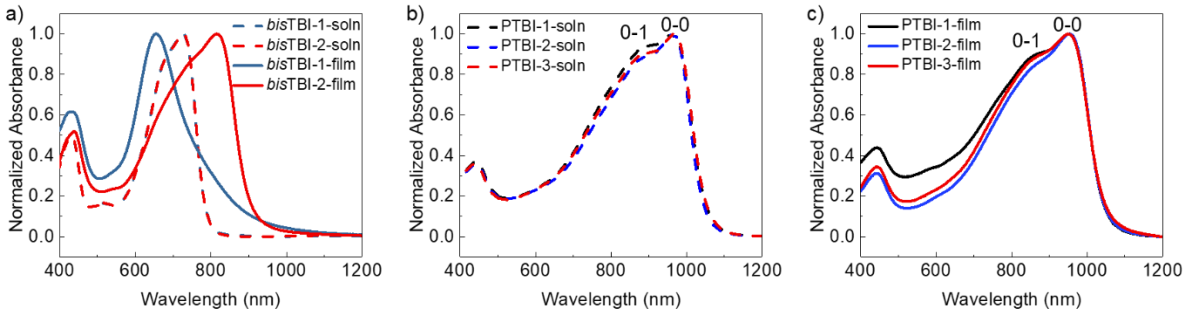

Figure 3.5 a) Solution and film Absorption spectra of *bis*-TBI-1 (blue) and *bis*-TBI-2 (red) in chloroform (1.0×10^{-5} M) (dashed line) and as film (solid line); b) Absorption spectra of PTBI-1 (black), PTBI-2 (blue), PTBI-3 (red) in *o*-DCB (1.0×10^{-5} M); c) Absorption spectra of PTBI-1 (black), PTBI-2 (blue), PTBI-3 (red) thin films spun from *o*-DCB solution.

This observation is in a good agreement with their 1H–NMR spectra collected in CDCl3 solutions, where the two isomers have identical chemical shifts in the aromatic region (Figure 3.6). *bis*-TBI-

2 only showed slightly broader peaks than *bis*-TBI-1 in the aromatic region, and their corresponding aromatic hydrogens basically share the same chemical shifts. The small discrepancy could be a shimming issue, or subtle change on the backbone chemical environment. The peaks of *bis*-TBI-2 and *bis*-TBI-1 in the aliphatic region are more distinguishable. It is worth noting that even the terminal methyl hydrogens (H_f) of branched $C_3C_{10}C_{10}$ alkyl chains have different chemical shifts, showing the two substitution positions (namely R_1 and R_2) have distinct chemical environments.

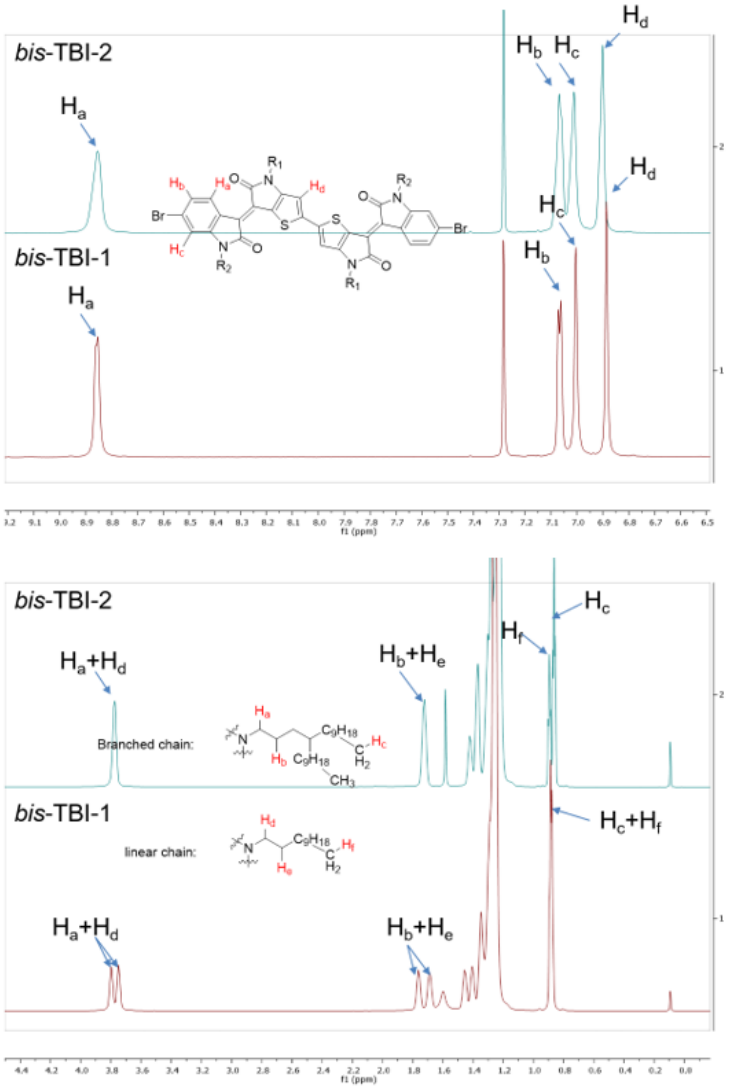

Figure 3.6 ^{1}H NMR spectra comparison of *bis*-TBI-1 and *bis*-TBI-2 in the aromatic region (top) and aliphatic region (bottom). NMR spectra were collected with 20 mg/mL $CDCl_3$ solution at room temperature.

Unexpectedly, the two isomers exhibit distinctly different absorption profiles in the solid states. bis-TBI-1 film presents a large blue shift of maximum absorbance (λ_{max}) from 726 nm to 652 nm from solution to thin film, while bis-TBI-2 film shows a strongly red-shifted absorption with λ_{max} at 815 nm in thin films. The blue and red shifts are attributed to two different packing motifs with predominant H- and J- aggregates respectively,[62,63] highlighting the crucial rule of the side-chain sequence in the highly aggregated bis-TBI molecules. Side-chain sequence also impacts photophysical properties of PTBI polymers, as shown by the solution and thin-film absorption profiles (Figure 3.5b and 3.5c). All polymers exhibit typical charge transfer peaks from 600 nm to 1100 nm. Peaks at around 950 nm and shoulders at around 870 nm are attributed to origin 0-0 and sideband 0-1 vibronic transitions respectively. Different from solutions of their monomers, the absorption spectra of PTBI polymers in dichlorobenzene (o-DCB) have a noticeable difference. Although PTBI polymers show nearly overlapped solution absorption profiles and λ_{max}, the relative intensities of 0-0 and 0-1 vibrational peaks of these polymers are different. It suggests that PTBI polymers form different pre-aggregates in solution. Thin-film absorption spectra of PTBI spun from ODCB solutions also have clear 0-0 and 0-1 vibrational peaks, indicative of their different solid-state packing. According to the HJ-aggregate model developed by Spano *et. al*. that describes semiconducting polymer assemblies, 0-0 and 0-1 vibrational peaks are attributed to a combination of intrachain (promotes J-like behavior) and interchain (promotes H-like behavior) coupling.[64–66] Their hybrid spectroscopic entities are referred to as HJ-aggregates. Therefore, the difference of 0-0/0-1 intensity ratios in PTBI polymers may indicate the relative strength of the H- and J-aggregates induced by side-chain sequence effect.[67] In this regard, PTBI-2 film has the highest 0-0/0-1 intensity ratio while PTBI-1 has the lowest, suggesting that J-coupling is most preferred in PTBI-2 film and least preferred in PTBI-1 film. Identical film absorption onsets at 1047 nm suggest all polymers have the same optical bandgap of 1.18 eV, consistent with the electrochemical estimations.

3.4 Electronic Devices Measurements

3.4.1 Film Morphology and Microstructural Analysis

Polymer thin film morphologies were analyzed by tapping-mode atomic force microscopy (AFM). All PTBI polymer films were spin coated from *o*-DCB solution on OTS-modified Si/SiO_2

substrates. As depicted in Figure 3.7, surface topography images of the PTBI-2 film show a smooth surface with crystalline fibrillar intercalating networks, while PTBI-1 and PTBI-3 films show less ordered structures and mesh-like morphologies. PTBI-1 and PTBI-2 have similar root-mean-square (RMS) roughness of 0.69 and 0.64 nm respectively, while PTBI-3 has a slightly rougher surface with RMS roughness of 1.1 nm.

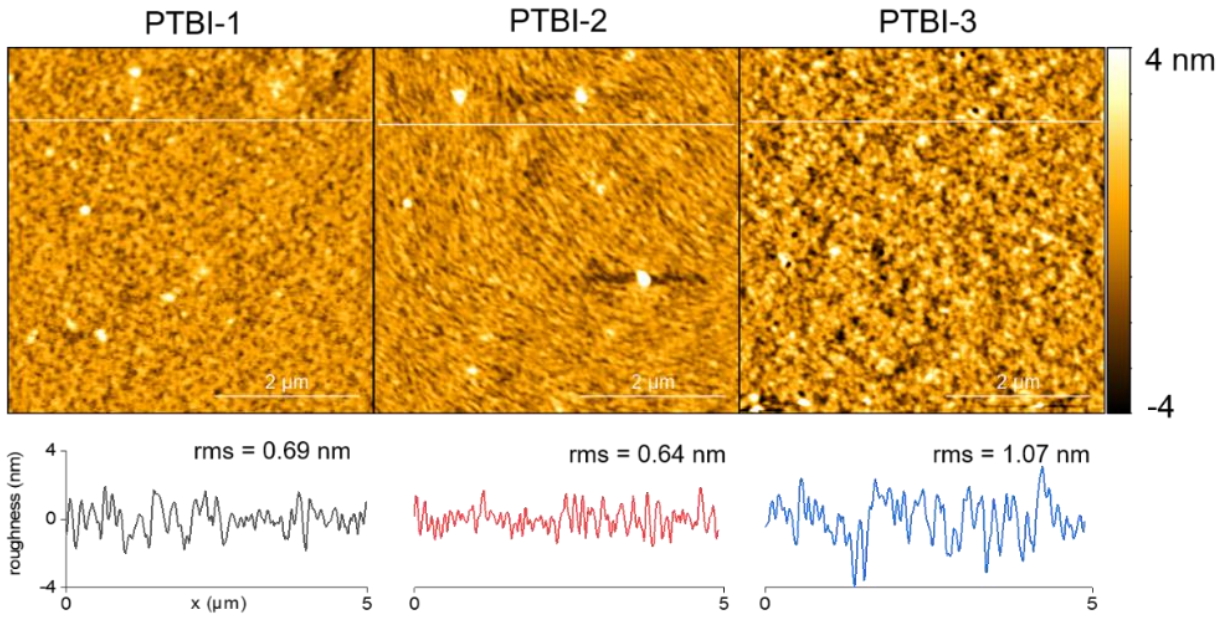

Figure 3.7 AFM height images of PTBI polymer thin films and the corresponding film roughness along white line profiles in the graphs for each film.

Varying the annealing temperature didn't change film morphology features (Figure 3.8). The comparison of PTBI polymer films provides clear evidence that the microstructure is affected by side-chain sequence regioisomerism.

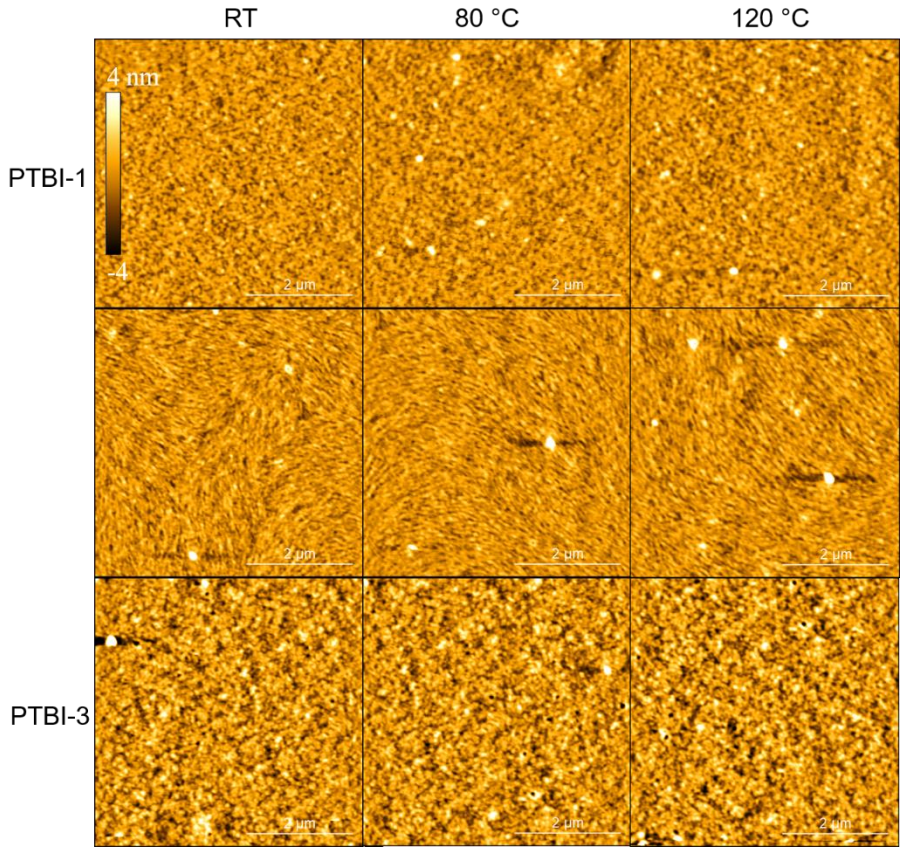

Figure 3.8 AFM height images of PTBI polymer thin films at different temperature. No change of morphology feature was observed from room temperature to 120 °C (device annealing temperature) *o*-DCB solutions.

Grazing Incident X-ray Diffraction (GIXRD) measurements of thermally annealed PTBI polymer films were also carried out to obtain further insights into molecular packing in thin films. All three polymers show bimodal packing with both edge-on ($\chi = 90°$) and face-on ($\chi = 0°$) orientations of π-π stacking. Such bimodal orientation is considered to be beneficial for charge transport in the previous reports (Figure 3.9).[43,55,64]

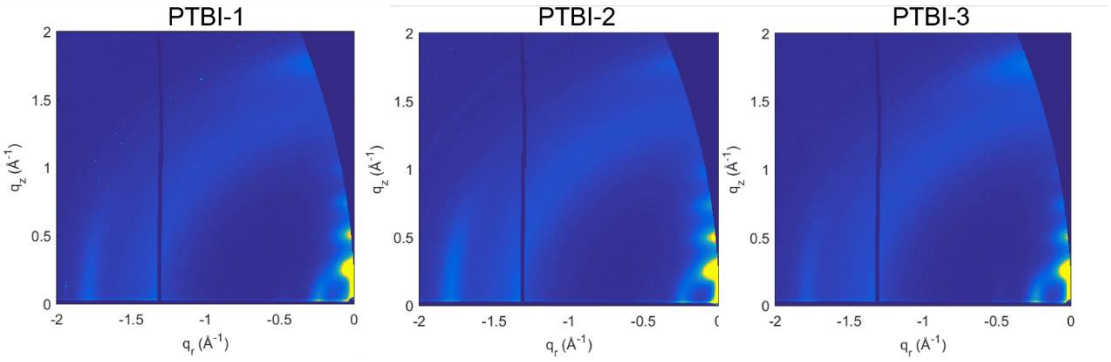

Figure 3.9 GIXRD images of PTBI polymer thin films annealed at 120 °C from *o*-DCB solutions.

Long range ordered lamellar packings up to (400) peak along face-on direction were also observed for all three polymers. As summarized in Table 3.1, the observed shortest π-π stacking distance among the three polymers is 3.51 Å of PTBI-2, only slightly shorter than PTBI-1 (3.52 Å) and PTBI-3 (3.53 Å). The small difference of GIXRD patterns is distinctly different from P3AT-like regioisomerism.[57,58,61] PTBI-2 in-plane π-π stacking was estimated to have a significantly lower full-width half-maximum (FWHM) of 0.098 than PTBI-1 of 0.129 and PTBI-3 of 0.140, as shown in Figure 3.10.

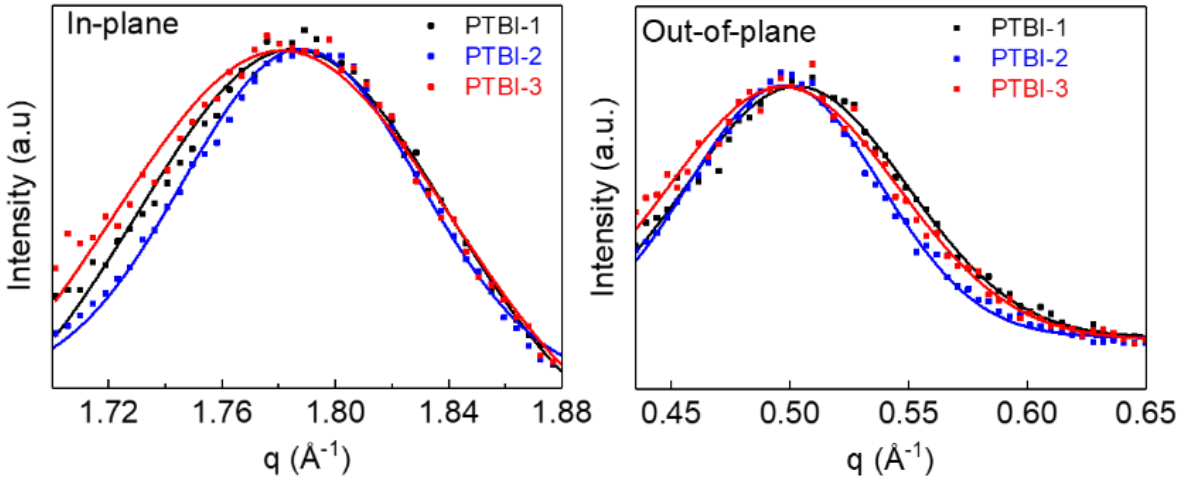

Figure 3.10 In-plane (010) and out-of-plane (200) plots of PTBI-1 (black), PTBI-2 (blue), PTBI-3 (red) and their fitted curves.

The same trend was also observed for out-of-plane (200) lamellar packing peaks. Although the three polymer films were estimated to have similar lamellar packing distances, PTBI-2 has a much smaller lamellar packing FWHM than other two polymers. According to Scherrer's equation, FWHM is inversely proportional to the crystal coherence length.[65] Thus, a lower FWHM value usually implies larger crystalline domains. These observations are in a good agreement with AFM images, where PTBI-2 film appears to have a morphology with larger ordered domains.

3.4.2 Charge Transport Measurements

To what extent side-chain sequence would impact charge transport properties is our primary interest of this study. Therefore, both field effect transistor measurements and space-charge-limited current (SCLC) method were employed to characterize charge mobilities of PTBI polymers. Details of the device fabrication are described in the Experimental Section. FET Devices of all PTBI polymer thin films with bottom-gate bottom-contact (BGBC) architecture and Au contacts under ambient conditions displayed p- type characteristics. (Figure 3.11)

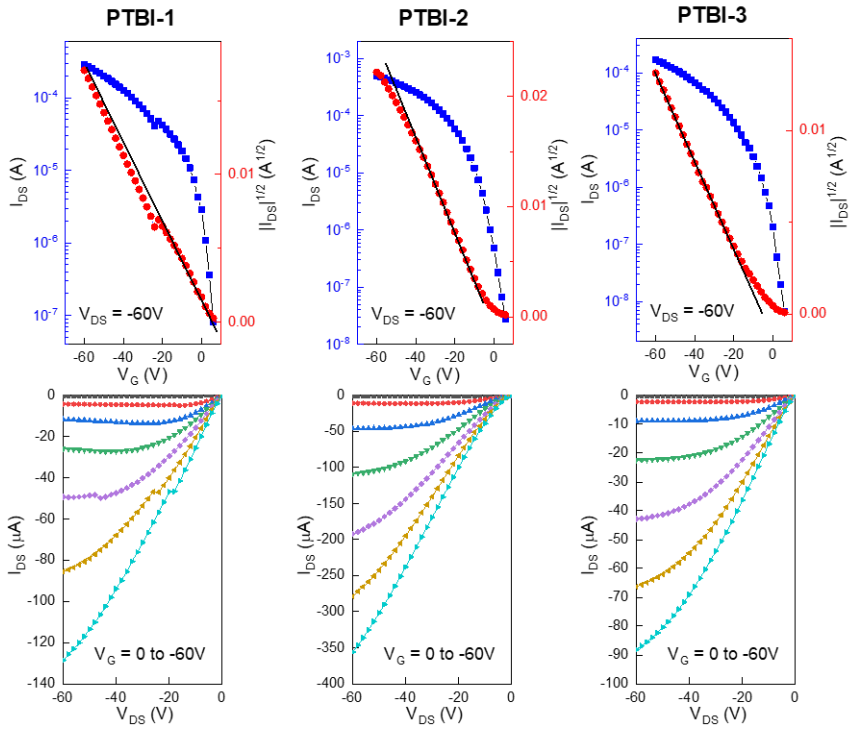

Figure 3.11 Representative transfer and output curves of PTBI-1, PTBI-2 and PTBI-3 thin film transistor devices.

Charge mobilities of all polymers were calculated based on more than 15 devices. The average mobilities of PTBI-2, PTBI-3 and PTBI-3 were estimated to be 0.40, 1.37 and 0.27 $cm^2V^{-1}s^{-1}$ respectively, and their corresponding highest mobilities were 0.53, 2.22 and 0.43 $cm^2V^{-1}s^{-1}$. The current on/off ratios for all FETs are around 10^4. The SCLC mobilities measured from hole-only diodes showed consistent trend with FET mobilities, where the mobilities of PTBI-2 (2.04×10^{-2} $cm^2V^{-1}s^{-1}$) were highest, PTBI-1 (1.85×10^{-2} $cm^2V^{-1}s^{-1}$) being the second highest and PTBI-3 (4.67×10^{-3} $cm^2V^{-1}s^{-1}$) being the lowest. (Figure 3.12)

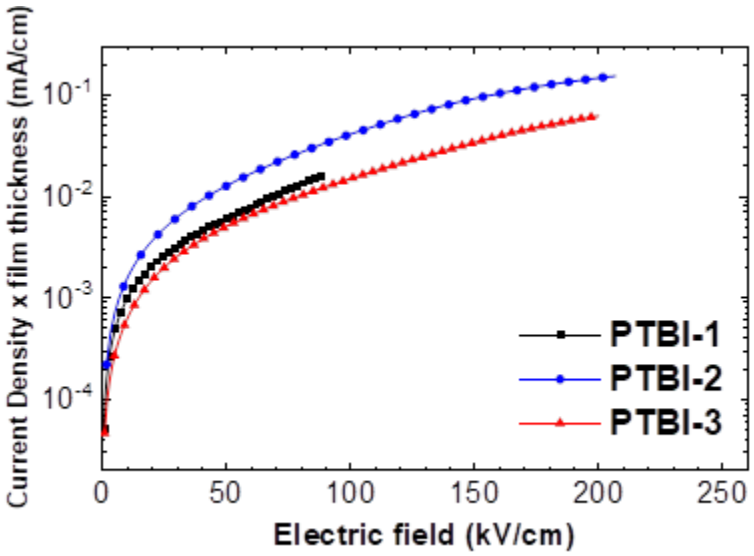

Figure 3.12 J-V characteristics of hole-only diodes of three PTBI polymers. Device structure: ITO/MoO_x/polymer/MoO_x/Ag.

Table 3.1 Summary of 2D-GIXRD data and FET device performance of PTBI polymers

Polymer	π-π distance (Å)	FWHM in-plane (010)	lamellar distance (Å)	FWHM out-of-plane (200)	μ_{ave} ($cm^2V^{-1}s^{-1}$)	μ_{max} ($cm^2V^{-1}s^{-1}$)	$I_{on/off}$	V_{th} (V)
PTBI-1	3.52	0.129	24.6	0.109	0.40 ± 0.065	0.53	10^4	-8 ± 4
PTBI-2	3.51	0.098	24.6	0.095	1.37 ± 0.36	2.22	10^4	-5 ± 3
PTBI-3	3.53	0.140	24.8	0.114	0.27 ± 0.070	0.43	10^4	-8 ± 3

3.5 Structure-Property Relationship

The highest performance of PTBI-2 can be attributed to its fibrillar morphology and largest crystalline domain, as observed from AFM and 2D-GIXRD measurements. Similarly, poor performance of PTBI-3 film may result from the smallest crystalline domain, reconfirming negative effects of regiorandom structures on polymer optoelectronic properties.[56,66,67] Intriguingly, although PTBI-1 is also a regioregular polymer like PTBI-2, noticeable differences were observed in solid state aggregation, morphology, crystalline domain size, and consequently device performance of the two polymers. A possible reason for such differences is the steric effect of side chains between repeating units, as supported by many reports.[54,68–71] Density functional theory calculations predicted a good planarity within the bis-TBI accepting moiety and twisted conformation between the donors and acceptors.[59] It is likely that the steric repulsion of side chains between bis-TBI and bithiophene (rather than inside the bis-TBI moiety) has a larger impact on the polymer chains. If the steric repulsion of side chains plays a role, the example of PTBI-1 and PTBI-2 pairs provides a scenario implying that moving bulky solubilizing side chains inside the planar or rigid moiety could help improve charge transport properties. Considering most long rigid/fused conjugated building blocks have bulkier branched side chains at sides of moieties,[72–76] this side-chain regioisomerism strategy may serve as versatile tool to optimize the structure for enhanced charge transport purposes.

3.6 Conclusions

In summary, side-chain sequence enabled regioreisomeric acceptors for D-A type copolymers are first demonstrated. Starting with these *bis*-TBI monomers, three polymers PTBI-1, PTBI-2 and PTBI-3 were synthesized and fully characterized. The three polymers are similar in their frontier orbital energy levels but have distinct aggregation states in thin films. AFM and 2D-GIXRD measurements indicate that the PTBI-2 thin film shows smooth fibrillar morphology and the largest ordered domains. As a result, PTBI-2 FET devices achieved the highest hole mobility of 2.22 $cm^2V^{-1}s^{-1}$, much higher than other two polymers with different side-chain sequences. We anticipate that the strategy of side-chain sequence regioisomerism could be applied in future design of building blocks for functional D-A type semiconducting polymers

3.7 Experimental Section

All reagents purchased from suppliers were used without further purification. ^{1}H- and ^{13}C-NMR spectra were recorded using Varian Inova 300, Bruker ARX 400 or Bruker Avance-III-800 in deuterated chloroform at 298 K. GPC was performed by high-temperature gel permeation chromatography at 150 °C using 1,2,4-trichlorobenzene (TCB) as eluent based on polystyrene standards. Differential scanning calorimetry (DSC) measurements were acquired using a TA Q1000 calorimeter at a heating rate of 10 °C min^{-1} with nitrogen as purge gas. UV-vis-NIR spectra were measured with an Agilent Technologies Cary 6000i UV-Vis-NIR spectrophotometer (400 – 1200 nm). All the electrochemistry related experiments (CV, DPV) were performed by BioLogic SP-150, using a three-electrode system in propylene carbonate with 0.2 M *n*-Bu_4NPF_6 as supporting electrolyte (scan rate: 20 mV s^{-1}). The working electrode is a platinum bottom coated by the polymer thin film; the pseudoreference electrode is an Ag wire coated by AgCl; the counter electrode is a platinum wire. The oxidation potential of ferrocene/ferrocenium (Fc/Fc^{+}) was measured under the same conditions to calibrate the reference, which was 0.38 V versus Ag/AgCl. 2D-GIXRD measurement was carried out in Argonne National Laboratory. AFM measurement was carried out using Asylum Cypher ES AFM. FET device characterization was carried out using Keithley 4200 in ambient air.

3.7.1 Synthetic Procedures

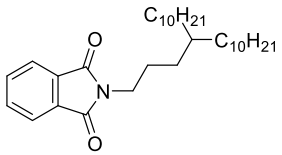

Compound b-pht: 11-(3-iodopropyl)henicosane (10.0 g, 21.5 mmol) and potassium phthalimide (4.78 g, 25.8 mmol) were added to DMF (60 mL). The mixture was stirred under N_2 at 80 °C overnight before being allowed to cool to room temperature. The reaction mixture was poured into water, extracted with haxanes and dried over Na_2SO_4. After removal of solvent under reduced pressure, the residue was purified by silica chromatography (hexanes:EtOAc = 30:1) to give the product (b-pht) as a colorless oil (9.4 g, 90%). ^{1}H NMR (400 MHz, $CDCl_3$, ppm) δ: 7.84 (dd, *J* = 5.4, 3.0 Hz, 2H), 7.70 (dd, *J* = 5.4, 3.0 Hz, 2H), 3.65 (t, *J* = 7.4 Hz, 2H), 1.70 – 1.59 (m, 2H), 1.39 – 1.14 (m, 39H), 0.86 (t, *J* = 6.6 Hz, 6H). ^{13}C NMR (100 MHz, $CDCl_3$, ppm) δ: 168.34, 133.69,

132.09, 123.02, 38.39, 37.02, 33.38, 31.82, 30.66, 29.98, 29.58, 29.54, 29.25, 26.54, 25.73, 22.58, 14.01.

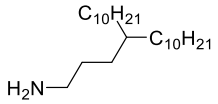

Compound b-NH_2: b-pht (9.4 g, 19.4 mmol) and hydrazine hydrate (2.92 g, 58.3 mmol) were added to CH_3OH (100 mL). The mixture was heated under N_2 at reflux for 12 h. After removal of MeOH under reduced pressure, the residue was diluted with hexanes and washed with 10% KOH twice. The combined aqueous layer was extracted with hexanes. The combined hexanes solutions were washed with brine and dried over Na_2SO_4. Removal of solvent under reduced pressure gives b-NH_2 as a colorless oil. The product was used without further purification (6.5 g, 95%). ^{1}H NMR (400 MHz, $CDCl_3$, ppm) δ: 2.67 (m, 2H), 1.76 (br, 2H), 1.42 (m, 2H), 1.42 – 1.18 (m, 39H), 0.87 (t, J = 6.7 Hz, 6H). ^{13}C NMR (100 MHz, $CDCl_3$, ppm) δ: 42.59, 37.18, 33.52, 31.82, 30.71, 30.03, 29.61, 29.56, 29.25, 26.58, 22.58, 14.01.

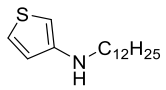

Compound 1a: 3-bromothiophene (5.03 g, 30.8 mmol), dodecan-1-amine (6.86 g, 37.0 mmol), tribasic potassium phosphate (13.1 g, 61.7 mmol) and copper (I) iodide (0.588 g, 3.08 mmol) were added to N,N-dimethylaminoethanol (60 mL). The mixture was stirred under N_2 at 80 °C for 48 h before being allowed to cool to room temperature. The reaction mixture was poured into saturated NH_4Cl aqueous solution, extracted three times with hexanes. The combined hexane solutions were washed with brine and dried over Na_2SO_4. After removal of solvent under reduced pressure, the residue was purified by flash silica chromatography (CH_2Cl_2) to give an air-sensitive crude product 1a (4.00 g, crude yield) as a brown oil. The crude product was used without further purification.

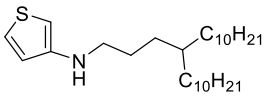

Compound 1b: Synthesized with the same procedure that was used for 1a except that 3-bromothiophene (2.73 g, 16.7 mmol), b-NH_2 (7.10 g, 20.1 mmol), tribasic potassium phosphate (7.10 g, 33.5 mmol) and copper (I) iodide (0.319 g, 1.67 mmol) were used. An air-sensitive crude product 1b (2.51 g, crude yield) was obtained as a brown oil. The crude product was used without further purification.

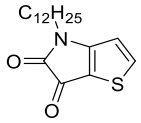

Compound 2a: A solution of oxalyl chloride (2.47 g, 19.4 mmol) in dichloromethane (20 mL) was cooled to 0 °C. 1a (4.00 g, 15.0 mmol) in 20 mL dichloromethane was added dropwise via an addition funnel. The solution was stirred at 0 °C for 30 min before dropwise addition of triethylamine (10 mL) in dichloromethane (10 mL). The mixture was stirred at room temperature overnight, after which it was poured into water, extracted with dichloromethane and dried over Na_2SO_4. After removal of solvent under reduced pressure, the residue was purified by silica chromatography (CH_2Cl_2) to give the product 2a as a red crystalline solid. (2.57 g, 26% over two steps) ^{1}H NMR (300 MHz, $CDCl_3$, ppm) δ: 8.01 (d, *J* = 4.9 Hz, 1H), 6.79 (d, *J* = 4.9 Hz, 1H), 3.60 (t, *J* = 7.0 Hz, 2H), 1.65-1.59 (m, 2H), 1.43-1.05 (m, 18H), 0.80 (t, *J* = 6.4 Hz, 3H). ^{13}C NMR (75 MHz, $CDCl_3$, ppm) δ: 172.82, 165.04, 161.33, 144.68, 113.04, 110.81, 42.16, 31.96, 29.65, 29.39, 28.25, 26.83, 22.77, 14.32.

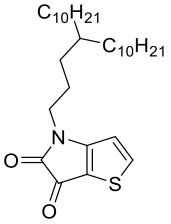

Compound 2b: Synthesized with the same procedure that was used for 2a except that 1b (2.50 g, 5.74 mmol), oxalyl chloride (0.947 g, 7.46 mmol) and triethylamine (4 mL) were used. Purification by silica chromatography (Hexanes:EtOAc = 20:1) provided the product 2b as an orange oil. (1.37 g, 17% over two steps) ^{1}H NMR (300 MHz, $CDCl_3$, ppm) δ: 7.99 (d, *J* = 4.9 Hz, 1H), 6.78 (d, *J* = 5.0 Hz, 1H), 3.63 (t, *J* = 7.3 Hz, 2H), 1.70 – 1.59 (m, 2H), 1.37 – 1.13 (m, 39H), 0.87 (t, *J* = 7.1 Hz, 6H). ^{13}C NMR (75 MHz, $CDCl_3$, ppm) δ: 172.80, 165.01, 161.31, 143.94, 113.00, 110.90, 42.56, 37.09, 33.50, 32.00, 30.65, 30.15, 29.76, 29.44, 26.69, 25.40, 22.79, 14.25.

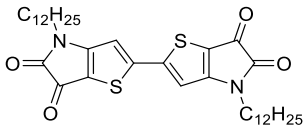

Compound 3a: 2a (950 mg, 2.96 mmol), Silver Fluoride (825 mg, 6.50 mmol) and Palladium(II) acetate (66.3 mg, 0.296 mmol) were added to 30 mL of DMSO. The mixture was stirred under N_2 at 90 °C for 24 h before being allowed to cool to room temperature. The reaction mixture was

poured into water, extracted with dichloromethane and dried over Na_2SO_4. After removal of solvent under reduced pressure, the residue was purified by silica chromatography (CH_2Cl_2) to give the product (3a) as a dark purple solid (446 mg, 47%). ^{1}H NMR (400 MHz, $CDCl_3$, ppm) δ: 6.99 (s, 2H), 3.69 (t, J = 7.2 Hz, 4H), 1.71 (m, 4H), 1.40-1.24 (m, 36H), 0.88 (t, J = 6.7 Hz, 6H). ^{13}C NMR (100 MHz, $CDCl_3$, ppm) δ: 172.20, 164.24, 160.28, 151.50, 111.58, 110.58, 42.26, 31.73, 29.42, 29.35, 29.29, 29.13, 28.97, 28.06, 26.64, 22.47, 13.84.

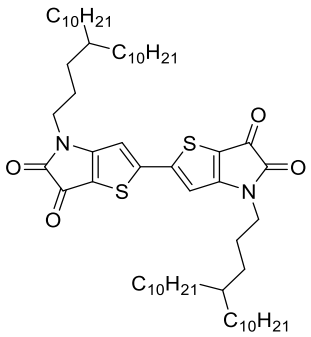

Compound 3b: Synthesized with the same procedure that was used for 3a except that 2b (729 mg, 1.49 mmol), Silver Fluoride (415 mg, 3.27 mmol) and Palladium(II) acetate (33.4 mg, 0.149 mmol) were added to a mixture of 15 mL DMSO and 15 mL dioxane (dioxane improves the solubility of 2b). Purification by silica chromatography ($CHCl_3$) provided the product (3b) as a dark purple solid (440 mg, 60%). ^{1}H NMR (300 MHz, $CDCl_3$, ppm) δ: 7.00 (s, 2H), 3.68 (t, *J* = 7.2 Hz, 4H), 1.68 (m, 4H), 1.43 – 1.11 (m, 78H), 0.87 (t, *J* = 6.8 Hz, 12H). ^{13}C NMR (75 MHz, $CDCl_3$, ppm) δ: 172.24, 164.28, 160.31, 151.71, 111.51, 110.74, 42.78, 37.12, 33.50, 32.01, 30.73, 30.19, 29.80, 29.75, 29.45, 26.71, 25.50, 22.80, 14.25.

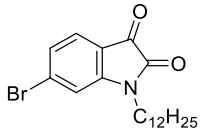

Compound 4a: 6-Bromoisatin (1.13 g, 5.02 mmol), potassium carbonate (1.04 g, 7.52 mmol) and 1-bromododecane (1.50 g, 6.02 mmol) were added into 50 mL DMF. The mixture was stirred under N_2 at 100 °C overnight before being allowed to cool to room temperature. The reaction mixture was extracted with dichloromethane and dried over Na_2SO_4. After removal of solvent under reduced pressure, the residue was purified by silica chromatography (hexanes:CH_2Cl_2 = 1:3) to give the product (5a) as a yellow solid (1.37 g, 69%). ^{1}H NMR (400 MHz, $CDCl_3$, ppm) δ: 7.44 (d, *J* = 7.9 Hz, 1H), 7.26 (dd, *J* = 7.9, 1.5 Hz, 1H), 7.05 (d, *J* = 1.5 Hz, 1H), 3.68 (t, *J* = 7.3 Hz, 2H), 1.66 (m, 2H), 1.50 – 1.12 (m, 18H), 0.86 (t, *J* = 6.8 Hz, 3H).

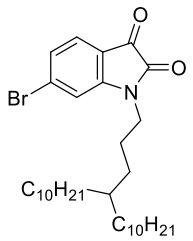

Compound 4b: Synthesized with the same procedure that was used for 4a except that 11-(3-iodopropyl)henicosane (2.47 g, 5.31 mmol), 6-Bromoisatin (1.00 g, 4.42 mmol), potassium carbonate (0.917 g, 6.64 mmol) were added to a mixture of 25 mL DMF and 25 mL THF. Purification by silica chromatography (hexanes:CH_2Cl_2 = 1:1) provided the product (4b) as an orange solid (2.07 g, 83%). ^{1}H NMR (400 MHz, $CDCl_3$, ppm) δ: 7.46 (d, *J* = 7.9 Hz, 1H), 7.27 (dd, *J* = 7.9, 1.2 Hz, 1H), 7.06 (d, *J* = 1.2 Hz, 1H), 3.68 (t, *J* = 7.3 Hz, 2H), 1.66 (m, 2H), 1.40 – 1.13 (m, 39H), 0.87 (t, *J* = 6.7 Hz, 6H).

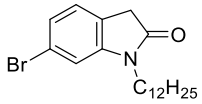

Compound 5a: 4a (1.37 g, 3.9 mmol) and hydrazine monohydrate (10 mL) were added to 10 mL of DMSO. The mixture was stirred under N_2 at 130 °C for 24 h before being allowed to cool to room temperature. The reaction was poured into water, extracted with dichloromethane and dried over Na_2SO_4. After removal of the solvent under reduced pressure, the residue was purified by silica chromatography (hexanes:CH_2Cl_2 = 2:3) to give the product (5a) as a yellow oil (811 mg, 61%). ^{1}H NMR (400 MHz, $CDCl_3$, ppm) δ: 7.14 (d, *J* = 7.9 Hz, 1H), 7.08 (d, *J* = 7.8 Hz, 1H), 6.94 (s, 1H), 3.65 (t, *J* = 7.5 Hz, 2H), 3.44 (s, 2H), 1.64 (m, 2H), 1.43 – 1.15 (m, 18H), 0.87 (t, *J* = 6.6 Hz, 3H). ^{13}C NMR (100 MHz, $CDCl_3$, ppm) δ: 174.56, 145.95, 125.52, 124.70, 123.35, 121.21, 111.58, 40.09, 35.26, 31.80, 29.51, 29.46, 29.40, 29.23, 29.16, 27.22, 26.82, 22.58, 14.02.

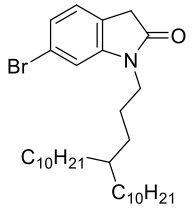

Compound 5b: Synthesized with the same procedure that was used for 5a except that 4b (2.07 g, 3.68 mmol) was used. Purification by silica chromatography (hexanes:CH_2Cl_2 = 1:1) provided the product (5b) as a yellow oil (1.43 mg, 71%). ^{1}H NMR (400 MHz, $CDCl_3$, ppm) δ: 7.15 (d, *J* = 8.0

Hz, 1H), 7.08 (d, *J* = 7.8 Hz, 1H), 6.94 (s, 1H), 3.63 (t, *J* = 7.5 Hz, 2H), 3.45 (s, 2H), 1.62 (t, *J* = 7.5 Hz, 2H), 1.23 (m, 39H), 0.87 (t, *J* = 6.4 Hz, 6H).

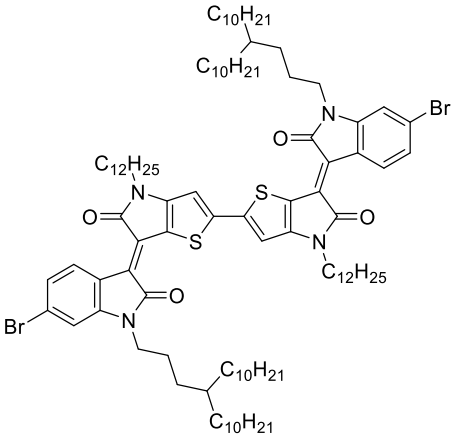

Compound *bis*-TBI-1: *p*-Toluenesulfonic acid monohydrate (16.2 mg, 0.0854 mmol) was added to a solution of 3a (137 mg, 0.213 mmol) and 5b (246 mg, 0.448 mmol) in Toluene (15 mL). The mixture was stirred under N_2 at 110 °C for 12 h before being allowed to cool to room temperature. After removal of the solvent under reduced pressure, the residue was purified by silica chromatography (hexanes:chloroform = 2:1) to give the product (*bis*-TBI-1) as a dark green solid (275 mg, 76%). ^{1}H NMR (800 MHz, $CDCl_3$, ppm) δ: 8.83 (d, *J* = 8.3 Hz, 2H), 7.04 (d, *J* = 8.3 Hz, 2H), 6.98 (s, 2H), 6.86 (s, 2H), 3.77 (t, *J* = 7.5 Hz, 4H), 3.72 (t, *J* = 7.9 Hz, 4H), 1.73 (m, 4H), 1.66 (m, 4H), 1.49 – 1.09 (m, 114H), 0.86 (m, 18H). ^{13}C NMR (200 MHz, $CDCl_3$, ppm) δ: 169.76, 168.64, 153.15, 147.15, 144.34, 129.58, 128.64, 125.10, 125.03, 120.68, 119.95, 116.46, 111.22, 107.13, 42.00, 40.61, 37.29, 33.58, 31.94, 30.91, 30.15, 29.73, 29.67, 29.65, 29.62, 29.46, 29.38, 28.60, 27.07, 26.72, 24.79, 22.70, 14.13. HRMS (APCI) calcd. for $C_{100}H_{157}Br_2N_4O_4S_2^+$ ($[M+H]^+$): 1700.0008; found 1700.0000.

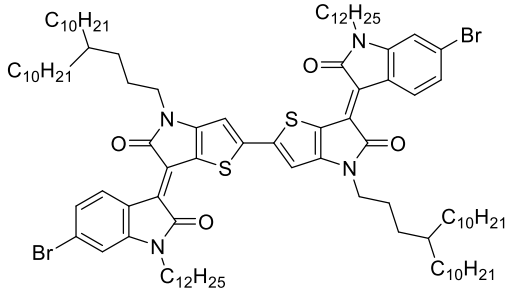

Compound *bis*-TBI-2: Synthesized with the same procedure that was used for *bis*-TBI-1 except that *p*-Toluenesulfonic acid monohydrate (11.67 mg, 0.0614 mmol) was added to a solution of 3b (150 mg, 0.154 mmol) and 5a (128 mg, 0.338 mmol) in Toluene. Purification by silica

chromatography (hexanes:chloroform = 2:1) provided the product (*bis*-TBI-2) as a dark green solid (225 mg, 86%). ^{1}H NMR (800 MHz, $CDCl_3$, ppm) δ: 8.82 (d, *J* = 8.5 Hz, 2H), 7.04 (d, *J* = 8.5 Hz, 2H), 6.98 (s, 2H), 6.87 (s, 2H), 3.81 – 3.66 (m, 8H), 1.80 – 1.65 (m, 8H), 1.45 – 1.09 (m, 114H), 0.87 (t, *J* = 7.2 Hz, 6H), 0.84 (t, *J* = 7.3 Hz, 12H). ^{13}C NMR (200 MHz, $CDCl_3$, ppm) δ: 169.80, 168.67, 153.17, 147.18, 144.36, 129.63, 128.64, 125.12, 124.99, 120.68, 119.99, 116.43, 111.17, 107.15, 42.34, 40.33, 37.36, 33.59, 31.93, 30.96, 30.16, 29.74, 29.67, 29.65, 29.63, 29.60, 29.44, 29.38, 27.73, 27.12, 26.73, 25.78, 22.69, 14.13, 14.12. HRMS (APCI) calcd. for $C_{100}H_{157}Br_2N_4O_4S_2^+$ ([M+H]$^+$): 1700.0008; found 1699.9986.

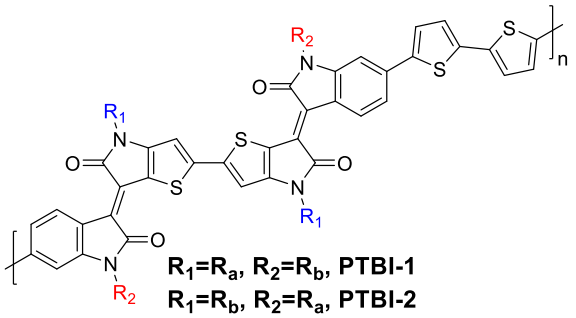

R_1=R_a, R_2=R_b, PTBI-1
R_1=R_b, R_2=R_a, PTBI-2
R_1=R_a R_2=R_b or R_1=R_b R_2=R_a, PTBI-3

To a Schlenk tube charged with a stir bar, *bis*-TBI-1 or *bis*-TBI-2 (1.0 equiv.), ditin Compound 6 (1.0 equiv.), $Pd_2(dba)_3$ (2.5 mol%), P(*o*-tol)$_3$ (4 mol%) and 15 mL of toluene were added. The resulting solution was bubbled with argon for 20 min, and the mixture was stirred for 1 h at 110 °C. After the polymerization was complete, the mixture was taken up and precipitated into methanol. The solids were collected by a soxhlet thimble, which was purified by Soxhlet extraction successively with acetone, hexane, dichloromethane and chloroform. To remove residual catalyst, *N*,*N*-diethyl-2-phenyldiazenecarbothioamide was added to the chloroform fraction, and the mixture was stirred for 30 min at 60 °C before being precipitated into methanol. The collected polymer was dried at 60 °C under vacuum.

PTBI-1: 69.91 mg (0.04107 mmol) of *bis*-TBI-1 and 20.20 mg of (0.04107 mmol) 6 were used. Precipitation provided 63.8 mg (85% yield) of a dark solid. M_n = 9.8 KDa, PDI = 1.5.

PTBI-2: 75.79 mg (0.04452 mmol) of *bis*-TBI-2 and 21.90 mg (0.04452 mmol) of 6 were used. Precipitation provided 67.4 mg (83% yield) of a dark solid. M_n = 8.6 KDa, PDI = 1.4.

PTBI-3: 36.34 mg (0.02134 mmol) of *bis*-TBI-1, 36.34 mg *bis*-TBI-2 (0.02134 mmol) and 21.00 mg (0.04269 mmol) of 6 were used. Precipitation provided 61.0 mg (79% yield) of a dark solid. M_n = 8.9 KDa, PDI = 1.5.

3.7.2 Device Fabrication and Characterization

A heavily n-doped Si wafer with a 300-nm SiO_2 surface layer (capacitance of 11 nF/cm^2) was employed as the substrate with Si wafer serving as the gate electrode and SiO_2 as the dielectric. The gold S/D electrodes were sputtered and patterned by photolithography technique. For the octadecyltrichlorosilane (OTS) modification, the silicon wafer (with Au bottom contact) was first cleaned with hot piranha solution (98%H_2SO_4:30%H_2O_2=2:1). It was then further subjected to sonication sequentially in water, ethanol, acetone for 6 min each. After drying at an oven, the silicon wafer was then put in a petri dish with a small drop of OTS. The dish was then covered and heated in a vacuum oven at 120 °C for 3 hours resulting in the formation of an OTS self-assembled monolayer on the surface. The OTS modified substrates were rinsed successively with hexane, ethanol, and chloroform, and dried by nitrogen before used. All polymers were dissolved in *o*-DCB at 5mg/mL at 50 °C for 1h. The polymers were then spin coated in ambient air on the substrate at 1500 rpm for 60 s, followed by 4000 rpm for 60s to wipe out residual solvent on the surface. All polymer films were annealed at 120 °C for 15 min inside the glovebox. The device channel length was 30 μm, and the channel width was 1000 μm. FET device characterization was carried out using Keithley 4200 in ambient air.

3.7.3 1H NMR and 13C NMR Spectra of New Compounds

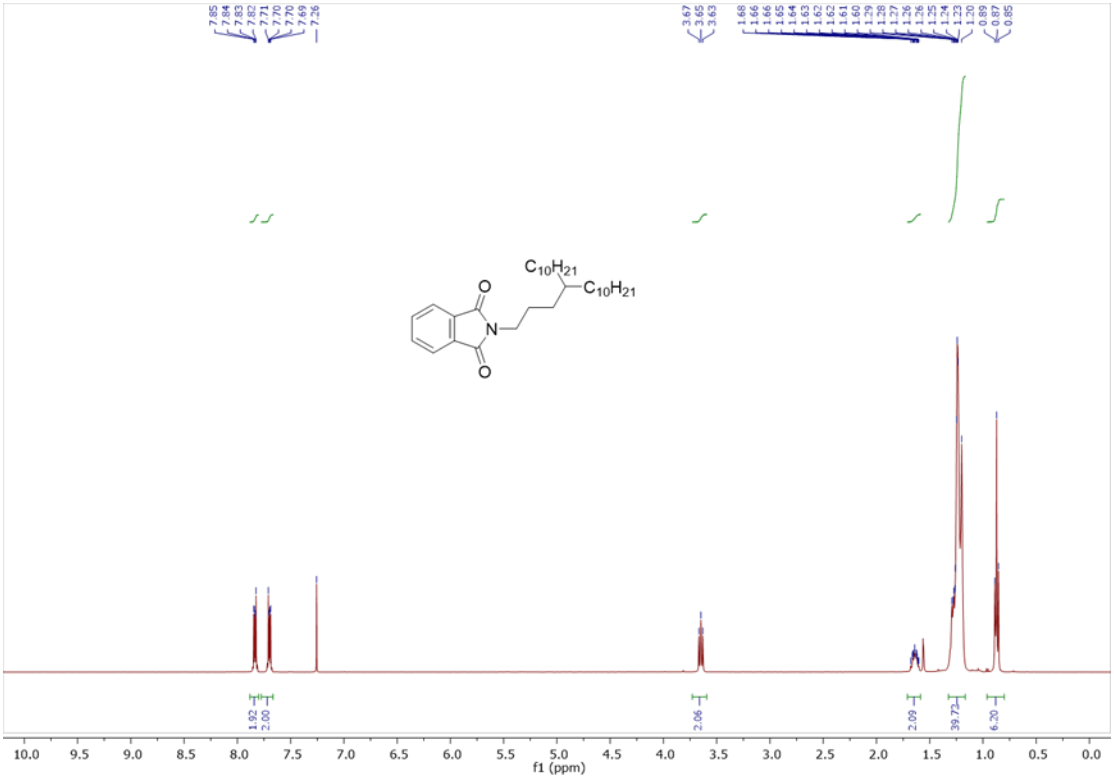

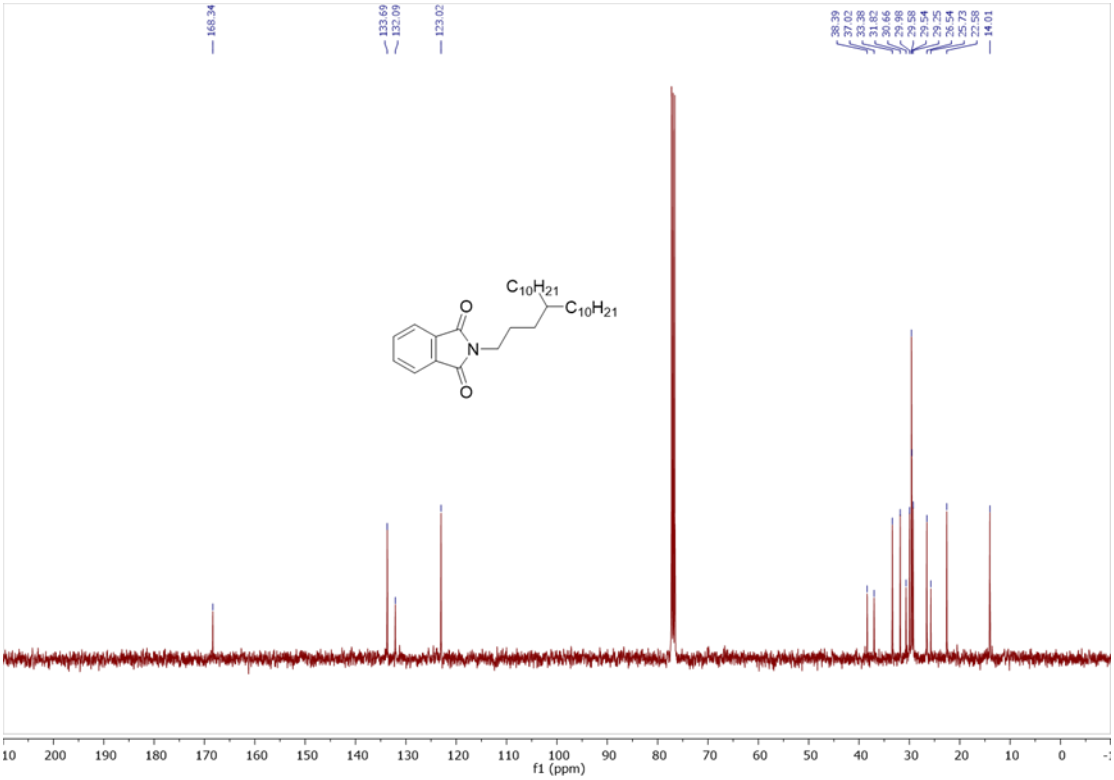

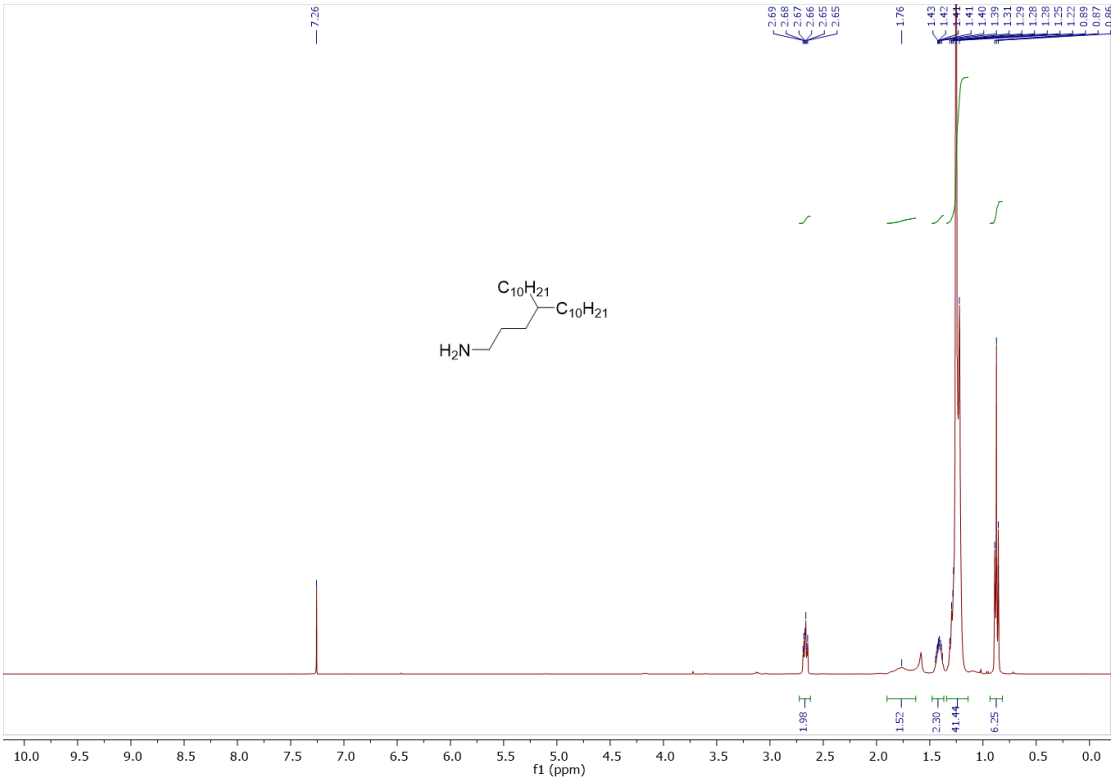
7.26
2.69
2.68
2.67
2.66
2.65
2.65
1.76
1.43
1.42
1.41
1.41
1.40
1.39
1.31
1.29
1.28
1.28
1.25
1.22
0.89
0.87
0.86
$C_{10}H_{21}$
$C_{10}H_{21}$
H_2N
1.98
1.52
2.30
41.44
6.25
10.0 9.5 9.0 8.5 8.0 7.5 7.0 6.5 6.0 5.5 5.0 4.5 4.0 3.5 3.0 2.5 2.0 1.5 1.0 0.5 0.0
f1 (ppm)

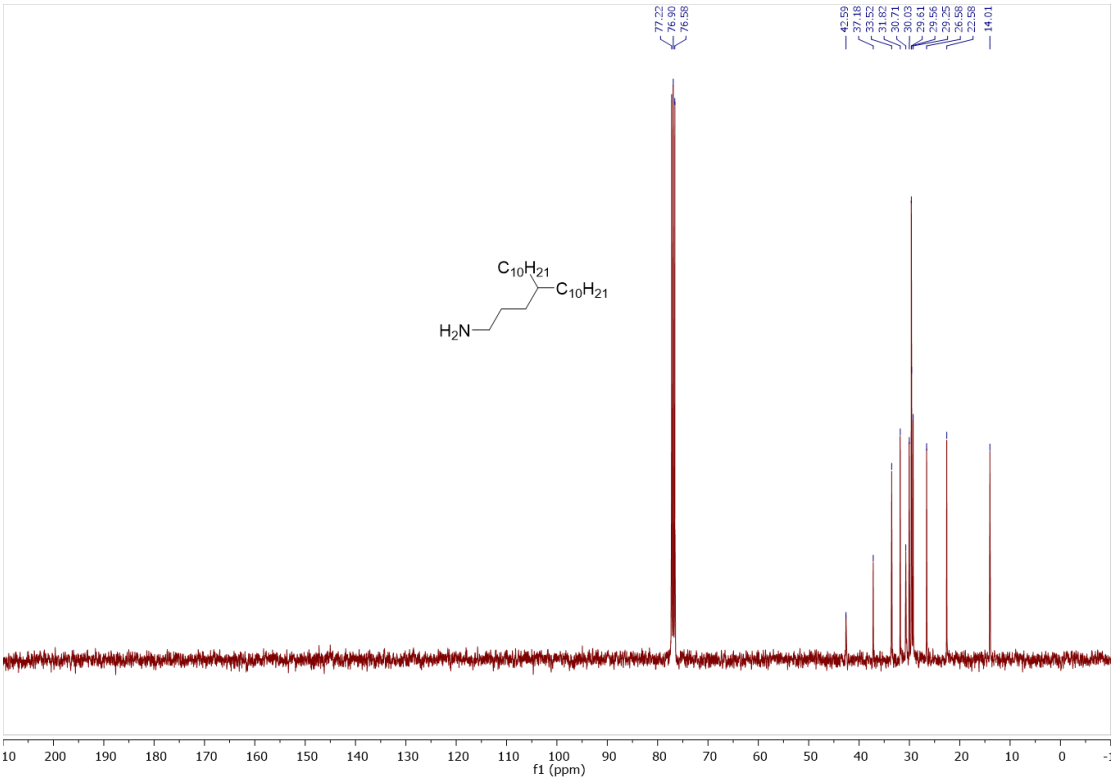
77.22
76.90
76.58
42.59
37.18
33.52
31.82
30.71
30.03
29.61
29.56
29.25
25.58
21.58
14.01
$C_{10}H_{21}$
$C_{10}H_{21}$
H_2N
10 200 190 180 170 160 150 140 130 120 110 100 90 80 70 60 50 40 30 20 10 0
f1 (ppm)

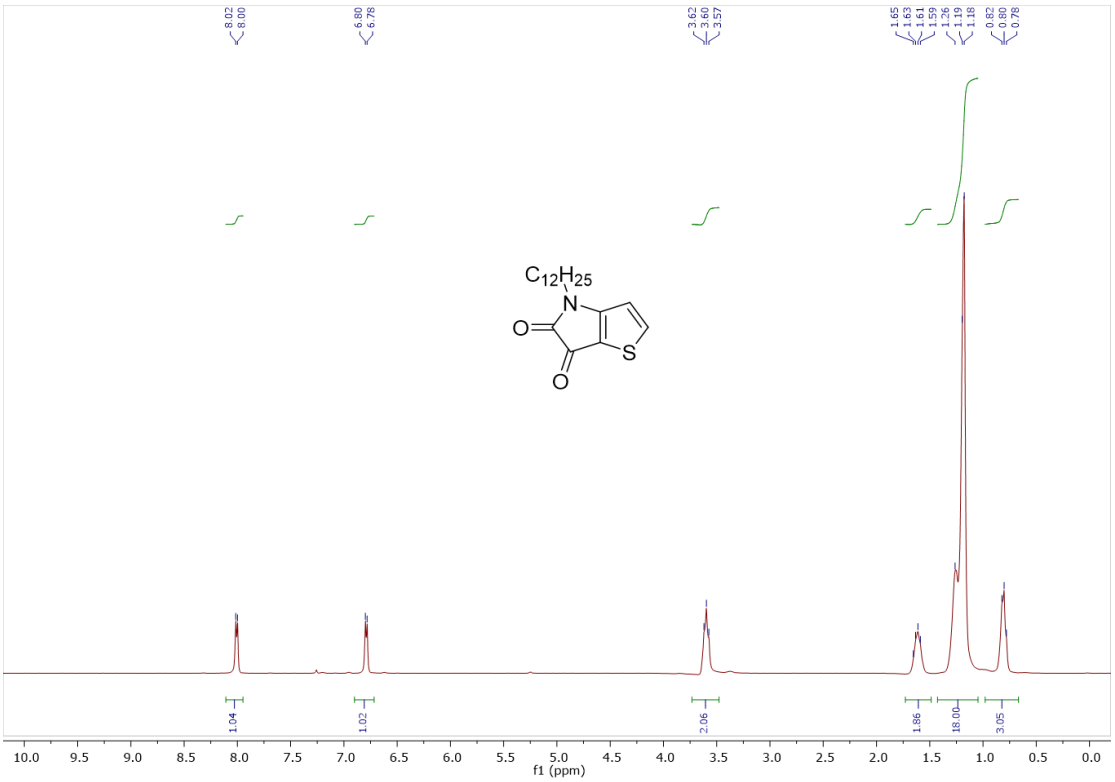
8.02
8.00
6.80
6.78
3.62
3.60
3.57
1.65
1.63
1.61
1.59
1.36
1.19
1.18
0.82
0.80
0.78
C12H25
N
O
O
S
1.04
1.02
2.06
1.86
18.00
3.05
f1 (ppm)

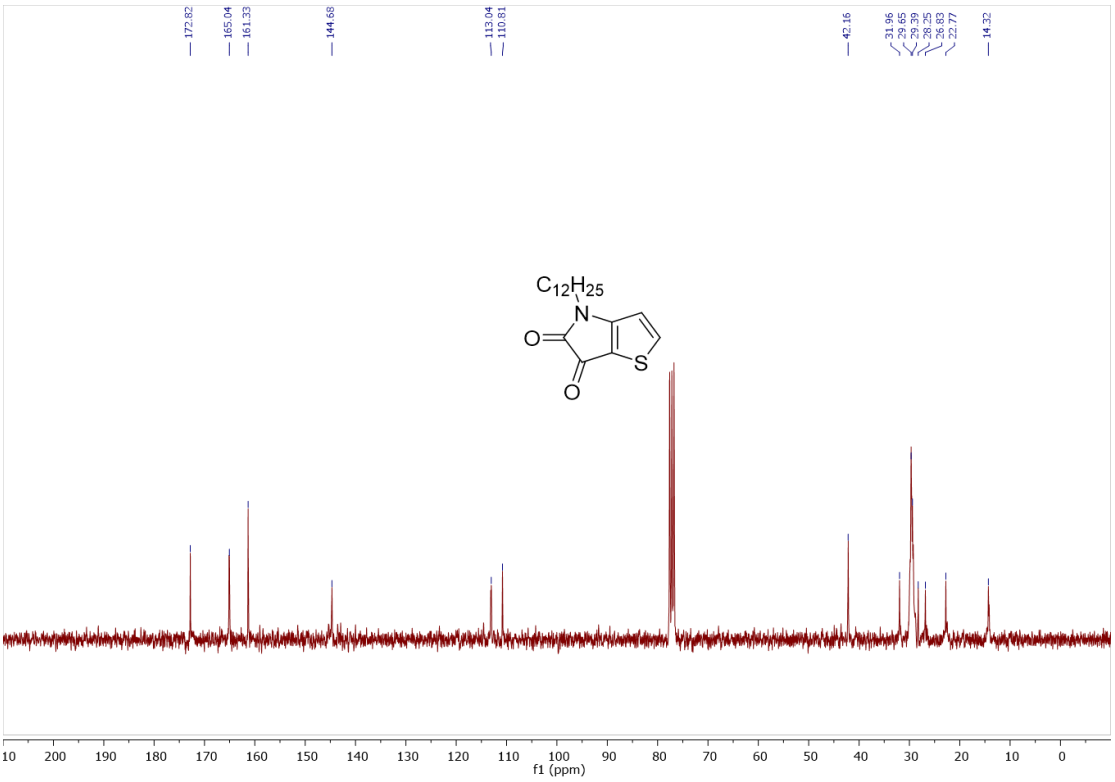
172.82
165.04
161.33
144.68
113.04
110.81
42.16
31.96
29.65
29.39
28.25
26.83
22.77
14.32
C12H25
N
O
O
S
f1 (ppm)

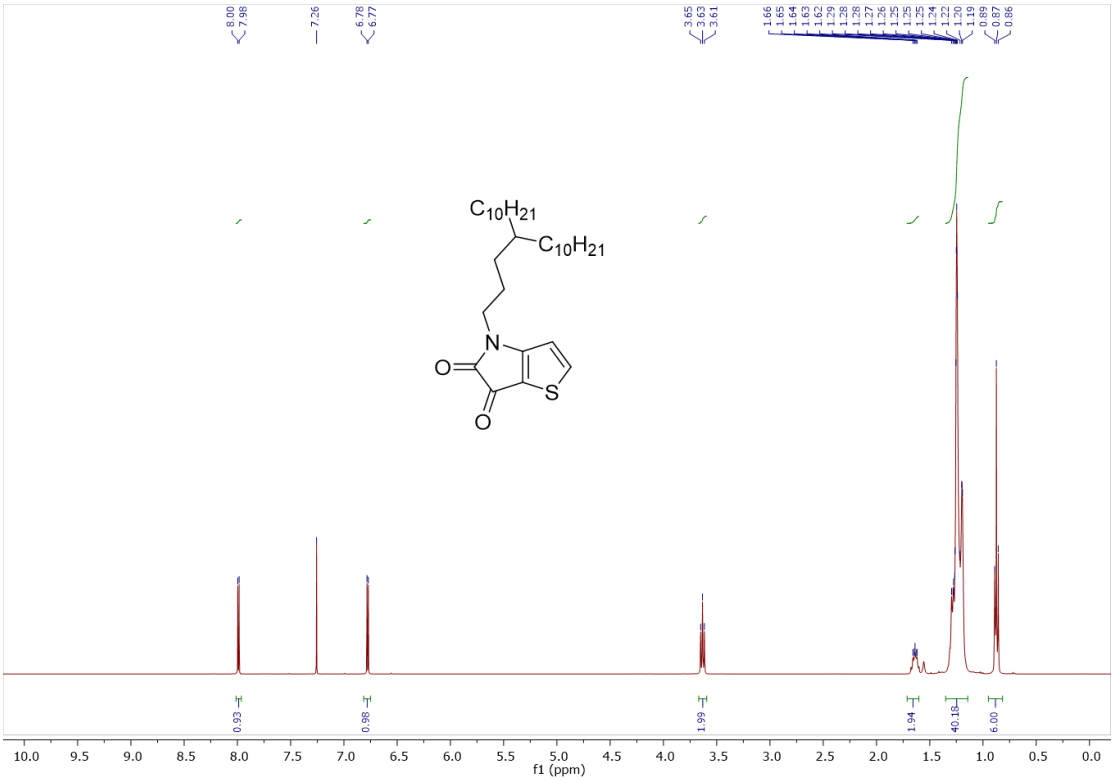
8.00
7.98
7.26
6.78
6.77
3.65
3.63
3.61
1.66
1.65
1.64
1.63
1.62
1.29
1.28
1.28
1.27
1.26
1.25
1.25
1.24
1.22
1.20
1.19
0.89
0.87
0.86
C10H21
C10H21
N
O
O
S
0.93
0.98
1.99
1.94
40.18
6.00
10.0 9.5 9.0 8.5 8.0 7.5 7.0 6.5 6.0 5.5 5.0 4.5 4.0 3.5 3.0 2.5 2.0 1.5 1.0 0.5 0.0
f1 (ppm)

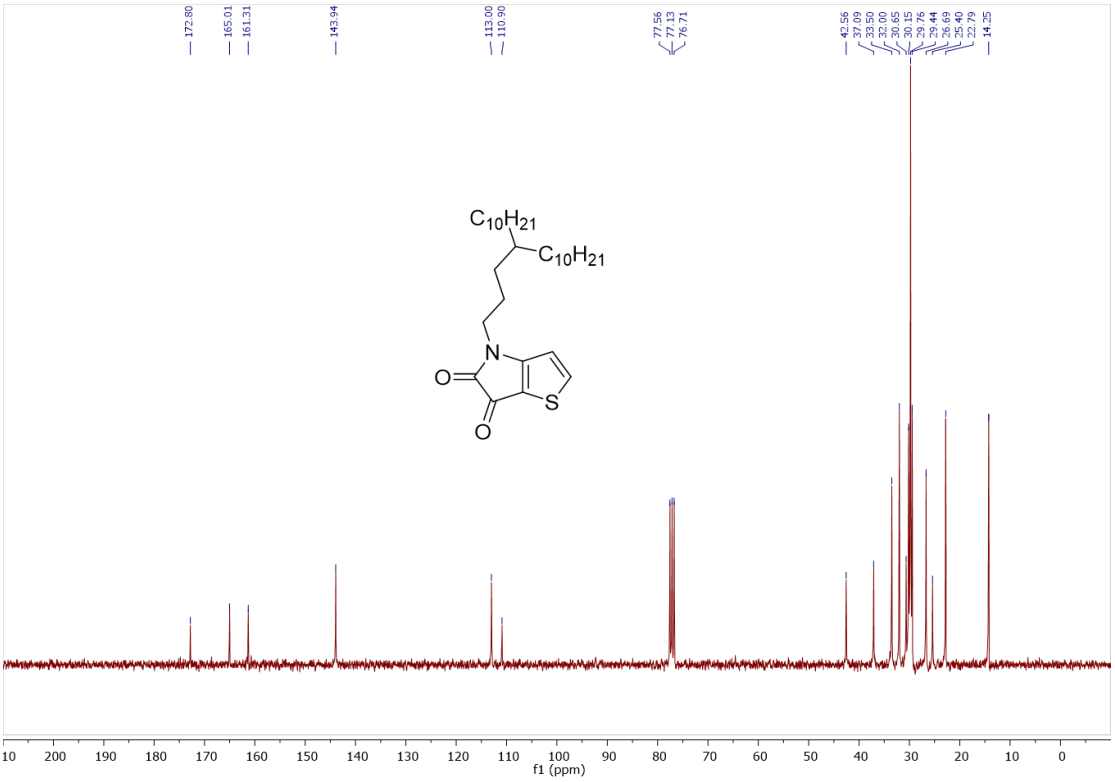
172.80
165.01
161.31
143.94
113.00
110.90
77.56
77.13
76.71
42.56
37.09
33.50
32.00
30.65
30.15
29.76
29.44
26.69
25.40
22.79
14.25
C10H21
C10H21
N
O
O
S
10 200 190 180 170 160 150 140 130 120 110 100 90 80 70 60 50 40 30 20 10 0
f1 (ppm)

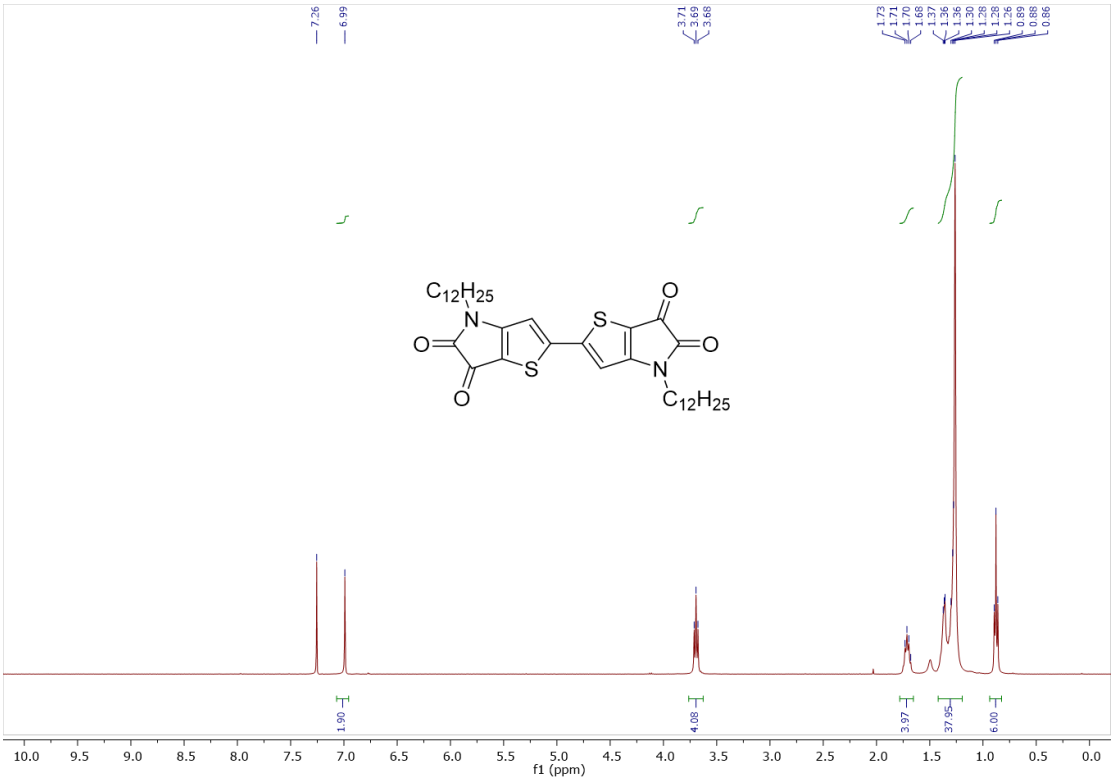
7.26
6.99
3.71
3.69
3.68
1.73
1.71
1.70
1.68
1.37
1.36
1.36
1.30
1.28
1.28
1.26
0.89
0.88
0.86
C12H25
N
O
O
S
S
O
O
N
C12H25
1.90
4.08
3.97
37.95
6.00
f1 (ppm)

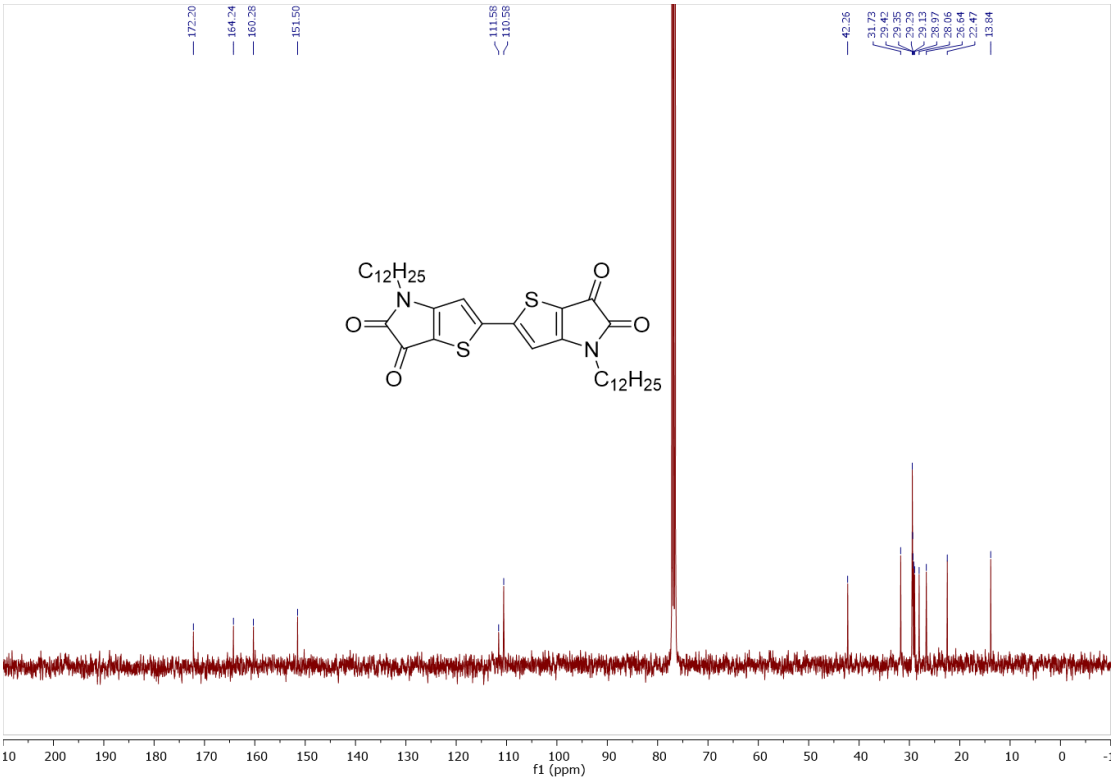
172.20
164.24
160.28
151.50
111.58
110.58
42.26
31.73
29.42
29.35
29.29
29.13
28.97
28.06
26.64
22.47
13.84
C12H25
N
O
O
S
S
O
O
N
C12H25
f1 (ppm)

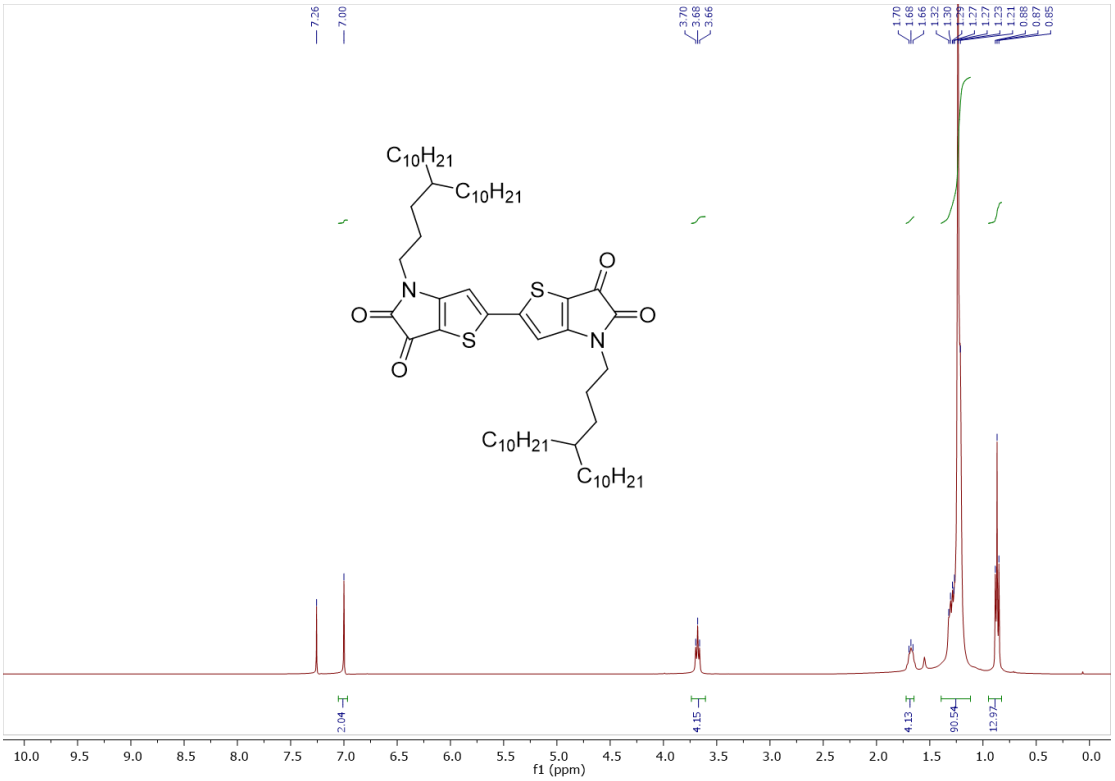
7.26
7.00
3.70
3.68
3.66
1.70
1.68
1.66
1.32
1.30
1.29
1.27
1.23
1.21
0.88
0.87
0.85
2.04
4.15
4.13
90.54
12.97
f1 (ppm)

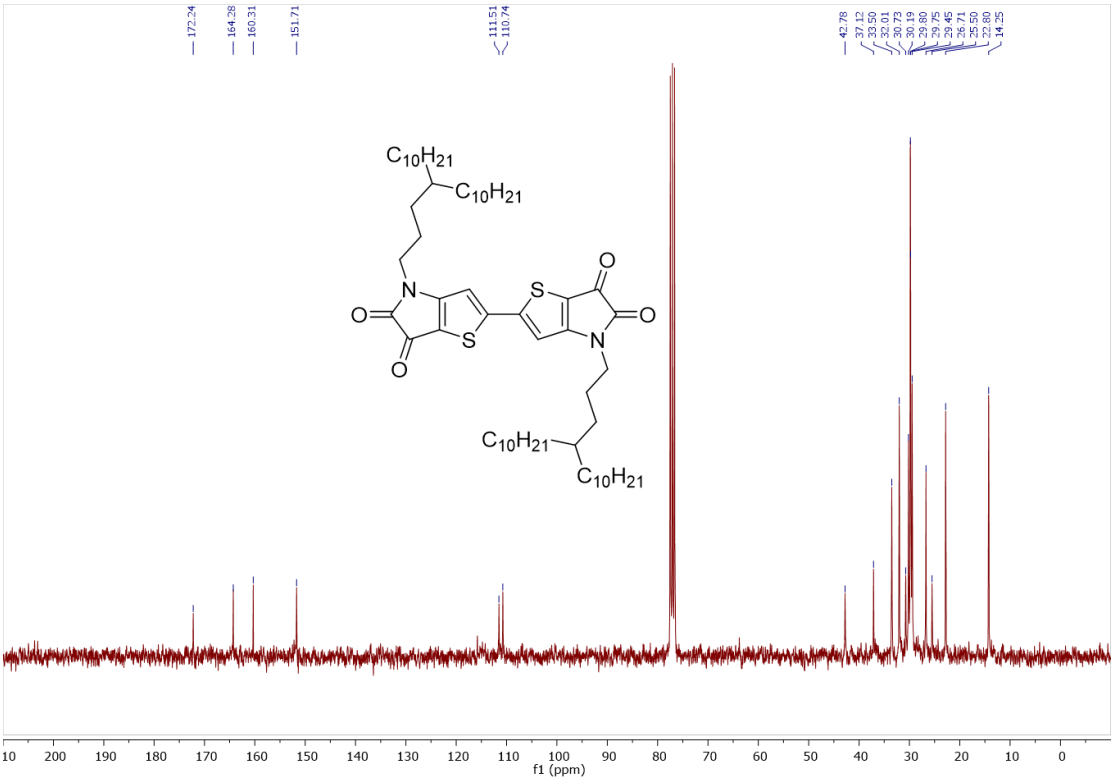
172.24
164.28
160.31
151.71
111.51
110.74
42.78
37.12
33.50
32.01
30.73
30.19
29.80
29.75
29.45
26.71
25.50
22.80
14.25
f1 (ppm)

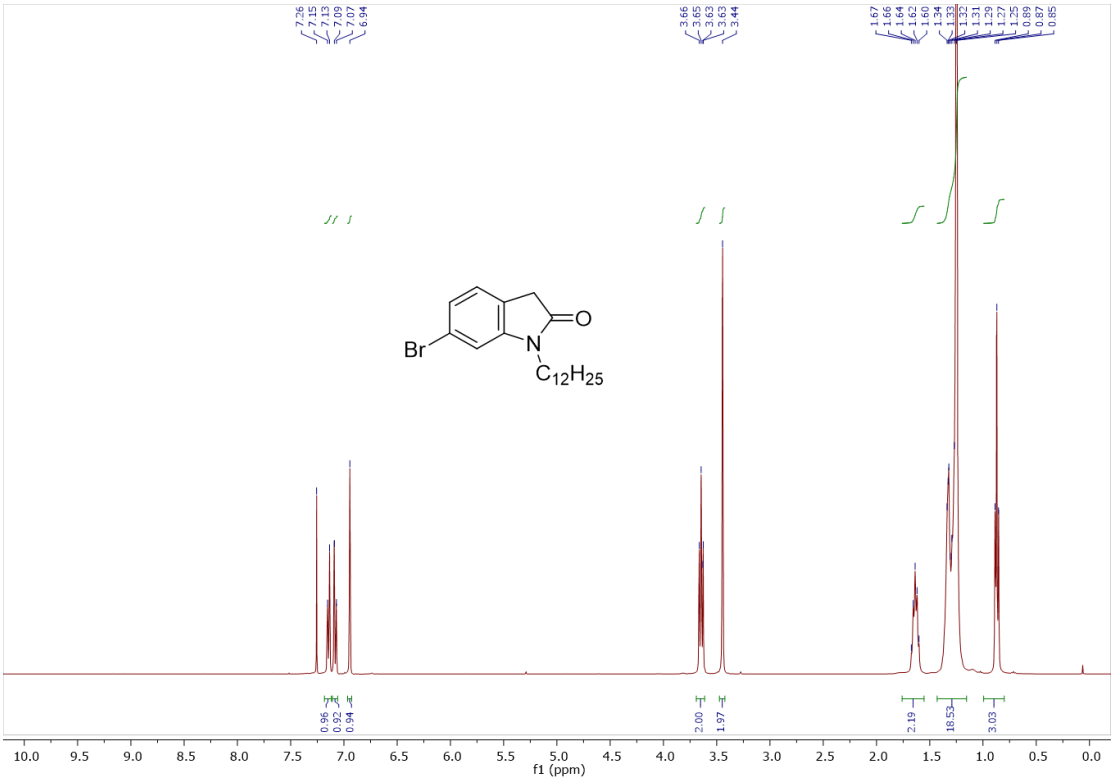
7.26
7.15
7.13
7.09
7.07
6.94
3.66
3.65
3.63
3.63
3.44
1.67
1.66
1.64
1.62
1.60
1.34
1.33
1.32
1.31
1.29
1.27
1.25
0.89
0.87
0.85
Br
O
N
C12H25
0.96
0.92
0.94
2.00
1.97
2.19
18.53
3.03
f1 (ppm)

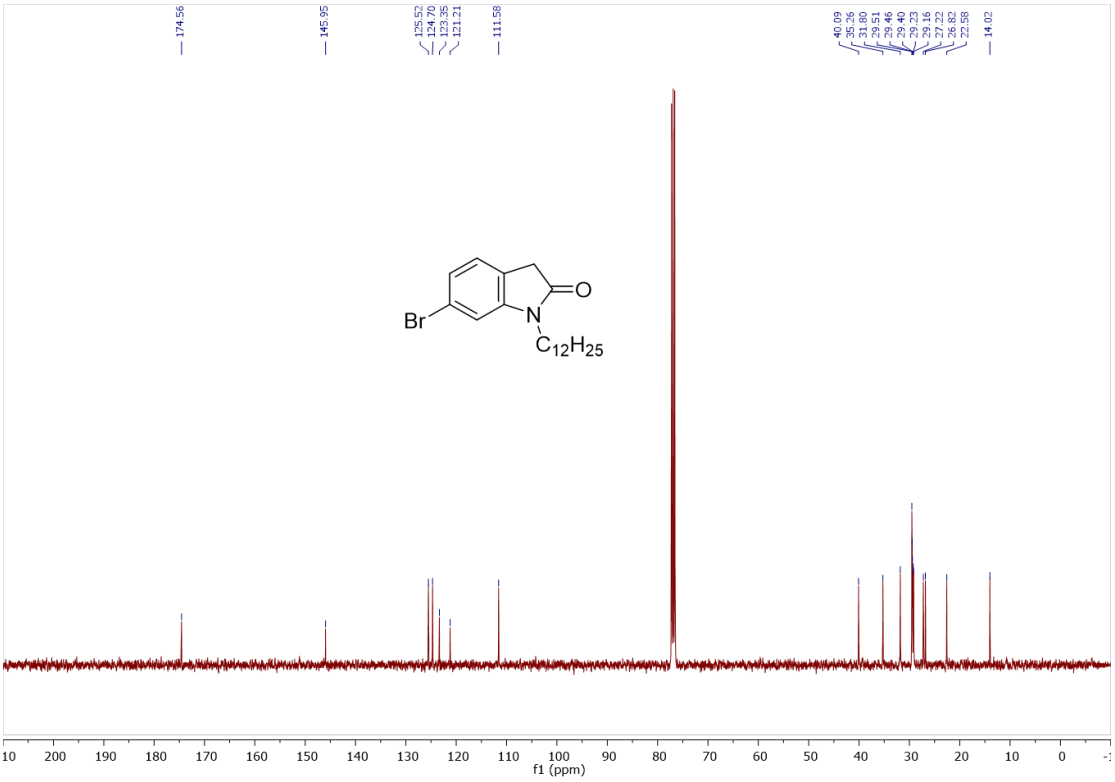
174.56
145.95
125.52
124.70
123.35
121.21
111.58
40.09
35.26
31.80
29.51
29.46
29.40
29.23
29.16
27.22
26.82
22.58
14.02
Br
O
N
C12H25
f1 (ppm)

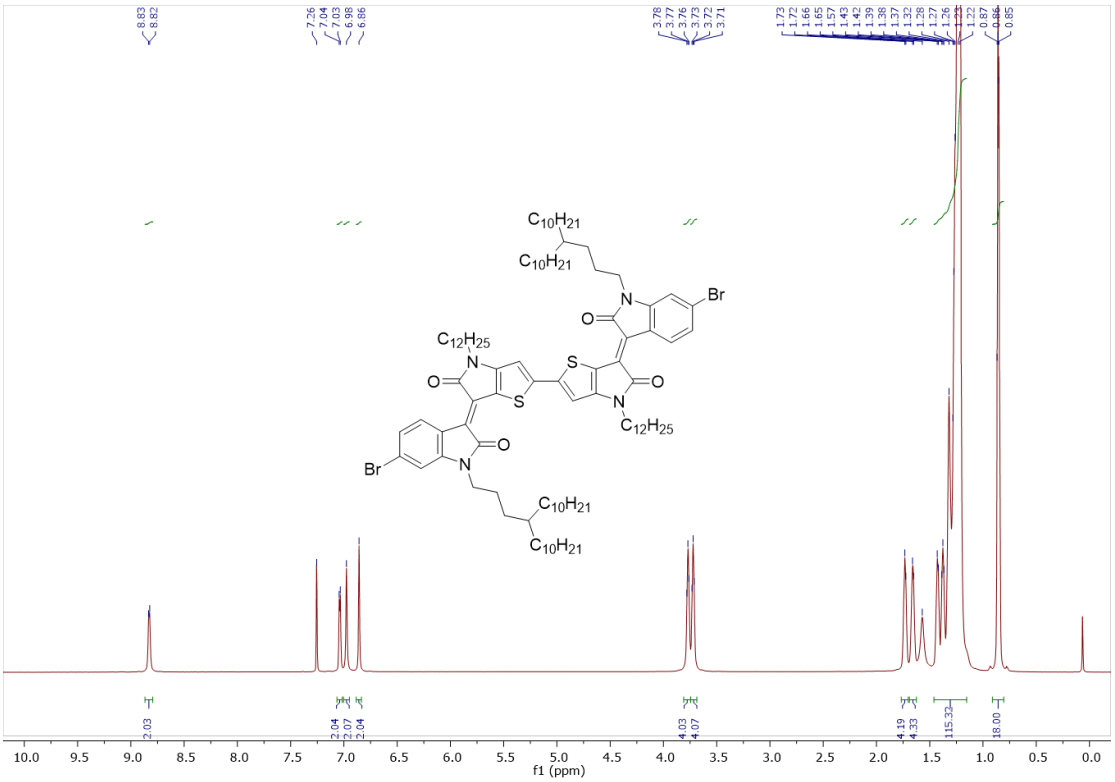
8.83
8.82
7.26
7.04
7.03
6.98
6.86
3.78
3.77
3.76
3.73
3.72
3.71
1.73
1.72
1.66
1.65
1.57
1.43
1.42
1.39
1.38
1.37
1.32
1.28
1.27
1.26
1.22
0.87
0.86
0.85
2.03
2.04
2.07
2.04
4.03
4.07
4.19
4.33
15.33
18.00
f1 (ppm)

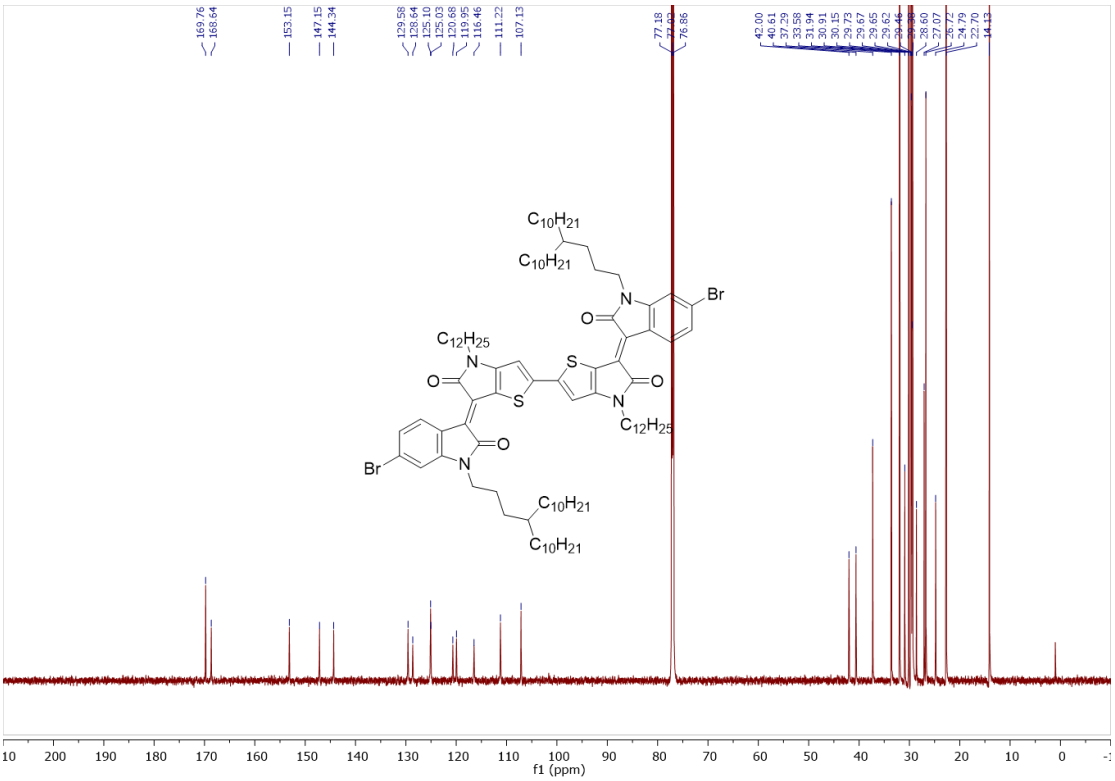
169.76
168.64
153.15
147.15
144.34
129.58
128.64
125.50
125.03
120.68
119.95
116.46
111.22
107.13
77.18
77.03
76.86
42.00
40.61
37.29
33.58
31.94
30.91
30.15
29.73
29.67
29.65
29.62
29.46
29.38
28.60
27.07
26.72
24.79
22.70
14.13
f1 (ppm)

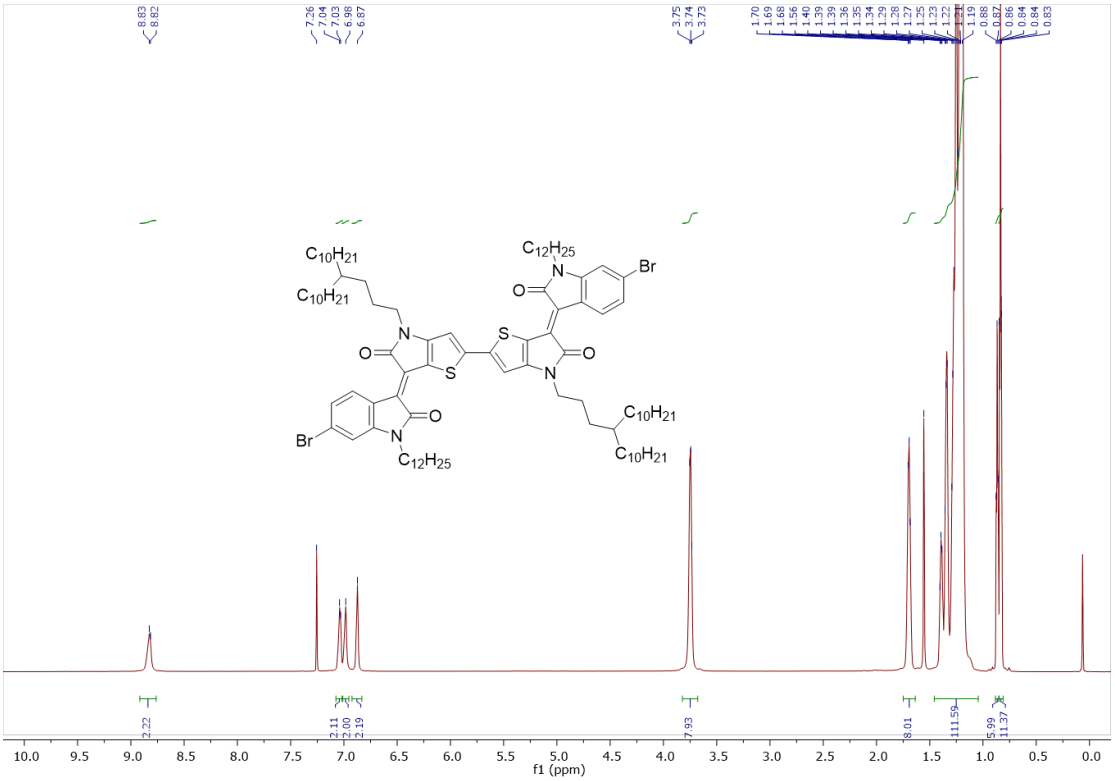
8.83
8.82
7.26
7.04
7.03
6.98
6.87
3.75
3.74
3.73
1.70
1.69
1.68
1.56
1.40
1.39
1.38
1.36
1.35
1.34
1.29
1.28
1.27
1.25
1.23
1.22
1.19
0.88
0.87
0.86
0.84
0.84
0.83
C10H21
C10H21
C12H25
Br
N
O
S
C12H25
2.22
2.11
2.00
2.19
7.93
8.01
111.59
5.99
11.37
10.0 9.5 9.0 8.5 8.0 7.5 7.0 6.5 6.0 5.5 5.0 4.5 4.0 3.5 3.0 2.5 2.0 1.5 1.0 0.5 0.0
f1 (ppm)

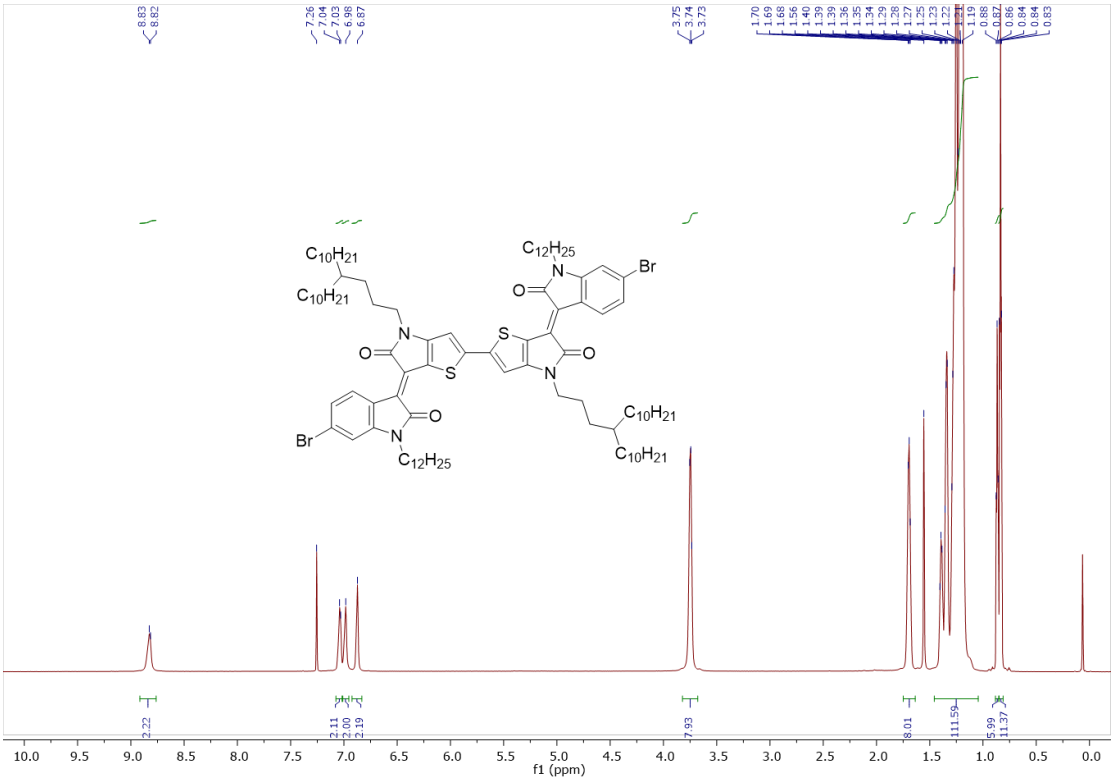
8.83
8.82
7.26
7.04
7.03
6.98
6.87
3.75
3.74
3.73
1.70
1.69
1.68
1.56
1.40
1.39
1.38
1.36
1.35
1.34
1.29
1.28
1.27
1.25
1.23
1.22
1.19
0.88
0.87
0.86
0.84
0.84
0.83
C10H21
C10H21
C12H25
Br
N
O
S
C12H25
2.22
2.11
2.00
2.19
7.93
8.01
111.59
5.99
11.37
10.0 9.5 9.0 8.5 8.0 7.5 7.0 6.5 6.0 5.5 5.0 4.5 4.0 3.5 3.0 2.5 2.0 1.5 1.0 0.5 0.0
f1 (ppm)

CHAPTER 4. DESIGNING DONOR-ACCEPTOR COPOLYMERS FOR STABLE AND HIGH-PERFORMANCE ORGANIC ELECTROCHEMICAL TRANSISTORS

4.1 Introduction

An organic electrochemical transistor (OECT) is a coupled ionic-electronic device where the active layer material undergoes doping and de-doping based upon the electrolytic components upon application of a gate bias.[77,78] Owing to the high-sensitivity sensing and sub-voltage operation properties of OECTs, various application advances have been achieved with respect to OECTs including biological sensors, memory and neuromorphic devices, and electrophysiological monitoring.[79–83] Despite the high degree of initial success that many oft-studied macromolecular systems have had in the realm of OECTs, there are significant opportunities to develop next-generation electrochemically-active polymers to improve device performance, switching speed, and cycling stability.[77,84–86]

Semiconducting polymers with solubilizing hydrophilic side chains exhibit high volumetric capacitance, efficient charge transport, and rapid ion injection, as well as compatibility with aqueous electrolytes.[87] Therefore, they have generated extensive scientific interest as a class of channel components for OECTs.[88–93] Among the various types of semiconducting polymers, 3,4-alkylenedioxythiophene-based polymers have achieved remarkable success in many electrochemical applications, such as electrochromic devices and supercapacitors.[94,95] Moreover, they are useful for OECT channel materials due to their high redox stability and charge capacity.[85,96–98] In fact, a model material for many studies, poly(3,4-ethylene dioxythiophene) doped with poly(styrene sulfonate) (PEDOT:PSS) has recently reached high figure-of-merit (i.e., the product of charge mobility and volumetric capacitance, μC^*) values of 1,500 F cm^{-1} V^{-1} s^{-1} in OECT devices.[99,100] 3,4-propylenedioxythiophene (ProDOT), an analogue of EDOT, is another example of this type of building block. ProDOT has two side chain substitution positions bringing about tunable solubility and versatility of synthetic design.[101] Because ProDOT is a weaker electron donor than EDOT, all-donor ProDOT-based polymers are more stable in their neutral state under ambient conditions.[102] However, ProDOT has not been implemented as extensively as EDOT in OECT studies with only a single report being provided to date.[103] Despite the fact that

OECT devices based on this design exhibited excellent electrochemical response and high charge-storage capacity, this ProDOT-based all-donor type polymer only achieved a μC* value of 7.0 F cm^{-1} V^{-1} s^{-1}, which is relatively low when compared with traditional thiophene-based polymer competitors. The performance of this material seems to be limited, in large part, by the completely amorphous nature of the polymer thin film, which resulted in a low charge carrier mobility.[88,89] While most reported OECT polymers, including the polythiophene-based polymer p(g2T2-g4T2) with the currently highest-reported μC* materials performance value, are all-donor type conjugated polymers,[90] donor-acceptor (D-A) conjugated polymers containing electron acceptors such as isoindigo (IID), naphthalenediimide (NDI), and diketopyrrolopyrrole (DPP) have been developed as other promising types of OECT materials. Particularly, p-type D-A conjugated polymers were recently shown to minimize electrochemical side reactions during OECT operation.[91,104,105] For instance, a recently-reported pyridine-flanked diketopyrrolopyrrole-containing (DPP-containing) polymer suggests that a D-A type polymer system prevents the OECT device from reacting with molecular oxygen.[105] A variety of thiophene-flanked diketopyrrolopyrrole (DPP-2T) derivatives were subsequently reported for OECT applications.[84,106,107] Moreover, the μC* values of these DPP polymers have exceeded 100 F cm^{-1} V^{-1} s^{-1} with particularly high charge mobilities being reported, highlighting the potential of DPP moieties to significantly improve the charge transport properties in OECT polymers.

4.2 Molecular Design

Here, a DPP-containing ProDOT monomer was designed, and this allowed for the eventual creation of a D-A conjugated polymer PProDOT-DPP. Then, using a straightforward polymerization method, the DPP motif, which affords strong interchain interactions, was incorporated into the PProDOT polymer backbone. Two ProDOT moieties were present in one repeat unit to maintain electrochemical performance and cycling stability while a single DPP-2T moiety was used as a planar core to enhance chain rigidity. In turn, this increased the ultimate thin film crystalline fraction and improved the charge transport properties relative to polymers that lacked the DPP functionality. The six triethylene glycol (TEG) side chains that are present in each repeat unit ensure solution processability and allow for enhanced ion infiltration during OECT device operation. Because of these principles the synthesized polymer, PProDOT-DPP, achieved a high μC* value of 310 F cm^{-1} V^{-1} s^{-1} during OECT device operation, which places it as one of

the top performing accumulation mode OECT macromolecules reported to date.[84,90,106] Moreover, the performance of PProDOT-DPP was maintained for 100 cycles over 2,000 s of cycling between the ON and OFF states. Thus, the proposed polymer design strategy may inspire next-generation polymers with both high performance and enhanced operational stability for mixed conduction applications.

4.3 Synthesis and Characterization

To take advantage of the exposed α positions and blocked β positions during the synthesis, we determined that the ProDOT moiety is particularly suitable as a C-H activation reaction substrate. In this way, we applied a direct arylation polymerization strategy (Figure 4.1).

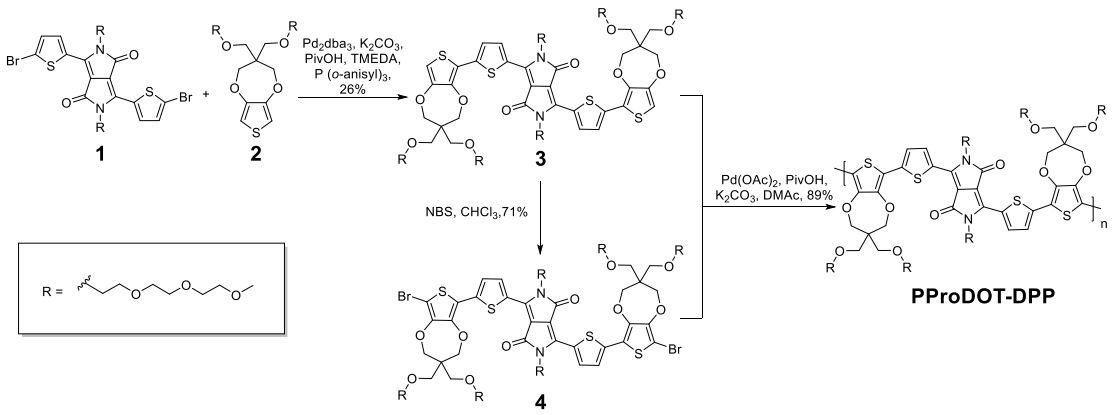

Figure 4.1 Synthetic Route for the Generation of PProDOT-DPP

First, Compound 1 was synthesized with triethylene glycol side chains functionalized on the DPP-2T core, and this species was then brominated. In a similar manner, substitution of triethylene glycol side chains on bis(bromomethyl) 3,4-propylenedioxythiophene afforded Compound 2. Compound 1 was then subjected to an optimized direct arylation reaction using tris(dibenzylideneacetone)dipalladium(0) and tetramethylethylenediamine (TMEDA) as co-catalysts with an excess of Compound 2, yielding Monomer 3 with a moderate yield of 26%.[108] Further bromination of Monomer 3 provided Monomer 4 in a yield of 71%. Finally, PProDOT-DPP was synthesized via direct arylation polymerization between Monomer 3 and Monomer 4 with a high yield of 89% (see Supporting Information for synthetic details). The molecular weights

of the polymers were initially evaluated by high temperature size exclusion chromatography (SEC) using trichlorobenzene as the eluent at 150 °C (Figure 4.2).

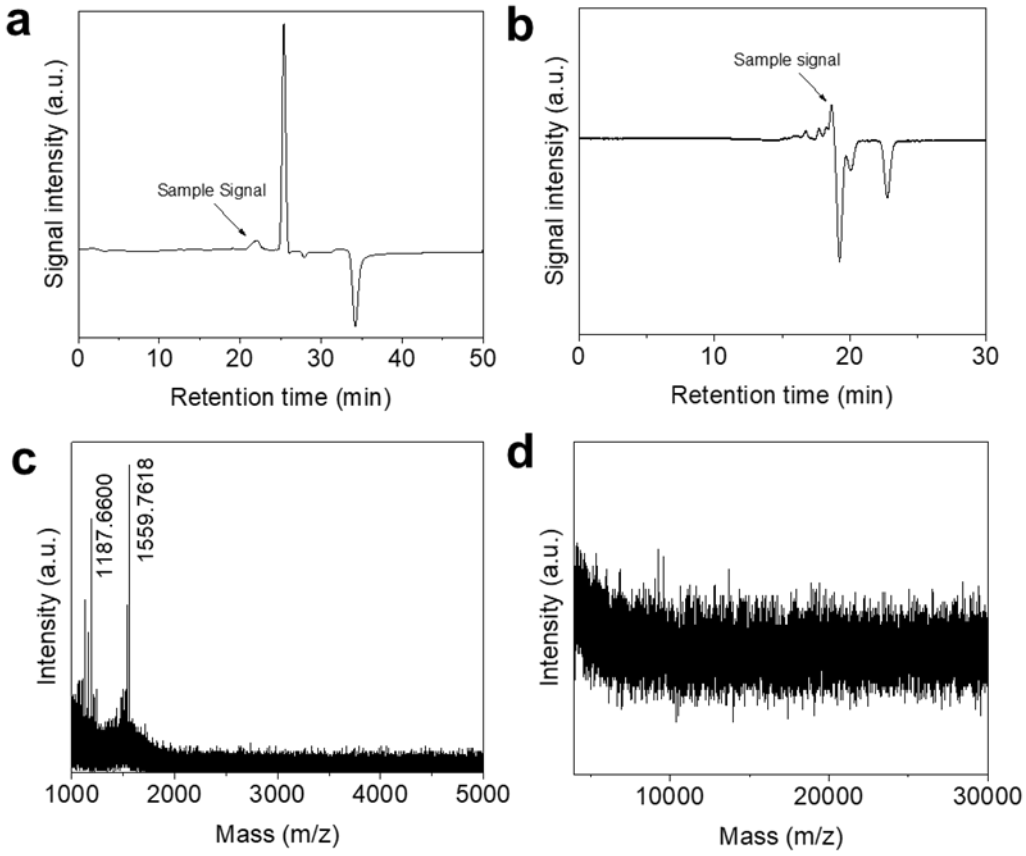

Figure 4.2 Attempts to estimate the molecular weight of PProDOT-DPP. (a) Size exclusion chromatogram of the PProDOT-DPP polymer collected at 150 °C using 1,2,4-trichlorobenzene (TCB) as the mobile phase. (b) Size exclusion chromatogram of the PProDOT-DPP polymer at 40 °C using tetrahydrofuran (THF) as the mobile phase. Note that PProDOT-DPP polymer solubility in THF at 40 °C is limited. (c) and (d) MALDI-TOF mass spectra of PProDOT-DPP from a m/z range of 1000 to 30000. No peak was detected greater than the molecular weight of the monomer.

However, the chromatogram only shows a weak signal associated with a low molecular weight species, which prevented us from providing a reasonable estimation of the true molecular weight of the polymer. Further attempts using size exclusion chromatography with tetrahydrofuran at 40 °C as the mobile phase and MALDI-TOF mass spectroscopy analyses were also unsuccessful (Figure 4.2c). This is an unfortunate, but not unreported, issue as abnormal SEC results of DPP-

based polymers with triethylene glycol side chains have been described previously.[84] Despite this inability to extract a quantitative molecular weight estimate, the 1H-NMR (Figure 4.3) and UV-Vis-NIR (Figure 4.4) spectra of the resulting material clearly show that the product is macromolecular in nature.

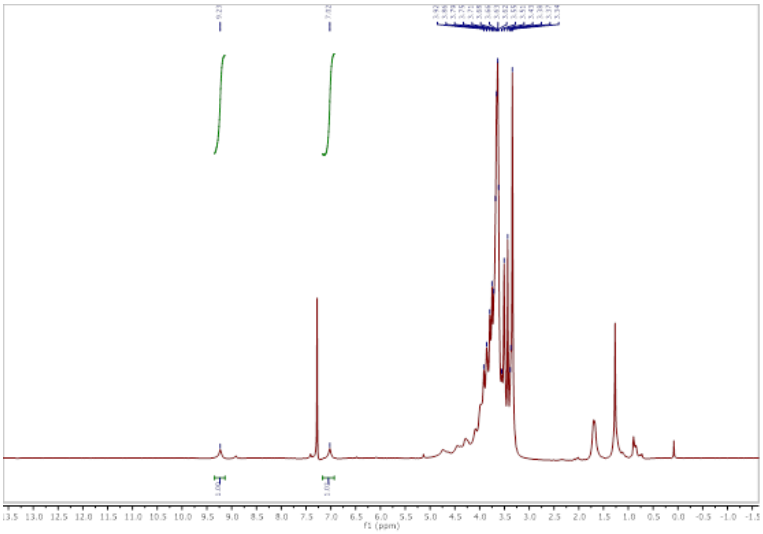

Figure 4.3 ^{1}H NMR of PProDOT-DPP in $CDCl_3$ at 323 K. The two protons remaining on the DPP moiety are integrated.

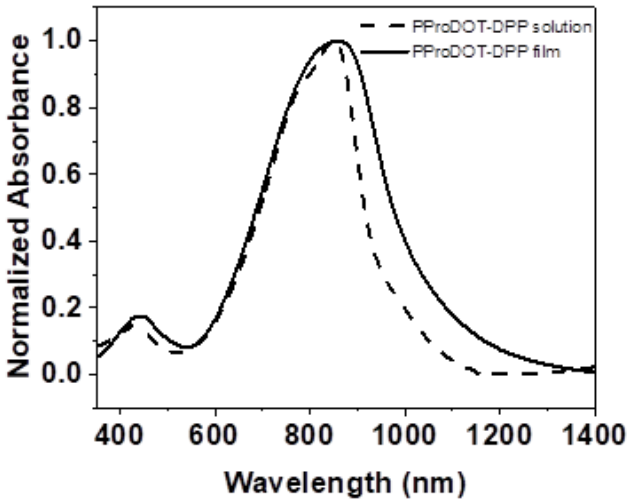

Figure 4.4 Normalized UV-Vis-NIR absorption spectra of PProDOT-DPP in chloroform solution and as a thin film. The PProDOT-DPP exhibited dual-band absorption features both in solution and as a thin film.

4.4 Electrochemical and Optical Properties

4.4.1 Cyclic Voltammetry

Cyclic voltammetry was employed to interrogate the electrochemical redox reactions and stability of PProDOT-DPP polymers as a function of the electrolyte chemistry (Figure 4.5). Due to the large difference in anion sizes of PF_6^- and Cl^-, $LiPF_6$ and LiCl aqueous solutions were selected as the electrolytes to establish the impact that anion size had on the electrochemical properties of the PProDOT-DPP when it was used in electrochemical environments.[92]

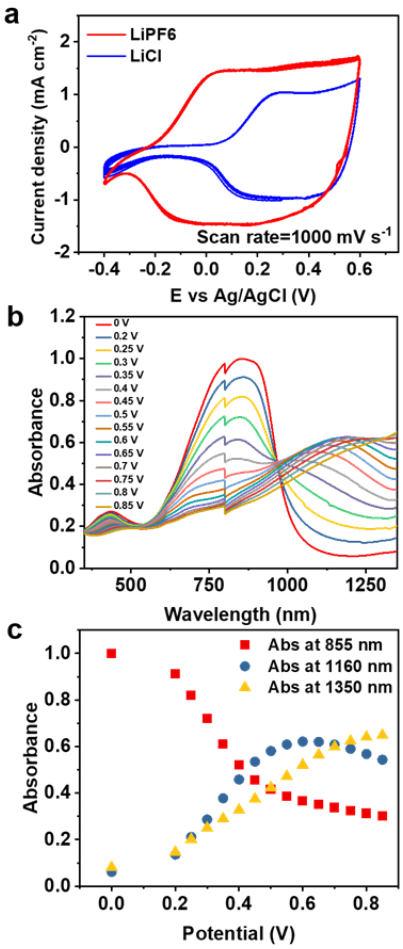

Figure 4.5 Electrochemical characterization of PProDOT-DPP thin films. (a) The cyclic voltammetry cycling test with a 0.2 M $LiPF_6$ (red) or 0.2 M LiCl (blue) aqueous solution as the supporting electrolyte. (b) UV-Vis-NIR spectra of PProDOT-DPP film from a spectroelectrochemical measurement with the 0.2 M $LiPF_6$ aqueous electrolyte. The tick around 800 nm is instrument response associated with the detector and grating change. (c) Absorbance of PProDOT-DPP recorded as a function of applied potential in the spectro-electrochemical measurement.

PProDOT-DPP exhibits excellent redox stability during 20 charge-discharge cycles between − 0.4 V ⩽ V ⩽ +0.6 V versus Ag/AgCl in both electrolytes. Importantly, PProDOT-DPP exhibits a lower oxidation onset potential (i.e., − 0.2 V) and a higher oxidation capacitance in the $LiPF_6$ electrolyte relative to the LiCl electrolyte. The more efficient ion exchange and improved electrochemical activity is attributed to the influence of the anion polarizability and anion solvation. As evidenced by many other reports, larger and more polarizable anions with a lower surface charge density require a smaller driving force for injection into the semiconducting polymer.[92,106,109] Notably, the electrochemical conditioning process for PProDOT-DPP in both supporting electrolytes was completed in the just the first cycle. Such efficient electrochemical conditioning processes are likely ascribed to the highly hydrophilic triethylene glycol side chain density present in one repeating unit, which allows for easier ion injection.

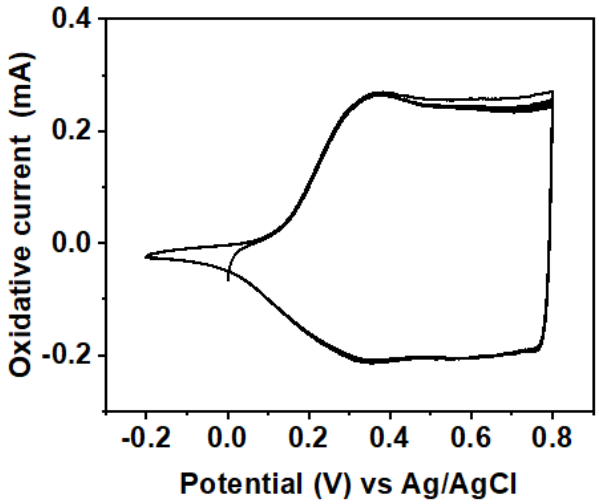

Figure 4.6 The cyclic voltammograms for the first 10 cycles of a PProDOT-DPP thin film in 0.2 M $TBAPF_6$ acetonitrile solution electrolyte at a scan rate of 200 mV s^{-1}. The ionization potential (IP) was estimated from the equation: IP (eV)= 4.8 + ($E_{onset} - E_{Fc/Fc+}$), where E_{onset} refers to polymer oxidation onset potential vs Ag/AgCl, and $E_{Fc/Fc+}$ refers to ferrocene oxidation potential (0.37 V, determined experimentally) vs Ag/AgCl.

Similar high cycling stability, high capacitance, and fast electrochemical conditioning of PProDOT-DPP are observed in an organic electrolyte, acetonitrile (Figure 4.6). An ionization potential of –4.57 eV (relative to vacuum) was also estimated from the oxidation onset of PProDOT-DPP in acetonitrile electrolyte.[110] These cyclic voltammetry results confirm PProDOT-

DPP as a potential p-type OECT channel material with a low operating voltage and indicate the versatility of the polymer for different electrochemical conditions.

4.4.2 The Spectroelectrochemical Measurements

The spectroelectrochemical measurements of PProDOT-DPP films in $LiPF_6$ aqueous electrolyte provide potential-dependent absorption changes, giving insights into polaron and/or bipolaron formation, which helps to describe charge and ionic transport at different doping states during the electrochemical process. As shown in Figure 4.5b and Figure 4.5c, the neutral peak absorption maximum of PProDOT-DPP is at ~855 nm, while the emerging peak at 1,160 nm during the oxidation process is the polaron absorption maximum.

Until an oxidation potential of +0.5 V versus Ag/AgCl is reached, an isosbestic point at 967 nm indicates pure polaron formation.[111] Further increases in potential lead to bipolaron formation as the intersections of adjacent curves deviate from the previous isosbestic point.[112] The presence of bipolaron formation also is evidenced by a decline in absorption at 1,150 nm and increase in absorption at 1,350 nm when the oxidation potential exceeds +0.5 V versus Ag/AgCl. However, due to strong the O-H stretching overtone of water that starts at 1,400 nm, the bipolaron absorption maximum cannot be detected.[113] These results suggest that the PProDOT-DPP film has a strong, reversible redox response and low threshold oxidation potential, which are characteristics of a good p-type OECT material that is compatible with water and aqueous electrolytes.

4.5 Microstructure Characterizations

To investigate the impact of the DPP moieties on the crystallinity and molecular packing in PProDOT-DPP thin films, grazing incidence wide-angle x-ray scattering measurements were performed on PProDOT-DPP polymer thin films spin-coated from 10 mg mL-1 chloroform solutions, as shown in Figure 4.7.

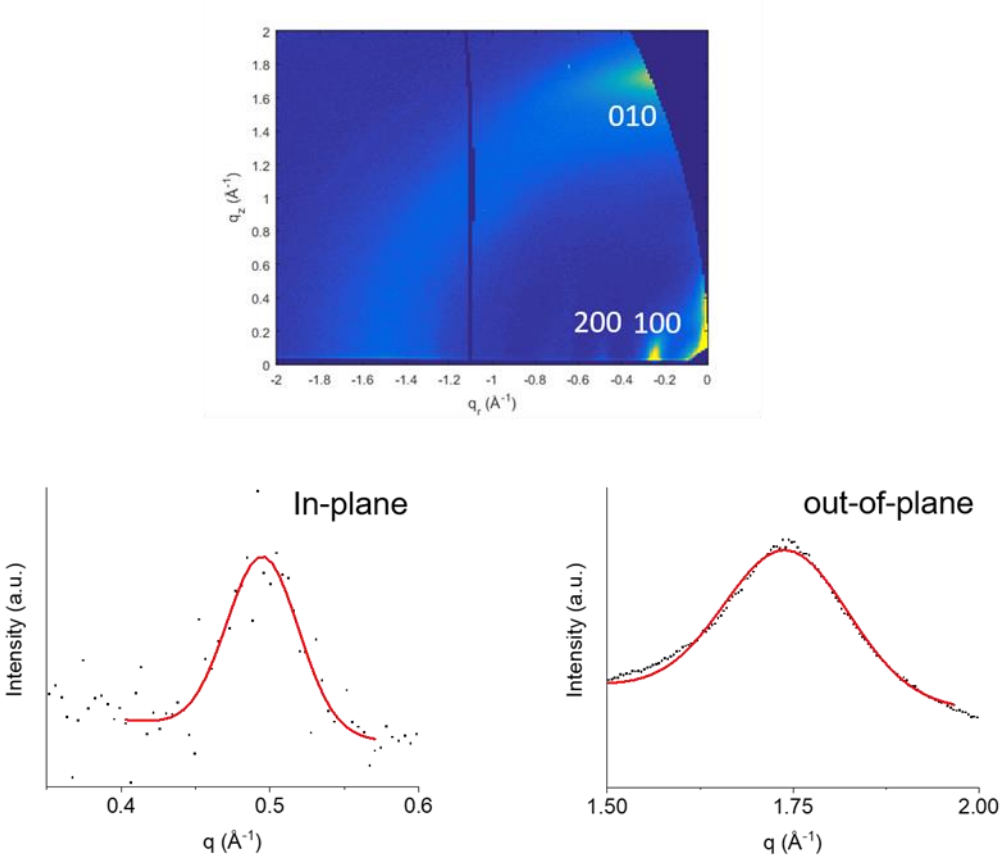

Figure 4.7 The 2D GIWAXS image, in-plane line cut at (200), and out-of-plane line cut at (010) of PProDOT-DPP. The PProDOT-DPP thin film was prepared by spin-coating the PProDOT-DPP solution (10 mg mL^{-1} in $CHCl_3$) onto SiO_2 substrates at a rotational rate of 1,500 rpm.

The polymer film shows an out-of-plane (010) peak, indicative of a face-on π–π stacking orientation. Two orders of in-plane packing patterns, (100) and (200), are attributed to lamellar scattering, and they are also observed. The π-π stacking distance is 3.61 Å and the lamellar spacing is 25.4 Å. The full-width-at-half-maximum (fwhm) of the out-of-plane [i.e., the (010)] peak is 0.195, which corresponds to a coherence length (L_c) of 32 Å. Relative to other DPP polymers, this polymer shows similar π-π stacking distances and slightly smaller crystalline domains.[114,115] Notably, the lamellar distance of PProDOT-DPP is significantly longer than those of other DPP polymers with triethylene glycol side chains (typically 10-20 Å), but it is almost identical to the lamellar distance of a doped poly(ProDOT) with ethylene glycol side chains (25.8 Å).[84,116] This comparison reveals that interchain triethylene glycol-triethylene glycol interactions on the ProDOT moieties are predominant, while triethylene glycol chains on the DPP moieties have less interactions than those in typical DPP polymers. Also, it should be noted that the poly(ProDOT)

polymer itself is amorphous in the neutral state.[108] Therefore, these observations reflect the influence of DPP moieties on the increase in the crystalline nature of a ProDOT-based polymer, in agreement with good charge transport properties estimated from OECT devices (vide infra).

4.6 Electronic Properties

4.6.1 OECT Performance

The electrical measurements of PProDOT-DPP-based OECTs were performed in two types of aqueous electrolytes: in (a) 0.1 M of LiCl and in (b) 0.1 M $LiPF_6$. An Ag/AgCl gate electrode was submerged in the electrolyte during the measurements (Figure 4.8).

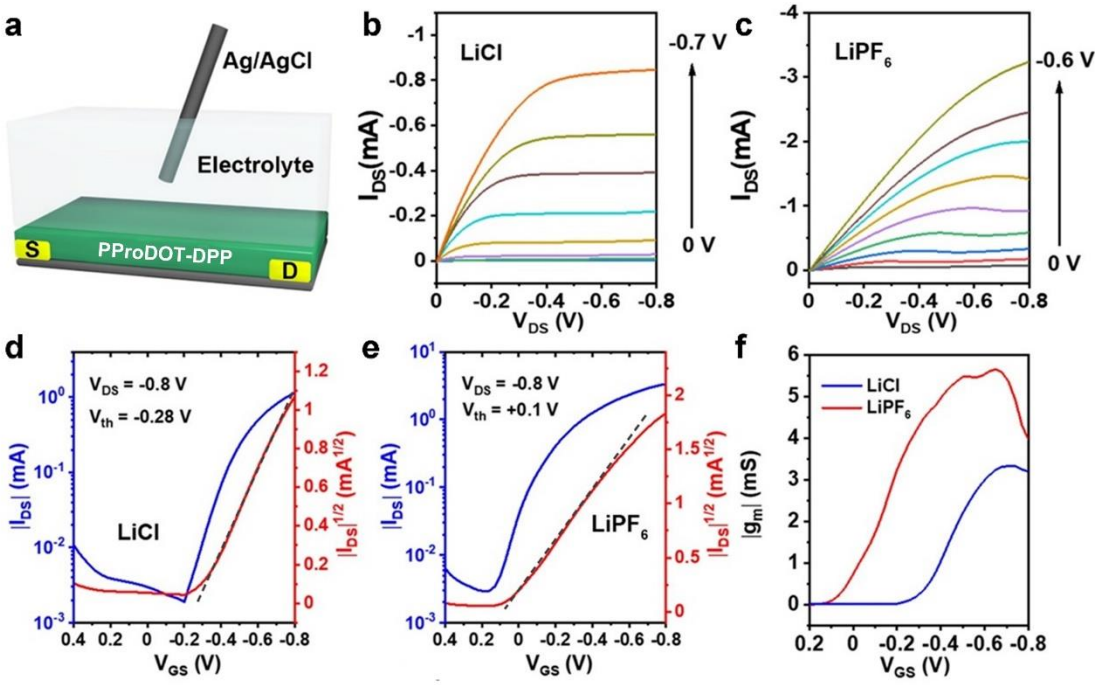

Figure 4.8 Device of the bottom-contact PProDOT-DPP-based OECTs. (a) Output characteristics of the PProDOT-DPP OECTs using (b) 0.1 M LiCl and (c) 0.1 M $LiPF_6$ as the salts for the aqueous electrolytes. Transfer characteristics of the PProDOT-DPP OECTs using (d) 0.1 M LiCl and (e) 0.1 M $LiPF_6$ salts for the aqueous electrolytes. (f) Transconductance values of PProDOT-DPP OECTs using LiCl and $LiPF_6$ electrolytes.

It is worth noting that typical output characteristics with clear linear and saturation regimes are observed in both LiCl and LiPF6 electrolytes (Figures 4.8b and 4.8c). The OECT transfer curves

are shown in Figures 4.8d and 4.8e, where a –0.8 V constant V_{DS} was applied. The OECTs predominantly operate in a hole-transporting accumulation mode where an ON/OFF ratio of ~103 is obtained for both LiCl and $LiPF_6$ electrolytes. The OECTs work mostly in the saturation regime; as a result, the slopes of the linear fit of the V_{GS}-$I_{DS}^{1/2}$ reveal threshold voltages (V_{TH}) of –0.28 V and +0.1 V for the LiCl and $LiPF_6$ electrolytes, respectively. The more positive threshold voltage associated with the $LiPF_6$ electrolyte can be attributed to the lower oxidation potential required to electrochemically dope the PProDOT-DPP films, which is consistent with the CV results shown above. Moreover, the higher ON current is obtained for OECT devices with a $LiPF_6$ electrolyte, which suggests that the PF_6^- anion provides for better electrochemical doping in these high performance OECTs that have low operating voltages. We highlight that the PProDOT-DPP OECTs demonstrated good device-to-device uniformity from the characterization of eight individual OECTs (Figure 4.9).

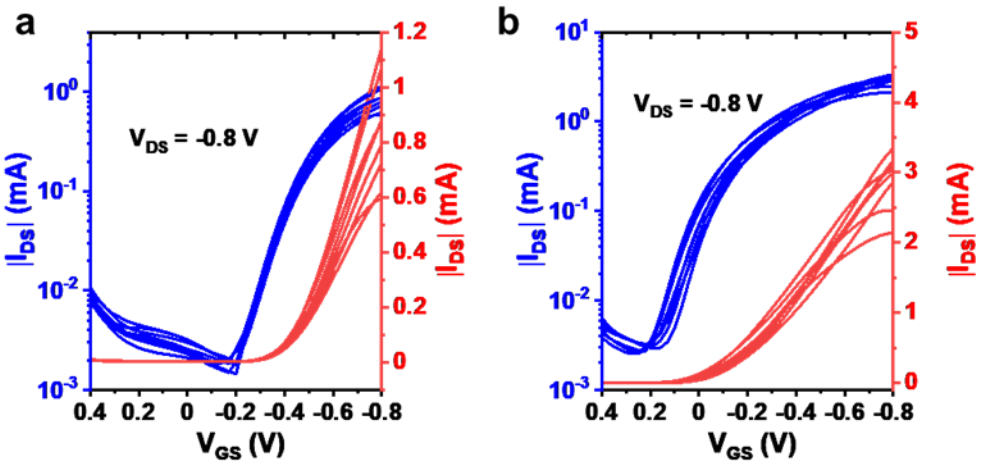

Figure 4.9 Device-to-device uniformity of PProDOT-DPP OECTs. Transfer curves of 8 individual OECTs using the (a) LiCl and (b) $LiPF_6$ electrolytes.

The transconductance (g_m) is considered as an important figure-of-merit of OECTs, and it is defined as $g_m=\Delta I_{DS}/\Delta V_{GS}$.[117] As is shown in Figure 4.8f, a maximum transconductance (g_m) of ~5.6 mS was achieved when the PProDOT-DPP thin films (with thickness of ~30 nm) were evaluated in $LiPF_6$ aqueous electrolyte, while a slightly lower peak transconductance value of ~3.3 mS is obtained in the LiCl electrolyte. These results indicate that PF_6^- with relative larger radius

and higher polarizability are advantageous to improve the doping efficiency in these DPP polymers, thus enabling a superior gm in aqueous electrolytes.[106]

4.6.2 Ion Impact on OECT Devices

The realization of robust operational stability is a fundamental requirement for OECT devices, and this remains a challenge for most conjugated polymer when they are used as the device active layer. To this end, bias stability measurements of PProDOT-DPP OECTs were first performed here under a constant V_{DS} of –0.1 V with various V_{GS} biases (Figure 4.10a and Figure 4.11).

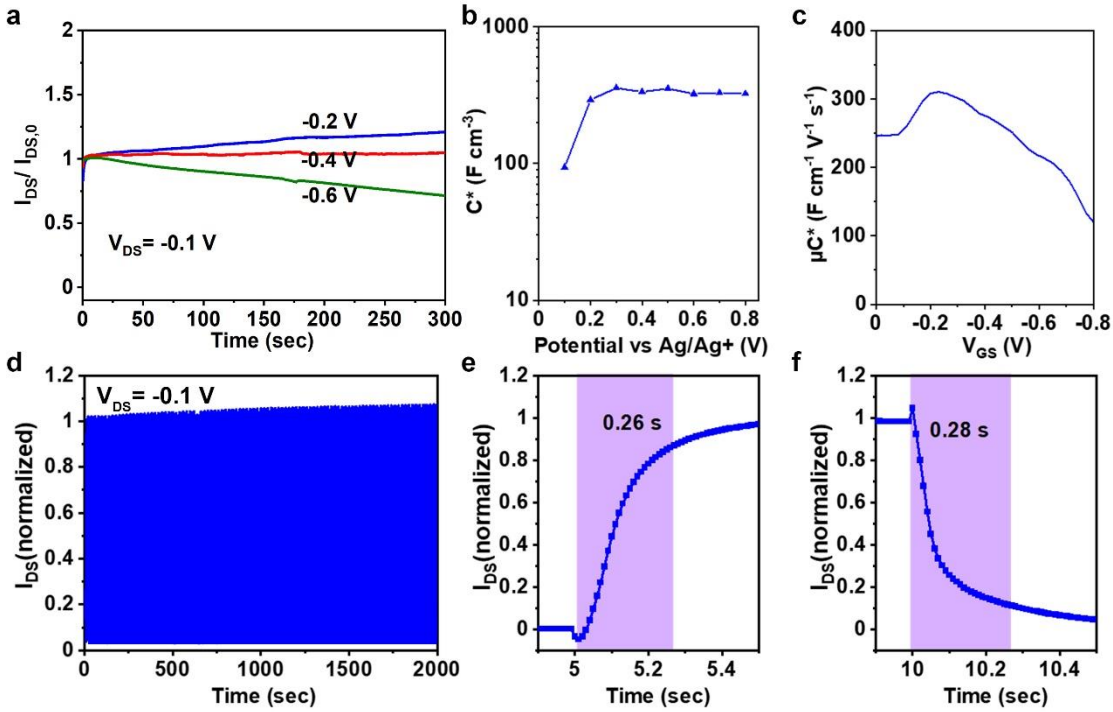

Figure 4.10 (a) Bias stabilities of PProDOT-DPP OECTs at different V_{GS} values using the 0.1 M $LiPF_6$ electrolyte. (b) Volumetric capacitance as a function of bias applied to the PProDOT-DPP working electrode via differential capacitance measurements using the 0.1 M $LiPF_6$ electrolyte. (c) μC* values of PProDOT-DPP OECTs as a function of V_{GS} using the 0.1 M $LiPF_6$ electrolyte. (d) Cyclic stability of PProDOT-DPP OECTs using the 0.1 M $LiPF_6$ electrolyte. A constant V_{DS} at –0.1 V and a square wave function of V_{GS} ($V_{GS,\,on}$ = –0.4 V and $V_{GS,\,off}$ = 0 V) were applied. (e) Switching on and (f) switching off responses of PProDOT-DPP OECTs ($V_{GS,\,on}$ = –0.4 V and $V_{GS,\,off}$ = 0 V) using the 0.1 M $LiPF_6$ electrolyte.

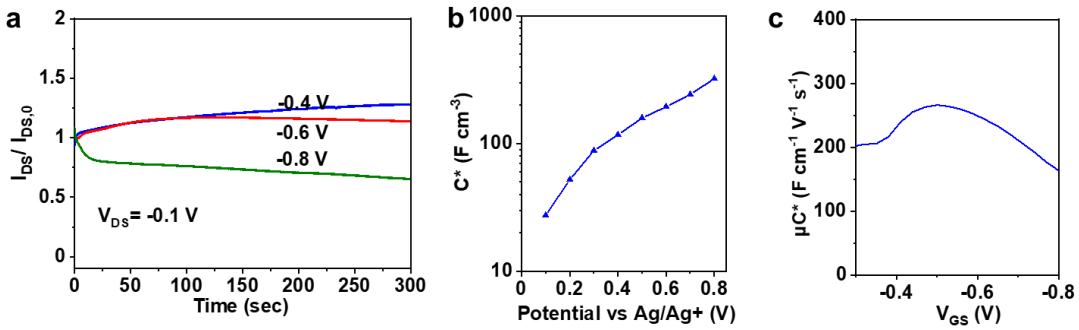

Figure 4.11(a) Bias stabilities of PProDOT-DPP OECTs at different V_{GS} values in 0.1 M LiCl. (b) Volumetric capacitance as a function of bias applied to the PProDOT-DPP working electrode via differential capacitance measurements in 0.1 M LiCl. (c) μC* values of PProDOT-DPP OECTs as a function of V_{GS} in 0.1 M LiCl.

For OECTs with the $LiPF_6$ electrolyte, the I_{DS} was maintained over 300 s when biasing the V_{GS} lower than –0.6 V; however, we do note the slight increase in I_{DS} for V_{GS} = –0.2 V. This might be attributed to the influence of the trapping of injected anions. For OECTs with the LiCl electrolyte, however, a stable I_{DS} was realized under higher gating potential when the V_{GS} was lower than –0.8 V. At high V_{GS} bias (i.e., –0.6 V for $LiPF_6$ and –0.8 V for LiCl), the I_{DS} decreased slightly with time. Importantly, this I_{DS} decrease at high V_{GS} biases is correlated with the same oxidation potential where bipolarons start to form, as evidenced by spectro-electrochemical measurements. Hence, the decreased operational stability at higher gating potentials is attributed to the instability of the bipolaron species when formed on PProDOT-DPP.

To better understand the stability maintenance and degradation mechanisms, we performed differential capacitance measurements of the PProDOT-DPP films (Figure 4.12).

The PProDOT-DPP film deposited on ITO served as the working electrode, and potential steps from +0.1 to +0.8 V vs. Ag/AgCl were applied. The measured capacitive current (I_c) upon the application of different voltage biases is therefore given by Equation 1.[118]

$$I(t)=E/R_s e^{-t/(R_s C)} \qquad \text{(Equation 1)}$$

Here, E is the potential step, Rs is the out-of-plane resistance of the PProDOT-DPP films, and C is the film capacitance. The potential-dependent volumetric capacitance (C*) is the following.

$$C^*=C/Ad \qquad \text{(Equation 2)}$$

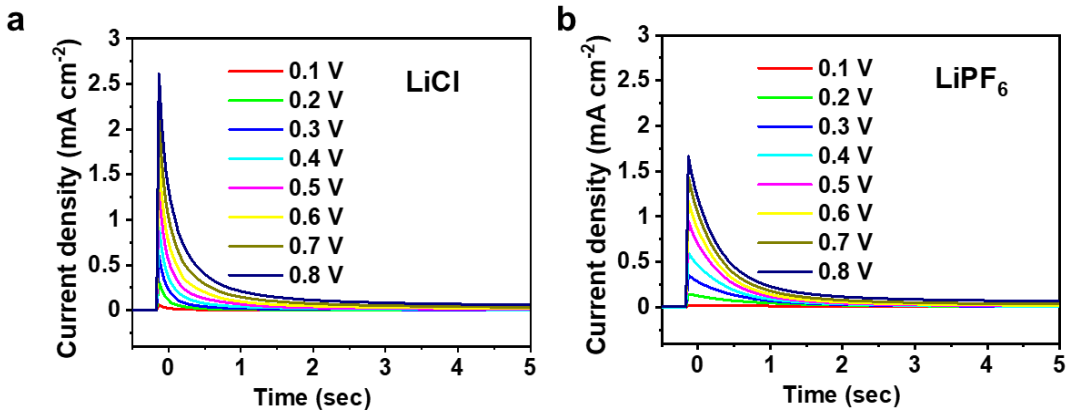

Figure 4.12 Differential capacitance measurements performed on a PProDOT-DPP on a patterned ITO electrode (0.5 cm^2) in 0.1 M (a) LiCl and (b) $LiPF_6$ aqueous solutions.

In this equation, A and d are the area and thickness of the PProDOT-DPP films, respectively. From the calculated volumetric capacitance results for the LiPF6 system (Figure 4.11b), the PProDOT-DPP exhibited a sharp increase of C* from +0.1 to +0.2 V vs Ag/AgCl, and the films then maintained a value of ~330 F cm^{-3} when the applied potential ranged from +0.2 V to +0.8 V vs Ag/AgCl. We also calculated the μC* values of PProDOT-DPP OECTs, which reflects the ionic and electronic merits of the polymer independent of the device geometry using the following the equation. We then calculated the μC* values of PProDOT-DPP OECTs, which reflects the intrinsic ionic and electronic merits of the polymer using the following equation.

$$\mu C^* = (g_m L)/(Wd(V_{TH}-V_{GS})) \quad \text{(Equation 3)}$$

Here, W, L, and d are the channel width (2500 μm), length (200 μm), and active layer thickness (~30 nm), respectively. Note that a relatively long channel (~200 μm) was applied for the OECT geometry to minimize any contact resistance effects and to provide an accurate evaluation of the intrinsic merits of PProDOT-DPP.[119] (Figure 4.13)

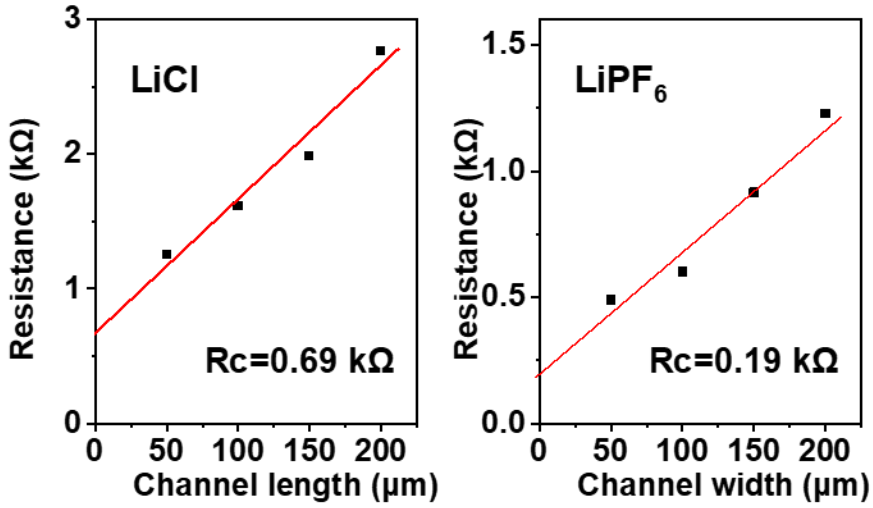

Figure 4.13 Total resistance of the PProDOT-DPP OECT channel as a function of channel length, the applied V_{GS} was -0.6 V for LiCl and -0.4 V for $LiPF_6$, respectively, both under a constant V_{DS} of -0.1 V.

As shown in Figure 4.11c, the μC* increased slightly as the applied voltage was altered from –0.1 V to –0.25 V; this is consistent with the trend of C* within the same potential window. Therefore, the initial increase of μC* can be attributed to the C* increase together with an almost constant carrier mobility. A peak μC* of 310 F cm^{-1} V^{-1} s^{-1} is obtained at –0.25 V, which is approaching the highest performance reported for accumulation-mode OECT materials. A good charge mobility ~0.94 cm^2 V^{-1} s^{-1} was also derived based on the μC* and C* values, allowing for robust hole transport at moderate V_{GS} bias. However, the μC* declined significantly when V_G more negative than –0.4 V was applied, and this is consistent with the trends in bias stability degradation. Given that C* was constant from +0.2 V to +0.8 V, the μC* decrease at high doping levels should be attributed to a decline in hole mobility accompanied with the bipolaron formation. When the unstable bipolaron species formed in PProDOT-DPP upon excessive incorporation of dopants, a loss in film crystallinity together with increased Coulomb scattering occurs, resulting in a lower charge mobility and non-ideality of transfer curve at VGS at magnitudes greater than –0.5 V.[120,121]

4.6.3 Stability Measurements in $LiPF_6$ Electrolyte

Based on the above discussions, cyclic stability measurements were performed for the PProDOT-DPP thin films using the $LiPF_6$ electrolyte where the turn-on V_{GS} was always kept more positive than –0.6 V to prevent performance degradation (Figure 4.10d). As expected, the initial current is retained for 100 cycles over 2,000 s of cycling and ON-OFF switching. Moderate switching timescales are obtained for PProDOT-DPP with the $LiPF_6$ electrolyte with a rise time of 0.26 s and a fall time of 0.28 s (i.e., these are calculated as the time it takes to reach 90% of the steady-state current switching value in either direction), respectively (Figure 4.10e-f). These data indicate good reversible and repeatable electrochemical switching capacities in the PProDOT-DPP based OECTs. Therefore, the combination of high operational stability and moderate switching speed will allow the rational design of PProDOT-DPP OECTs for both electrical signal conversion and amplification applications. Volumetric capacitance and switching timescales for PProDOT-DPP with the LiCl electrolyte were also measured. (Figure 4.11b-c and Figure 4.14)

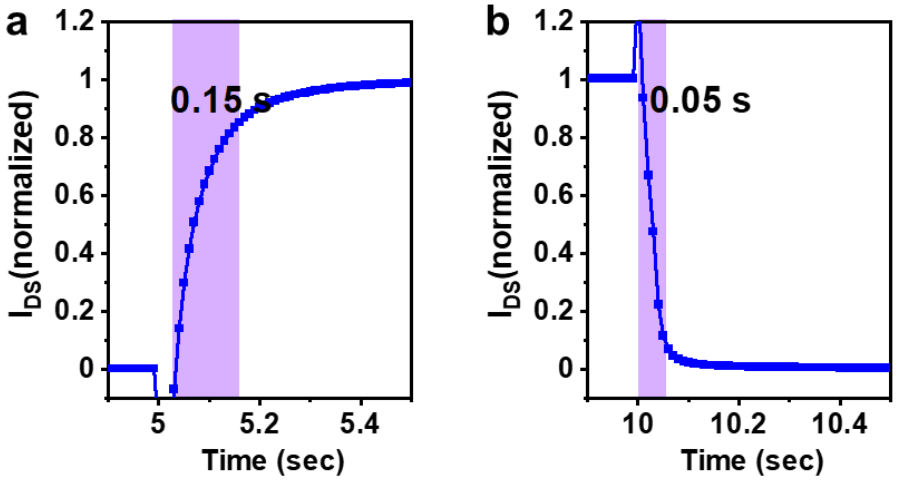

Figure 4.14 (a) Switching ON and (b) switching OFF responses of PProDOT-DPP OECTs ($V_{GS,\ on}$ = –0.4 V and $V_{GS,\ off}$ = 0 V) in LiCl electrolytes.

The OECT performance metrics of the PProDOT-DPP-based OECTs in different electrolytes (including mobility, capacitance, μC*, threshold voltage, on-off ratio, switching speed and operating stability) are summarized in Table 4.1.

Table 4.1 Performance Metrics of the PProDOT-DPP OECTs in different electrolytes.

Electrolyte (0.1 M)	$LiPF_6$	LiCl
μC^*_{max} (F cm^{-1} V^{-1} s^{-1})	310	269
μ_{max} (cm^2 V^{-1} s^{-1})	0.94	0.88
C^* (F cm^{-3})	330	305
V_{th} (V)	+0.10	–0.28
ON-OFF ratio	10^2 - 10^3	10^2 - 10^3
Switching time (s)	0.26	0.15
Stability (90% I_{DS} decrease, s)	>2000	1000

4.7 Conclusions

In summary, PProDOT-DPP was synthesized from a DPP-containing ProDOT monomer. As expected, the DPP moiety provides the ProDOT polymer with higher crystallinity while the polymer also maintains good electrochemical activity and a low oxidation potential. As a result, PProDOT-DPP thin films exhibit high charge transport properties, high volumetric capacitance, and high redox stability. A peak μC^* value of 310 F cm^{-1} V^{-1} s^{-1} was obtained at for PProDOT-DPP-based OECTs, which is comparable with the best performing accumulation mode OECT polymers reported to date. PProDOT-DPP also demonstrated solid operational stability across 100 cycles over 2,000 s of cycling. The strategy of incorporating crystalline DPP cores into all-donor OECT polymers provides a useful foothold to design future generations of polymers for mixed conduction applications that should have both high performance and enhanced operational stability.

4.8 Experimental Section

All reagents were purchased from the suppliers noted, and they were used without further purification. ^1H and ^{13}C NMR spectra were recorded using Bruker ARX 400 or Bruker Avance-III-800 in deuterated chloroform at 298 K unless specified. Size exclusion chromatography (SEC) was performed on a high-temperature size exclusion chromatography system at 150 °C using 1,2,4-trichlorobenzene (TCB) as the mobile phase with molecular weight values being based on polystyrene standards. Ultraviolet-visible-near infrared (UV-Vis-NIR) spectra were measured with an Agilent Technologies Cary 6000i UV-Vis-NIR spectrophotometer (350 nm $\leq \lambda \leq$ 2000 nm). Cyclic voltammetry (CV) was performed using a BioLogic SP-150 electrochemistry setup. 2D-grazing-incidence wide-angle X-ray scattering (GI-WAXS) measurements were carried out at Argonne National Laboratory. The PProDOT-DPP thin film for 2D GIWAXS was prepared by

spin-coating the PProDOT-DPP solution (10 mg mL^{-1} in $CHCl_3$) onto SiO_2 substrates at a rotational rate of 1,500 rpm.

4.8.1 Synthetic Procedures

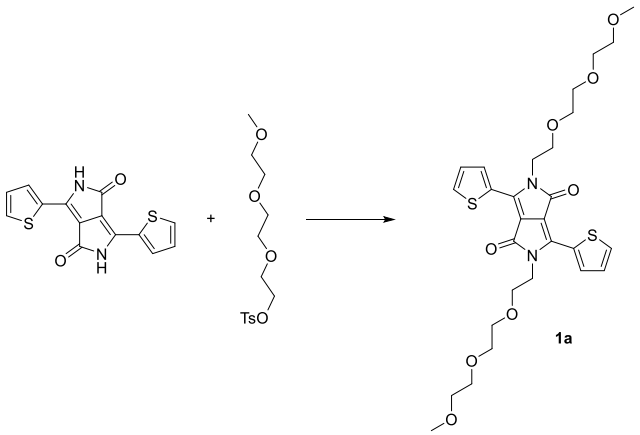

Compound 1a. 3,6-di(thiophen-2-yl)-2,5-dihydropyrrolo[3,4-c]pyrrole-1,4-dione (1.00 g, 3.33 mmol), 2-(2-(2-methoxyethoxy)ethoxy)ethyl 4-methylbenzenesulfonate (2.21 g, 7.32 mmol), and potassium carbonate (1.38 g, 9.99 mmol) were added to dimethylformamide (DMF, 50 mL). The mixture was heated under N_2 at 100 °C for 24 h. The reaction mixture was poured into water, extracted with dichloromethane (DCM), and dried over Na_2SO_4. After removal of solvent under reduced pressure, the residue was purified by silica chromatography (CH_2Cl_2:Ethyl Acetate = 10:1) to give the product 1a as a purple solid. (753mg, 38%) ^{1}H NMR (400 MHz, $CDCl_3$, ppm) δ: 8.74 (dd, *J* = 3.9, 1.2 Hz, 2H), 7.63 (dd, *J* = 5.0, 1.2 Hz, 2H), 7.24 (dd, *J* = 5.0, 3.9 Hz, 2H), 4.27 (t, *J* = 6.3 Hz, 4H), 3.79 (t, *J* = 6.3 Hz, 4H), 3.70 – 3.44 (m, 16H), 3.34 (s, 6H).

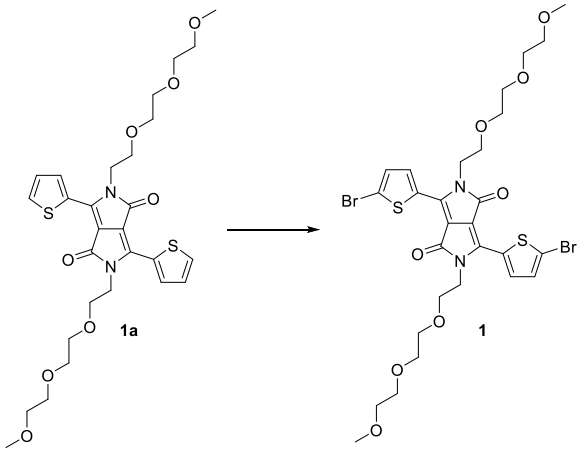

Compound 1. Compound 1a (700 mg, 1.18 mmol) and *N*-bromosuccinimide (431 mg, 2.42 mmol) were added to 20 mL chloroform. The mixture was stirred under N_2 at 60 °C for 1.5 h. After removal of solvent under reduced pressure, the residue was purified by silica chromatography (CH_2Cl_2:Ethyl Acetate = 20:1) to give the product 1 as a dark purple solid. (712 mg, 80%) ^{1}H NMR (400 MHz, $CDCl_3$, ppm) δ: 8.49 (d, *J* = 4.2 Hz, 2H), 7.21 (d, *J* = 4.1 Hz, 2H), 4.17 (t, *J* = 6.0 Hz, 4H), 3.89 – 3.41 (m, 20H), 3.35 (s, 6H).

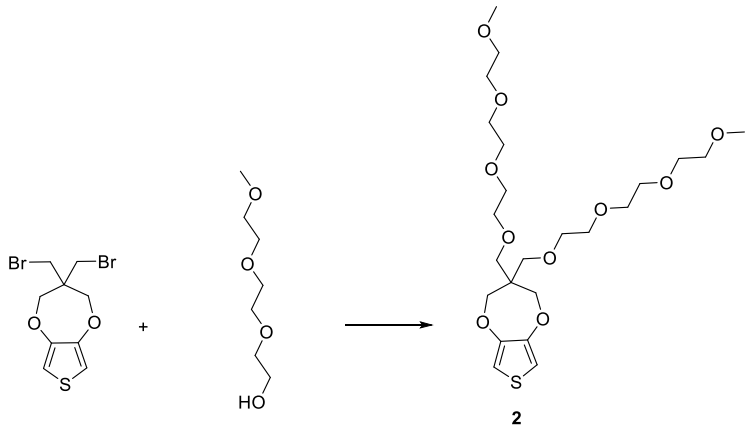

Compound 2. 3,3-bis(bromomethyl)-3,4-dihydro-2H-thieno[3,4-b][1,4]dioxepine (5.00 g, 14.6 mmol), triethylene glycol monomethyl ether (7.20 g, 43.8 mmol), and sodium hydride (3.51 g, 60% dispersion in mineral oil) were added to 100 mL dimethylformamide (DMF). The mixture was stirred under N_2 at room temperature for 30 min and at 100 °C for 12 h. The reaction mixture was extracted with DCM and dried over Na_2SO_4. After removal of solvent under reduced pressure, the residue was purified by silica chromatography (CH_2Cl_2:Ethyl Acetate = 10:1) to give the product 2 as a near colorless oil. ^{1}H NMR (400 MHz, $CDCl_3$, ppm) δ: 6.44 (s, 2H), 4.01 (s, 4H), 3.66 – 3.51 (s, 28H), 3.37 (s, 6H).

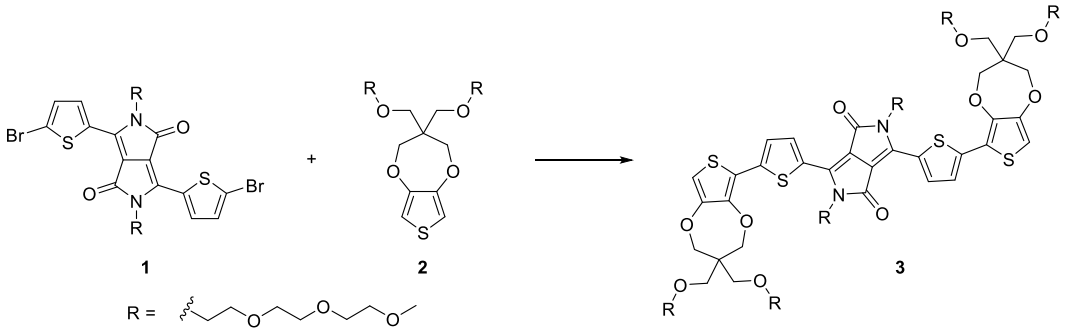

Compound 3. Compound 1 (489 mg, 0.652 mmol), Compound 2 (2.65 g, 5.21 mmol), $Pd_2(dba)_3$ (11.9 mg, 0.0130 mmol), tris(2-methoxyphenyl)phosphine (18.4 mg, 0.0521 mmol), cesium carbonate (637 mg, 1.95 mmol), pivalic acid (66.6 mg, 0.652 mmol), and

tetramethylethylenediamine (TMEDA) (37.9 mg, 0.326 mmol) were added to toluene (10 mL). The resulting solution was bubbled with N_2 for 20 min and stirred at 110 °C for 12 h. After removal of solvent under reduced pressure, the residue was purified by flash silica chromatography (CH_2Cl_2:Methanol = 20:1) to give the product 3 as a dark blue solid. (268 mg, 27%) ^{1}H NMR (800 MHz, $CDCl_3$, ppm) δ: 8.77 (d, *J* = 3.7 Hz, 2H), 7.28 (d, *J* = 3.4 Hz, 2H), 6.42 (s, 2H), 4.28 (t, *J* = 6.3 Hz, 4H), 4.16 (s, 4H), 4.04 (s, 4H), 3.76 (t, *J* = 6.3 Hz, 4H), 3.63 – 3.39 (m, 72H), 3.31 (s, 12H), 3.27 (s, 6H). ^{13}C NMR (200 MHz, $CDCl_3$, ppm) δ: 161.29, 149.86, 146.52, 140.65, 139.35, 135.46, 127.67, 123.87, 116.13, 108.01, 104.23, 73.88, 73.67, 71.81, 71.78, 71.01, 70.61, 70.55, 70.50, 70.46, 70.42, 70.26, 70.06, 68.96, 58.89, 58.83, 47.75, 41.76. HRMS (APCI) calculated for $C_{74}H_{113}N_2O_{28}S_4^+$ ($[M+H]^+$): 1605.6357; found 1605.6412.

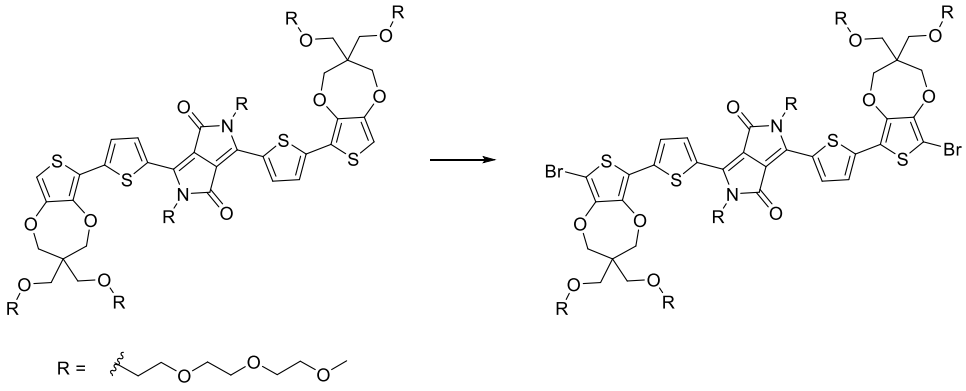

Compound 4. Compound 3 (104.7 mg, 0.06520 mmol) and *N*-bromosuccinimide (23.79 mg, 0.1336 mmol) were added to 20 mL chloroform. The mixture was stirred under N_2 at 25 °C overnight. After removal of solvent under reduced pressure, the residue was purified by flash silica chromatography (CH_2Cl_2:Methanol = 20:1) to give the product 4 as a dark blue solid. (85.1 mg, 74%) ^{1}H NMR (400 MHz, $CDCl_3$, ppm) δ: 8.78 (d, *J* = 4.1 Hz, 2H), 7.27 (d, *J* = 4.2 Hz, 2H), 4.31 (t, *J* = 6.3 Hz, 4H), 4.22 (s, 4H), 4.17 (s, 4H), 3.80 (t, *J* = 6.3 Hz, 4H), 3.68 – 3.45 (m, 72H), 3.37 (s, 12H), 3.33 (s, 6H). ^{13}C NMR (100 MHz, $CDCl_3$, ppm) δ: 161.37, 147.96, 145.48, 139.56, 139.40, 135.43, 128.02, 124.12, 115.80, 108.26, 93.37, 74.22, 74.03, 71.86, 71.82, 71.04, 70.65, 70.59, 70.54, 70.49, 70.47, 70.29, 70.02, 68.98, 58.95, 58.91, 47.85, 41.85. HRMS (APCI) calculated for $C_{74}H_{111}Br_2N_2O_{28}S_4^+$ ($[M+H]^+$): 1761.4567; found 1761.4588.

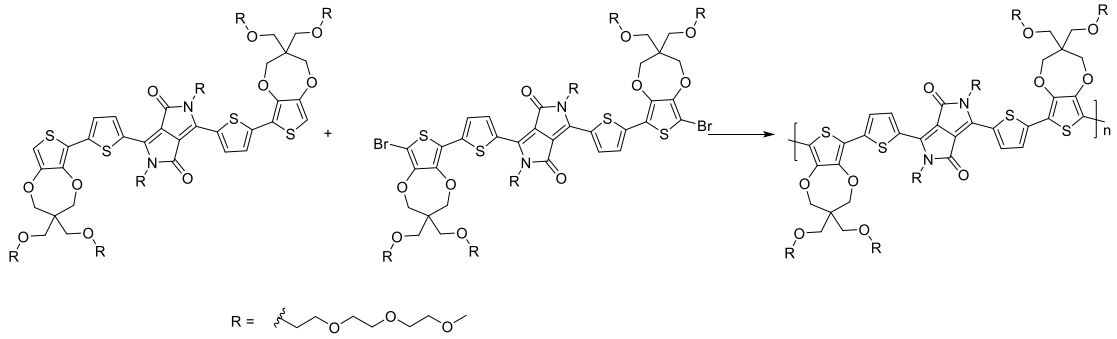

PProDOT-DPP. To a Schlenk tube charged with a stir bar, Compound 3 (37.97 mg, 0.02364 mmol), Compound 4, (41.70 mg, 0.02364 mmol), $Pd(OAc)_2$ (0.16 mg, 0.00071 mmol), pivalic acid (1.45 mg, 0.00142 mmol), potassium carbonate (8.50 mg, 0.0615 mmol), and 5 mL of dimethylacetamide (DMAc) were added. The resulting solution was bubbled with N_2 for 20 min, and the mixture was stirred at 130 °C under N_2 for 24 h. After the polymerization was complete, *N*,*N*-diethyl-2-phenyldiazenecarbothioamide was added, and the mixture was stirred for 30 min at 60 °C before being precipitated into hexanes. The solid was collected by a Soxhlet thimble, which was purified by Soxhlet extraction under N_2 successively with hexanes, methanol, acetone and chloroform. The collected polymer solution (chloroform fraction) was reprecipitated into hexanes and dried at 60 °C under vacuum, providing 69.8 mg (92% yield) of a black solid.

4.8.2 Device Fabrication and Characterization

OECTs based on PProDOT-DPP were fabricated using glass substrates (Dow Corning, 2×2 cm^2 in size). The glass substrates were cleaned with deionized (DI) water, ethanol, and acetone, in a sequential manner, and then dried in an oven for 30 min at ~110 °C. Patterned Ti (5 nm)/Au (20 nm) source and drain electrodes were then thermally deposited onto the substrates using shadow masks, achieving channel length and width of 200 and 2,500 μm, respectively. The polymer, PProDOT-DPP, was dissolved in chloroform at a concentration of 10 mg mL^{-1} and stirred overnight, and was then spin-coated onto the substrates at 1,500 rpm for 20 s. After the spin-coating process, the devices were placed in vacuum for 1 h to remove the residual solvents. Afterwards, the OECT channels were covered by patterned Polydimethylsiloxane (PDMS) masks to protect the channel areas, while unwanted PProDOT-DPP was etched by oxygen plasma (PE-25, Plasma Etch, Inc.) for 1 h, resulting in well-patterned PProDOT-DPP that was left only in the OECT channels.

During the electrical characterization of the OECTs, the OECT channels were surrounded by PDMS micro-wells to confine the liquid electrolytes. Lithium salts (LiCl or $LiPF_6$, Sigma-Aldrich) were dissolved in DI water at 0.1 M serving as the electrolytes. The electrolytes were then dropped in the PDMS wells using a pipette. The OECT electrical measurements were performed using a Keysight B2902, and an Ag/AgCl pellet was immersed into the electrolytes serving as the gate electrode.

4.8.3 1H NMR and 13C NMR Spectra of New Compounds

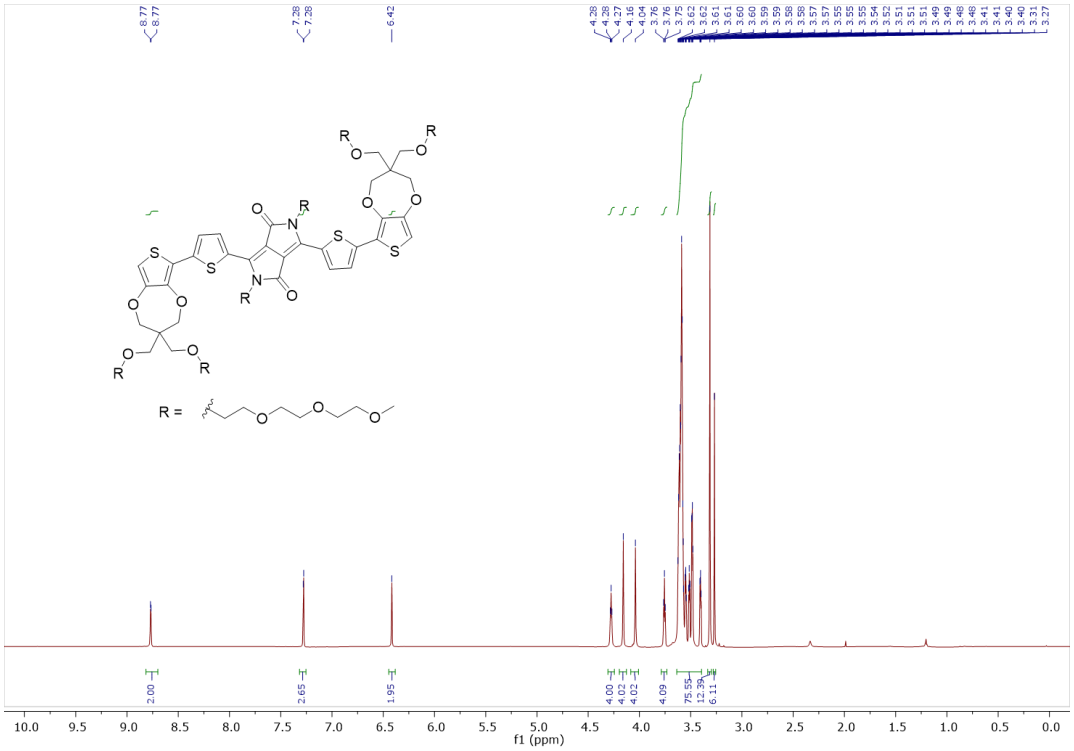

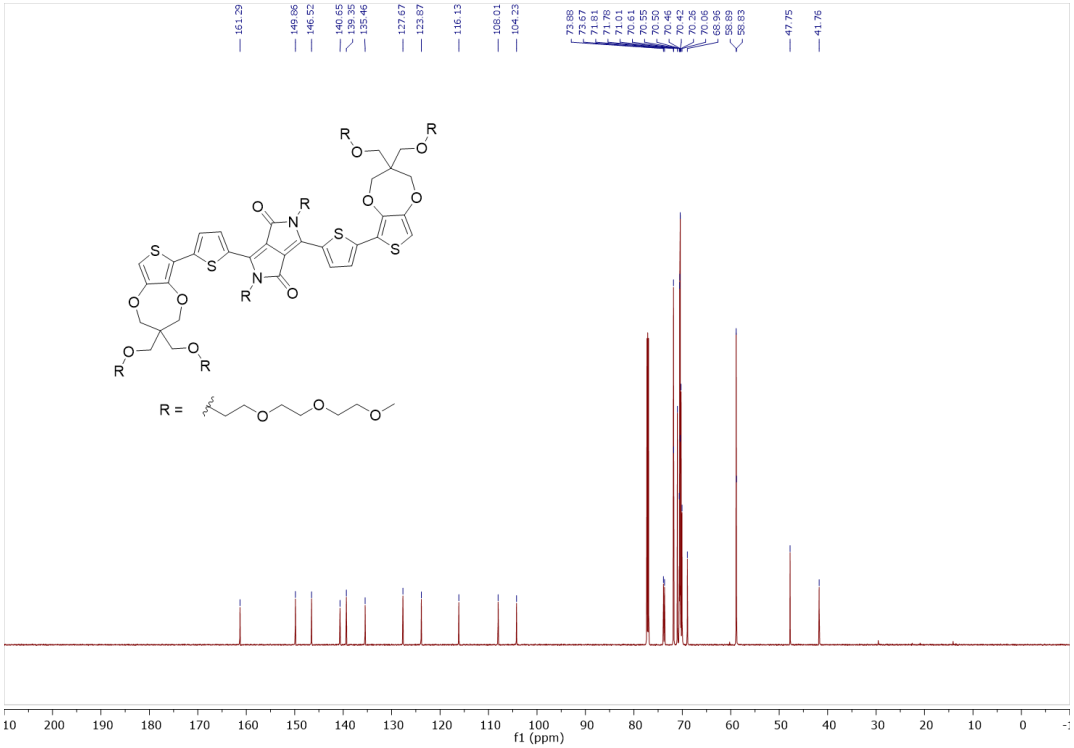

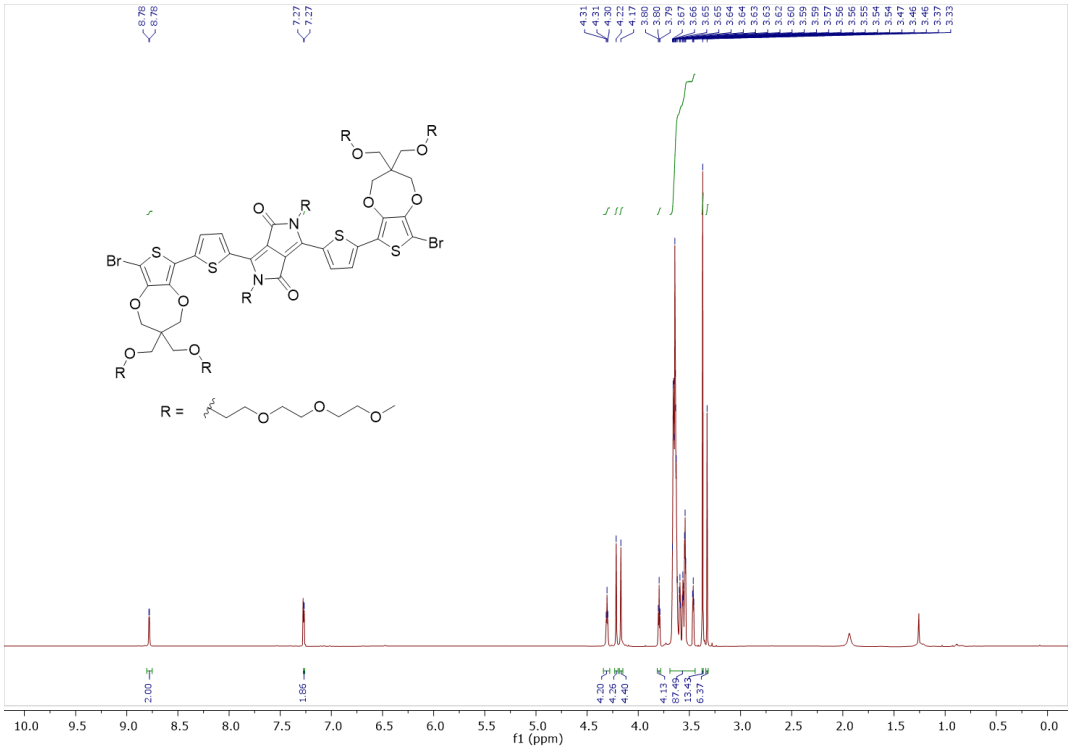
8.78
8.78
7.27
7.27
4.31
4.31
4.30
4.22
4.17
3.80
3.80
3.79
3.67
3.66
3.65
3.65
3.64
3.64
3.63
3.63
3.62
3.60
3.59
3.59
3.57
3.56
3.56
3.55
3.54
3.54
3.47
3.46
3.46
3.37
3.33
R =
2.00
1.86
4.20
4.25
4.40
4.13
87.46
13.43
6.37
f1 (ppm)

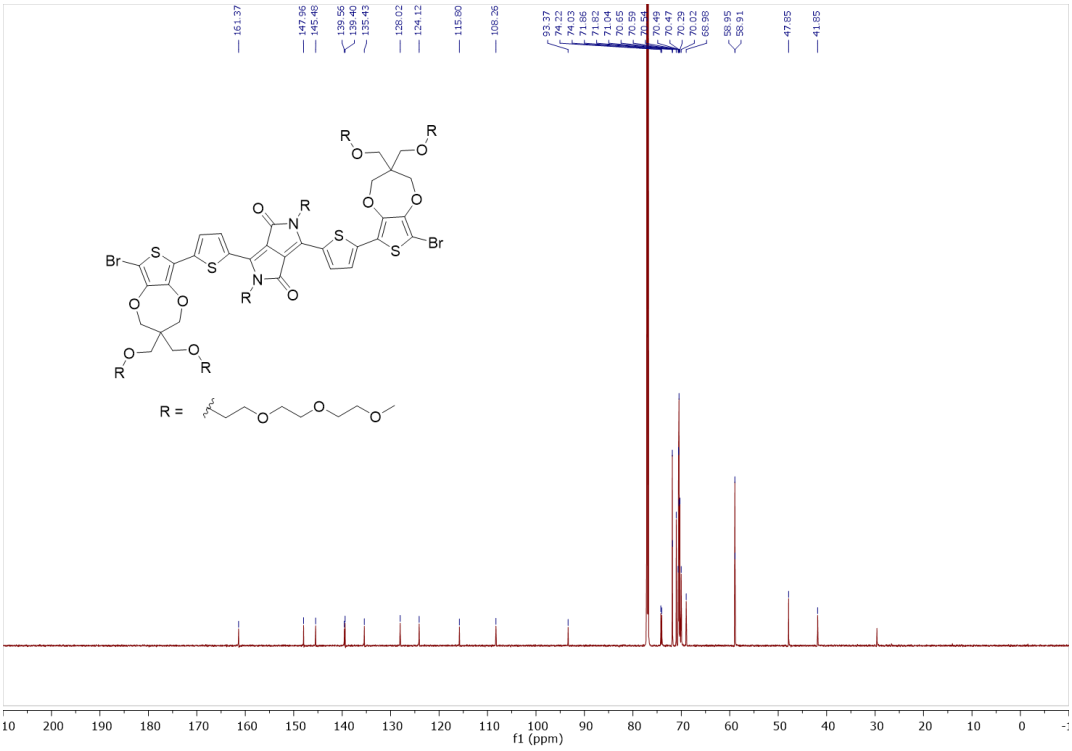
161.37
147.96
145.48
139.56
139.40
135.43
128.02
124.12
115.80
108.26
93.37
74.22
74.03
71.86
71.82
71.04
70.65
70.59
70.54
70.49
70.47
70.29
70.02
68.98
58.95
58.91
47.85
41.85
R =
f1 (ppm)

CHAPTER 5. CONCLUSIONS AND OUTLOOK

Organic semiconductors, especially polymer thin films have witnessed tremendous advancements for the past three decades owing their promising solution processability, flexibility, stretchability, and in some cases bio-compatibility. Our research identified that one of the fields that has yet to capitalize on these advantages is the synthetic advances in organic electronics. With these studies, more high-performance polymer semiconductors will be available for applications and comprehensive understanding will guide new molecular designs.

In the first study, incorporation of acceptor-acceptor (A-A) type moieties into donor-acceptor (D-A) type conjugated polymers becomes a new strategy to tune their electronic properties. In this work, we first demonstrate an efficient convergent route to prepare isoindigo-based A-A type building blocks - bis-isoindigos - via the palladium-catalyzed oxidative coupling. Bis-isoindigo-based polymers show high planarity and delocalized frontier molecular orbitals with lowered LUMO and intact HOMO energy levels, in comparison with their corresponding mono-isoindigo counterparts. Moreover, fluorine substitution on donors only lowers HOMO levels of Bis-IID polymers. This study asserts that the D-A-A strategy is effective in selectively tuning FMO energy levels of conjugated polymers, complementary to the D-D-A approach for the HOMO energy level tuning.

In the second study, Side-chain sequence enabled regioisomeric acceptors, bearing different side-chain sequences on the same conjugated backbone, are reported. Two regioregular polymers PTBI-1 and PTBI-2 and one regiorandom polymer PTBI-3 were synthesized from these two regioisomeric acceptors for a comparative study. UV−vis−NIR absorption spectroscopy and electrochemical study confirmed similar frontier molecular orbital levels of the three polymers in their solid state. More intriguingly, absorption profiles suggest that the sequence of side chains greatly governs the aggregation behaviors. Furthermore, the PTBI-2 film shows larger ordered domains than PTBI-1 and PTBI-3 films, as supported by AFM and GIWAXS measurements. As a result, PTBI-2-based FET devices achieved an average hole mobility of 1.37 $cm^2\ V^{-1}\ s^{-1}$, much higher than the two polymers with other side-chain sequences. The regiorandom PTBI-3 exhibited the lowest average hole mobility of 0.27 $cm^2\ V^{-1}\ s^{-1}$. This study highlights the significant impact of side-chain sequence regioisomerism on aggregation behaviors, morphologies, and subsequently charge transport properties of donor−acceptor type conjugated polymers.

In the third study, we implemented a next-generation design of polymers for OECTs. Specifically, diketopyrrolopyrrole (DPP) building blocks were copolymerized with propylene dioxythiophene-based (Pro-based) monomers to create a donor−acceptor-type conjugated polymer (PProDOT-DPP). These PProDOT-DPP macromolecules were synthesized using a straightforward direct arylation polymerization synthetic route. The PProDOT-DPP polymer thin film exhibited excellent electrochemical response, low oxidation potential, and high crystallinity, as evidenced by spectroelectrochemical measurements and grazing incidence wide-angle X-ray scattering measurements. Thus, the resultant polymer thin films had high charge mobility and volumetric capacitance values (i.e., μC* as high as 310 F cm^{-1} V^{-1} s^{-1}) when they were used as the active layer materials in OECT devices, which places PProDOT-DPP among the highest performing accumulation-mode OECT polymers reported to date. The performance of the PProDOT-DPP thin films was also retained for 100 cycles and over 2000 s of ON−OFF cycling, indicating the robust stability of the materials. Therefore, this effort provides a clear roadmap for the design of electrochemically active macromolecules for accumulation-mode OECTs, where crystalline acceptor cores are incorporated into an all-donor polymer. We anticipate that this will ultimately inspire future polymer designs to enable OECTs with both high electrical performance and operational stability.

With these demonstrations of semiconductor molecular design, we hope to spark new research directions especially on deeper investigation of charge transport dependence on chemical structures, and more acceptor moieties with extended conjugation for semiconducting polymers will be developed for targeted applications.

REFERENCES

(1) M. M. Szumilo, E. H. Gann, C. R. McNeill, V. Lemaur, Y. Oliver, L. Thomsen, Y. Vaynzof, M. Sommer, H. Sirringhaus, Chem. Mater. 2014, 26, 6796–6804.

(2) Z. Ma, W. Sun, S. Himmelberger, K. Vandewal, Z. Tang, J. Bergqvist, A. Salleo, J. W. Andreasen, O. Inganäs, M. R. Andersson, et al., Energy Environ. Sci. 2014, 7, 361–369.

(3) X. Liu, B. He, C. L. Anderson, J. Kang, T. Chen, J. Chen, S. Feng, L. Zhang, M. A. Kolaczkowski, S. J. Teat, et al., J. Am. Chem. Soc. 2017, 139, 8355–8363.

(4) P. Berrouard, F. Grenier, J.-R. Pouliot, E. Gagnon, C. Tessier, M. Leclerc, Org. Lett. 2011, 13, 38–41.

(5) P. Murto, Z. Genene, C. M. Benavides, X. Xu, A. Sharma, X. Pan, O. Schmidt, C. J. Brabec, M. R. Andersson, S. F. Tedde, et al., ACS Macro Lett. 2018, 7, 395–400.

(6) X. Qiao, Q. Wu, H. Wu, J. Zhang, H. Li, Adv. Funct. Mater. 2017, 27, 1–8.

(7) L. E. Polander, A. S. Romanov, S. Barlow, D. K. Hwang, B. Kippelen, T. V. Timofeeva, S. R. Marder, Org. Lett. 2012, 14, 918–921.

(8) J. Yang, H. Wang, J. Chen, J. Huang, Y. Jiang, J. Zhang, L. Shi, Y. Sun, Z. Wei, G. Yu, et al., Adv. Mater. 2017, 29, 1606162.

(9) J. Chen, Y. Jiang, J. Yang, Y. Sun, L. Shi, Y. Ran, Q. Zhang, Y. Yi, S. Wang, Y. Guo, et al., ACS Appl. Mater. Interfaces 2018, acsami.7b16516.

(10) D. I. James, S. Wang, W. Ma, S. Hedström, X. Meng, P. Persson, S. Fabiano, X. Crispin, M. R. Andersson, M. Berggren, et al., Adv. Electron. Mater. 2016, 2, 1500313.

(11) C. Zhu, Z. Zhao, H. Chen, L. Zheng, X. Li, J. Chen, Y. Sun, F. Liu, Y. Guo, Y. Liu, J. Am. Chem. Soc. 2017, 139, 17735–17738.

(12) J. Mei, K. R. Graham, R. Stalder, J. R. Reynolds, Org. Lett. 2010, 12, 660–663.

(13) E. Wang, W. Mammo, M. R. Andersson, Adv. Mater. 2014, 26, 1801–1826.

(14) T. Lei, J. H. Dou, J. Pei, Adv. Mater. 2012, 24, 6457–6461.

(15) J. Mei, D. H. Kim, A. L. Ayzner, M. F. Toney, Z. Bao, J. Am. Chem. Soc. 2011, 133, 20130–20133.

(16) R. S. Ashraf, A. J. Kronemeijer, D. I. James, H. Sirringhaus, I. McCulloch, Chem. Commun. 2012, 48, 3939–3941.

(17) J. Huang, Z. Mao, Z. Chen, D. Gao, C. Wei, W. Zhang, G. Yu, Chem. Mater. 2016, 28, 2209–2218.

(18) I. Meager, M. Nikolka, B. C. Schroeder, C. B. Nielsen, M. Planells, H. Bronstein, J. W. Rumer, D. I. James, R. S. Ashraf, A. Sadhanala, et al., Adv. Funct. Mater. 2014, 24, 7109–7115.

(19) T. Lei, J.-H. Dou, X.-Y. Cao, J.-Y. Wang, J. Pei, J. Am. Chem. Soc. 2013, 135, 12168–12171.

(20) Y. Deng, B. Sun, Y. He, J. Quinn, C. Guo, Y. Li, Chem. Commun. 2015, 51, 13515–13518.

(21) Y. He, C. Guo, B. Sun, J. Quinn, Y. Li, Chem. Commun. 2015, 51, 8093–8096.

(22) Y. Jiang, Y. Gao, H. Tian, J. Ding, D. Yan, Y. Geng, F. Wang, Macromolecules 2016, 49, 2135–2144.

(23) T. Hasegawa, M. Ashizawa, J. Hiyoshi, S. Kawauchi, J. Mei, Z. Bao, H. Matsumoto, Polym. Chem. 2016, 7, 1181–1190.

(24) J. Yang, Z. Zhao, H. Geng, C. Cheng, J. Chen, Y. Sun, L. Shi, Y. Yi, Z. Shuai, Y. Guo, et al., Adv. Mater. 2017, 29, 1702115.

(25) K. Masui, H. Ikegami, A. Mori, J. Am. Chem. Soc. 2004, 126, 5074–5075.

(26) M. S. Chen, J. R. Niskala, D. A. Unruh, C. K. Chu, O. P. Lee, J. M. J. Fréchet, Chem. Mater. 2013, 25, 4088–4096.

(27) G. W. P. Van Pruissen, F. Gholamrezaie, M. M. Wienk, R. A. J. Janssen, J. Mater. Chem. 2012, 22, 20387.

(28) K. Kawabata, M. Saito, I. Osaka, K. Takimiya, J. Am. Chem. Soc. 2016, 138, 7725–7732.

(29) T. Ma, K. Jiang, S. Chen, H. Hu, H. Lin, Z. Li, J. Zhao, Y. Liu, Y.-M. Chang, C.-C. Hsiao, et al., Adv. Energy Mater. 2015, 5, 1501282.

(30) R. S. Ashraf, I. Meager, M. Nikolka, M. Kirkus, M. Planells, B. C. Schroeder, S. Holliday, M. Hurhangee, C. B. Nielsen, H. Sirringhaus, et al., J. Am. Chem. Soc. 2015, 137, 1314–1321.

(31) L. R. Bard, A. J.; Faulkner, Electrochemical Methods: Fundamentals and Applications, Wiley, New York, 2001.

(32) J. D. Yuen, J. Fan, J. Seifter, B. Lim, R. Hufschmid, A. J. Heeger, F. Wudl, J. Am. Chem. Soc. 2011, 133, 20799–20807.

(33) K. Takimiya, I. Osaka, M. Nakano, Chem. Mater. 2014, 26, 587–593.

(34) Forrest, S. R. *Nature* **2004**, *428* (6986), 911–918.

(35) Hammock, M. L.; Chortos, A.; Tee, B. C.-K.; Tok, J. B.-H.; Bao, Z. *Adv. Mater.* **2013**, *25* (42), 5997–6038.

(36) Sirringhaus, H. *Adv. Mater.* **2014**, *26* (9), 1319–1335.

(37) Fukuda, K.; Someya, T. *Adv. Mater.* **2017**, *29* (25), 1602736.

(38) Würthner, F.; Stolte, M. *Chem. Commun.* **2011**, *47* (18), 5109.

(39) Wang, E.; Mammo, W.; Andersson, M. R. *Adv. Mater.* **2014**, *26* (12), 1801–1826.

(40) Guo, X.; Facchetti, A.; Marks, T. J. *Chem. Rev.* **2014**, *114* (18), 8943–9021.

(41) Yi, Z.; Wang, S.; Liu, Y. *Adv. Mater.* **2015**, *27* (24), 3589–3606.

(42) Quinn, J. T. E.; Zhu, J.; Li, X.; Wang, J.; Li, Y. *J. Mater. Chem. C* **2017**, *5* (34), 8654–8681.

(43) Mei, J.; Kim, D. H.; Ayzner, A. L.; Toney, M. F.; Bao, Z. *J. Am. Chem. Soc.* **2011**, *133* (50), 20130–20133.

(44) Lei, T.; Dou, J.-H.; Pei, J. *Adv. Mater.* **2012**, *24* (48), 6457–6461.

(45) Lee, J.; Han, A.-R.; Kim, J.; Kim, Y.; Oh, J. H.; Yang, C. *J. Am. Chem. Soc.* **2012**, *134* (51), 20713–20721.

(46) Dou, J.-H.; Zheng, Y.-Q.; Lei, T.; Zhang, S.-D.; Wang, Z.; Zhang, W.-B.; Wang, J.-Y.; Pei, J. *Adv. Funct. Mater.* **2014**, *24* (40), 6270–6278.

(47) Kang, B.; Kim, R.; Lee, S. B.; Kwon, S.-K.; Kim, Y.-H.; Cho, K. *J. Am. Chem. Soc.* **2016**, *138* (11), 3679–3686.

(48) Yao, J.; Yu, C.; Liu, Z.; Luo, H.; Yang, Y.; Zhang, G.; Zhang, D. *J. Am. Chem. Soc.* **2016**, *138* (1), 173–185.

(49) Ocheje, M. U.; Charron, B. P.; Cheng, Y.-H.; Chuang, C.-H.; Soldera, A.; Chiu, Y.-C.; Rondeau-Gagné, S. *Macromolecules* **2018**, *51* (4), 1336–1344.

(50) Giovannitti, A.; Maria, I. P.; Hanifi, D.; Donahue, M. J.; Bryant, D.; Barth, K. J.; Makdah, B. E.; Savva, A.; Moia, D.; Zetek, M.; Barnes, P. R. F.; Reid, O. G.; Inal, S.; Rumbles, G.; Malliaras, G. G.; Nelson, J.; Rivnay, J.; McCulloch, I. *Chem. Mater.* **2018**, *30* (9), 2945–2953.

(51) Wen, H.-F.; Wu, H.-C.; Aimi, J.; Hung, C.-C.; Chiang, Y.-C.; Kuo, C.-C.; Chen, W.-C. *Macromolecules* **2017**, *50* (13), 4982–4992.

(52) Yang, S.-F.; Liu, Z.-T.; Cai, Z.-X.; Dyson, M. J.; Stingelin, N.; Chen, W.; Ju, H.-J.; Zhang, G.-X.; Zhang, D.-Q. *Adv. Sci.* **2017**, *4* (8), 1700048.

(53) Ma, J.; Liu, Z.; Wang, Z.; Yang, Y.; Zhang, G.; Zhang, X.; Zhang, D. *Mater. Chem. Front.* **2017**, *1* (12), 2547–2553.

(54) Wang, Z.; Liu, Z.; Ning, L.; Xiao, M.; Yi, Y.; Cai, Z.; Sadhanala, A.; Zhang, G.; Chen, W.; Sirringhaus, H.; Zhang, D. *Chem. Mater.* **2018**, *30* (9), 3090–3100.

(55) Xue, G.; Zhao, X.; Qu, G.; Xu, T.; Gumyusenge, A.; Zhang, Z.; Zhao, Y.; Diao, Y.; Li, H.; Mei, J. *ACS Appl. Mater. Interfaces* **2017**, *9* (30), 25426–25433.

(56) Ying, L.; Huang, F.; Bazan, G. C. *Nat. Commun.* **2017**, *8*, 14047.

(57) Quinn, J. T. E.; Guo, C.; Haider, F.; Patel, H.; Khan, D. A.; Li, Y. *J. Mater. Chem. C* **2017**, *5* (24), 5902–5909.

(58) Wang, X.; Choi, H. H.; Zhang, G.; Ding, Y.; Lu, H.; Cho, K.; Qiu, L. *J. Mater. Chem. C* **2016**, *4* (26), 6391–6400.

(59) Luo, X.; Tran, D. T.; Sun, H.; Mi, T.; Kadlubowski, N. M.; Zhao, Y.; Zhao, K.; Mei, J. *Asian J. Org. Chem.* **2018**, DOI: 10.1002/ajoc.201800360.

(60) Cho, H. J.; Kang, S.-J.; Lee, S. M.; Jeong, M.; Kim, G.; Noh, Y.-Y.; Yang, C. *ACS Appl. Mater. Interfaces* **2017**, *9* (36), 30755–30763.

(61) Wang, X.-Y.; Zhang, M.-W.; Zhuang, F.-D.; Wang, J.-Y.; Pei, J. *Polym. Chem.* **2016**, *7* (12), 2264–2271.

(62) Kasha, M. *Radiat. Res.* **1963**, *20* (1), 55.

(63) Más-Montoya, M.; Janssen, R. A. J. *Adv. Funct. Mater.* **2017**, *27* (16), 1605779.

(64) Park, S.; Lee, M. H.; Ahn, K. S.; Choi, H. H.; Shin, J.; Xu, J.; Mei, J.; Cho, K.; Bao, Z.; Lee, D. R.; Kang, M. S.; Kim, D. H. *Adv. Funct. Mater.* **2016**, *26* (26), 4627–4634.

(65) Rivnay, J.; Mannsfeld, S. C. B.; Miller, C. E.; Salleo, A.; Toney, M. F. *Chem. Rev.* **2012**, *112* (10), 5488–5519.

(66) Ying, L.; Hsu, B. B. Y.; Zhan, H.; Welch, G. C.; Zalar, P.; Perez, L. A.; Kramer, E. J.; Nguyen, T.-Q.; Heeger, A. J.; Wong, W.-Y.; Bazan, G. C. *J. Am. Chem. Soc.* **2011**, *133* (46), 18538–18541.

(67) Wang, M.; Wang, H.; Yokoyama, T.; Liu, X.; Huang, Y.; Zhang, Y.; Nguyen, T.-Q.; Aramaki, S.; Bazan, G. C. *J. Am. Chem. Soc.* **2014**, *136* (36), 12576–12579.

(68) Durban, M. M.; Kazarinoff, P. D.; Luscombe, C. K. *Macromolecules* **2010**, *43* (15), 6348–6352.

(69) Yi, Z.; Sun, X.; Zhao, Y.; Guo, Y.; Chen, X.; Qin, J.; Yu, G.; Liu, Y. *Chem. Mater.* **2012**, *24* (22), 4350–4356.

(70) Chen, M. S.; Lee, O. P.; Niskala, J. R.; Yiu, A. T.; Tassone, C. J.; Schmidt, K.; Beaujuge, P. M.; Onishi, S. S.; Toney, M. F.; Zettl, A.; Fréchet, J. M. J. *J. Am. Chem. Soc.* **2013**, *135* (51), 19229–19236.

(71) Grand, C.; Zajaczkowski, W.; Deb, N.; Lo, C. K.; Hernandez, J. L.; Bucknall, D. G.; Müllen, K.; Pisula, W.; Reynolds, J. R. *ACS Appl. Mater. Interfaces* **2017**, *9* (15), 13357–13368.

(72) Lei, T.; Dou, J.-H.; Cao, X.-Y.; Wang, J.-Y.; Pei, J.*J. Am. Chem. Soc.* **2013**, *135* (33), 12168–12171.

(73) Cao, Y.; Yuan, J.-S.; Zhou, X.; Wang, X.-Y.; Zhuang, F.-D.; Wang, J.-Y.; Pei, J. *Chem. Commun.* **2015**, *51* (52), 10514–10516.

(74) Dai, Y.-Z.; Ai, N.; Lu, Y.; Zheng, Y.-Q.; Dou, J.-H.; Shi, K.; Lei, T.; Wang, J.-Y.; Pei, J. *Chem. Sci.* **2016**, *7* (9), 5753–5757.

(75) James, D. I.; Wang, S.; Ma, W.; Hedström, S.; Meng, X.; Persson, P.; Fabiano, S.; Crispin, X.; Andersson, M. R.; Berggren, M.; Wang, E. *Adv. Electron. Mater.* **2016**, *2* (4), 1500313.

(76) Randell, N. M.; Radford, C. L.; Yang, J.; Quinn, J.; Hou, D.; Li, Y.; Kelly, T. L. *Chem. Mater.* **2018**, *30* (14), 4864–4873.

(77) Chung, J.; Khot, A.; Savoie, B. M.; Boudouris, B. W. *ACS Macro Lett.* **2020**, *9* (5), 646–655.

(78) Rivnay, J.; Inal, S.; Salleo, A.; Owens, R. M.; Berggren, M.; Malliaras, G. G. *Nat. Rev. Mater.* **2018**, *3* (2), 17086.

(79) Kim, J. H.; Kim, S.; Kim, G.; Yoon, M. *Macromol. Biosci.* **2020**, *20* (11), 2000211.

(80) Inal, S.; Rivnay, J.; Suiu, A. O.; Malliaras, G. G.; McCulloch, I. *Acc. Chem. Res.* **2018**, *51* (6), 1368–1376.

(81) Strakosas, X.; Bongo, M.; Owens, R. M. *J. Appl. Polym. Sci.* **2015**, *132* (15), 41735.

(82) Ling, H.; Koutsouras, D. A.; Kazemzadeh, S.; van de Burgt, Y.; Yan, F.; Gkoupidenis, P. *Appl. Phys. Rev.* **2020**, *7* (1), 011307.

(83) Chen, S.; Surendran, A.; Wu, X.; Lee, S. Y.; Stephen, M.; Leong, W. L. *Adv. Mater. Technol.* **2020**, *5* (12), 2000523.

(84) Moser, M.; Savva, A.; Thorley, K.; Paulsen, B. D.; Hidalgo, T. C.; Ohayon, D.; Chen, H.; Giovannitti, A.; Marks, A.; Gasparini, N.; Wadsworth, A.; Rivnay, J.; Inal, S.; McCulloch, I. *Angew. Chemie Int. Ed.* **2021**, *60* (14), 7777–7785.

(85) Inal, S.; Malliaras, G. G.; Rivnay, J. *Nat. Commun.* **2017**, *8* (1), 1767.

(86) Bronstein, H.; Nielsen, C. B.; Schroeder, B. C.; McCulloch, I. *Nat. Rev. Chem.* **2020**, *4* (2), 66–77.

(87) Moser, M.; Ponder, J. F.; Wadsworth, A.; Giovannitti, A.; McCulloch, I. *Adv. Funct. Mater.* **2019**, *29* (21), 1807033.

(88) Giovannitti, A.; Sbircea, D. T.; Inal, S.; Nielsen, C. B.; Bandiello, E.; Hanifi, D. A.; Sessolo, M.; Malliaras, G. G.; McCulloch, I.; Rivnay, J. *Proc. Natl. Acad. Sci. U. S. A.* **2016**, *113* (43), 12017–12022.

(89) Nielsen, C. B.; Giovannitti, A.; Sbircea, D. T.; Bandiello, E.; Niazi, M. R.; Hanifi, D. A.; Sessolo, M.; Amassian, A.; Malliaras, G. G.; Rivnay, J.; McCulloch, I. *J. Am. Chem. Soc.* **2016**, *138* (32), 10252–10259.

(90) Moser, M.; Hidalgo, T. C.; Surgailis, J.; Gladisch, J.; Ghosh, S.; Sheelamanthula, R.; Thiburce, Q.; Giovannitti, A.; Salleo, A.; Gasparini, N.; Wadsworth, A.; Zozoulenko, I.; Berggren, M.; Stavrinidou, E.; Inal, S.; McCulloch, I. *Adv. Mater.* **2020**, *32* (37), 2002748.

(91) Giovannitti, A.; Nielsen, C. B.; Sbircea, D.-T.; Inal, S.; Donahue, M.; Niazi, M. R.; Hanifi, D. A.; Amassian, A.; Malliaras, G. G.; Rivnay, J.; McCulloch, I. *Nat. Commun.* **2016**, *7* (1), 13066.

(92) Flagg, L. Q.; Bischak, C. G.; Onorato, J. W.; Rashid, R. B.; Luscombe, C. K.; Ginger, D. S. *J. Am. Chem. Soc.* **2019**, *141* (10), 4345–4354.

(93) Moser, M.; Savagian, L. R.; Savva, A.; Matta, M.; Ponder, J. F.; Hidalgo, T. C.; Ohayon, D.; Hallani, R.; Reisjalali, M.; Troisi, A.; Wadsworth, A.; Reynolds, J. R.; Inal, S.; McCulloch, I. *Chem. Mater.* **2020**, *32* (15), 6618–6628.

(94) Bryan, A. M.; Santino, L. M.; Lu, Y.; Acharya, S.; D'Arcy, J. M. *Chem. Mater.* **2016**, *28* (17), 5989–5998.

(95) Beaujuge, P. M.; Reynolds, J. R. *Chem. Rev.* **2010**, *110* (1), 268–320.

(96) Wu, X.; Surendran, A.; Moser, M.; Chen, S.; Muhammad, B. T.; Maria, I. P.; Mcculloch, I.; Leong, W. L. *ACS Appl. Mater. Interfaces* **2020**, *12* (18), 20757–20764.

(97) Inal, S.; Rivnay, J.; Hofmann, A. I.; Uguz, I.; Mumtaz, M.; Katsigiannopoulos, D.; Brochon, C.; Cloutet, E.; Hadziioannou, G.; Malliaras, G. G. *J. Polym. Sci. Part B Polym. Phys.* **2016**, *54* (2), 147–151.

(98) Rivnay, J.; Inal, S.; Collins, B. A.; Sessolo, M.; Stavrinidou, E.; Strakosas, X.; Tassone, C.; Delongchamp, D. M.; Malliaras, G. G. *Nat. Commun.* **2016**, *7* (1), 11287.

(99) Kim, Y.; Noh, H.; Paulsen, B. D.; Kim, J.; Jo, I.; Ahn, H.; Rivnay, J.; Yoon, M. *Adv. Mater.* **2021**, *33* (10), 2007550.

(100) Kim, S.-M.; Kim, C.-H.; Kim, Y.; Kim, N.; Lee, W.-J.; Lee, E.-H.; Kim, D.; Park, S.; Lee, K.; Rivnay, J.; Yoon, M.-H. *Nat. Commun.* **2018**, *9* (1), 3858.

(101) Perera, K.; Yi, Z.; You, L.; Ke, Z.; Mei, J. *Polym. Chem.* **2020**, *11* (2), 508–516.

(102) Reeves, B. D.; Grenier, C. R. G.; Argun, A. A.; Cirpan, A.; McCarley, T. D.; Reynolds, J. R. *Macromolecules* **2004**, *37* (20), 7559–7569.

(103) Savagian, L. R.; Österholm, A. M.; Ponder, J. F.; Barth, K. J.; Rivnay, J.; Reynolds, J. R. *Adv. Mater.* **2018**, *30* (50), 1804647.

(104) Wang, Y.; Zeglio, E.; Liao, H.; Xu, J.; Liu, F.; Li, Z.; Maria, I. P.; Mawad, D.; Herland, A.; McCulloch, I.; Yue, W. *Chem. Mater.* **2019**, *31* (23), 9797–9806.

(105) Giovannitti, A.; Rashid, R. B.; Thiburce, Q.; Paulsen, B. D.; Cendra, C.; Thorley, K.; Moia, D.; Mefford, J. T.; Hanifi, D.; Weiyuan, D.; Moser, M.; Salleo, A.; Nelson, J.; McCulloch, I.; Rivnay, J. *Adv. Mater.* **2020**, *32* (16), 1908047.

(106) Wu, X.; Liu, Q.; Surendran, A.; Bottle, S. E.; Sonar, P.; Leong, W. L. *Adv. Electron. Mater.* **2021**, *7* (1), 2000701.

(107) Jia, H.; Huang, Z.; Li, P.; Zhang, S.; Wang, Y.; Wang, J.-Y.; Gu, X.; Lei, T. *J. Mater. Chem. C* **2021**, *9* (14), 4927–4934.

(108) Wakioka, M.; Takahashi, R.; Ichihara, N.; Ozawa, F. *Macromolecules* **2017**, *50* (3), 927–934.

(109) Cendra, C.; Giovannitti, A.; Savva, A.; Venkatraman, V.; McCulloch, I.; Salleo, A.; Inal, S.; Rivnay, J. *Adv. Funct. Mater.* **2019**, *29* (5), 1807034.

(110) Cardona, C. M.; Li, W.; Kaifer, A. E.; Stockdale, D.; Bazan, G. C. *Adv. Mater.* **2011**, *23* (20), 2367–2371.

(111) Zozoulenko, I.; Singh, A.; Singh, S. K.; Gueskine, V.; Crispin, X.; Berggren, M. *ACS Appl. Polym. Mater.* **2019**, *1* (1), 83–94.

(112) Enengl, C.; Enengl, S.; Pluczyk, S.; Havlicek, M.; Lapkowski, M.; Neugebauer, H.; Ehrenfreund, E. *ChemPhysChem* **2016**, *17* (23), 3836–3844.

(113) Wilson, R. H.; Nadeau, K. P.; Jaworski, F. B.; Tromberg, B. J.; Durkin, A. J. *J. Biomed. Opt.* **2015**, *20* (3), 030901.

(114) Di Pietro, R.; Erdmann, T.; Carpenter, J. H.; Wang, N.; Shivhare, R. R.; Formanek, P.; Heintze, C.; Voit, B.; Neher, D.; Ade, H.; Kiriy, A. *Chem. Mater.* **2017**, *29* (23), 10220–10232.

(115) Yang, S. F.; Liu, Z. T.; Cai, Z. X.; Dyson, M. J.; Stingelin, N.; Chen, W.; Ju, H. J.; Zhang, G. X.; Zhang, D. Q. *Adv. Sci.* **2017**, *4* (8), 1700048.

(116) Mazaheripour, A.; Thomas, E. M.; Segalman, R. A.; Chabinyc, M. L. *Macromolecules* **2019**, *52* (5), 2203–2213.

(117) Khodagholy, D.; Rivnay, J.; Sessolo, M.; Gurfinkel, M.; Leleux, P.; Jimison, L. H.; Stavrinidou, E.; Herve, T.; Sanaur, S.; Owens, R. M.; Malliaras, G. G. *Nat. Commun.* **2013**, *4* (1), 2133.

(118) Gudjonsdottir, S.; van der Stam, W.; Kirkwood, N.; Evers, W. H.; Houtepen, A. J. *J. Am. Chem. Soc.* **2018**, *140* (21), 6582–6590.

(119) Paterson, A. F.; Faber, H.; Savva, A.; Nikiforidis, G.; Gedda, M.; Hidalgo, T. C.; Chen, X.; McCulloch, I.; Anthopoulos, T. D.; Inal, S. *Adv. Mater.* **2019**, *31* (37), 1902291.

(120) Wegner, B.; Lungwitz, D.; Mansour, A. E.; Tait, C. E.; Tanaka, N.; Zhai, T.; Duhm, S.; Forster, M.; Behrends, J.; Shoji, Y.; Opitz, A.; Scherf, U.; List-Kratochvil, E. J. W.; Fukushima, T.; Koch, N. *Adv. Sci.* **2020**, *7* (17), 2001322.

(121) Salzmann, I.; Heimel, G.; Oehzelt, M.; Winkler, S.; Koch, N. *Acc. Chem. Res.* **2016**, *49* (3), 370–378.

Macromolecules
Cite This: Macromolecules 2018, 51, 8486−8492
Article
pubs.acs.org/Macromolecules

Side-Chain Sequence Enabled Regioisomeric Acceptors for Conjugated Polymers

Xuyi Luo,[†] Dung T. Tran,[†] Natalie M. Kadlubowski,[†] Carr Hoi Yi Ho,[‡] Parand Riley,[‡] Franky So,[‡] and Jianguo Mei*,[†]

[†]Department of Chemistry, Purdue University, West Lafayette, Indiana 47907, United States
[‡]Department of Materials Science and Engineering, North Carolina State University, Raleigh, North Carolina 27606, United States

Supporting Information

ABSTRACT: Side-chain sequence enabled regioisomeric acceptors, bearing different side-chain sequences on the same conjugated backbone, are herein reported. Two regioregular polymers PTBI-1 and PTBI-2 and one regiorandom polymer PTBI-3 were synthesized from these two regioisomeric acceptors for a comparative study. UV−vis−NIR absorption spectroscopy and electrochemical study confirmed similar frontier molecular orbital levels of the three polymers in their solid state. More intriguingly, absorption profiles suggest that the sequence of side chains greatly governs the aggregation behaviors. Furthermore, the PTBI-2 film shows larger ordered domains than PTBI-1 and PTBI-3 films, as supported by AFM and GIWAXS measurements. As a result, PTBI-2-based FET devices achieved an average hole mobility of 1.37 $cm^2 V^{-1} s^{-1}$, much higher than the two polymers with other side-chain sequences. The regiorandom PTBI-3 exhibited the lowest average hole mobility of 0.27 $cm^2 V^{-1} s^{-1}$. This study highlights the significant impact of side-chain sequence regioisomerism on aggregation behaviors, morphologies, and subsequently charge transport properties of donor−acceptor type conjugated polymers.

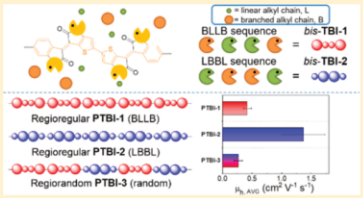

INTRODUCTION

Donor−acceptor (D−A) type conjugated polymers have attracted a great deal of attention as organic semiconductors in printed and flexible electronics because of the versatile chemistry available to tune their optical and electronic properties.[1−4] This potential has spurred the development of numerous π-conjugated polymer systems.[5−9] In the molecular design of D−A polymers, side-chain engineering has proved to be effective in tuning electronic and morphological properties of resulting polymer thin films.[10−16] A rational combination of different side chains is one of such strategies.[17−21] There are generally two approaches to introduce a combination of side chains. The first approach deals with the copolymerization of two monomers bearing the targeted side chains (Scheme 1a). For an example, Zhang et al. developed a DPP (diketopyrrolopyrrole) monomer bearing urea-containing alkyl chains.[15] Changing the ratio of the urea-chain DPP monomers to the branched-alkyl-chain DPP monomers in polymerization provided a series of DPP random copolymers with enhanced charge mobilities. The second approach involves a single monomer bearing two different side chains, which would produce alternating copolymers (Scheme 1a). We previously reported such an isoindigo building block with one alkyl chain and one siloxane hybrid chain.[22] The corresponding polymer thin films adopted bimodal packing orientation and exhibited improved charge transport performance.

The presence of different types of side chains brings up the issue of side-chain sequence along the polymer backbones. It has been repeatedly shown in the case of polyalkylthiophenes that the side-chain sequence affects both physical and electronic properties.[23] (Scheme 1b) However, little has been known about side-chain regioisomerism in D−A polymers.[24,25] Herein, we demonstrate for the first time side-chain sequence enabled regioisomeric acceptors for D−A copolymers based on the bis-thieno-benzo-isoindigo (bis-TBI) acceptor−acceptor type building block (Scheme 1c). Owing to its convergent synthetic approach, two pairs of side chains can be efficiently mounted onto the bis-TBI compound.[26] In this study, bulky branched alkyl chains (B) and linear alkyl chains (L) are placed in two different sequences along the backbones, providing side-chain regioisomeric monomers bis-TBI-1 with a branched−linear−linear−branched (BLLB) side-chain sequence and bis-TBI-2 with a linear−branched−branched−linear (LBBL) side-chain sequence. It is worth noting that the two monomers share an identical conjugated core but with different side-chain sequences away from the charge transport pathway; hence, they are a different category of isomers than P3AT-like regioisomers. The corresponding D−A copolymers PTBI-1 and PTBI-2 and a regiorandom copolymer PTBI-3 with mixed bis-TBI moieties are subsequently prepared to investigate the impact of side-chain-sequence regioisomerism on aggregation behaviors and charge transport properties of the polymers.

Received: September 10, 2018
Revised: October 2, 2018
Published: October 17, 2018

DOI: 10.1021/acs.macromol.8b01946
Macromolecules 2018, 51, 8486−8492

Scheme 1. Previous Work and Illustration of the Design Rationale for bis-TBI Regioisomeric Acceptors

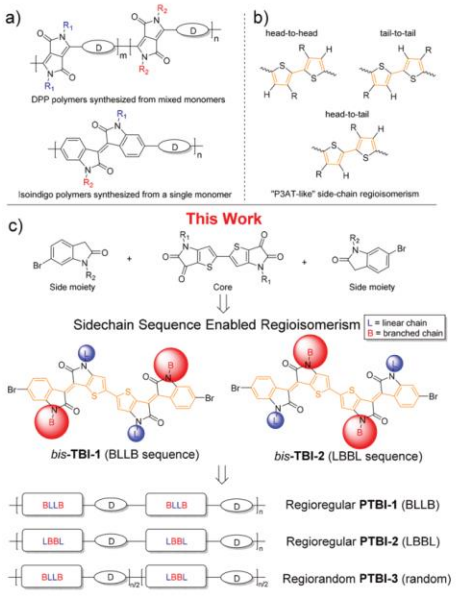

RESULTS AND DISCUSSION

Synthesis and Characterization. The synthesis of PTBI polymers follows a similar convergent synthetic route we previously developed for bis-TBI moieties,[26] as illustrated in Scheme 2. The core bis-thieno-isatin **3** bearing one type of side chain and the side moiety oxindole **5** bearing the other type were synthesized in good yields. After an aldol condensation reaction of compounds **3** and **5**, regioisomers bis-TBI-1 (with BLLB sequence) and bis-TBI-2 (with LBBL sequence) were obtained in 76% and 86% yield, respectively. Subsequently, Stille polymerization of bis-TBI monomers with bithiophene ditin compound **6** provided two regioregular PTBI polymers PTBI-1 and PTBI-2 in 85% and 83% yields. The regiorandom PTBI-3 was also synthesized from the 1:1 bis-TBIs mixture and compound **6**, giving a 79% yield. Because of solubility issue, all polymerizations were performed for 1 h. The synthesis details are described in the Supporting Information. All polymers were purified by the Soxhlet extraction and fully characterized. Molecular weights of PTBI polymers were evaluated by high-temperature gel permeation chromatography (Figure S1). All of PTBI polymers were estimated to have number-average molecular weights around 9 kDa and polydispersity indices (PDI) around 1.5. Similar molecular weight and polydispersity exclude the potential molecular weight effect when comparing PTBI polymers.[27]

Electrochemical and Optical Properties. The redox properties of PTBI polymers were evaluated by cyclic voltammetry (CV) and differential pulse voltammetry (DPV). Cyclic voltammograms of all polymer thin films show similar redox profiles and quasi-reversible redox behavior (Figure 1). HOMO/LUMO energy levels of PTBI polymers were estimated from the respective redox onset potentials of both CV and DPV. As summarized in Table 1, all three polymers show similar HOMO/LUMO levels within a range of 0.03 eV. The side-chain sequence has little impact on electrochemical properties of PTBI polymers. It is worth noting that for polymers having alkyl chain substitution positions directly on aromatic rings (i.e., P3AT-like side-chain regioisomers), their regioisomers typically present a noticeable HOMO/LUMO energy level difference.[24,25,28]

Photophysical properties of bis-TBI monomers and their polymers were characterized by solution and solid-state UV−vis−NIR spectroscopy. As shown in Figure 2a, two bis-TBI monomers bis-TBI-1 and bis-TBI-2 exhibit identical absorption profiles in diluted chloroform solutions, suggesting that their absorption properties are not influenced by the sequence of side chains in solutions. This observation is in a good agreement with their ^{1}H NMR spectra collected in $CDCl_3$ solutions, where the two isomers have identical chemical shifts in the aromatic region (Figure S2). Unexpectedly, the two isomers exhibit distinctly different absorption profiles in the solid states. bis-TBI-1 film presents a large blue-shift of maximum absorbance (λ_{max}) from 726 to 652 nm from solution to thin film, while bis-TBI-2 film shows a strongly red-shifted absorption with λ_{max} at 815 nm in thin films. The blue- and red-shifts are attributed to two different packing motifs with predominant H- and J-aggregates, respectively,[29,30] highlighting the crucial rule of the side-chain sequence in the highly aggregated bis-TBI molecules. Side-chain sequence also impacts photophysical properties of PTBI polymers, as shown by the solution and thin-film absorption profiles (Figures 2b and 2c). All polymers exhibit typical charge transfer peaks from 600 to 1100 nm. Peaks at around 950 nm and shoulders at around 870 nm are attributed to origin 0−0 and sideband 0−1 vibronic transitions, respectively. Different from solutions of their monomers, the absorption spectra of PTBI polymers in dichlorobenzene (*o*-DCB) have a noticeable difference. Although PTBI polymers show nearly overlapped solution absorption profiles and λ_{max}, the relative intensities of 0−0 and 0−1 vibrational peaks of these polymers are different. It suggests that PTBI polymers form different preaggregates in solution. Thin-film absorption spectra of PTBI spun from ODCB solutions also have clear 0−0 and 0−1 vibrational peaks, indicative of their different solid-state packing. Identical film absorption onsets at 1047 nm suggest all polymers have the same optical bandgap of 1.18 eV, consistent with the electrochemical estimations.

Film Morphology and Microstructural Analysis. Polymer thin film morphologies were analyzed by tapping-mode atomic force microscopy (AFM). All PTBI polymer films were spin-coated from *o*-DCB solution on OTS-modified Si/SiO_2 substrates. As depicted in Figure 3, surface topography images of the PTBI-2 film show a smooth surface with crystalline fibrillar intercalating networks, while PTBI-1 and PTBI-3 films show less ordered structures and mesh-like morphologies. PTBI-1 and PTBI-2 have similar root-mean-square (rms) roughness of 0.69 and 0.64 nm, respectively, while PTBI-3 has a slightly rougher surface with rms roughness of 1.1 nm. Varying the annealing temperature did not change film morphology features (Figure S5). The comparison of PTBI polymer films provides clear evidence that the microstructure is affected by side-chain sequence regioisomerism.

Grazing Incident X-ray diffraction (GIXRD) measurements of thermally annealed PTBI polymer films were also performed

DOI: 10.1021/acs.macromol.8b01946
Macromolecules 2018, 51, 8486−8492

Scheme 2. Synthetic Route to bis-TBI Monomers and PTBI Polymers[a]

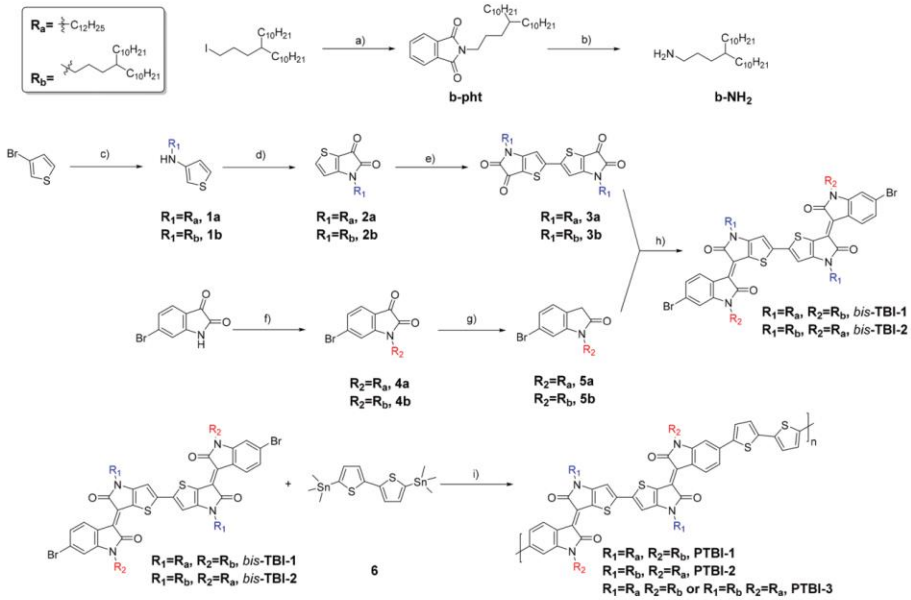

[a]Reagents and conditions: (a) potassium phthalimide, DMF, 80 °C, overnight, 90%; (b) hydrazine hydrate, MeOH, reflux, 12 h, 95%; (c) alkylamine, CuI, K_3PO_4, DMEA, 80 °C, 48 h; (d) oxalyl chloride, NEt_3, DCM, 0 °C to RT, overnight, 26% (**2a**)/17% (**2b**) over two steps; (e) AgF, $Pd(OAc)_2$, DMSO/dioxane, 90 °C, 24 h, 47% (**3a**)/60% (**3b**); (f) K_2CO_3, alkyl halide, DMF, 100 °C, overnight, 69% (**4a**)/83% (**4b**); (g) hydrazine hydrate, DMSO, 130 °C, 24 h, 61% (**5a**)/71% (**5b**); (h) PTSA, toluene, 110 °C, 12 h, 76% (bis-TBI-1)/86% (bis-TBI-2); (i) $Pd_2(dba)_3$, $P(o\text{-tol})_3$, toluene, 110 °C, 1 h, 79%–85%.

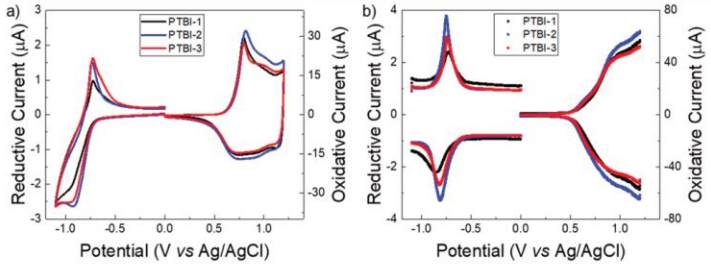

Figure 1. (a) Cyclic voltammograms of PTBI-1 (black), PTBI-2 (blue), and PTBI-3 (red). (b) Differential pulse voltammograms of PTBI-1 (black), PTBI-2 (blue), and PTBI-3 (red). All polymer thin films were tested in propylene carbonate with 0.2 M n-Bu_4NPF_6 as supporting electrolyte (scan rate: 20 mV s^{-1}).

Table 1. Optical and Electrochemical Properties of PTBI Polymers

	film absorption spectroscopy		cyclic voltammetry[b]			differential pulse voltammetry[b]		
polymer	onset (nm)	E_g[a] (eV)	LUMO (eV)	HOMO (eV)	E_g (eV)	LUMO (eV)	HOMO (eV)	E_g (eV)
PTBI-1	1047	1.18	4.01	5.42	1.41	4.06	5.28	1.22
PTBI-2	1047	1.18	4.01	5.43	1.42	4.07	5.25	1.18
PTBI-3	1048	1.18	4.01	5.42	1.41	4.08	5.26	1.18

[a]Optical band gaps are estimated from $E_g = 1240\ \text{nm}/\lambda_{onset}$. [b]The HOMO and LUMO energy levels are estimated from HOMO = $-(5.10 + E_{ox} - E_{Fc/Fc^+})$ and LUMO = $-(5.10 + E_{red} - E_{Fc/Fc^+})$, where E_{ox} and E_{red} are onset potentials.

DOI: 10.1021/acs.macromol.8b01946
Macromolecules 2018, 51, 8486–8492

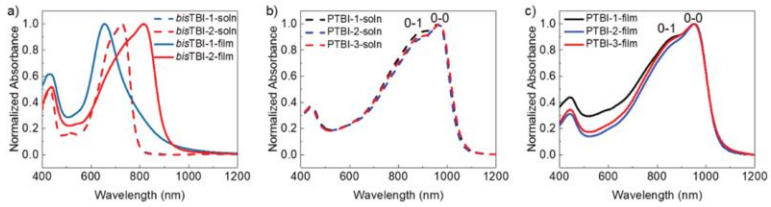

Figure 2. (a) Solution and film absorption spectra of bis-TBI-1 (blue) and bis-TBI-2 (red) in chloroform (1.0×10^{-5} M) (dashed line) and as film (solid line). (b) Absorption spectra of PTBI-1 (black), PTBI-2 (blue), and PTBI-3 (red) in *o*-DCB (1.0×10^{-5} M). (c) Absorption spectra of PTBI-1 (black), PTBI-2 (blue), and PTBI-3 (red) thin films spun from *o*-DCB solution.

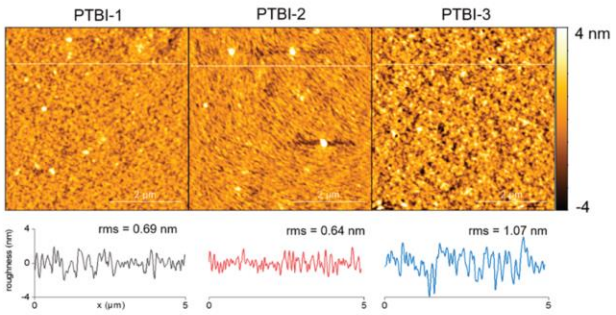

Figure 3. AFM height images of PTBI polymer thin films and the corresponding film roughness along white line profiles in the graphs for each film.

Table 2. Summary of 2D-GIXRD Data and FET Device Performance of PTBI Polymers

polymer	$\pi-\pi$ distance (Å)	fwhm in-plane (010)	lamellar distance (Å)	fwhm out-of-plane (200)	μ_{ave} ($cm^2 V^{-1} s^{-1}$)	μ_{max} ($cm^2 V^{-1} s^{-1}$)	$I_{on/off}$	V_{th} (V)
PTBI-1	3.52	0.129	24.6	0.109	0.40 ± 0.065	0.53	10^4	−8 ± 4
PTBI-2	3.51	0.098	24.6	0.095	1.37 ± 0.36	2.22	10^4	−5 ± 3
PTBI-3	3.53	0.140	24.8	0.114	0.27 ± 0.070	0.43	10^4	−8 ± 3

to obtain further insights into molecular packing in thin films. All three polymers show bimodal packing with both edge-on (χ = 90°) and face-on (χ = 0°) orientations of $\pi-\pi$ stacking. Such bimodal orientation is considered to be beneficial for charge transport in the previous reports (Figure S6).[10,22,31] Long-range ordered lamellar packings up to (400) peak along face-on direction were also observed for all three polymers. As summarized in Table 2, the observed shortest $\pi-\pi$ stacking distance among the three polymers is 3.51 Å of PTBI-2, only slightly shorter than PTBI-1 (3.52 Å) and PTBI-3 (3.53 Å). The small difference of GIXRD patterns is distinctly different from P3AT-like regioisomerism.[24,25,28] PTBI-2 in-plane $\pi-\pi$ stacking was estimated to have a significantly lower full width at half-maximum (fwhm) of 0.098 than PTBI-1 of 0.129 and PTBI-3 of 0.140, as shown in Figure 4. The same trend was also observed for out-of-plane (200) lamellar packing peaks. Although the three polymer films were estimated to have similar lamellar packing distances, PTBI-2 has a much smaller lamellar packing fwhm than other two polymers. According to Scherrer's equation, fwhm is inversely proportional to the crystal coherence length.[32] Thus, a lower fwhm value usually implies larger crystalline domains. These observations are in a good agreement with AFM images, where PTBI-2 film appears to have a morphology with larger ordered domains.

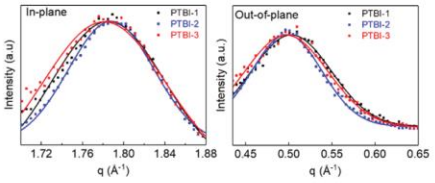

Figure 4. In-plane (010) and out-of-plane (200) peak line cuts of 2D diffraction patterns of PTBI-1 (black), PTBI-2 (blue), and PTBI-3 (red) and their fitted curves.

Charge Transport Measurements. To what extent side-chain sequence would impact charge transport properties is our primary interest of this study. Therefore, both field effect transistor measurements and space-charge-limited current (SCLC) method were employed to characterize charge mobilities of PTBI polymers. Details of the device fabrication are described in the Supporting Information. FET devices of all PTBI polymer thin films with bottom-gate bottom-contact (BGBC) architecture and Au contacts under ambient conditions displayed p-type characteristics. (Figure 5) Charge mobilities of all polymers were calculated based on more than 15 devices. The average mobilities of PTBI-2, PTBI-3, and

DOI: 10.1021/acs.macromol.8b01946
Macromolecules 2018, 51, 8486−8492

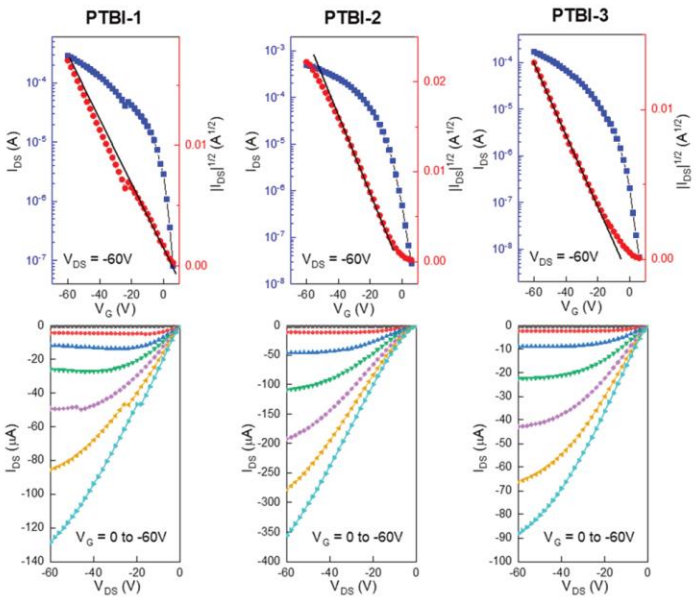

Figure 5. Representative transfer and output curves of PTBI-1, PTBI-2, and PTBI-3 thin film transistor devices.

PTBI-3 were estimated to be 0.40, 1.37, and 0.27 $cm^2 V^{-1} s^{-1}$, respectively, and their corresponding highest mobilities were 0.53, 2.22, and 0.43 $cm^2 V^{-1} s^{-1}$. The current on/off ratios for all FETs are around 10^4. The SCLC mobilities measured from hole-only diodes showed consistent trend with FET mobilities, where the mobilities of PTBI-2 (2.04×10^{-2} $cm^2 V^{-1} s^{-1}$) were highest, PTBI-1 (1.85×10^{-2} $cm^2 V^{-1} s^{-1}$) being the second highest, and PTBI-3 (4.67×10^{-3} $cm^2 V^{-1} s^{-1}$) being the lowest (Figure S7).

The highest performance of PTBI-2 can be attributed to its fibrillar morphology and largest crystalline domain, as observed from AFM and 2D-GIXRD measurements. Similarly, poor performance of PTBI-3 film may result from the smallest crystalline domain, reconfirming negative effects of regiorandom structures on polymer optoelectronic properties.[23,33,34] Intriguingly, although PTBI-1 is also a regioregular polymer like PTBI-2, noticeable differences were observed in solid state aggregation, morphology, crystalline domain size, and consequently device performance of the two polymers. A possible reason for such differences is the steric effect of side chains between repeating units, as supported by many reports.[21,35−38] Density functional theory calculations predicted a good planarity within the bis-TBI accepting moiety and twisted conformation between the donors and acceptors.[26] It is likely that the steric repulsion of side chains between bis-TBI and bithiophene (rather than inside the bis-TBI moiety) has a larger impact on the polymer chains. If the steric repulsion of side chains plays a role, the example of PTBI1- and PTBI-2 pairs provides a scenario implying that moving bulky solubilizing side chains inside the planar or rigid moiety could help improve charge transport properties. Considering most long rigid/fused conjugated building blocks have bulkier branched side chains at sides of moieties,[39−43] this side-chain regioisomerism strategy may serve as versatile tool to optimize the structure for enhanced charge transport purposes.

■ CONCLUSION

In summary, side-chain sequence enabled regioreisomeric acceptors for D−A type copolymers are first demonstrated. Starting with these bis-TBI monomers, three polymers PTBI-1, PTBI-2, and PTBI-3 were synthesized and fully characterized. The three polymers are similar in their frontier orbital energy levels but have distinct aggregation states in thin films. AFM and 2D-GIXRD measurements indicate that the PTBI-2 thin film shows smooth fibrillar morphology and the largest ordered domains. As a result, PTBI-2 FET devices achieved the highest hole mobility of 2.22 $cm^2 V^{-1} s^{-1}$, much higher than other two polymers with different side-chain sequences. We anticipate that the strategy of side-chain sequence regioisomerism could be applied in future design of building blocks for functional D−A type semiconducting polymers.

■ ASSOCIATED CONTENT

Supporting Information

The Supporting Information is available free of charge on the ACS Publications website at DOI: 10.1021/acs.macromol.8b01946.

Experimental details, figures and tables, and compound characterization data (PDF)

■ AUTHOR INFORMATION

Corresponding Author

*E-mail jgmei@purdue.edu (J.M.).

DOI: 10.1021/acs.macromol.8b01946
Macromolecules 2018, 51, 8486−8492

ORCID
Carr Hoi Yi Ho: 0000-0001-9004-2762
Franky So: 0000-0002-8310-677X
Jianguo Mei: 0000-0002-5743-2715

Notes
The authors declare no competing financial interest.

■ ACKNOWLEDGMENTS

The authors acknowledge the financial support from Purdue University and from the National Science Foundation (NSF CAREER Award, #1653909). We thank Ge Qu and Ying Diao for collecting the X-ray data. This research used resources of the Advanced Photon Source, a U.S. Department of Energy (DOE) Office of Science User Facility operated for the DOE Office of Science by Argonne National Laboratory under Contract DE-AC02-06CH11357.

■ REFERENCES

(1) Forrest, S. R. The Path to Ubiquitous and Low-Cost Organic Electronic Appliances on Plastic. *Nature* **2004**, *428* (6986), 911−918.
(2) Hammock, M. L.; Chortos, A.; Tee, B. C.-K.; Tok, J. B.-H.; Bao, Z. 25th Anniversary Article: The Evolution of Electronic Skin (E-Skin): A Brief History, Design Considerations, and Recent Progress. *Adv. Mater.* **2013**, *25* (42), 5997−6038.
(3) Sirringhaus, H. 25th Anniversary Article: Organic Field-Effect Transistors: The Path Beyond Amorphous Silicon. *Adv. Mater.* **2014**, *26* (9), 1319−1335.
(4) Fukuda, K.; Someya, T. Recent Progress in the Development of Printed Thin-Film Transistors and Circuits with High-Resolution Printing Technology. *Adv. Mater.* **2017**, *29* (25), 1602736.
(5) Würthner, F.; Stolte, M. Naphthalene and Perylene Diimides for Organic Transistors. *Chem. Commun.* **2011**, *47* (18), 5109.
(6) Wang, E.; Mammo, W.; Andersson, M. R. 25th Anniversary Article: Isoindigo-Based Polymers and Small Molecules for Bulk Heterojunction Solar Cells and Field Effect Transistors. *Adv. Mater.* **2014**, *26* (12), 1801−1826.
(7) Guo, X.; Facchetti, A.; Marks, T. J. Imide- and Amide-Functionalized Polymer Semiconductors. *Chem. Rev.* **2014**, *114* (18), 8943−9021.
(8) Yi, Z.; Wang, S.; Liu, Y. Design of High-Mobility Diketopyrrolopyrrole-Based π-Conjugated Copolymers for Organic Thin-Film Transistors. *Adv. Mater.* **2015**, *27* (24), 3589−3606.
(9) Quinn, J. T. E.; Zhu, J.; Li, X.; Wang, J.; Li, Y. Recent Progress in the Development of N-Type Organic Semiconductors for Organic Field Effect Transistors. *J. Mater. Chem. C* **2017**, *5* (34), 8654−8681.
(10) Mei, J.; Kim, D. H.; Ayzner, A. L.; Toney, M. F.; Bao, Z. Siloxane-Terminated Solubilizing Side Chains: Bringing Conjugated Polymer Backbones Closer and Boosting Hole Mobilities in Thin-Film Transistors. *J. Am. Chem. Soc.* **2011**, *133* (50), 20130−20133.
(11) Lei, T.; Dou, J.-H.; Pei, J. Influence of Alkyl Chain Branching Positions on the Hole Mobilities of Polymer Thin-Film Transistors. *Adv. Mater.* **2012**, *24* (48), 6457−6461.
(12) Lee, J.; Han, A.-R.; Kim, J.; Kim, Y.; Oh, J. H.; Yang, C. Solution-Processable Ambipolar Diketopyrrolopyrrole−Selenophene Polymer with Unprecedentedly High Hole and Electron Mobilities. *J. Am. Chem. Soc.* **2012**, *134* (51), 20713−20721.
(13) Dou, J.-H.; Zheng, Y.-Q.; Lei, T.; Zhang, S.-D.; Wang, Z.; Zhang, W.-B.; Wang, J.-Y.; Pei, J. Systematic Investigation of Side-Chain Branching Position Effect on Electron Carrier Mobility in Conjugated Polymers. *Adv. Funct. Mater.* **2014**, *24* (40), 6270−6278.
(14) Kang, B.; Kim, R.; Lee, S. B.; Kwon, S.-K.; Kim, Y.-H.; Cho, K. Side-Chain-Induced Rigid Backbone Organization of Polymer Semiconductors through Semifluoroalkyl Side Chains. *J. Am. Chem. Soc.* **2016**, *138* (11), 3679−3686.
(15) Yao, J.; Yu, C.; Liu, Z.; Luo, H.; Yang, Y.; Zhang, G.; Zhang, D. Significant Improvement of Semiconducting Performance of the Diketopyrrolopyrrole−Quaterthiophene Conjugated Polymer through Side-Chain Engineering via Hydrogen-Bonding. *J. Am. Chem. Soc.* **2016**, *138* (1), 173−185.
(16) Ocheje, M. U.; Charron, B. P.; Cheng, Y.-H.; Chuang, C.-H.; Soldera, A.; Chiu, Y.-C.; Rondeau-Gagné, S. Amide-Containing Alkyl Chains in Conjugated Polymers: Effect on Self-Assembly and Electronic Properties. *Macromolecules* **2018**, *51* (4), 1336−1344.
(17) Giovannitti, A.; Maria, I. P.; Hanifi, D.; Donahue, M. J.; Bryant, D.; Barth, K. J.; Makdah, B. E.; Savva, A.; Moia, D.; Zetek, M.; Barnes, P. R. F.; Reid, O. G.; Inal, S.; Rumbles, G.; Malliaras, G. G.; Nelson, J.; Rivnay, J.; McCulloch, I. The Role of the Side Chain on the Performance of N-Type Conjugated Polymers in Aqueous Electrolytes. *Chem. Mater.* **2018**, *30* (9), 2945−2953.
(18) Wen, H.-F.; Wu, H.-C.; Aimi, J.; Hung, C.-C.; Chiang, Y.-C.; Kuo, C.-C.; Chen, W.-C. Soft Poly(butyl Acrylate) Side Chains toward Intrinsically Stretchable Polymeric Semiconductors for Field-Effect Transistor Applications. *Macromolecules* **2017**, *50* (13), 4982−4992.
(19) Yang, S.-F.; Liu, Z.-T.; Cai, Z.-X.; Dyson, M. J.; Stingelin, N.; Chen, W.; Ju, H.-J.; Zhang, G.-X.; Zhang, D.-Q. Diketopyrrolopyrrole-Based Conjugated Polymer Entailing Triethylene Glycols as Side Chains with High Thin-Film Charge Mobility without Post-Treatments. *Adv. Sci.* **2017**, *4* (8), 1700048.
(20) Ma, J.; Liu, Z.; Wang, Z.; Yang, Y.; Zhang, G.; Zhang, X.; Zhang, D. Charge Mobility Enhancement for Diketopyrrolopyrrole-Based Conjugated Polymers by Partial Replacement of Branching Alkyl Chains with Linear Ones. *Mater. Chem. Front.* **2017**, *1* (12), 2547−2553.
(21) Wang, Z.; Liu, Z.; Ning, L.; Xiao, M.; Yi, Y.; Cai, Z.; Sadhanala, A.; Zhang, G.; Chen, W.; Sirringhaus, H.; Zhang, D. Charge Mobility Enhancement for Conjugated DPP-Selenophene Polymer by Simply Replacing One Bulky Branching Alkyl Chain with Linear One at Each DPP Unit. *Chem. Mater.* **2018**, *30* (9), 3090−3100.
(22) Xue, G.; Zhao, X.; Qu, G.; Xu, T.; Gumyusenge, A.; Zhang, Z.; Zhao, Y.; Diao, Y.; Li, H.; Mei, J. Symmetry Breaking in Side Chains Leading to Mixed Orientations and Improved Charge Transport in Isoindigo- Alt -Bithiophene Based Polymer Thin Films. *ACS Appl. Mater. Interfaces* **2017**, *9* (30), 25426−25433.
(23) Ying, L.; Huang, F.; Bazan, G. C. Regioregular Narrow-Bandgap-Conjugated Polymers for Plastic Electronics. *Nat. Commun.* **2017**, *8*, 14047.
(24) Quinn, J. T. E.; Guo, C.; Haider, F.; Patel, H.; Khan, D. A.; Li, Y. Regioisomerism of an Alkyl-Substituted Bithiophene Comonomer in (3E,8E)-3,8-bis(2-Oxoindolin-3-Ylidene)naphtho-[1,2-b:5,6-B′]-difuran-2,7(3H,8H)-Dione (INDF)-Based D−A Polymers for Organic Thin Film Transistors. *J. Mater. Chem. C* **2017**, *5* (24), 5902−5909.
(25) Wang, X.; Choi, H. H.; Zhang, G.; Ding, Y.; Lu, H.; Cho, K.; Qiu, L. Bis(2-Oxoindolin-3-Ylidene)-Benzodifuran-Dione and Bithiophene-Based Conjugated Polymers for High Performance Ambipolar Organic Thin-Film Transistors: The Impact of Substitution Positions on Bithiophene Units. *J. Mater. Chem. C* **2016**, *4* (26), 6391−6400.
(26) Luo, X.; Tran, D. T.; Sun, H.; Mi, T.; Kadlubowski, N. M.; Zhao, Y.; Zhao, K.; Mei, J. Bis-Isoindigos: New Electron-Deficient Building Blocks for Constructing Conjugated Polymers with Extended Electron Delocalization. *Asian J. Org. Chem.* **2018**, DOI: 10.1002/ajoc.201800360.
(27) Cho, H. J.; Kang, S.-J.; Lee, S. M.; Jeong, M.; Kim, G.; Noh, Y.-Y.; Yang, C. Influence of Simultaneous Tuning of Molecular Weights and Alkyl Substituents of Poly(thienoisoindigo- Alt -Naphthalene)s on Morphology and Change Transport Properties. *ACS Appl. Mater. Interfaces* **2017**, *9* (36), 30755−30763.
(28) Wang, X.-Y.; Zhang, M.-W.; Zhuang, F.-D.; Wang, J.-Y.; Pei, J. Lactone-Fused Electron-Deficient Building Blocks for N-Type Polymer Field-Effect Transistors: Synthesis, Properties, and Impact of Alkyl Substitution Positions. *Polym. Chem.* **2016**, *7* (12), 2264−2271.
(29) Kasha, M. Energy Transfer Mechanisms and the Molecular Exciton Model for Molecular Aggregates. *Radiat. Res.* **1963**, *20* (1), 55.

DOI: 10.1021/acs.macromol.8b01946
Macromolecules 2018, 51, 8486−8492

(30) Más-Montoya, M.; Janssen, R. A. J. The Effect of H- and J-Aggregation on the Photophysical and Photovoltaic Properties of Small Thiophene-Pyridine-DPP Molecules for Bulk-Heterojunction Solar Cells. *Adv. Funct. Mater.* **2017**, *27* (16), 1605779.
(31) Park, S.; Lee, M. H.; Ahn, K. S.; Choi, H. H.; Shin, J.; Xu, J.; Mei, J.; Cho, K.; Bao, Z.; Lee, D. R.; Kang, M. S.; Kim, D. H. Combinatorial Study of Temperature-Dependent Nanostructure and Electrical Conduction of Polymer Semiconductors: Even Bimodal Orientation Can Enhance 3D Charge Transport. *Adv. Funct. Mater.* **2016**, *26* (26), 4627−4634.
(32) Rivnay, J.; Mannsfeld, S. C. B.; Miller, C. E.; Salleo, A.; Toney, M. F. Quantitative Determination of Organic Semiconductor Microstructure from the Molecular to Device Scale. *Chem. Rev.* **2012**, *112* (10), 5488−5519.
(33) Ying, L.; Hsu, B. B. Y.; Zhan, H.; Welch, G. C.; Zalar, P.; Perez, L. A.; Kramer, E. J.; Nguyen, T.-Q.; Heeger, A. J.; Wong, W.-Y.; Bazan, G. C. Regioregular Pyridal[2,1,3]thiadiazole π-Conjugated Copolymers. *J. Am. Chem. Soc.* **2011**, *133* (46), 18538−18541.
(34) Wang, M.; Wang, H.; Yokoyama, T.; Liu, X.; Huang, Y.; Zhang, Y.; Nguyen, T.-Q.; Aramaki, S.; Bazan, G. C. High Open Circuit Voltage in Regioregular Narrow Band Gap Polymer Solar Cells. *J. Am. Chem. Soc.* **2014**, *136* (36), 12576−12579.
(35) Durban, M. M.; Kazarinoff, P. D.; Luscombe, C. K. Synthesis and Characterization of Thiophene-Containing Naphthalene Diimide N-Type Copolymers for OFET Applications. *Macromolecules* **2010**, *43* (15), 6348−6352.
(36) Yi, Z.; Sun, X.; Zhao, Y.; Guo, Y.; Chen, X.; Qin, J.; Yu, G.; Liu, Y. Diketopyrrolopyrrole-Based π-Conjugated Copolymer Containing β-Unsubstituted Quintetthiophene Unit: A Promising Material Exhibiting High Hole-Mobility for Organic Thin-Film Transistors. *Chem. Mater.* **2012**, *24* (22), 4350−4356.
(37) Chen, M. S.; Lee, O. P.; Niskala, J. R.; Yiu, A. T.; Tassone, C. J.; Schmidt, K.; Beaujuge, P. M.; Onishi, S. S.; Toney, M. F.; Zettl, A.; Fréchet, J. M. J. Enhanced Solid-State Order and Field-Effect Hole Mobility through Control of Nanoscale Polymer Aggregation. *J. Am. Chem. Soc.* **2013**, *135* (51), 19229−19236.
(38) Grand, C.; Zajaczkowski, W.; Deb, N.; Lo, C. K.; Hernandez, J. L.; Bucknall, D. G.; Müllen, K.; Pisula, W.; Reynolds, J. R. Morphology Control in Films of Isoindigo Polymers by Side-Chain and Molecular Weight Effects. *ACS Appl. Mater. Interfaces* **2017**, *9* (15), 13357−13368.
(39) Lei, T.; Dou, J.-H.; Cao, X.-Y.; Wang, J.-Y.; Pei, J. Electron-Deficient Poly(P -Phenylene Vinylene) Provides Electron Mobility over 1 Cm 2 V − 1 S − 1 under Ambient Conditions. *J. Am. Chem. Soc.* **2013**, *135* (33), 12168−12171.
(40) Cao, Y.; Yuan, J.-S.; Zhou, X.; Wang, X.-Y.; Zhuang, F.-D.; Wang, J.-Y.; Pei, J. N-Fused BDOPV: A Tetralactam Derivative as a Building Block for Polymer Field-Effect Transistors. *Chem. Commun.* **2015**, *51* (52), 10514−10516.
(41) Dai, Y.-Z.; Ai, N.; Lu, Y.; Zheng, Y.-Q.; Dou, J.-H.; Shi, K.; Lei, T.; Wang, J.-Y.; Pei, J. Embedding Electron-Deficient Nitrogen Atoms in Polymer Backbone towards High Performance N-Type Polymer Field-Effect Transistors. *Chem. Sci.* **2016**, *7* (9), 5753−5757.
(42) James, D. I.; Wang, S.; Ma, W.; Hedström, S.; Meng, X.; Persson, P.; Fabiano, S.; Crispin, X.; Andersson, M. R.; Berggren, M.; Wang, E. High-Performance Hole Transport and Quasi-Balanced Ambipolar OFETs Based on D-A-A Thieno-Benzo-Isoindigo Polymers. *Adv. Electron. Mater.* **2016**, *2* (4), 1500313.
(43) Randell, N. M.; Radford, C. L.; Yang, J.; Quinn, J.; Hou, D.; Li, Y.; Kelly, T. L. Effect of Acceptor Unit Length and Planarity on the Optoelectronic Properties of Isoindigo−Thiophene Donor−Acceptor Polymers. *Chem. Mater.* **2018**, *30* (14), 4864−4873.

DOI: 10.1021/acs.macromol.8b01946
Macromolecules 2018, 51, 8486−8492

10.1002/ajoc.201800360

WILEY-VCH

FULL PAPER

Bis-isoindigos: New Electron-Deficient Building Blocks for Constructing Conjugated Polymers with Extended Electron Delocalization

Xuyi Luo[a], Dung T. Tran[a], Hong Sun[b], Tianxiong Mi[c], Natalie M. Kadlubowski[a], Yan Zhao[a], Kejie Zhao[b], Jianguo Mei*[a]

[a] Xuyi Luo, Dung T. Tran, Natalie M. Kadlubowski, Dr. Yan Zhao, Dr. Jianguo Mei
Department of Chemistry
Purdue University
560 Oval Drive, West Lafayette Indiana 47907, United States
E-mail: jgmei@purdue.edu
[b] Hong Sun, Dr. Kejie Zhao
School of Mechanical Engineering
560 Oval Drive, West Lafayette Indiana 47907, United States
[c] Tianxiong Mi
College of Chemistry and Molecular Engineering
Peking University, Beijing, China

Supporting information for this article is given via a link at the end of the document.

Abstract: Incorporation of acceptor-acceptor (A-A) type moieties into donor-acceptor (D-A) type conjugated polymers becomes a new strategy to tune their electronic properties. In this work, we first demonstrate an efficient convergent route to prepare isoindigo-based A-A type building blocks - bis-isoindigos - via the palladium-catalyzed oxidative coupling. Bis-isoindigo-based polymers show high planarity and delocalized frontier molecular orbitals with lowered LUMO and intact HOMO energy levels, in comparison with their corresponding mono-isoindigo counterparts. Moreover, fluorine substitution on donors only lowers HOMO levels of Bis-IID polymers. This study asserts that the D-A-A strategy is effective in selectively tuning FMO energy levels of conjugated polymers, complementary to the D-D-A approach for the HOMO energy level tuning.

Introduction

Conjugated polymers have attracted a wide range of attention as functional organic materials for solar cells, light emitting diodes and field-effect transistors, among others. A myriad of conjugated polymers have been made by introducing the combination of electron-rich aromatic donors (D) and electron-deficient aromatic acceptors (A). It is widely practiced that two or more donors (D-D) are chosen to tune the optoelectronic properties such as the HOMO levels and absorption profiles of D-A polymers.[1–3] In contrast, the incorporation of a conjugated building block containing two electron-accepting subunits (A-A) is comparatively less adopted. A limited number of reports on A-A building blocks have only appeared in recent years, as summarized in Scheme 1. Berrouard *et al.* first obtained a thieno[3,4-c]pyrrole-4,6-dione (TPD) dimer by Ullmann reaction in 2011.[4] Bis-TPD copolymers were subsequently reported with efficient ambipolar charge transport properties.[5,6] Polander *et al.* synthesized a naphthalene diimides (NDI) dimer via Stille coupling, which showed a higher electron mobility than its monomeric parent.[7] Yang *et al.* reported a bis-diketopyrrolopyrrole (bis-DPP) moiety as an electron acceptor.[8] It is noted that Stille coupling with large excess of DPP dibromide was adopted in the synthetic approach. Several bis-DPP copolymers have shown excellent ambipolar mobilities.[9] James *et al.* reported a di-thieno-benzo-isoindigo (BdiTBI) based building block, connecting two thieno-benzo-isoindigo moieties at two phenyl groups by Suzuki coupling.[10] More recently, a bis-Pyridalthiadiazole based building block was reported by Zhu *et al.*. A regioregular dual-acceptor strategy rendered the polymer with an outstanding charge transport behavior.[11]

Scheme 1. Examples of acceptor-acceptor building blocks

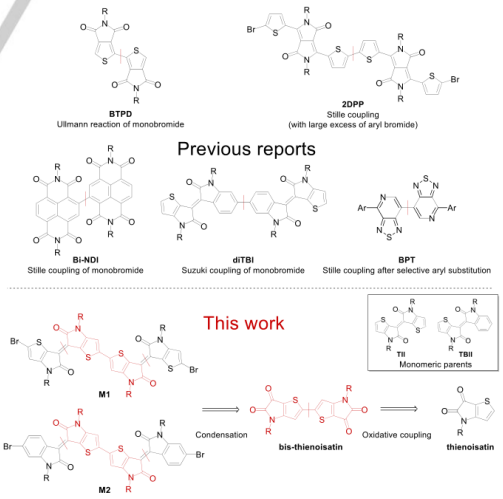

We envision the D-A-A design as an alternative strategy to adjust the optoelectronic properties with an advantage of effective HOMO/LUMO level tuning and render desired optoelectronic properties, when A-A building blocks become readily available.

10.1002/ajoc.201800360

Unfortunately, we noticed that the synthesis of A-A building blocks listed above is undoubtedly challenging. For the coupling involving homocoupling of acceptor dihalides, it usually leads to low yields due to the presence of undesired oligomerization. It also makes the purification difficult. For the homocoupling involving acceptor monohalides, the mono-functionalization of an electron deficient building block itself is very inefficient and challenging (Scheme S1). To make the A-A strategy more appealing in synthesis of D-A conjugated polymers, it is imperative to design new synthetic routes to readily access functionalized A-A building blocks.

Here, we report two new isoindigo based A-A moieties (Bis-IIDs) **M1** and **M2** through an efficient synthetic route. Isoindigo (IID), first introduced by Reynolds *et al.*, was among the most studied building blocks.[12] Owing to its electron withdrawing lactam groups, rigid backbone, and straightforward synthesis, IID widely serves as an electron acceptor in D-A conjugated polymers.[13] Extensive design efforts including side chain engineering,[14,15] heteroatom fusion,[16–18] and conjugation length extension,[19–22] have been made to tune their optoelectronic properties and morphologies. In this report, **M1** and **M2** have two IID subunits linked through α positions of the corresponding thiophenes. We envision that such linkage would enable small thiophene-thiophene dihedral angles, ensuring the retention of planarity throughout the moiety.[23] This feature would further render planarized D-A-A type polymers with extended effective conjugation lengths and enhanced interchain interactions, which can be beneficial to charge transport. Moreover, we choose two different donors to study energy levels of their corresponding polymers (**P1**, **P1F**, **P2** and **P2F**, Scheme 2). In particular, we expect to obtain fine-tuned FMO levels. **P1** and **P2** should exhibit considerably lowered LUMO levels but only slightly altered HOMO levels compared to their monomeric based analogues, while **P1F** and **P2F** have further tuning on FMO levels due to fluorine substitution.[24]

Results and Discussion

The synthesis for all Bis-IIDs was proposed and carried out in this work, as illustrated in Scheme 2. We initially intended to prepare bis-thienoisatin **2** through cross-coupling of thienoisatin halide and its boronic ester.[9] Unfortunately, all attempts to turn thienoisatin **1** into its halide failed. Inspired by an oxidative coupling of thiophene derivatives, we decided to test oxidative coupling of **1** directly. To our delight, **2** was successfully synthesized from **1** in a single step, in spite of a low yield of 23%. After the optimization of reaction conditions, we were able to improve the yield up to 54% with palladium acetate as the catalyst and silver fluoride as the oxidant (Table S1).[25] After the aldol condensation with compound **3** and **4**, **M1a** and **M2** were obtained with high yields of 88% and 89%, respectively. Bromination of **M1a** gave **M1** in a good yield of 87%. Finally, the polymers **P1**, **P2**, **P1F** and **P2F** were synthesized via Stille coupling of **M1**/**M2** with compound **5**/**6**. For a comparison, monomeric TII- and TBII-based analogues, **P1-ref** and **P2-ref**, were also synthesized following the reported procedures (Scheme S2).[26] All polymers were purified by the Soxhlet extraction and fully characterized (see the supporting information). The molecular weights of **P2** and **P2F** was evaluated by high-temperature gel permeation chromatography at 150 °C using 1,2,4-trichlorobenzene as eluent. It's worth noting that the molecular weights for **P1** and **P1F** cannot be accessed from the GPC measurements. Similar observations with TII substructures were previously reported, where thienoisoindigo polymers are believed to interact strongly with the column material.[23,27]

Scheme 2. Synthetic scheme to Bis-IID polymers

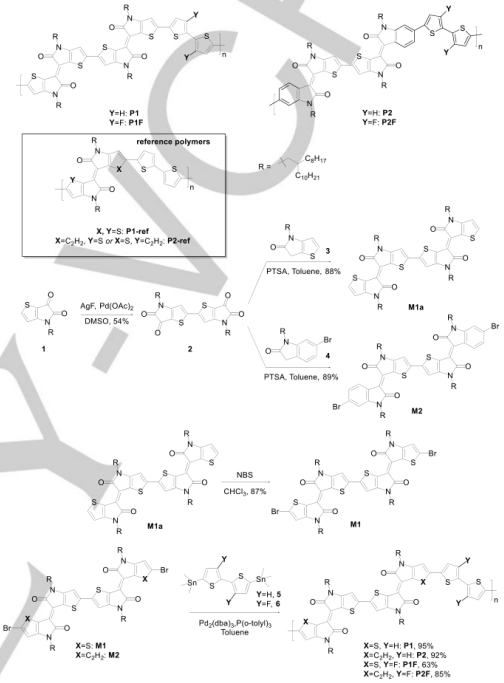

To estimate the geometries and intrinsic electronic properties of Bis-IID polymers, density functional theory (DFT) calculations were performed on the trimers of Bis-IID polymers with methyl side chains as model molecules, shown in Figure 1. Computation was performed with Gaussian 09 using a hybrid B3LYP correlation functional and 6-31G(d) basis set. **P1** and **P1F** display almost perfectly planar backbones with negligible dihedral angles between all thiophene-thiophene planes. By contrast, backbones of **P2** and **P2F** are more twisted due to a 21° dihedral angle between thienyl and phenyl groups. Despite this, both A-A moieties (bis-IID subunits) still retain high planarity (2.9° and 0.9° dihedral angle between thiophene-thiophene planes respectively). The FMO electron distribution diagrams (Figure S1) reveal well dispersed frontier orbital electrons of all Bis-IID polymers, indicative of an effective delocalization along all polymer backbones. Fluorine substitutions on bithiophene have two major influences on the Bis-IID polymers. First, bithiophene subunits of **P2F** (1.2°) are much planer than those of **P2** (13.4°), indicating F-S noncovalent interactions. Also, fluorine p_z orbitals contribute to HOMOs of **P1F** or **P2F**. Interestingly, fluorine p_z orbitals barely participate in LUMOs, showing that fluorine substitutions could have larger impact on HOMOs of Bis-IID polymers. Such prediction is verified in electrochemical estimations.

10.1002/ajoc.201800360

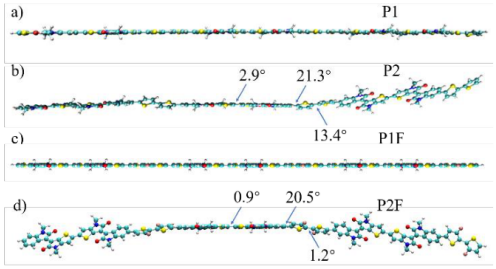

Figure 1. DFT optimized geometries of a) **P1**, b) **P2**, c) **P1F** and d) **P2F** trimer fragments (B3LYP/6-311g(d) level). Dihedral angles around single bonds are shown on **P2** and **P2F** backbones.

The photophysical properties of the polymers were studied with solution and solid-state UV-Vis-NIR spectroscopy. As shown in Figure 2 and S2, all polymers exhibit high energy π-π^* transition bands and low energy charge transfer bands. All Bis-IID polymer films have most of charge transfer bands at NIR region. They show much higher absorption onsets than **P1-ref** and **P2-ref**. This observation agrees with our initial design of extended conjugation lengths. In addition, **P1**/**P1F** have much smaller band gaps than **P2**/**P2F**, which is attributed to their backbones with high planarity and quinoidal character.[23,28]

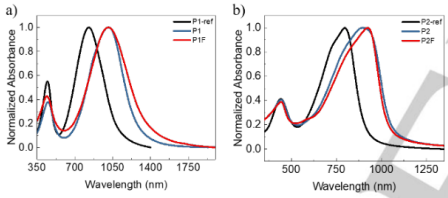

Figure 2. Normalized absorption spectra of a) **P1-ref** (black), **P1** (blue) and **P1F** (red) films; b) Normalized absorption spectra of a) **P2-ref** (black), **P2** (blue) and **P2F** (red) films.

The absorption profiles also reveal the different aggregation behaviors. While TII derivatives **P1-ref** and the TII monomer **M1** show hypsochromic shifts in solid states, this phenomenon was not observed in TII derivative **P1** and **P1F**. In fact, the solution and solid-state absorption profiles of Bis-IID polymers nearly overlap. This phenomenon strongly indicates a strong pre-aggregation in their solutions. To further understand the aggregation behavior of Bis-IIDs in solutions, temperature-dependent absorption spectra were taken at increasing temperature intervals of 10 °C in *o*-dichlorobenzene (Figure S3). Upon heating, **P2** and **P2F**'s intramolecular charge transfer peaks increase while the aggregation peaks noticeably decrease. By contrast, **P1** and **P1F** only show a trend of peak intensity change, indicative of strong aggregation in *o*-dichlorobenzene even at 100 °C. The stronger aggregation behavior of **P1** and **P1F** reflects their strong interchain interaction induced by high planarity.[29,30]

To study the redox properties of polymer thin films, cyclic voltammetry (CV) and differential pulse voltammetry (DPV) were employed. Cyclic voltammograms of all Bis-IID polymers show quasi-reversible redox behavior, suggesting their potential as ambipolar semiconducting polymers (Figure 3). CV redox onsets are widely used to estimate HOMO/LUMO levels of semiconducting materials. However, like many IID based polymers, the optical band gaps of Bis-IID polymers are much narrower than those estimated from CV. This observation is partially attributed to the sensitivity limitation of the CV measurement, resulting from its high capacitive charging currents background. With a reduced contribution from capacitive charging currents, differential pulse voltammetry (DPV) provides a much higher sensitivity than normal voltammetry measurements. It allows to record a sharper and clearer redox onset.[31] Thus, HOMO/LUMO energy levels of Bis-IID polymers were estimated from redox onset potentials of DPV (Figure 3). As references, **P1-ref** and **P2-ref** films were also characterized (Figure S4). The corresponding data were summarized in Table 1. Compared with D-A type **P1-ref**, D-A-A type **P1** shows a drop of 0.12 eV in LUMO level, while the HOMO level is almost unchanged. In further comparison between **P1** and **P1F**, **P1F** has a lowered HOMO level without changing the LUMO level. The trends are similar for the **P2-ref**, **P2** and **P2F** group. A 0.09 eV drop in LUMO and only a marginally deepened HOMO were observed from **P2-ref** to **P2**. Introduction of fluorine in **P2F** rendered a selective deepened HOMO level by 0.15 eV. The energy levels estimated by CV measurements also agree with DPV trends. The comparison between D-A polymers and D-A-A polymers clearly shows the potential of D-A-A strategy in selective tuning of the LUMO/HOMO energy lying, which makes it an attractive method to render ambipolar semiconducting materials and functional optoelectronic materials.

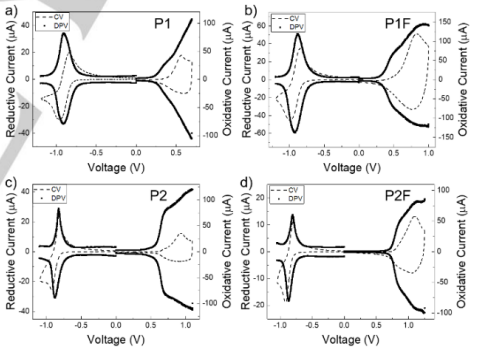

Figure 3. Cyclic Voltammograms (dashed lines) and differential pulse voltammograms (solid dots) of a) **P1**, b) **P1F**, c) **P2** and d) **P2F** films in acetonitrile with 0.2 M *n*-Bu_4NPF_6 as supporting electrolyte. (scan rate: 40 mV s^{-1})

Charge carrier transport properties of Bis-IID polymers were characterized by field-effect transistor measurements. Details of the device fabrication are described in the Experimental Section. Devices with bottom-gate bottom-contact (BGBC) architecture and Au as contacts under ambient conditions only shows p- type performance. Devices based on **P2** and **P2F** films showed a typical p- type performance with highest μ_h of 0.024 cm^2 V^{-1} s^{-1} and 0.030 cm^2 V^{-1} s^{-1}, respectively (Figure S7). Distinguished from **P2** and **P2F**, both **P1** and **P1F** devices exhibited an abnormally high "threshold" voltage and a small on-off ratio of 10^1.

The high V_{th} and high off current imply a doping process by oxygen, given that materials with HOMO energy level above 5.0 eV are likely to make OFET devices unstable in air (Figure S7 and S8).[32,33] Therefore, **P2** and **P2F** were devices were tested under vacuum. These devices show normal p- type output and transfer characteristics, with highest μ_h of 0.017 $cm^2 V^{-1} s^{-1}$ and 0.013 $cm^2 V^{-1} s^{-1}$ respectively, and a moderate on-off ratio of 10^2 (Figure S9). Such result is also a corroboration of the doping behavior in its all-acceptor analogue, TII homo polymer, which has an even higher HOMO lying of 4.83 eV.[23] All Bis-IID devices with bottom-gate top-contact (BGTC) architecture and Al as contacts exhibit ambipolar characters with μ_e around 10^{-4} to 10^{-3} $cm^2 V^{-1} s^{-1}$ and μ_h around 10^{-3} to 10^{-2} $cm^2 V^{-1} s^{-1}$ (Figure S10 and S11), showing n- type potential properties of A-A type Bis-IID building blocks.

Table 1. Energy levels of polymer thin films and their highest OFET performance

Polymer	Differential Pulse Voltammetry[a]			Cyclic Voltammetry[a]			OFET performance	
	LUMO/eV	HOMO/eV	E_{gap}/eV	LUMO/eV	HOMO/eV	E_{gap}/eV	μ_e/$cm^2 V^{-1} s^{-1}$	μ_h/$cm^2 V^{-1} s^{-1}$
P1-ref	-3.83	-4.99	1.16	-3.80	-5.16	1.36	N/A	0.43[b]
P1	-3.95	-4.96	1.01	-3.89	-5.13	1.24	0.00046[c]	0.017[d]
P1F	-3.98	-5.05	1.07	-3.90	-5.28	1.38	0.00022[c]	0.013[d]
P2-ref	-3.88	-5.29	1.41	-3.85	-5.46	1.61	N/A	0.088[b]
P2	-3.97	-5.30	1.33	-3.90	-5.45	1.55	0.0022[c]	0.024[d]
P2F	-3.98	-5.45	1.47	-3.91	-5.54	1.63	0.0017[c]	0.030[d]

[a] The HOMO and LUMO energy levels are estimated from HOMO = − (5.10 + E_{ox} – $E_{Fc/Fc+}$) and LUMO = − (5.10 + E_{red} – $E_{Fc/Fc+}$), where E_{ox} and E_{red} are onset potentials. [b] Data adopted from ref 24. All mobilities shown in table 1 are highest values. [c] Results obtained from BGTC architecture, Al contacts. [d] Results obtained from BGBC architecture, Au contacts.

Conclusions

In summary, we developed a new synthetic approach to obtain two isoinidgo-based acceptor-acceptor type building blocks **M1** and **M2.** With thiophene-thiophene connection along the building block, the corresponding D-A-A polymers **P1**, **P2**, **P1F** and **P2F** show high planarity and extended conjugation length, which thus lead to strong interchain interaction. Compared with their D-A analogues, D-A-A polymers have noticeably lowered LUMO, but relatively unchanged HOMO. Further introduction of fluorine atoms into Bis-IID polymers only lowers their HOMO levels. This discovery asserts that our D-A-A design can tune FMO energy levels selectively. All Bis-IID polymers exhibit ambipolar charge transport properties. We expect the D-A-A approach will play a significant role in developing ambipolar materials. We also anticipate that our key intermediate bis-thienoisatin **2** could serve as a moiety to build up novel functional conjugated polymers for organic electronics.

Experimental Section

All reagents purchased from suppliers were used without further purification. ^{1}H- and ^{13}C-NMR spectra were recorded using Varian Inova 300 in deuterated chloroform at 293 K. GPC was performed by high-temperature gel permeation chromatography at 150 °C using 1,2,4-trichlorobenzene (TCB) as eluent. Differential scanning calorimetry (DSC) measurements were acquired using a TA Q1000 calorimeter at a heating rate of 10 °C min^{-1} with nitrogen as purge gas. UV-vis-NIR spectra were measured with an Agilent Technologies Cary 6000i UV-Vis-NIR spectrophotometer (350-1800 nm). All the electrochemistry related experiments (CV, DPV) were performed using BioLogic SP-150. platinum electrode was used as a working electrode and a platinum wire as a counter electrode, and all potentials were recorded versus Ag/AgCl (saturated) as a reference electrode (scan rate: 40 mV s^{-1}). FET device characterization was carried out using Keithley 4200.

Device fabrication and characterization

Top-contact/Bottom-gate OTFT devices: The SiO_2/Si substrates were cleaned by piranha solution (H_2SO_4 98%: H_2O_2 30% = 2:1) at 85 °C for 20 mins. They were then washed with DI water, Ethanol and acetone for 6 mins each. After drying inside oven, the substrates were put in a clean petri dish with a small drop of OTS. The dish was annealed in a vacuum oven at 120 °C for at least 3h resulting in the formation of an OTS self-assembled monolayer on the surface. The OTS modified substrates were rinsed with hexane, ethanol and chloroform to remove physically-adsorbed OTS molecules before used. All polymers were dissolved in Chloroform and spin coated on the substrate at 2000 RPM inside a glove box. All the films were annealed inside the glovebox at 120 °C. To deposit Al electrode, A 40 nm layer of Al was thermally evaporated on top of the semiconductor film through a shadow mask. The channel length was 80 µm and the channel width was 4800 µm. All the devices were characterized by using Keithley 2400 in vacuum of 10^{-4} mbar.

Bottom-contact/Bottom-gate OTFT devices: The substrates have SiO_2 as dielectric layer and gold electrode were pre-patterned by photolithography. They were cleaned by piranha solution and OTS modified as the procedure above. All polymers were dissolved in Chloroform and spin coated on the substrate at 2000 RPM in air. All the films were annealed inside the glovebox at 120 °C. The channel width was 1000 µm and the channel length was ranging from 10 µm to 100 µm.

Synthetic procedures

Compound 2: 4-(2-octyldodecyl)-4H-thieno[3,2-b]pyrrole-5,6-dione (1.17 g, 2.70 mmol) (**1**), Silver Fluoride (0.719 g, 5.67 mmol) and Palladium(II) acetate (60.6 mg, 0.270 mmol) were added to 30 mL of DMSO. The mixture was stirred under N_2 at 90 °C for 24 h before being allowed to cool to room temperature. The reaction was poured into water, extracted with dichloromethane and dried over Na_2SO_4. After removal of the solvent

under reduced pressure, the residue was purified by silica chromatography (hexanes:CH_2Cl_2=1:3) to give the product (**2**) as a dark purple solid (627 mg, 54%). About 15% of the starting material was also recovered. ^{1}H NMR (300 MHz, $CDCl_3$, ppm) δ: 6.93 (s, 2H), 3.57 (d, J = 7.3 Hz, 4H), 1.80 (m, 2H), 1.32-1.25 (m, 64H), 0.87 (t, J = 6.6 Hz, 12H). ^{13}C NMR (75 MHz, $CDCl_3$, ppm) δ: 172.17, 164.69, 160.57, 151.59, 111.49, 110.88, 46.69, 37.08, 31.96, 31.37, 30.04, 29.72, 29.64, 29.43, 29.39, 26.37, 22.78, 14.24. HRMS (APCI) calcd. for $C_{52}H_{85}N_2O_4S_2$ ([M+H]$^+$): 865.5945; found 865.5939.

Compound 4: 6-bromo-1-(2-octyldodecyl)indoline-2,3-dione (**4a**) (2.0 g, 3.9 mmol) and hydrazine monohydrate (10 mL) were added to 10 mL of DMSO. The mixture was stirred under N_2 at 130 °C for 24 h before being allowed to cool to room temperature. The reaction was poured into water, extracted with dichloromethane and dried over Na_2SO_4. After removal of the solvent under reduced pressure, the residue was purified by silica chromatography (hexanes:CH_2Cl_2=3:2) to give the product (**4**) as a light-yellow oil (1.28 g, 66%). ^{1}H NMR (300 MHz, $CDCl_3$, ppm) δ: 7.16 – 7.06 (m, 2H), 6.91 (d, *J* = 1.6 Hz, 1H), 3.54 (d, *J* = 7.5 Hz, 2H), 3.45 (s, 2H), 1.92 – 1.73 (m, 1H), 1.29 – 1.24 (m, 32H), 0.87 (t, *J* = 6.6 Hz, 6H). ^{13}C NMR (75 MHz, $CDCl_3$, ppm) δ: 174.83, 146.30, 125.46, 124.69, 123.28, 121.19, 111.88, 44.66, 35.94, 35.40, 32.00, 31.55, 30.09, 29.74, 29.69, 29.64, 29.45, 29.40, 26.46, 22.80, 14.27. HRMS (ESI) calcd. for $C_{18}H_{46}BrNONa$ ([M+Na]$^+$): 514.2661; found 514.2657.

Compound M1a: *p*-Toluenesulfonic acid monohydrate (9.0 mg 0.052 mmol) was added to a solution of bis-tisatin **2** (150 mg, 0.173 mmol) and 4-(2-octyldodecyl)-4,6-dihydro-5H-thieno[3,2-b]pyrrol-5-one (**3**) (291 mg, 0.693 mmol) in Toluene (15 mL). The mixture was stirred under N_2 at 110 °C for 12 h before being allowed to cool to room temperature. After removal of the solvent under reduced pressure, the residue was purified by silica chromatography (hexanes:CH_2Cl_2=3:2) to give the product (**M1a**) as a dark green solid (256 mg, 88%). ^{1}H NMR (300 MHz, $CDCl_3$, ppm) δ: 7.37 (d, *J* = 5.1 Hz, 2H), 6.94 (s, 2H), 6.65 (d, *J* = 5.2 Hz, 2H), 3.67 (t, *J* = 6.8 Hz, 8H), 1.96-1.85 (m, 4H), 1.31-1.22 (m, 128H), 0.84 (t, *J* = 3.2 Hz, 24H). ^{13}C NMR (75 MHz, $CDCl_3$, ppm) δ: 170.93, 170.50, 151.88, 151.05, 145.31, 134.08, 119.74, 119.57, 115.49, 114.81, 111.12, 107.36, 46.60, 46.32, 37.25, 37.03, 31.99, 31.61, 31.31, 30.26, 30.10, 29.74, 29.45, 26.65, 26.38, 22.79, 14.23. HRMS (MALDI) calcd. for $C_{104}H_{170}N_4O_4S_4$ ([M+H]$^+$): 1668.5439; found 1668.5463.

Compound M1: To a solution of **M1a** (232 mg, 0.139 mmol) in Chloroform (10 mL) at 0 °C, a solution of *N*-Bromosuccinimide (54.4 mg 0.305 mmol) in Chloroform (10 mL) was added dropwise in 5 min. The mixture was stirred at 0 °C for another 30 min. The reaction was quenched by addition of saturated aqueous solution of $Na_2S_2O_3$. The organic phase was extracted with dichloromethane and dried over Na_2SO_4. After removal of the solvent under reduced pressure, the residue was purified by silica chromatography (hexanes:CH_2Cl_2=1:1) to give the product (**M1**) as a dark green solid (221 mg, 87%). ^{1}H NMR (300 MHz, $CDCl_3$, ppm) δ: 6.88 (s, 2H), 6.67 (s, 2H), 3.68 (m, 8H), 1.98 (s, 2H), 1.81 (s, 2H), 1.40 – 1.21 (m, 128H), 0.87 – 0.81 (m, 24H). ^{13}C NMR (75 MHz, $CDCl_3$, ppm) δ: 170.48, 169.74, 152.16, 149.50, 145.64, 122.66, 119.02, 118.24, 116.03, 115.13, 114.69, 107.20, 46.96, 46.45, 37.29, 37.15, 32.01, 31.63, 31.35, 30.34, 30.14, 29.84, 29.76, 29.69, 29.48, 26.71, 26.51, 22.80, 14.24. HRMS (MALDI) calcd. for $C_{104}H_{168}Br_2N_4O_4S_4$ ([M+H]$^+$): 1827.2345; found 1827.2419.

Compound M2: *p*-Toluenesulfonic acid monohydrate (16.5 mg, 0.087 mmol) was added to a solution of bis-tisatin **2** (150 mg, 0.173 mmol) and 6-bromo-1-(2-octyldodecyl)indolin-2-one (**4**) (172 mg, 0.350mmol) in Toluene (15 mL). The mixture was stirred under N_2 at 110 °C for 12 h before being allowed to cool to room temperature. After removal of the solvent under reduced pressure, the residue was purified by silica chromatography (hexanes:CH_2Cl_2=1:1) to give the product (**M2**) as a dark green solid (279 mg, 89%). ^{1}H NMR (300 MHz, $CDCl_3$, ppm) δ: 8.84 (d, *J* = 8.5 Hz, 2H), 7.03 (d, *J* = 8.6 Hz, 2H), 6.93 (s, 2H), 6.86 (s, 2H), 3.65 (d, *J* = 7.5 Hz, 8H), 1.96 – 1.90 (m, 4H), 1.34 – 1.22 (m, 128H), 0.87 – 0.83 (m, 24H). ^{13}C NMR (75 MHz, $CDCl_3$, ppm) δ: 169.80, 168.84, 153.51, 147.05, 144.60, 129.47, 128.40, 124.96, 124.76, 120.45, 119.86, 116.37, 111.37, 107.34, 46.77, 44.88, 37.00, 36.19, 32.01, 31.70, 31.37, 30.29, 30.14, 29.77, 29.67, 29.47, 26.70, 26.44, 22.80, 14.24. HRMS (MALDI) calcd. for $C_{108}H_{172}Br_2N_4O_4$ ([M+H]$^+$): 1815.4630; found 1815.4193.

General procedure for polymerization: To a Schlenk tube charged with a stir bar, **M1** or **M2** (1.0 equiv.), ditin Compound **5** or **6** (1.0 equiv.), $Pd_2(dba)_3$ (2.5 mol%), P(*o*-tol)$_3$ (4 mol%) and 15 mL of toluene were added. The resulting solution was bubbled with argon for 20 min, and the mixture was stirred for 16 h at 110 °C. After the polymerization was complete, the mixture was taken up and precipitated into methanol. The solids were collected by a soxhlet thimble, which was purified by Soxhlet extraction successively with acetone, hexane, and chloroform. To remove residual catalyst, *N,N*-diethyl-2-phenyldiazenecarbothioamide was added to the chloroform fraction, and the mixture was stirred for 30 min at 60 °C before being precipitated into methanol. The collected polymer was dried at 60 °C under vacuum.

P1: 60.0 mg (0.033 mmol) of **M1** and 16.2 mg of (0.033 mmol) **5** were used. Precipitation provided 57.0 mg (95% yield) of a dark solid. As mentioned in the main text, the exact molecular weight of **P1** can't be determined.

P2: 103.8 mg (0.057 mmol) of **M2** and 28.1 mg (0.057 mmol) of **5** were used. Precipitation provided 95.8 mg (92% yield) of a dark solid. M_n = 121 KDa, PDI = 1.70.

P1F: 81.0 mg (0.044 mmol) of **M1** and 23.4 mg of (0.044 mmol) **6** were used. Precipitation provided 50.8 mg (63% yield) of a dark solid. As mentioned in the main text, the exact molecular weight of **P1F** can't be determined.

P2F: 80.1 mg (0.044 mmol) of **M2** and 23.3 mg (0.044 mmol) of **6** were used. Precipitation provided 68.6 mg (85% yield) of a dark solid. M_n = 28 KDa, PDI = 3.0.

Acknowledgements

The authors acknowledge the financial support from Purdue University and from National Science Foundation (NSF CAREER Award, #1653909). This research used resources of the Advanced Photon Source, a U.S. Department of Energy (DOE) Office of Science User Facility operated for the DOE Office of Science by Argonne National Laboratory under Contract DE-AC02-06CH11357.

Keywords: conjugated polymers • bis-isoindigo • donor-acceptor systems • acceptor-acceptor type moieties

References:

[1] M. M. Szumilo, E. H. Gann, C. R. McNeill, V. Lemaur, Y. Oliver, L. Thomsen, Y. Vaynzof, M. Sommer, H. Sirringhaus, *Chem. Mater.* **2014**, *26*, 6796–6804.

[2] Z. Ma, W. Sun, S. Himmelberger, K. Vandewal, Z. Tang, J. Bergqvist, A. Salleo, J. W. Andreasen, O. Inganäs, M. R. Andersson, et al., *Energy Environ. Sci.* **2014**, *7*, 361–369.

[3] X. Liu, B. He, C. L. Anderson, J. Kang, T. Chen, J. Chen, S. Feng, L. Zhang, M. A. Kolaczkowski, S. J. Teat, et al., *J. Am. Chem. Soc.* **2017**, *139*, 8355–8363.

[4] P. Berrouard, F. Grenier, J.-R. Pouliot, E. Gagnon, C. Tessier, M. Leclerc, *Org. Lett.* **2011**, *13*, 38–41.

[5] P. Murto, Z. Genene, C. M. Benavides, X. Xu, A. Sharma, X. Pan, O. Schmidt, C. J. Brabec, M. R. Andersson, S. F. Tedde, et al., **2018**, 8–13.

[6] X. Qiao, Q. Wu, H. Wu, J. Zhang, H. Li, *Adv. Funct. Mater.* **2017**, *27*, 1–8.

[7] L. E. Polander, A. S. Romanov, S. Barlow, D. K. Hwang, B. Kippelen, T. V. Timofeeva, S. R. Marder, *Org. Lett.* **2012**, *14*, 918–921.

[8] J. Yang, H. Wang, J. Chen, J. Huang, Y. Jiang, J. Zhang, L. Shi, Y. Sun, Z. Wei, G. Yu, et al., *Adv. Mater.* **2017**, *29*, 1606162.

[9] J. Chen, Y. Jiang, J. Yang, Y. Sun, L. Shi, Y. Ran, Q. Zhang, Y. Yi, S. Wang, Y. Guo, et al., *ACS Appl. Mater. Interfaces* **2018**, acsami.7b16516.

[10] D. I. James, S. Wang, W. Ma, S. Hedström, X. Meng, P. Persson, S. Fabiano, X. Crispin, M. R. Andersson, M. Berggren, et al., *Adv. Electron. Mater.* **2016**, *2*, 1500313.

[11] C. Zhu, Z. Zhao, H. Chen, L. Zheng, X. Li, J. Chen, Y. Sun, F. Liu, Y. Guo, Y. Liu, *J. Am. Chem. Soc.* **2017**, *139*, 17735–17738.

[12] J. Mei, K. R. Graham, R. Stalder, J. R. Reynolds, *Org. Lett.* **2010**, *12*, 660–663.

[13] E. Wang, W. Mammo, M. R. Andersson, *Adv. Mater.* **2014**, *26*, 1801–1826.

[14] T. Lei, J. H. Dou, J. Pei, *Adv. Mater.* **2012**, *24*, 6457–6461.

[15] J. Mei, D. H. Kim, A. L. Ayzner, M. F. Toney, Z. Bao, *J. Am. Chem. Soc.* **2011**, *133*, 20130–20133.

[16] R. S. Ashraf, A. J. Kronemeijer, D. I. James, H. Sirringhaus, I. McCulloch, *Chem. Commun.* **2012**, *48*, 3939–3941.

[17] J. Huang, Z. Mao, Z. Chen, D. Gao, C. Wei, W. Zhang, G. Yu, *Chem. Mater.* **2016**, *28*, 2209–2218.

[18] I. Meager, M. Nikolka, B. C. Schroeder, C. B. Nielsen, M. Planells, H. Bronstein, J. W. Rumer, D. I. James, R. S. Ashraf, A. Sadhanala, et al., *Adv. Funct. Mater.* **2014**, *24*, 7109–7115.

[19] T. Lei, J.-H. Dou, X.-Y. Cao, J.-Y. Wang, J. Pei, *J. Am. Chem. Soc.* **2013**, *135*, 12168–12171.

[20] Y. Deng, B. Sun, Y. He, J. Quinn, C. Guo, Y. Li, *Chem. Commun.* **2015**, *51*, 13515–13518.

[21] Y. He, C. Guo, B. Sun, J. Quinn, Y. Li, *Chem. Commun.* **2015**, *51*, 8093–8096.

[22] Y. Jiang, Y. Gao, H. Tian, J. Ding, D. Yan, Y. Geng, F. Wang, *Macromolecules* **2016**, *49*, 2135–2144.

[23] T. Hasegawa, M. Ashizawa, J. Hiyoshi, S. Kawauchi, J. Mei, Z. Bao, H. Matsumoto, *Polym. Chem.* **2016**, *7*, 1181–1190.

[24] J. Yang, Z. Zhao, H. Geng, C. Cheng, J. Chen, Y. Sun, **2017**, *1702115*, 1–8.

[25] K. Masui, H. Ikegami, A. Mori, *J. Am. Chem. Soc.* **2004**, *126*, 5074–5075.

[26] M. S. Chen, J. R. Niskala, D. A. Unruh, C. K. Chu, O. P. Lee, J. M. J. Fréchet, *Chem. Mater.* **2013**, *25*, 4088–4096.

[27] G. W. P. Van Pruissen, F. Gholamrezaie, M. M. Wienk, R. A. J. Janssen, *J. Mater. Chem.* **2012**, *22*, 20387.

[28] K. Kawabata, M. Saito, I. Osaka, K. Takimiya, *J. Am. Chem. Soc.* **2016**, *138*, 7725–7732.

[29] T. Ma, K. Jiang, S. Chen, H. Hu, H. Lin, Z. Li, J. Zhao, Y. Liu, Y.-M. Chang, C.-C. Hsiao, et al., *Adv. Energy Mater.* **2015**, *5*, 1501282.

[30] R. S. Ashraf, I. Meager, M. Nikolka, M. Kirkus, M. Planells, B. C. Schroeder, S. Holliday, M. Hurhangee, C. B. Nielsen, H. Sirringhaus, et al., *J. Am. Chem. Soc.* **2015**, *137*, 1314–1321.

[31] L. R. Bard, A. J.; Faulkner, *Electrochemical Methods: Fundamentals and Applications*, Wiley, New York, **2001**.

[32] J. D. Yuen, J. Fan, J. Seifter, B. Lim, R. Hufschmid, A. J. Heeger, F. Wudl, *J. Am. Chem. Soc.* **2011**, *133*, 20799–20807.

[33] K. Takimiya, I. Osaka, M. Nakano, *Chem. Mater.* **2014**, *26*, 587–593.

Entry for the Table of Contents

Insert graphic for Table of Contents here.

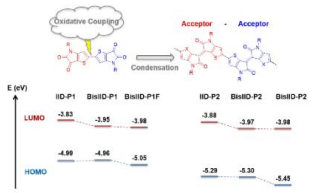

Insert text for Table of Contents here. Isoindigo-based A-A type building blocks - bis-isoindigos - were synthesized via the palladium-catalyzed oxidative coupling. Bis-isoindigo-based polymers show high planarity and delocalized frontier molecular orbitals with selective tuning ability of LUMO/HOMO levels, complementary to the D-D-A approach for the HOMO energy level tuning.

ACS Macro Letters

pubs.acs.org/macroletters Letter

Designing Donor–Acceptor Copolymers for Stable and High-Performance Organic Electrochemical Transistors

Xuyi Luo, Hongguang Shen, Kuluni Perera, Dung Trong Tran, Bryan W. Boudouris,* and Jianguo Mei*

Cite This: ACS Macro Lett. 2021, 10, 1061–1067 Read Online

ACCESS | Metrics & More | Article Recommendations | Supporting Information

ABSTRACT: Organic electrochemical transistors (OECTs) are oft-used for bioelectronic applications, and a variety of OECT channel materials have been developed in recent years. However, the majority of these materials are still limited by long-term performance and stability challenges. To resolve these issues, we implemented a next-generation design of polymers for OECTs. Specifically, diketopyrrolopyrrole (DPP) building blocks were copolymerized with propylene dioxythiophene-based (Pro-based) monomers to create a donor–acceptor-type conjugated polymer (PProDOT-DPP). These PProDOT-DPP macromolecules were synthesized using a straightforward direct arylation polymerization synthetic route. The PProDOT-DPP polymer thin film exhibited excellent electrochemical response, low oxidation potential, and high crystallinity, as evidenced by spectroelectrochemical measurements and grazing incidence wide-angle X-ray scattering measurements. Thus, the resultant polymer thin films had high charge mobility and volumetric capacitance values (i.e., μC^* as high as 310 F cm^{-1} V^{-1} s^{-1}) when they were used as the active layer materials in OECT devices, which places PProDOT-DPP among the highest performing accumulation-mode OECT polymers reported to date. The performance of the PProDOT-DPP thin films was also retained for 100 cycles and over 2000 s of ON–OFF cycling, indicating the robust stability of the materials. Therefore, this effort provides a clear roadmap for the design of electrochemically active macromolecules for accumulation-mode OECTs, where crystalline acceptor cores are incorporated into an all-donor polymer. We anticipate that this will ultimately inspire future polymer designs to enable OECTs with both high electrical performance and operational stability.

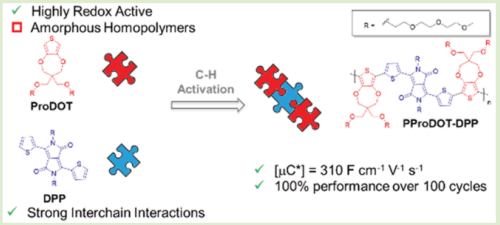

An organic electrochemical transistor (OECT) is a coupled ionic-electronic device, where the active layer material undergoes doping and dedoping based on the electrolytic components upon application of a gate bias.[1,2] Owing to the high-sensitivity sensing and subvoltage operation properties of OECTs, various application advances have been achieved with respect to OECTs, including biological sensors, memory and neuromorphic devices, and electrophysiological monitoring.[3−7] Despite the high degree of initial success that many oft-studied macromolecular systems have had in the realm of OECTs, there are significant opportunities to develop next-generation electrochemically active polymers to improve device performance, switching speed, and cycling stability.[1,8−10]

Semiconducting polymers with solubilizing hydrophilic side chains exhibit high volumetric capacitance, efficient charge transport, and rapid ion injection, as well as compatibility with aqueous electrolytes.[11] Therefore, they have generated extensive scientific interest as a class of channel components for OECTs.[12−17] Among the various types of semiconducting polymers, 3,4-alkylenedioxythiophene-based polymers have achieved remarkable success in many electrochemical applications, such as electrochromic devices and supercapacitors.[18,19] Moreover, they are useful for OECT channel materials due to their high redox stability and charge capacity.[9,20−22] In fact, a model material for many studies, poly(3,4-ethylene dioxythiophene) doped with poly(styrenesulfonate) (PEDOT:PSS), has recently reached a high figure-of-merit (i.e., the product of charge mobility and volumetric capacitance, μC^*) value of 1500 F cm^{-1} V^{-1} s^{-1} in OECT devices.[23,24] 3,4-Propylenedioxythiophene (ProDOT), an analogue of EDOT, is another example of this type of building block. ProDOT has two side chain substitution positions bringing about tunable solubility and versatility of synthetic design.[25] Because ProDOT is a weaker electron donor than EDOT, all-donor ProDOT-based polymers are more stable in their neutral state under ambient conditions.[26] However, ProDOT has not been implemented as extensively as EDOT in OECT studies, with only a single report being provided to date.[27] Despite the fact that OECT devices based on this design exhibited an excellent electrochemical response

Received: May 12, 2021
Accepted: July 26, 2021

Scheme 1. Synthetic Route for the Generation of PProDOT-DPP

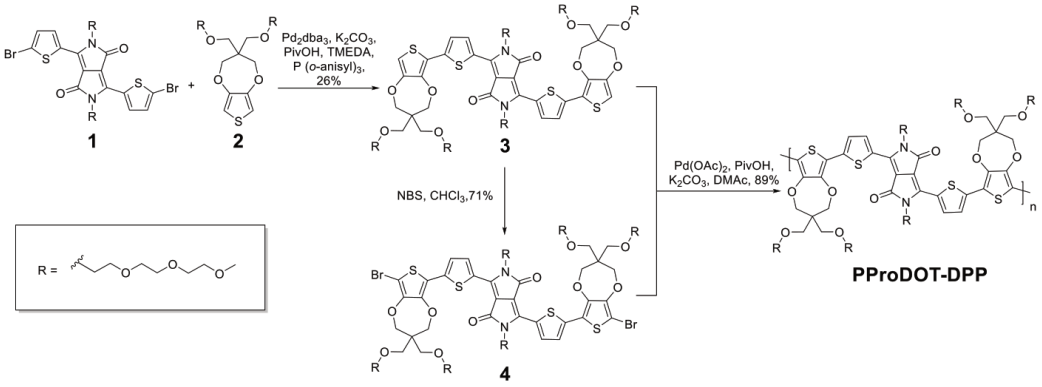

and high charge-storage capacity, this ProDOT-based all-donor-type polymer only achieved a μC^* value of 7.0 F cm^{-1} V^{-1} s^{-1}, which is relatively low when compared with traditional thiophene-based polymer competitors. The performance of this material seems to be limited, in large part, by the completely amorphous nature of the polymer thin film, which resulted in a low charge carrier mobility.[12,13]

While most reported OECT polymers, including the polythiophene-based polymer p(g2T2-g4T2) with the currently highest-reported μC^* materials performance value, are all-donor-type conjugated polymers,[14] donor−acceptor (D-A) conjugated polymers containing electron acceptors such as isoindigo (IID), naphthalenediimide (NDI), and diketopyrrolopyrrole (DPP) have been developed as other promising types of OECT materials. Particularly, p-type D-A conjugated polymers were recently shown to minimize electrochemical side reactions during OECT operation.[15,28,29] For instance, a recently reported pyridine-flanked diketopyrrolopyrrole-containing (DPP-containing) polymer suggests that a D-A-type polymer system prevents the OECT device from reacting with molecular oxygen.[29] A variety of thiophene-flanked diketopyrrolopyrrole (DPP-2T) derivatives were subsequently reported for OECT applications.[8,30,31] Moreover, the μC^* values of these DPP polymers have exceeded 100 F cm^{-1} V^{-1} s^{-1} with particularly high charge mobilities being reported, highlighting the potential of DPP moieties to significantly improve the charge transport properties in OECT polymers.

Here, a DPP-containing ProDOT monomer was designed, and this allowed for the eventual creation of a D-A-conjugated polymer PProDOT-DPP. Then, using a straightforward polymerization method, the DPP motif, which affords strong interchain interactions, was incorporated into the PProDOT polymer backbone. Two ProDOT moieties were present in one repeat unit to maintain electrochemical performance and cycling stability, while a single DPP-2T moiety was used as a planar core to enhance chain rigidity. In turn, this increased the ultimate thin film crystalline fraction and improved the charge transport properties relative to polymers that lacked the DPP functionality. The six triethylene glycol (TEG) side chains that are present in each repeat unit ensure solution processability and allow for enhanced ion infiltration during OECT device operation. Because of these principles, the synthesized polymer, PProDOT-DPP, achieved a high μC^* value of 310 F cm^{-1} V^{-1} s^{-1} during OECT device operation, which places it as one of the top performing accumulation-mode OECT macromolecules reported to date.[8,14,30] Moreover, the performance of PProDOT-DPP was maintained for 100 cycles over 2000 s of cycling between the ON and OFF states. Thus, the proposed polymer design strategy may inspire next-generation polymers with both high performance and enhanced operational stability for mixed conduction applications.

To take advantage of the exposed α positions and blocked β positions during the synthesis, we determined that the ProDOT moiety is particularly suitable as a C−H activation reaction substrate. In this way, we applied a direct arylation polymerization strategy (Scheme 1). First, compound **1** was synthesized with triethylene glycol side chains functionalized on the DPP-2T core, and this species was then brominated. In a similar manner, substitution of triethylene glycol side chains on bis(bromomethyl) 3,4-propylenedioxythiophene afforded compound **2**. Compound **1** was then subjected to an optimized direct arylation reaction using tris(dibenzylideneacetone)-dipalladium(0) and tetramethylethylenediamine (TMEDA) as cocatalysts with an excess of compound **2**, yielding monomer **3** with a moderate yield of 26%.[32] Further bromination of monomer **3** provided monomer **4** in a yield of 71%. Finally, PProDOT-DPP was synthesized via direct arylation polymerization between monomer **3** and monomer **4** with a high yield of 89% (see Supporting Information for synthetic details). The molecular weights of the polymers were initially evaluated by high temperature size exclusion chromatography (SEC) using trichlorobenzene as the eluent at 150 °C (Figure S1). However, the chromatogram only shows a weak signal associated with a low molecular weight species, which prevented us from providing a reasonable estimation of the true molecular weight of the polymer. Further attempts using size exclusion chromatography with tetrahydrofuran at 40 °C as the mobile phase and MALDI-TOF mass spectroscopy analyses were also unsuccessful (Figure S1). This is an unfortunate, but not unreported, issue, as abnormal SEC results of DPP-based polymers with triethylene glycol side chains have been described previously.[8] Despite this inability to extract a quantitative molecular weight estimate, the ^{1}H NMR (Figure S2) and UV−vis-NIR (Figure

https://doi.org/10.1021/acsmacrolett.1c00328
ACS Macro Lett. 2021, 10, 1061−1067

S3) spectra of the resulting material clearly show that the product is macromolecular in nature.

Cyclic voltammetry was employed to interrogate the electrochemical redox reactions and stability of PProDOT-DPP polymers as a function of the electrolyte chemistry (Figure 1a). Due to the large difference in anion sizes of PF_6^-

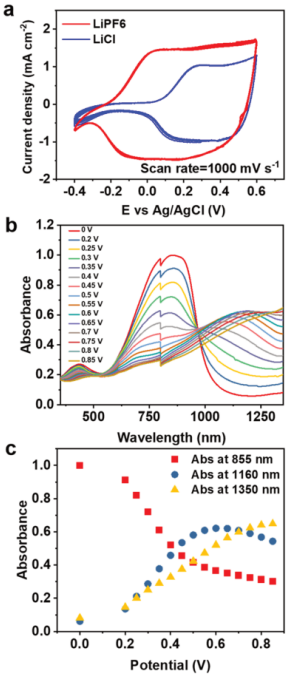

Figure 1. Electrochemical characterization of PProDOT-DPP thin films. (a) The cyclic voltammetry cycling test with a 0.2 M $LiPF_6$ (red) or 0.2 M LiCl (blue) aqueous solution as the supporting electrolyte. (b) UV−vis-NIR spectra of PProDOT-DPP film from a spectroelectrochemical measurement with the 0.2 M $LiPF_6$ aqueous electrolyte. The tick around 800 nm is an instrument response associated with the detector and grating change. (c) Absorbance of PProDOT-DPP recorded as a function of applied potential in the spectro-electrochemical measurement.

and Cl^-, $LiPF_6$ and LiCl aqueous solutions were selected as the electrolytes to establish the impact that anion size had on the electrochemical properties of the PProDOT-DPP when it was used in electrochemical environments.[16] PProDOT-DPP exhibits excellent redox stability during 20 charge−discharge cycles between $-0.4\ V \leq V \leq +0.6$ V versus Ag/AgCl in both electrolytes. Importantly, PProDOT-DPP exhibits a lower oxidation onset potential (i.e., −0.2 V) and a higher oxidation capacitance in the $LiPF_6$ electrolyte relative to the LiCl electrolyte. The more efficient ion exchange and improved electrochemical activity is attributed to the influence of the anion polarizability and anion solvation. As evidenced by many other reports, larger and more polarizable anions with a lower surface charge density require a smaller driving force for injection into the semiconducting polymer.[16,30,33] Notably, the electrochemical conditioning process for PProDOT-DPP in both supporting electrolytes was completed in just the first cycle. Such efficient electrochemical conditioning processes are likely ascribed to the highly hydrophilic triethylene glycol side chain density present in one repeating unit, which allows for easier ion injection. Similar high cycling stability, high capacitance, and fast electrochemical conditioning of PProDOT-DPP are observed in an organic electrolyte, acetonitrile (Figure S4). An ionization potential of −4.57 eV (relative to vacuum) was also estimated from the oxidation onset of PProDOT-DPP in the acetonitrile electrolyte.[34] These cyclic voltammetry results confirm PProDOT-DPP as a potential p-type OECT channel material with a low operating voltage and indicate the versatility of the polymer for different electrochemical conditions.

The spectroelectrochemical measurements of PProDOT-DPP films in $LiPF_6$ aqueous electrolyte provide potential-dependent absorption changes, giving insights into polaron and bipolaron formation, which helps to describe charge and ionic transport at different doping states during the electrochemical process. As shown in Figure 1b,c, the neutral peak absorption maximum of PProDOT-DPP is at ∼855 nm, while the emerging peak at 1160 nm during the oxidation process is the polaron absorption maximum. Until an oxidation potential of +0.5 V versus Ag/AgCl is reached, an isosbestic point at 967 nm indicates pure polaron formation.[35] Further increases in potential lead to bipolaron formation as the intersections of adjacent curves deviate from the previous isosbestic point.[36] The presence of bipolaron formation also is evidenced by a decline in absorption at 1150 nm and an increase in absorption at 1350 nm when the oxidation potential exceeds +0.5 V versus Ag/AgCl. However, due to the strong O−H stretching overtone of water that starts at 1400 nm, the bipolaron absorption maximum cannot be detected.[37] These results suggest that the PProDOT-DPP film has a strong, reversible redox response and a low threshold oxidation potential, which are characteristics of a good p-type OECT material that is compatible with water and aqueous electrolytes.

To investigate the impact of the DPP moieties on the crystallinity and molecular packing in PProDOT-DPP thin films, grazing incidence wide-angle X-ray scattering measurements were performed on PProDOT-DPP polymer thin films spin-coated from 10 mg mL^{-1} chloroform solutions, as shown in Figure S5. The polymer film shows an out-of-plane (010) peak, indicative of a face-on $\pi-\pi$ stacking orientation. Two orders of in-plane packing patterns, (100) and (200), are attributed to lamellar scattering, and they are also observed. The $\pi-\pi$ stacking distance is 3.61 Å and the lamellar spacing is 25.4 Å. The full-width-at-half-maximum (fwhm) of the out-of-plane [i.e., the (010)] peak is 0.195, which corresponds to a coherence length (L_c) of 32 Å. Relative to other DPP polymers, this polymer shows similar $\pi-\pi$ stacking distances and slightly smaller crystalline domains.[38,39] Notably, the lamellar distance of PProDOT-DPP is significantly longer than those of other DPP polymers with triethylene glycol side chains (typically 10−20 Å), but it is almost identical to the lamellar distance of a doped poly(ProDOT) with ethylene glycol side chains (25.8 Å).[8,40] This comparison reveals that interchain triethylene glycol−triethylene glycol interactions on the ProDOT moieties are predominant, while triethylene glycol chains on the DPP moieties have less interactions than those in typical DPP polymers. Also, it should be noted that the poly(ProDOT) polymer itself is amorphous in the neutral state.[32] Therefore, these observations reflect the influence of

https://doi.org/10.1021/acsmacrolett.1c00328
ACS Macro Lett. 2021, 10, 1061−1067

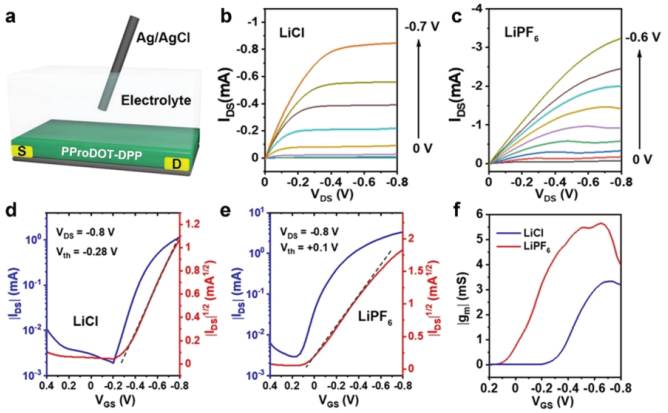

Figure 2. (a) Device structure of the bottom-contact PProDOT-DPP-based OECTs. Output characteristics of the PProDOT-DPP OECTs using (b) 0.1 M LiCl and (c) 0.1 M $LiPF_6$ as the salts for the aqueous electrolytes. Transfer characteristics of the PProDOT-DPP OECTs using (d) 0.1 M LiCl and (e) 0.1 M $LiPF_6$ salts for the aqueous electrolytes. (f) Transconductance values of PProDOT-DPP OECTs using LiCl and $LiPF_6$ electrolytes.

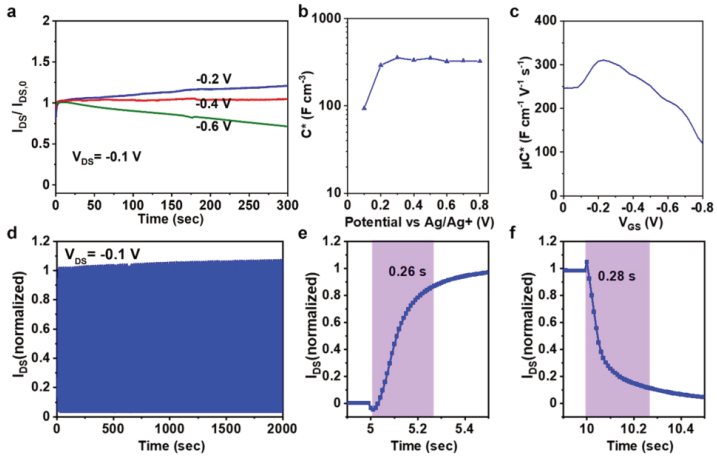

Figure 3. (a) Bias stabilities of PProDOT-DPP OECTs at different V_{GS} values using the 0.1 M $LiPF_6$ electrolyte. (b) Volumetric capacitance as a function of bias applied to the PProDOT-DPP working electrode via differential capacitance measurements using the 0.1 M $LiPF_6$ electrolyte. (c) μC^* values of PProDOT-DPP OECTs as a function of V_{GS} using the 0.1 M $LiPF_6$ electrolyte. (d) Cyclic stability of PProDOT-DPP OECTs using the 0.1 M $LiPF_6$ electrolyte. A constant V_{DS} at −0.1 V and a square wave function of V_{GS} ($V_{GS,on}$ = −0.4 V and $V_{GS,off}$ = 0 V) were applied. (e) Switching on and (f) switching off responses of PProDOT-DPP OECTs ($V_{GS,on}$ = −0.4 V and $V_{GS,off}$ = 0 V) using the 0.1 M $LiPF_6$ electrolyte.

DPP moieties on the increase in the crystalline nature of a ProDOT-based polymer, in agreement with good charge transport properties estimated from OECT devices (vide infra).

The electrical measurements of PProDOT-DPP-based OECTs were performed in two types of aqueous electrolytes: in (a) 0.1 M of LiCl and in (b) 0.1 M $LiPF_6$. An Ag/AgCl gate electrode was submerged in the electrolyte during the measurements (Figure 2a). Typical output characteristics with clear linear and saturation regimes are observed in both LiCl and $LiPF_6$ electrolytes (Figure 2b,c). The OECT transfer curves are shown in Figure 2d,e, where a −0.8 V constant V_{DS} was applied. The OECTs predominantly operate in a hole-transporting accumulation mode where an ON/OFF ratio of $\sim 10^3$ is obtained for both LiCl and $LiPF_6$ electrolytes. The OECTs work mostly in the saturation regime; as a result, the slopes of the linear fit of the V_{GS}−$I_{DS}^{1/2}$ reveal threshold voltages (V_{th}) of −0.28 V and +0.1 V for the LiCl and $LiPF_6$ electrolytes, respectively. The more positive threshold voltage associated with the $LiPF_6$ electrolyte can be attributed to the lower oxidation potential required to electrochemically dope the PProDOT-DPP films, which is consistent with the CV results shown above. Moreover, the higher ON current is obtained for OECT devices with a $LiPF_6$ electrolyte, which suggests that the PF_6^- anion provides for better electrochemical doping in these high performance OECTs that have

https://doi.org/10.1021/acsmacrolett.1c00328
ACS Macro Lett. 2021, 10, 1061−1067

low operating voltages. We highlight that the PProDOT-DPP OECTs demonstrated good device-to-device uniformity from the characterization of eight individual OECTs (Figure S6).

The transconductance (g_m) is considered as an important figure-of-merit of OECTs, and it is defined as $g_m = \Delta I_{DS}/\Delta V_{GS}$.[41] As is shown in Figure 2f, a maximum transconductance (g_m) of ∼5.6 mS was achieved when the PProDOT-DPP thin films (with thickness of ∼30 nm) were evaluated in a $LiPF_6$ aqueous electrolyte, while a slightly lower peak transconductance value of ∼3.3 mS is obtained in the LiCl electrolyte. These results indicate that PF_6^- with a relatively larger radius and higher polarizability is advantageous in improving the doping efficiency in these DPP polymers, thus, enabling a superior g_m in aqueous electrolytes.[30]

The realization of robust operational stability is a fundamental requirement for OECT devices, and this remains a challenge for most conjugated polymers when they are used as the device active layer. To this end, bias stability measurements of PProDOT-DPP OECTs were first performed here under a constant V_{DS} of −0.1 V with various V_{GS} biases (Figures 3a and S7a). For OECTs with the $LiPF_6$ electrolyte, the I_{DS} was maintained over 300 s when biasing the V_{GS} lower than −0.6 V; however, we do note the slight increase in I_{DS} for $V_{GS} = -0.2$ V. This might be attributed to the influence of the trapping of injected anions. For OECTs with the LiCl electrolyte, however, a stable I_{DS} was realized under higher gating potential when the V_{GS} was lower than −0.8 V. At high V_{GS} bias (i.e., − 0.6 V for $LiPF_6$ and −0.8 V for LiCl), the I_{DS} decreased slightly with time. Importantly, this I_{DS} decrease at high V_{GS} biases is correlated with the same oxidation potential where bipolarons start to form, as evidenced by spectroelectrochemical measurements. Hence, the decreased operational stability at higher gating potentials is attributed to the instability of the bipolaron species when formed on PProDOT-DPP.

To better understand the stability maintenance and degradation mechanisms, we performed differential capacitance measurements of the PProDOT-DPP films (Figure S8). The PProDOT-DPP film deposited on ITO served as the working electrode, and potential steps from +0.1 to +0.8 V versus Ag/AgCl were applied. The measured capacitive current (I_c) upon the application of different voltage biases is therefore given by eq 1.[42]

$$I(t) = \frac{E}{R_s}\exp\left(\frac{-t}{R_s C}\right) \tag{1}$$

Here, E is the potential step, R_s is the out-of-plane resistance of the PProDOT-DPP films, and C is the film capacitance. The potential-dependent volumetric capacitance (C^*) is the following.

$$C^* = \frac{C}{Ad} \tag{2}$$

In this equation, A and d are the area and thickness of the PProDOT-DPP films, respectively. From the calculated volumetric capacitance results for the $LiPF_6$ system (Figure 3b), the PProDOT-DPP exhibited a sharp increase of C^* from +0.1 to +0.2 V versus Ag/AgCl, and the polymers then maintained a value of ∼330 F cm^{-3} when the applied potential ranged from +0.2 V to +0.8 V versus Ag/AgCl. We then calculated the μC^* values of PProDOT-DPP OECTs, which reflects the intrinsic ionic and electronic merits of the polymer using the following equation.

$$\mu C^* = \frac{g_m L}{Wd(V_{th} - V_{GS})} \tag{3}$$

Here, W, L, and d are the channel width (2500 μm), length (200 μm), and active layer thickness (∼30 nm), respectively. Note that a relatively long channel (∼200 μm) was applied for the OECT geometry to minimize any contact resistance effects and to provide an accurate evaluation of the intrinsic merits of PProDOT-DPP[43] (Figure S9). As shown in Figure 3c, the μC^* increased slightly as the applied voltage was altered from −0.1 V to −0.25 V; this is consistent with the trend of C^* within the same potential window. Therefore, the initial increase of μC^* can be attributed to the C^* increase together with an almost constant carrier mobility. A peak μC^* of 310 F cm^{-1} V^{-1} s^{-1} is obtained at −0.25 V, which is approaching the highest performance reported for accumulation-mode OECT materials. A good charge mobility ∼0.94 cm^2 V^{-1} s^{-1} was also derived based on the μC^* and C^* values, allowing for robust hole transport at moderate V_{GS} bias. However, the μC^* declined significantly when V_G that was more negative than −0.4 V was applied, and this is consistent with the trends in bias stability degradation. Given that C^* was constant from +0.2 to +0.8 V, the μC^* decrease at high doping levels should be attributed to a decline in hole mobility accompanied with the bipolaron formation. When the unstable bipolaron species formed in PProDOT-DPP upon excessive incorporation of dopants, a loss in film crystallinity together with increased Coulomb scattering occurs, resulting in a lower charge mobility and nonideality of transfer curve at V_{GS} at magnitudes greater than −0.5 V.[44,45]

Based on the above discussions, cyclic stability measurements were performed for the PProDOT-DPP thin films using the $LiPF_6$ electrolyte where the turn-on V_{GS} was always kept more positive than −0.6 V to prevent performance degradation (Figure 3d). As expected, the initial current is retained for 100 cycles over 2000 s of cycling and ON−OFF switching. Moderate switching time scales are obtained for PProDOT-DPP with the $LiPF_6$ electrolyte with a rise time of 0.26 s and a fall time of 0.28 s (i.e., these are calculated as the time it takes to reach 90% of the steady-state current switching value in either direction), respectively (Figure 3e,f). These data indicate good reversible and repeatable electrochemical switching capacities in the PProDOT-DPP-based OECTs. Therefore, the combination of high operational stability and moderate switching speed will allow for the rational design of PProDOT-DPP OECTs for both electrical signal conversion and amplification applications. Volumetric capacitance and switching time scales for PProDOT-DPP with the LiCl electrolyte were also measured (Figures S7b,c and S10). The OECT performance metrics of the PProDOT-DPP-based OECTs in different electrolytes (including mobility, capacitance, μC^*, threshold voltage, on−off ratio, switching speed, and operating stability) are summarized in Table 1.

In summary, PProDOT-DPP was synthesized from a DPP-containing ProDOT monomer. As expected, the DPP moiety provides the ProDOT polymer with higher crystallinity, while the polymer also maintains good electrochemical activity and a low oxidation potential. As a result, PProDOT-DPP thin films exhibit high charge transport properties, high volumetric capacitance, and high redox stability. A peak μC^* value of

https://doi.org/10.1021/acsmacrolett.1c00328
ACS Macro Lett. 2021, 10, 1061−1067

Table 1. Performance Metrics of the PProDOT-DPP OECTs in Different Electrolytes

electrolyte (0.1 M)	$LiPF_6$	LiCl
μC^*_{max} (F cm^{-1} V^{-1} s^{-1})	310	269
μ_{max} (cm^2 V^{-1} s^{-1})	0.94	0.88
C^* (F cm^{-3})	330	305
V_{th} (V)	+0.10	−0.28
ON−OFF ratio	10^2−10^3	10^2−10^3
switching time (s)	0.26	0.15
stability (90% I_{DS} decrease, s)	>2000	1000

310 F cm^{-1} V^{-1} s^{-1} was obtained for the PProDOT-DPP-based OECTs, which is comparable with the best performing accumulation mode OECT polymers reported to date. PProDOT-DPP also demonstrated solid operational stability across 100 cycles over 2000 s of cycling. The strategy of incorporating crystalline DPP cores into all-donor OECT polymers provides a useful foothold to design future generations of polymers for mixed conduction applications that should have both high performance and enhanced operational stability.

■ ASSOCIATED CONTENT

Supporting Information

The Supporting Information is available free of charge at https://pubs.acs.org/doi/10.1021/acsmacrolett.1c00328.

Experimental and synthetic procedures; size exclusion chromatography data; MALDI-TOF MS data; ^1H and ^{13}C NMR data; CV data; X-ray scattering data; OECT device performance curves; OECT contact resistance measurements and extrapolations; OECT switching response time data (PDF)

■ AUTHOR INFORMATION

Corresponding Authors

Bryan W. Boudouris − *Department of Chemistry and Charles D. Davidson School of Chemical Engineering, Purdue University, West Lafayette, Indiana 47907, United States;* orcid.org/0000-0003-0428-631X; Email: boudouris@purdue.edu

Jianguo Mei − *Department of Chemistry, Purdue University, West Lafayette, Indiana 47907, United States;* orcid.org/0000-0002-5743-2715; Email: jgmei@purdue.edu

Authors

Xuyi Luo − *Department of Chemistry, Purdue University, West Lafayette, Indiana 47907, United States*

Hongguang Shen − *Department of Chemistry and Charles D. Davidson School of Chemical Engineering, Purdue University, West Lafayette, Indiana 47907, United States*

Kuluni Perera − *Department of Chemistry, Purdue University, West Lafayette, Indiana 47907, United States*

Dung Trong Tran − *Department of Chemistry, Purdue University, West Lafayette, Indiana 47907, United States*

Complete contact information is available at: https://pubs.acs.org/10.1021/acsmacrolett.1c00328

Notes

The authors declare no competing financial interest.

■ ACKNOWLEDGMENTS

X.L. and J.M. are grateful for the financial support from the National Science Foundation (NSF CAREER Award: 1653909). The work of H.S. and B.W.B. was supported by the Polymers Program at the National Science Foundation (Award No.: 1554957; Program Manager: Dr. Andrew Lovinger), and we are extremely appreciative of this support.

■ REFERENCES

(1) Chung, J.; Khot, A.; Savoie, B. M.; Boudouris, B. W. 100th Anniversary of Macromolecular Science Viewpoint: Recent Advances and Opportunities for Mixed Ion and Charge Conducting Polymers. *ACS Macro Lett.* **2020**, *9* (5), 646−655.

(2) Rivnay, J.; Inal, S.; Salleo, A.; Owens, R. M.; Berggren, M.; Malliaras, G. G. Organic Electrochemical Transistors. *Nat. Rev. Mater.* **2018**, *3* (2), 17086.

(3) Kim, J. H.; Kim, S.; Kim, G.; Yoon, M. Designing Polymeric Mixed Conductors and Their Application to Electrochemical-Transistor-Based Biosensors. *Macromol. Biosci.* **2020**, *20* (11), 2000211.

(4) Inal, S.; Rivnay, J.; Suiu, A. O.; Malliaras, G. G.; McCulloch, I. Conjugated Polymers in Bioelectronics. *Acc. Chem. Res.* **2018**, *51* (6), 1368−1376.

(5) Strakosas, X.; Bongo, M.; Owens, R. M. The Organic Electrochemical Transistor for Biological Applications. *J. Appl. Polym. Sci.* **2015**, *132* (15), 41735.

(6) Ling, H.; Koutsouras, D. A.; Kazemzadeh, S.; van de Burgt, Y.; Yan, F.; Gkoupidenis, P. Electrolyte-Gated Transistors for Synaptic Electronics, Neuromorphic Computing, and Adaptable Biointerfacing. *Appl. Phys. Rev.* **2020**, *7* (1), 011307.

(7) Chen, S.; Surendran, A.; Wu, X.; Lee, S. Y.; Stephen, M.; Leong, W. L. Recent Technological Advances in Fabrication and Application of Organic Electrochemical Transistors. *Adv. Mater. Technol.* **2020**, *5* (12), 2000523.

(8) Moser, M.; Savva, A.; Thorley, K.; Paulsen, B. D.; Hidalgo, T. C.; Ohayon, D.; Chen, H.; Giovannitti, A.; Marks, A.; Gasparini, N.; Wadsworth, A.; Rivnay, J.; Inal, S.; McCulloch, I. Polaron Delocalization in Donor−Acceptor Polymers and Its Impact on Organic Electrochemical Transistor Performance. *Angew. Chem., Int. Ed.* **2021**, *60* (14), 7777−7785.

(9) Inal, S.; Malliaras, G. G.; Rivnay, J. Benchmarking Organic Mixed Conductors for Transistors. *Nat. Commun.* **2017**, *8* (1), 1767.

(10) Bronstein, H.; Nielsen, C. B.; Schroeder, B. C.; McCulloch, I. The Role of Chemical Design in the Performance of Organic Semiconductors. *Nat. Rev. Chem.* **2020**, *4* (2), 66−77.

(11) Moser, M.; Ponder, J. F.; Wadsworth, A.; Giovannitti, A.; McCulloch, I. Materials in Organic Electrochemical Transistors for Bioelectronic Applications: Past, Present, and Future. *Adv. Funct. Mater.* **2019**, *29* (21), 1807033.

(12) Giovannitti, A.; Sbircea, D. T.; Inal, S.; Nielsen, C. B.; Bandiello, E.; Hanifi, D. A.; Sessolo, M.; Malliaras, G. G.; McCulloch, I.; Rivnay, J. Controlling the Mode of Operation of Organic Transistors through Side-Chain Engineering. *Proc. Natl. Acad. Sci. U. S. A.* **2016**, *113* (43), 12017−12022.

(13) Nielsen, C. B.; Giovannitti, A.; Sbircea, D. T.; Bandiello, E.; Niazi, M. R.; Hanifi, D. A.; Sessolo, M.; Amassian, A.; Malliaras, G. G.; Rivnay, J.; McCulloch, I. Molecular Design of Semiconducting Polymers for High-Performance Organic Electrochemical Transistors. *J. Am. Chem. Soc.* **2016**, *138* (32), 10252−10259.

(14) Moser, M.; Hidalgo, T. C.; Surgailis, J.; Gladisch, J.; Ghosh, S.; Sheelamanthula, R.; Thiburce, Q.; Giovannitti, A.; Salleo, A.; Gasparini, N.; Wadsworth, A.; Zozoulenko, I.; Berggren, M.; Stavrinidou, E.; Inal, S.; McCulloch, I. Side Chain Redistribution as a Strategy to Boost Organic Electrochemical Transistor Performance and Stability. *Adv. Mater.* **2020**, *32* (37), 2002748.

(15) Giovannitti, A.; Nielsen, C. B.; Sbircea, D.-T.; Inal, S.; Donahue, M.; Niazi, M. R.; Hanifi, D. A.; Amassian, A.; Malliaras, G.

G.; Rivnay, J.; McCulloch, I. N-Type Organic Electrochemical Transistors with Stability in Water. *Nat. Commun.* **2016**, *7* (1), 13066.
(16) Flagg, L. Q.; Bischak, C. G.; Onorato, J. W.; Rashid, R. B.; Luscombe, C. K.; Ginger, D. S. Polymer Crystallinity Controls Water Uptake in Glycol Side-Chain Polymer Organic Electrochemical Transistors. *J. Am. Chem. Soc.* **2019**, *141* (10), 4345−4354.
(17) Moser, M.; Savagian, L. R.; Savva, A.; Matta, M.; Ponder, J. F.; Hidalgo, T. C.; Ohayon, D.; Hallani, R.; Reisjalali, M.; Troisi, A.; Wadsworth, A.; Reynolds, J. R.; Inal, S.; McCulloch, I. Ethylene Glycol-Based Side Chain Length Engineering in Polythiophenes and Its Impact on Organic Electrochemical Transistor Performance. *Chem. Mater.* **2020**, *32* (15), 6618−6628.
(18) Bryan, A. M.; Santino, L. M.; Lu, Y.; Acharya, S.; D'Arcy, J. M. Conducting Polymers for Pseudocapacitive Energy Storage. *Chem. Mater.* **2016**, *28* (17), 5989−5998.
(19) Beaujuge, P. M.; Reynolds, J. R. Color Control in π-Conjugated Organic Polymers for Use in Electrochromic Devices. *Chem. Rev.* **2010**, *110* (1), 268−320.
(20) Wu, X.; Surendran, A.; Moser, M.; Chen, S.; Muhammad, B. T.; Maria, I. P.; Mcculloch, I.; Leong, W. L. Universal Spray-Deposition Process for Scalable, High-Performance, and Stable Organic Electrochemical Transistors. *ACS Appl. Mater. Interfaces* **2020**, *12* (18), 20757−20764.
(21) Inal, S.; Rivnay, J.; Hofmann, A. I.; Uguz, I.; Mumtaz, M.; Katsigiannopoulos, D.; Brochon, C.; Cloutet, E.; Hadziioannou, G.; Malliaras, G. G. Organic Electrochemical Transistors Based on PEDOT with Different Anionic Polyelectrolyte Dopants. *J. Polym. Sci., Part B: Polym. Phys.* **2016**, *54* (2), 147−151.
(22) Rivnay, J.; Inal, S.; Collins, B. A.; Sessolo, M.; Stavrinidou, E.; Strakosas, X.; Tassone, C.; Delongchamp, D. M.; Malliaras, G. G. Structural Control of Mixed Ionic and Electronic Transport in Conducting Polymers. *Nat. Commun.* **2016**, *7* (1), 11287.
(23) Kim, Y.; Noh, H.; Paulsen, B. D.; Kim, J.; Jo, I.; Ahn, H.; Rivnay, J.; Yoon, M. Strain-Engineering Induced Anisotropic Crystallite Orientation and Maximized Carrier Mobility for High-Performance Microfiber-Based Organic Bioelectronic Devices. *Adv. Mater.* **2021**, *33* (10), 2007550.
(24) Kim, S.-M.; Kim, C.-H.; Kim, Y.; Kim, N.; Lee, W.-J.; Lee, E.-H.; Kim, D.; Park, S.; Lee, K.; Rivnay, J.; Yoon, M.-H. Influence of PEDOT:PSS Crystallinity and Composition on Electrochemical Transistor Performance and Long-Term Stability. *Nat. Commun.* **2018**, *9* (1), 3858.
(25) Perera, K.; Yi, Z.; You, L.; Ke, Z.; Mei, J. Conjugated Electrochromic Polymers with Amide-Containing Side Chains Enabling Aqueous Electrolyte Compatibility. *Polym. Chem.* **2020**, *11* (2), 508−516.
(26) Reeves, B. D.; Grenier, C. R. G.; Argun, A. A.; Cirpan, A.; McCarley, T. D.; Reynolds, J. R. Spray Coatable Electrochromic Dioxythiophene Polymers with High Coloration Efficiencies. *Macromolecules* **2004**, *37* (20), 7559−7569.
(27) Savagian, L. R.; Österholm, A. M.; Ponder, J. F.; Barth, K. J.; Rivnay, J.; Reynolds, J. R. Balancing Charge Storage and Mobility in an Oligo(Ether) Functionalized Dioxythiophene Copolymer for Organic- and Aqueous- Based Electrochemical Devices and Transistors. *Adv. Mater.* **2018**, *30* (50), 1804647.
(28) Wang, Y.; Zeglio, E.; Liao, H.; Xu, J.; Liu, F.; Li, Z.; Maria, I. P.; Mawad, D.; Herland, A.; McCulloch, I.; Yue, W. Hybrid Alkyl−Ethylene Glycol Side Chains Enhance Substrate Adhesion and Operational Stability in Accumulation Mode Organic Electrochemical Transistors. *Chem. Mater.* **2019**, *31* (23), 9797−9806.
(29) Giovannitti, A.; Rashid, R. B.; Thiburce, Q.; Paulsen, B. D.; Cendra, C.; Thorley, K.; Moia, D.; Mefford, J. T.; Hanifi, D.; Weiyuan, D.; Moser, M.; Salleo, A.; Nelson, J.; McCulloch, I.; Rivnay, J. Energetic Control of Redox-Active Polymers toward Safe Organic Bioelectronic Materials. *Adv. Mater.* **2020**, *32* (16), 1908047.
(30) Wu, X.; Liu, Q.; Surendran, A.; Bottle, S. E.; Sonar, P.; Leong, W. L. Enhancing the Electrochemical Doping Efficiency in Diketopyrrolopyrrole-Based Polymer for Organic Electrochemical Transistors. *Adv. Electron. Mater.* **2021**, *7* (1), 2000701.
(31) Jia, H.; Huang, Z.; Li, P.; Zhang, S.; Wang, Y.; Wang, J.-Y.; Gu, X.; Lei, T. Engineering Donor−Acceptor Conjugated Polymers for High-Performance and Fast-Response Organic Electrochemical Transistors. *J. Mater. Chem. C* **2021**, *9* (14), 4927−4934.
(32) Wakioka, M.; Takahashi, R.; Ichihara, N.; Ozawa, F. Mixed-Ligand Approach to Palladium-Catalyzed Direct Arylation Polymerization: Highly Selective Synthesis of π-Conjugated Polymers with Diketopyrrolopyrrole Units. *Macromolecules* **2017**, *50* (3), 927−934.
(33) Cendra, C.; Giovannitti, A.; Savva, A.; Venkatraman, V.; McCulloch, I.; Salleo, A.; Inal, S.; Rivnay, J. Role of the Anion on the Transport and Structure of Organic Mixed Conductors. *Adv. Funct. Mater.* **2019**, *29* (5), 1807034.
(34) Cardona, C. M.; Li, W.; Kaifer, A. E.; Stockdale, D.; Bazan, G. C. Electrochemical Considerations for Determining Absolute Frontier Orbital Energy Levels of Conjugated Polymers for Solar Cell Applications. *Adv. Mater.* **2011**, *23* (20), 2367−2371.
(35) Zozoulenko, I.; Singh, A.; Singh, S. K.; Gueskine, V.; Crispin, X.; Berggren, M. Polarons, Bipolarons, And Absorption Spectroscopy of PEDOT. *ACS Appl. Polym. Mater.* **2019**, *1* (1), 83−94.
(36) Enengl, C.; Enengl, S.; Pluczyk, S.; Havlicek, M.; Lapkowski, M.; Neugebauer, H.; Ehrenfreund, E. Doping-Induced Absorption Bands in P3HT: Polarons and Bipolarons. *ChemPhysChem* **2016**, *17* (23), 3836−3844.
(37) Wilson, R. H.; Nadeau, K. P.; Jaworski, F. B.; Tromberg, B. J.; Durkin, A. J. Review of Short-Wave Infrared Spectroscopy and Imaging Methods for Biological Tissue Characterization. *J. Biomed. Opt.* **2015**, *20* (3), 030901.
(38) Di Pietro, R.; Erdmann, T.; Carpenter, J. H.; Wang, N.; Shivhare, R. R.; Formanek, P.; Heintze, C.; Voit, B.; Neher, D.; Ade, H.; Kiriy, A. Synthesis of High-Crystallinity DPP Polymers with Balanced Electron and Hole Mobility. *Chem. Mater.* **2017**, *29* (23), 10220−10232.
(39) Yang, S. F.; Liu, Z. T.; Cai, Z. X.; Dyson, M. J.; Stingelin, N.; Chen, W.; Ju, H. J.; Zhang, G. X.; Zhang, D. Q. Diketopyrrolopyrrole-Based Conjugated Polymer Entailing Triethylene Glycols as Side Chains with High Thin-Film Charge Mobility without Post-Treatments. *Adv. Sci.* **2017**, *4* (8), 1700048.
(40) Mazaheripour, A.; Thomas, E. M.; Segalman, R. A.; Chabinyc, M. L. Nonaggregating Doped Polymers Based on Poly(3,4-Propylenedioxythiophene). *Macromolecules* **2019**, *52* (5), 2203−2213.
(41) Khodagholy, D.; Rivnay, J.; Sessolo, M.; Gurfinkel, M.; Leleux, P.; Jimison, L. H.; Stavrinidou, E.; Herve, T.; Sanaur, S.; Owens, R. M.; Malliaras, G. G. High Transconductance Organic Electrochemical Transistors. *Nat. Commun.* **2013**, *4* (1), 2133.
(42) Gudjonsdottir, S.; van der Stam, W.; Kirkwood, N.; Evers, W. H.; Houtepen, A. J. The Role of Dopant Ions on Charge Injection and Transport in Electrochemically Doped Quantum Dot Films. *J. Am. Chem. Soc.* **2018**, *140* (21), 6582−6590.
(43) Paterson, A. F.; Faber, H.; Savva, A.; Nikiforidis, G.; Gedda, M.; Hidalgo, T. C.; Chen, X.; McCulloch, I.; Anthopoulos, T. D.; Inal, S. On the Role of Contact Resistance and Electrode Modification in Organic Electrochemical Transistors. *Adv. Mater.* **2019**, *31* (37), 1902291.
(44) Wegner, B.; Lungwitz, D.; Mansour, A. E.; Tait, C. E.; Tanaka, N.; Zhai, T.; Duhm, S.; Forster, M.; Behrends, J.; Shoji, Y.; Opitz, A.; Scherf, U.; List-Kratochvil, E. J. W.; Fukushima, T.; Koch, N. An Organic Borate Salt with Superior p -Doping Capability for Organic Semiconductors. *Adv. Sci.* **2020**, *7* (17), 2001322.
(45) Salzmann, I.; Heimel, G.; Oehzelt, M.; Winkler, S.; Koch, N. Molecular Electrical Doping of Organic Semiconductors: Fundamental Mechanisms and Emerging Dopant Design Rules. *Acc. Chem. Res.* **2016**, *49* (3), 370−378.

https://doi.org/10.1021/acsmacrolett.1c00328
ACS Macro Lett. 2021, 10, 1061−1067